Resonantly interacting degenerate Bose gas oddities

by

Catherine Ellen Klauss

B.S. Physics, University of Arizona, 2011

A thesis submitted to the
Faculty of the Graduate School of the
University of Colorado in partial fulfillment
of the requirements for the degree of
Doctor of Philosophy
Department of Physics
2017

This thesis entitled:
Resonantly interacting degenerate Bose gas oddities
written by Catherine Ellen Klauss
has been approved for the Department of Physics

Dr. Eric A. Cornell

Dr. Jun Ye

Date

The final copy of this thesis has been examined by the signatories, and we find that both the content and the form meet acceptable presentation standards of scholarly work in the above mentioned discipline.

Klauss, Catherine Ellen (Ph.D., Physics)

Resonantly interacting degenerate Bose gas oddities

Thesis directed by Dr. Eric A. Cornell

The progression from two- through few- to many-body physics is an open and interesting question. Experiments that can test these theories must walk the fine line between cultivating a rich many-body system, yet preventing the interactions from completely destroying the system before study. This thesis explores the two- and few-body interactions present in a resonantly interacting degenerate Bose gas. We explore these interactions as a function of the density of the initial Bose-Einstein condensate. We use loss rates to characterize the interactions and find that a significant portion of the perceived atomic loss is from sweeping the atoms into loosely bound molecules. The decay dynamics identify a molecule mixture of both Feshbach dimers and Efimov trimers.

Dedication

To my mother and father, Fiona and Peter Klauss.

Thank you for always encouraging me to be strong, smart, and stubborn.

Acknowledgements

The most important section of this thesis, by far, is the acknowledgements. I would not be the scientist I am today without the patient mentoring that makes JILA so great. And I would no be writing a thesis today without the many people who encouraged me to keep pushing through graduate school admist life's many challenges.

First, I would like to thank my late advisor, Debbie Jin. Thank you for hiring me six years ago, agreeing to take me on as a mentee. Though I would have liked many more years of your mentorship, you taught me so much in just five. You taught me to focus on the details, to not treat anything as a "black box", and how to effectively communicate science in meetings and presentations. You taught me to never be afraid to ask questions, and to never blame myself for not immediately understanding every scientific technique. Thank you for coming in to talk to me, one-on-one, after my dad died; it meant a lot to have someone I looked up to tell me that they knew this was difficult. Thank for letting me come into your office and ask questions, even if they were more about life than science. And thank you for all the countless hours you stopped by lab, eager to help us solve our current problem.

Second (but no less), I'd like to thank the advisor that stuck around, Eric Cornell. Thank you for having respect for me, but even more so, thank you for letting me know that you have respect for me. I've dealt with a great deal of self-doubt while pushing forward through graduate school, but your opinion that I might actually be "good" at this science thing reminds me to remain confident. Thank you for teaching me how to think of the big picture in science, and for showing me first-hand how creativity merges with science. You and Debbie complimented each other very well as mentors, covering both the big picture and the small details.

Third, I'd like to thank all of the lab mates I've shared mutual suffering with. Xin, you are a reliable lab mate and great friend. It was inspiring how quickly you learned the in's and out's of the experiment; your excitement about science kept me motivated on days when everything in lab seemed to be breaking. Phil, thank you for teaching me that four bikes is not too many bikes, and that morning meetings are better with fresh-pressed coffee. Rob, thank you for letting me live vicariously through your post-graduate world travels, and reminding me that one day, I too could graduate. Our undergraduate Carlos, thank you for being an easy undergraduate: you were self-motivated, and I was continually amazed at the minimal instruction I could away with. Lastly, I'd like to thank Krista Beck for keeping our group running smoothly, always making sure I had plane tickets to conferences, and for the occasional fresh-baked cookie!

While I directly worked on the contents of this thesis with the people mentioned above, there were also a large group of graduate students at JILA and CU physics that are still responsible for the completion of this thesis. While I have learned a great deal of science in the past six years, I've learned even more how valuable a small act of kindness can be. Yomay Shyur, you win the award of best roommate I've ever had. Thank you for the many cakes and macaroons over the years, and thank you for the food you cooked and left in the freezer for me after my dad died. Liz Shanblatt, thank you for all the feminist talks and bottles of wine, and the many dinners we've shared together. Sara Campbell, thank you for the all of the night hikes and climbing you led over the years, and thank you for letting me vent all of my frustrations during these outings. Thank you for the card you made for me after my surgery, and for that time you snuck a bag of chips out of a lab meeting for me. AJ Johnson, thank you for starting Holmes place, although I have never lived there, it is my home away from home, the safe haven of Boulder. Thank you for starting wine nights, and for the giving me the ride to the airport the day after my mom died. Ben Pollard, thank for watching the pups many times over, and taking on the very important role of Teddy's favorite person. And thank you for the many hikes you do not remember. Andrew Koller, thank you for the many chats, the stupid jokes, and for dragging me up North Arapahoe. And thank for giving me half of your sandwich that day. And Helen McCreery, thank you for sending me the book of Colorado scrambles to remind me to look toward fun, future days while I was cleaning out my parents' house. And thank you for coming over with bee suits to help me kill the nest of wasps at my house, I'm sorry I sprayed insecticide on your suit. Andy Missert, thank you for the many delicious foods you have cooked over the years, and for teaching me how properly appreciate food pairings. Scott Johnson, thank you for the company on many walks to the hill to get lunch, and the many evenings climbing at the BRC - exercise and fresh air are necessary ingredients for good science. Bob Peterson, thank you always being around to answer my many questions about fixing nearly everything, and reminding me whenever one could, to question if one should. Brian O'Callahan, thank for you those brownies you baked for me after my cat died. Ben Chapman, thank you for letter you wrote my cat, and for starting (and ending) book club. Judith Olson, thank for you all the midday coffee chats about how to best help our mothers. Will Kindel, thank you for bringing over ginger tea and that amazing ginger soda after my surgery, and thank you for your always positive outlook on life. And everyone else from the lunch table - Michelle, Jack, Oscar, Nico, Victor - for many days of grad school my favorite part was the hour from noon to 1, having the grad school equivalence of family dinner, discussing life and making fun of it even more; it would not have been the same without all of the lunch-family members.

Lastly, several people helped me crush grad school from afar. Jen Akazawa, thank you for the many hours of life advice and the home-roasted coffee beans that fueled this thesis. Laura Healy, thank for being a grad school buddy, thank you for your advice on how to keep pushing through, and how to decide what to do after. Erika Spreiser, girl, thank you for all of the editing you have done and will probably still do in the future for me. And very lastly, my brother, Alex Klauss, thanks for supporting me, for being proud of me, and reminding me that Dad and Mom were proud of me as well.

Contents

Chapter

Appendix

Chapter 1

Motivation

1.1 History of ultracold gases

The neutrons at the center of a neutron star, the electrons in a high-temperature superconductor, and the atoms that compose liquid helium are all subject to the fascinating yet barely-understood physics: quantum degenerate many-body physics. The systems are fascinating, but are also complicated by many interacting, overlapping particles constantly fighting for their space.

The progression from two- through few- to many-body physics is an open and interesting question today in physics. What is easily modeled analytically with only two bodies becomes nearly impossible to model with three or more bodies. Many theorists have developed models to describe few- and many-body interactions [1, 2, 3, 4, 5, 6, 7, 8, 9, 10, 11, 12]. Experiments that can test these models must walk the fine line between cultivating a rich many-body system, yet preventing the interactions from completely destroying the system before study.

Ultracold atomic gases are a great candidate for these studies because they are easy to control. There are two types of ultracold atomic gases: Bose-Einstein condensates (BEC) and degenerate Fermi gases. The former was experimentally realized in 1995 [13, 14, 15], the latter in 1999 [16]. The thermodynamics of a trapped BEC are described in detail in [17] and [18]. It is generally more difficult to study a Bose gas than a Fermi gas in the strongly interacting regime due to increased loss from three-body recombination. However, three-body interactions heavily influence the few- and many-body physics that we are interested in studying, making Bose gases worth the effort to study. In this thesis, we use a ^{85}Rb BEC to study quantum many-body interactions.

1.2 Thesis contents

The apparatus on which all of the experiments recorded in this thesis were performed is now dismantled. A new, shiny experiment is currently being set up by several bright graduate students eager to continue JILA's resonantly interacting Boson (JRIB) experiments. The purpose of this thesis is to explain what we saw in the first generation, in hopes of inspiring future experiments and preventing some (many, we made many) time-wasting mistakes.

Chapter 2 discusses the background of strongly-interacting Bose gas experiments, from the weakly interacting mean-field regime, through the strongly-interacting regime, to the unitary regime centered about the Feshbach resonance.

Chapter 3 describes our imaging techniques. It covers a basic review of our high-intensity imaging techniques to obtain reliable measurements of large optical depths, and discusses the higher-magnification telescope implemented into our apparatus to enable imaging on resonance. It also reviews the non-standard image analysis techniques necessary when using high-intensity imaging.

Chapter 4 covers our application of time-variable interactions to vary the density of our condensate by over two orders of magnitude.

Chapter 5 describes our magnetic ramp to and from resonance. It discusses the effects of varying both the ramp in to, the evolution time on, and the ramp away from resonance. We present a measurement of the observed loss on resonance across two orders of magnitude in density. We also present evidence that the ramp away from resonance can sweep some resonant atoms into shallow molecules.

Chapter 6 discusses various techniques for transferring Feshbach dimers to the imaging state.

Chapter 7 describes a simple model to explain the formation of Feshbach molecules with the ramp away from resonance. We find that this model works well for systems that have evolved on resonance for a long time with respect to the density-determined time scale t_n, defined in Chapter 2.

In Chapter 8 we investigate the lifetime of the resonantly produced molecules for various initial densities and find that the loss rate is best described by two lifetimes. When we consider both spontaneous decay and atom-dimer collisions, the slower loss rates agree with predictions for the Feshbach dimer. We find the larger loss rate to be both density independent and in good agreement with predictions for the first-excited Efimov trimer lifetime.

In Chapter 9 we attempt to study the production of both dimers and trimers as a function of evolution time as a means to study the many-body interactions on resonance. We very quickly run into problems when we discover that for short evolution times the molecule lifetimes (which we previously used to distinguish between dimers and trimers) change. We present a theory that these altered lifetimes are evidence of the resonant atoms being swept into a superposition of dimers and trimers. We also suggest a future experiment to untangle dwell dependencies from ramp out dependencies.

In Appendix A there is a plot legend that explains the formatting of information found in most of the plots in this thesis. Appendix B has the long-lifetime data used to determine the dimer lifetime in Chapter 8. Appendix C has our best molecule lifetime data as a function of dwell time at resonance. All data were taken with an intermediate density cloud of 1.3 E12/cc, at $a_f = 700\,a_0$. Appendix D has more molecule lifetime data at different densities. Appendix E has molecule lifetime data where we used a square (rather than curved) microwave envelope to transfer the molecules to the imaging state. Appendix F has dwell data of both atoms and molecules. Appendix G has ramp out data of both atoms and molecules. And finally, to tie it all together, Appendix H has a table recording the conditions of all the molecule lifetime data in this thesis, along with their figure number for easy reference.

Chapter 2

Background

In this chapter we present previous experimental and theoretical progress towards using ultracold atomic gases to understand quantum many-body interactions. We first consider weak two-body interactions between atoms in our condensate, then consider these interactions becoming stronger, and eventually infinite (effectively infinite really, as they are larger than any other energy scale in the system). We then consider the possibility of three-body interactions, and finally discuss loss rates as a key observable.

2.1 Mean-field approximation

2.1.1 Gross-Pitaevskii equation

We begin first by considering a a dilute condensate with minimal interactions between the particles. When the interactions between atoms are relatively weak, we can describe these interactions using the mean-field approximation. The approximation was first developed in 1947 by Bogoliubov [19] by minimizing a perturbation to the energy of the system. The time-independent mean-field energy of a harmonically trapped Bose gas is [20]

$$E(\psi) = \int \frac{\hbar^2}{2m}|\nabla\psi|^2 + V(\vec{r})|\psi(\vec{r})|^2 + \frac{U_0}{2}|\psi(\vec{r})|^4 \, d\vec{r}. \tag{2.1}$$

The terms in the equation above represent the kinetic, trapping, and interaction energy, respectively. $V(\vec{r})$ is the trapping potential of the system with trapping frequencies ω_i, equal to

$\frac{m}{2}\left(\omega_x^2 x^2 + \omega_y^2 y^2 + \omega_z^2 z^2\right)$. The interaction energy between a pair of particles is U_0/V, where V is the volume of the dilute gas.

The number of Bosons in the condensate is given by N. By minimizing $E - \mu N$, where μ is a Lagrange multiplier equal to the chemical potential, $\mathrm{d}E/\mathrm{d}N$, we derive the Gross-Pitaevskii equation [17],

$$\frac{-\hbar^2}{2m}\nabla^2\psi(\vec{r}) + V(\vec{r})\psi(\vec{r}) + U_0|\psi(\vec{r})|^2\psi(\vec{r}) = \mu\psi(\vec{r}). \tag{2.2}$$

We define $a_{\mathrm{osc_i}}$ as the harmonic oscillator length $= \sqrt{\frac{\hbar}{m\omega_i}}$, and $a_{\bar{\mathrm{osc}}}$ is the geometric mean of the harmonic oscillator lengths for three dimensions. If the number of bosons in the condensate is sufficiently large such that $N \gg a_{\bar{\mathrm{osc}}}/a$ (where a is the two-body scattering length defined in the next section), the kinetic energy term of the Gross-Pitaevskii equation can be neglected [20]. This is called the Thomas-Fermi approximation. Equation (2.2) then reduces to

$$V(\vec{r}) + U_0|\psi(\vec{r})|^2 = \mu, \tag{2.3}$$

$$\psi(\vec{r}) = \sqrt{\frac{\mu - V(\vec{r})}{U_0}}. \tag{2.4}$$

$\psi(\vec{r})$ is not real for any value of $V(\vec{r}) > \mu$; this restricts the radii of the condensate to

$$R_{\mathrm{TF_i}} = \sqrt{\frac{2\mu}{m\omega_i^2}}. \tag{2.5}$$

This radius is called the Thomas-Fermi radius. Plugging in the relation between the chemical potential μ and the geometric mean of the trapping frequencies, $\bar{\omega}$,

$$\mu = \frac{15^{2/3}}{2}\left(\frac{Na}{a_{\bar{\mathrm{osc}}}}\right)^{2/5}\hbar\bar{\omega}, \tag{2.6}$$

we get the geometric mean of the Thomas-Fermi radius in terms of the number of atoms in the condensate:

$$R_{\mathrm{TF}} = \left(\frac{15Na}{a_{\bar{\mathrm{osc}}}}\right)^{1/5} a_{\bar{\mathrm{osc}}}. \tag{2.7}$$

2.1.2 Two-body scattering

In scattering theory, the presence of a weakly-bound state can strongly modify the scattering in the unbound state [17]. Where the energy of the bound state is equal to that of the zero kinetic energy unbound state is called the center of the Feshbach resonance. When the magnetic moments of the two states are different, the Feshbach resonance makes it possible to control the scattering interaction strength magnetically [21].

The strength of the interaction potential is defined by the s-wave scattering length, a. For low-energy scattering, the scattering length is the distance from the origin at which the approximated scattering wave function intercepts the x-axis [17]. A more intuitive picture of a is that it is the radius of a "hard shell" that approximates the low-energy scattering of the atoms [22]. Near the Feshbach resonance, a is described by

$$a(B) = a_{\mathrm{bg}} \left(1 - \frac{\Delta}{B - B_0}\right), \tag{2.8}$$

where a_{bg} is the background scattering length, Δ is the width of the resonance, and B_0 is the resonance position [23]. For the ^{85}Rb resonance centered at $B_0 = 155.041(18)$ G, $\Delta = 10.71(2)$ G and $a_{\mathrm{bg}} = -443(3)\, a_0$ [24]. This ^{85}Rb Feshbach resonance is plotted in figure 2.1.

The low-energy bound state that creates our Feshbach resonance is that of the Feshbach molecule. The Feshbach molecule is a state where two atoms are weakly bound together, we colloquially call this molecule a dimer. The energy of the Feshbach molecule is given by

$$E_b = \frac{-\hbar^2}{m\, a^2}, \tag{2.9}$$

where m is the mass of the ^{85}Rb atom [21]. This binding energy is plotted in figure 2.2.

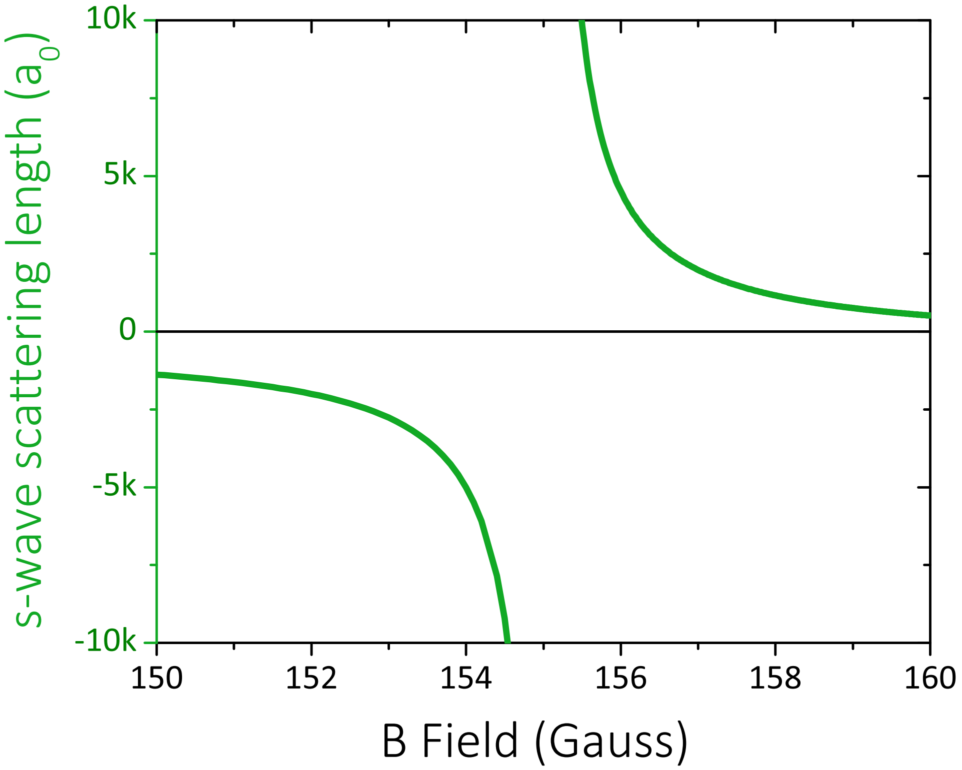

Figure 2.1: The two-body s-wave scattering length near the 155 G Feshbach resonance of ^{85}Rb.

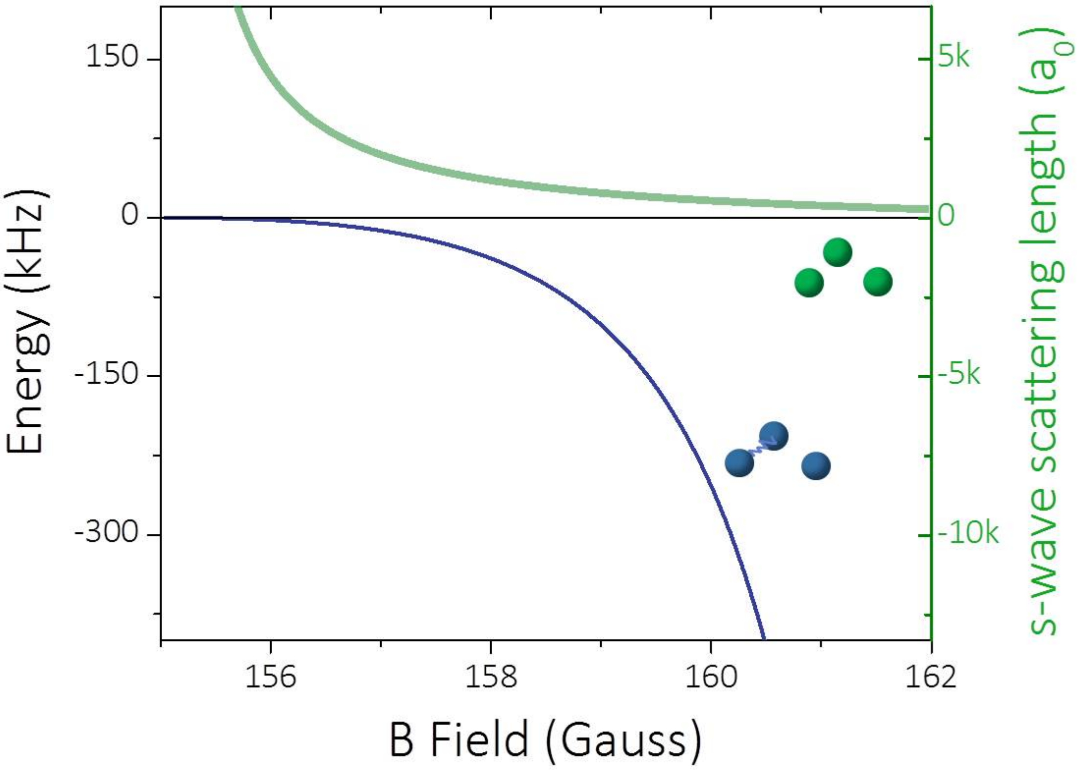

Figure 2.2: The blue line shows the calculated molecular energy for the Fesbach dimer, E_b. The green line is the two-body scattering length.

2.2 Beyond mean-field

The mean-field energy of the interacting Bose gas is to first order equal to

$$E = 4\pi \frac{\hbar^2 a}{m} n, \tag{2.10}$$

where n is the density of the system. This approximation is valid when the system is in the weakly-interacting regime, $na^3 \ll 1$.

When the interactions increase, the energy is corrected perturbatively to

$$E = 4\pi \frac{\hbar^2 a}{m} n \left(1 + \frac{128}{15\sqrt{\pi}} \sqrt{na^3} + ... \right). \tag{2.11}$$

The right-most term in the equation above is known the the Lee-Haung-Yang (LHY) correction [1, 25].

For our analysis, we arbitrarily define the weakly interacting to strongly interacting boundary to be where the LHY correction is equal to 10%. This occurs at the still surprisingly small value of $na^3 = 0.000431$. In the strongly-interacting regime, Bose gases are more subject to few-body effects, including three-body recombination [26, 27, 28, 29, 30] and two- and three-body contact (the non-classical probability to find two or three particles near each other) [11]. There has been much experimental advance in probing Bose gases in the strongly interacting regime [31, 32, 33, 34].

2.3 Unitarity: the resonant regime

Approaching closer to the Feshbach resonance, the interactions in a Bose gas become stronger. We define a third regime when $na^3 > 1$ as the resonant or unitary regime. The latter name stems from unitarity, aptly named because the scattering probability saturates to 1.

When $na^3 > 1$, the "hard shell" of the atoms is larger than the interparticle spacing between the atoms, $n^{-1/3}$. In this picture then, the atoms are overlapping. Exactly on the resonance the scattering length a is formally infinite. What happens then to the energy of the system? Because a is formally infinite, it is no longer a relevant parameter in the system and we can assume $a \rightarrow \sim n^{-1/3}$.

The energy of the system can then be parameterized by the density,

$$E_n \equiv \hbar^2 \left(6\pi^2 n\right)^{2/3} /2m. \tag{2.12}$$

Because the system is apparently defined solely by one parameter, we anticipate behavior that is universal with density. Universal behavior in itself is exciting: other quantum degenerate universal systems are high-temperature superconductors and neutron stars.

We can also define the momentum and time scales at which the system should evolve as

$$\kappa_n \equiv \left(6\pi^2 n\right)^{1/3}, \tag{2.13}$$

$$t_n \equiv \hbar/E_n. \tag{2.14}$$

The system's quick evolution at resonance, with t_n on the order to tens of microseconds for standard condensate densities, complicates experiments. However for several years now experimentalists have found novel solutions to overcome these obstacles. By studying post-resonance momentum generation, we have previously shown that degenerate Bose gases have a short-lived quasi-equilibrium state on resonance [35, 36]. Other experiments have studied the perceived loss after a resonant Bose gas is brought back to weak interactions [37, 38, 39], and most recently the two- and three-body contacts of a resonant Bose gas were measured [40]. The fact that there are many theoretical predictions for behaviors expected to emerge from many-body effects present in the resonant Bose gases has made experimental progress in this regime a rewarding endeavor [41, 42, 43, 44, 45, 46, 10, 11, 12, 47, 48].

2.4 Beyond universality: Efimov trimers

Interactions become even more interesting when we look beyond two-body interactions to few- and many-body interactions. The first step to this extension is the study of three-body interactions. Three-body interactions were first studied by nuclear physicists to describe the interactions between nuclei [49]. In particular, Vitaly Efimov derived the existence of an infinite series of three-body bound states in 1970 [2, 3]. Each bound state is larger than the last by a scaling factor of $\mathrm{e}^{\pi/s_0} \approx 22.7$, where $s_0 = 1.00624$ [4, 50], and the binding energy $E_{\mathrm{T}}^{(p)}$ $(p = 0, 1, 2...)$ is smaller by a factor of

22.7^2 [4, 9]. Efimov bound states are also considered “universal” - not because their energy depends only on density, but because they have discrete scale-invariance, and the physics can therefore be applied to a broad spectrum of physical systems.

Ultracold atomic physics experiments (in particular Boson experiments that, unlike their Fermionic counterparts, are subject to three-body influence) have proven that Efimov bound states exist as a bound three-atom molecule, called a trimer. These experiments have proven the existence of Efimov states through observation of inelastic collision rates in atomic samples [51, 52, 34, 53, 54, 55, 56] and atom-dimer resonances [57, 58, 59, 60, 61], and observation of atomic loss after RF association into Efimov states [62, 63, 64]. While these experiments send atoms into the Efimov bound state, they do not directly observe the atoms in the Efimov bound state but instead surmise their existence from loss rates of unbound atoms or two-body bound dimers. Very loosely bound trimers have been observed in diffracted molecular beams of gaseous helium [65]. However, direct observation of Efimov trimers in a cold, controlled gas has yet to be experimentally realized.

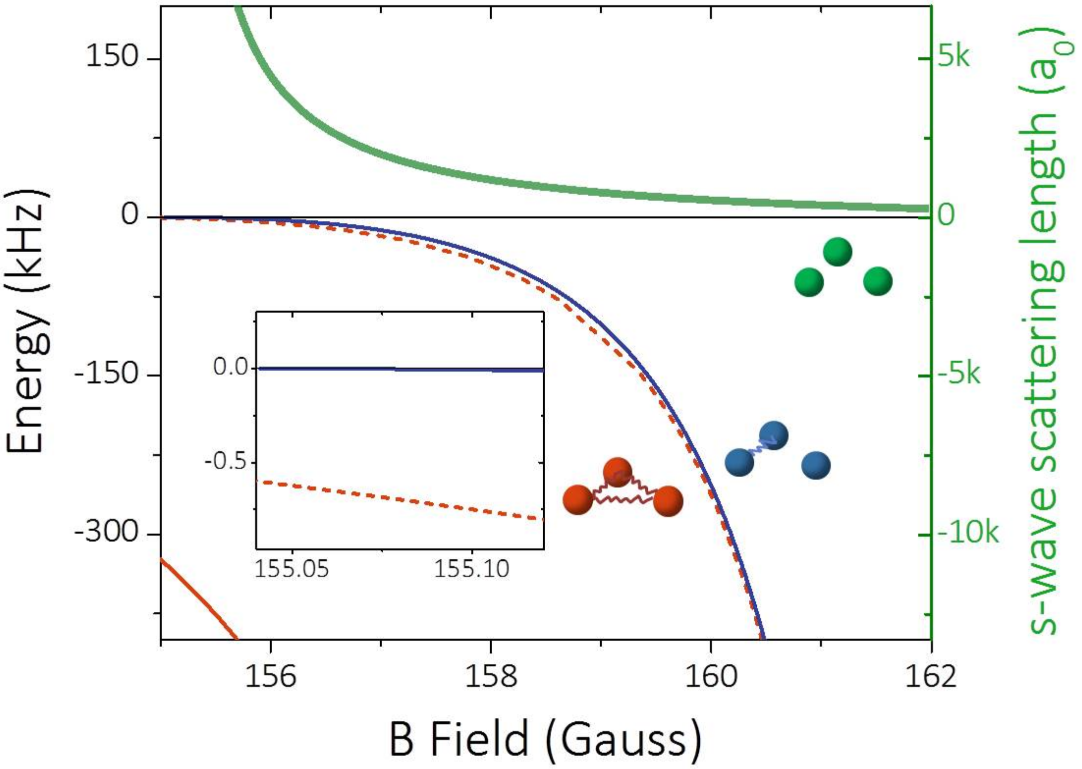

Figure 2.3: The solid and dashed red line represent the energies of the ground and first-excited Efimov states, relative to three non-interacting atoms. These energies were calculated in the adiabatic hyper spherical representation [43, 8, 66]. Like the previous figures in this chapter, the blue line represents the energy of the Feshbach dimer plus one free atom, and the green is the two-body scattering length.

2.5 Experimental observations: loss rates

We discussed earlier how observing loss rates in both unbound atoms and two-body bound dimers gives insight into the production of Efimov trimers. Loss rates are an invaluable tool for ultracold gas experiments. They are simple to measure, as it is relatively easy to count the number of atoms over time. The rate and spatial extent of the loss, however, gives rise to a plethora of information as to the cause of the loss.

There are many mechanisms that can cause loss in a BEC. Of interest in our regime is three-body recombination. Three-body recombination describes the event of three atoms colliding - two of these atoms bond to form a molecule, and both the molecule and the third atom recoil with kinetic energy gained from the new molecule's binding energy [27]. This event results in overall loss and heating of the condensate.

The three-body loss rate, Γ_3, is defined by

$$\dot{N} = -\Gamma_3 N. \tag{2.15}$$

Γ_3 is related to the three-body loss rate constant, L_3 by $\Gamma_3 = L_3\langle n^2\rangle$, where $\langle n^2\rangle$ is the density-averaged square density, or $\int n^2(r)\cdot n(r)\ \mathrm{d}^3r/N$. In the zero-temperature, mean-field limit,

$$L_3 \sim \frac{\hbar}{m}a^4, \tag{2.16}$$

therefore $\Gamma_3 \sim n^2a^4$ [67, 68, 27, 28, 29]. As a formally diverges on resonance, however, a plausible physical limit is $a \sim n^{-1/3}$, yielding $\Gamma \sim n^{2/3}$ [69, 70]. This loss rate scaling at unitarity is consistent with universal scaling with density.

At finite a however, the presence of Efimov states modulates the three-body inelastic collision rates by a dimensionless log-periodic function of a [68, 27, 28, 4, 51, 52, 7, 71, 72, 21]. Because Efimov states are still bound when $1/a \to 0$, it is not unreasonable to suspect that they may influence the loss rates on resonance. Observation of an Efimov perturbation on the resonant loss rates of a Bose gas would therefore demonstrate a breakdown of universal scaling with density in the system.

The measurement of the three-body loss rate of a resonant Bose gas has been studied intensely over the past several years [70]. The loss rates of a finite-temperature resonant Bose gas have been measured in [37, 38, 39]. The loss rate of a zero-temperature resonant Bose gas was measured for two densities in [35] and was found to be consistent with universal density scaling.

In Chapter 5 of this thesis we present a measurement of the apparent loss observed in a $1/a \to 0$, $T \to 0$ Bose gas for densities ranging over two orders of magnitude. However, in later chapters we explore how our measurement technique, which involves ramping back to weak interactions before imaging, sweep our resonant atoms into weakly-bound molecules. Therefore the observed loss is not solely a measurement of the resonant three-body loss rate, and may be even more than merely the rate of the three-body loss summed with the production rate of shallow (weakly bound) molecules. The evolution of the atoms' propensity to be swept into shallow molecules occurs simultaneously with the three-body loss to deeply-bound molecules. The questions that arise from this entanglement are furthered following the revelation that the shallow molecules are a mixture of both dimer and trimers. Strange effects seen for short evolution times even suggest that some atoms may be in a superposition of dimer and trimer states.

Chapter 3

Imaging corrections

3.1 Review of previous imaging setup

The experiments written about in this thesis took place on an apparatus originally built by Scott Papp [73]. This experiment used ^{87}Rb to sympthathetically cool ^{85}Rb into a BEC of around 70×10^4 atoms. Changes to this original set up include a nearly-spherical 10 Hz trap detailed in [74], a high-intensity imaging setup detailed in [75], and a pair of Fast-B coils detailed in [36]. This experiment is now dismantled, however a new and improved experiment is in the process of being built to continue the resonantly interacting boson research this thesis explores.

In this chapter we discuss further changes made to the high-intensity imaging. These changes enabled us to image the clouds in-trap and on resonance, thereby deducing how the density of a resonant degenerate Bose gas changes on resonance. We will first review the high-intensity imaging setup detailed in [75], then discuss why and what changes were necessary, and finally examine the positive effects of these changes.

3.1.1 Absorption imaging: review

A very thorough review of absorption imaging can be found in [76]. Basically, incident light shines on atoms, the atoms absorb the light thereby creating a shadow, and a camera down the line images this shadow - we call this the shadow frame, I_S. The cold collection of atoms are "destroyed" by this process, meaning that they are heated enough that they leave, and probably end up being adsorbed onto the walls of the science cell. After this destruction, a second, identical light pulse is sent through the now empty science cell and imaged by the camera - we call this the light frame, I_L. Because our experimental set up is not perfect we also image a dark frame (I_D), where the camera takes an image with no incident laser light to collect information on the background light and dark counts. By comparing the light and shadow frames (and subtracting the dark frame from each), we deduce the measured optical depth (OD):

$$OD_{\mathrm{ml}} = \ln\left(I_i/I_f\right), \tag{3.1}$$

where $I_f \equiv I_S - I_D$ and $I_i \equiv I_L - I_D$. The peak optical depth (pkOD) is the largest optical depth in the image, and occurs at the center of the cold cloud, pkOD $= OD_{\mathrm{ml}}(r=0)$. We generally fit our OD with a 2D Gaussian fit with an amplitude of pkOD and x and y sizes of σ_x and σ_y. When the frequency of the imaging laser is on resonance with the atomic transition (i.e. zero detuning), the number of atoms in the cold cloud is then

$$N = \frac{2\pi}{\sigma_0} \cdot \mathrm{pkOD} \cdot \sigma_x \sigma_y, \tag{3.2}$$

where σ_0 is the resonant cross section, $= 3 \times 780$ nm / 2π, and σ_x and σ_y are the axial and radial cloud sizes defined by a 2D Gaussian fit[76].

Optical depth is a very useful term but the word is used in variety of manners. For clarity, we define several OD's that will be used throughout this chapter. The actual optical depth of our cloud is OD_{real}, defined by the density integrated along the imaging direction, $\int n \mathrm{d}z$. The maximum value of OD_{real} occurs at the center of the cloud, pkOD $= OD_{\mathrm{ml}}(r=0)$. If our imaging set up had perfect polarization, zero detuning, and all around perfect imaging, the intensity of the shadow frame would be reduced by $I_s = I_L \mathrm{e}^{-OD_{\mathrm{real}}}$. In equation (3.1) we defined the measured OD, defined by the amount of missing light (ml) in the shadow image. This is the standard optical depth measurement, but it is affected by bad polarization, laser detuning, and saturation. We use the value of OD_{max} to determine the amount "bad light" (e.g. light with bad polarization or frequency) in our system, $OD_{\mathrm{max}} \equiv OD_{\mathrm{ml}}$ in the limit of $OD_{\mathrm{real}} \to \infty$. We later define an OD_{high} in equation (3.3) that overcomes the saturation limitations of OD_{ml} and therefore enables measurements of large (high) optical depths. OD_{high} is a good approximation for OD_{real} when the detuning is zero, the polarization is pure, and OD_{real} is below 15.

The camera we use to image this laser light is a Roper Scientific (Model 1024B) with 1024x1024 pixels that are each 13 μm wide per side. The camera is back illuminated to ensure high quantum efficiency of 72%, meaning that 0.72 electrons are emitted for each photon. The least significant bits (LSB) per electron of the camera was measured on April 27 2010 (before my time) to be 0.96 ± 0.1 electrons/ct.

We use a two-lens telescope to magnify our images before the camera. The first lens is $f = 8$ cm located about 8 cm away from the atoms, the second a $f = 18$ cm lens about 18 cm away from the camera. The magnification of this lens system is 2.25. This results in a pixel-to-size calibration of 5.8 μm/px. This calibration was measured to be $px_{\text{calib}} = 5.7$ μm/px by imaging untapped falling atoms and comparing their acceleration to that of gravity.

The resolution of this system was calculated (by measuring the expansion of the cloud under known conditions) to be 1.07 and 1.14 pixels in the x and y directions, respectively. This corresponds to a resolution of 6 and 6.5 μm. The diffraction-limited resolution of our lens system is only 1.05 μm [77]. Our actual resolution is so much larger because of spherical aberrations, more on this in the next section.

3.1.2 High-intensity imaging: review

There is a maximum intensity of incident light beyond which the atom's absorption begins to saturate, see [75] for more thorough explanation of this saturation. We account for this saturation by defining a new, high-intensity OD:

$$OD_{\text{high}} = \ln\left(I_i/I_f\right) + \frac{I_i - I_f}{I_{\text{sat}}} \tag{3.3}$$

[78]. I_{sat} was measured for ^{85}Rb to be 1.669 mW/cm^2 for the $|3,-3\rangle \rightarrow |4,-4\rangle$ transition [79]. For our purposes it is easier to define the effective I_{sat} in our system,

$$I_{\text{sat}}^{\text{eff}} = \frac{\alpha \cdot T \cdot I_{\text{sat}} \cdot t \cdot \text{px}_{\text{calib}}{}^2}{\text{C}_{\text{pp}} \cdot h \cdot \nu}, \tag{3.4}$$

where $\alpha = 2$ to account for our polarization axis (see figure 3.1), $T = 53.4\%$ is the transmittance through the camera ND filter, C_{pp} is the quantum efficiency of our camera (0.72 electrons/photon) divided by the measured LSB/e^- (0.96 electrons/ct) = 0.75 counts per photon, t is the length of the imaging pulse (normally 50 μs for low-intensity imaging, and 5 μs for high-intensity imaging) and ν is the frequency of our laser, given by $c/\lambda = c/780.24$ nm ≈ 384.2 THz. $I_{\mathrm{sat}}^{\mathrm{eff}}$ for our system is calculated to be 8730 light counts.

We measure $I_{\mathrm{sat}}^{\mathrm{eff}}$ by imaging clouds (with an actual OD of OD_{real}) with different amounts of incident light (I_L) and comparing to the OD_{ml}. $I_{\mathrm{sat}}^{\mathrm{eff}}$ relates these quantities by

$$I_L = \frac{\mathrm{OD}_{\mathrm{real}} - \mathrm{OD}_{\mathrm{ml}} \cdot I_{\mathrm{sat}}^{\mathrm{eff}}}{1 - \mathrm{e}^{-}\mathrm{OD}_{\mathrm{ml}}}. \tag{3.5}$$

We find that the measured value of $I_{\mathrm{sat}}^{\mathrm{eff}}$ appears to change with the actual optical density of the cloud, OD_{real}. This was because optical depth saturation is also affected by bad light, i.e. light

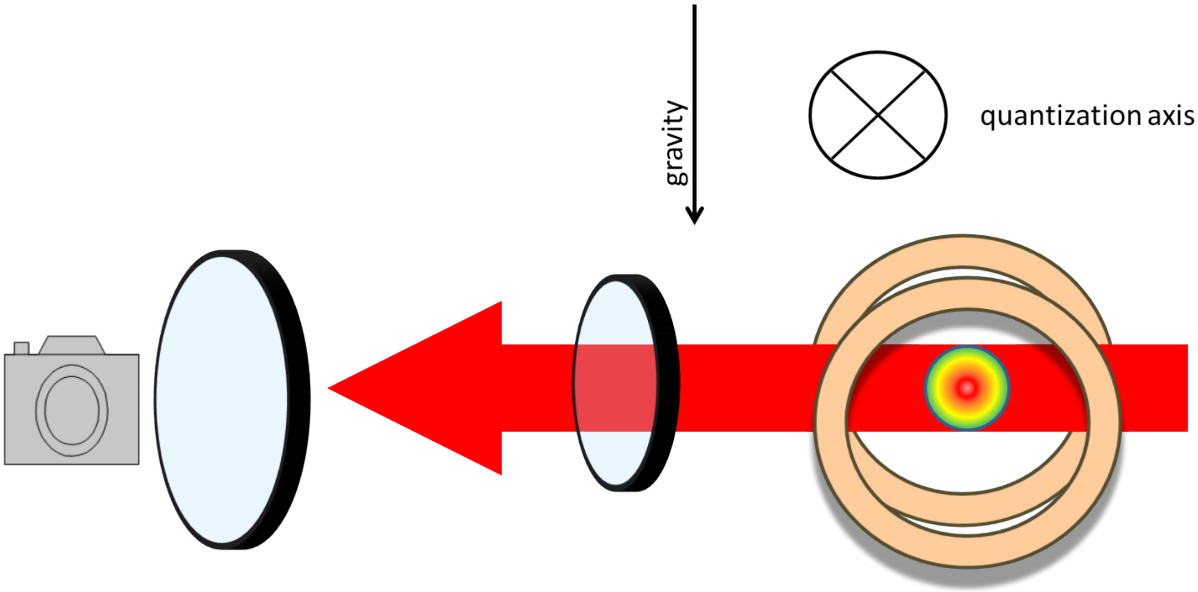

Figure 3.1: When taking an image of the cloud in-trap, we have the Bias coils define the quantization axis. This axis is perpendicular to the incident light. Because the incident light is linearly polarized, half of the light can be absorbed by the atoms, the other half cannot. We account for this by including a factor of 2 in our OD calculations.

that cannot be absorbed by the atoms (because it has an incorrect frequency or polarization, etc.). When there is unabsorbed light, I_f cannot become as low as necessary for a large OD, therefore the OD saturates. Fortunately we account for the bad light in our system by redefining our intensities as

$$I_i \equiv I_S - bI_L - I_D, \tag{3.6}$$

$$I_f \equiv I_L - bI_L - I_D. \tag{3.7}$$

The fraction of bad light, b, is defined by

$$b \equiv \frac{1}{\mathrm{e}^{OD_{\mathrm{max}}} + 1}, \tag{3.8}$$

where OD_{max} is the maximum measurable OD in our system. We both minimized and measured b by measuring the maximum optical depth as we varied the angle of polarization of the light, see figure 3.2. This technique only minimizes bad light due to impure polarization, but it measures bad light due to impure polarization, laser detuning, and saturation.

After accounting for the bad light fraction, we find that the effective $I_{\mathrm{sat}}^{\mathrm{eff}}$ fits to about 9000 light counts, regardless of the optical depth of the cloud, see figure 3.3. This is very close to our predicted value of 8730 light counts. We continue to include bad light corrections in all future images by using our redefined I_i and I_f in our optical density calculations.

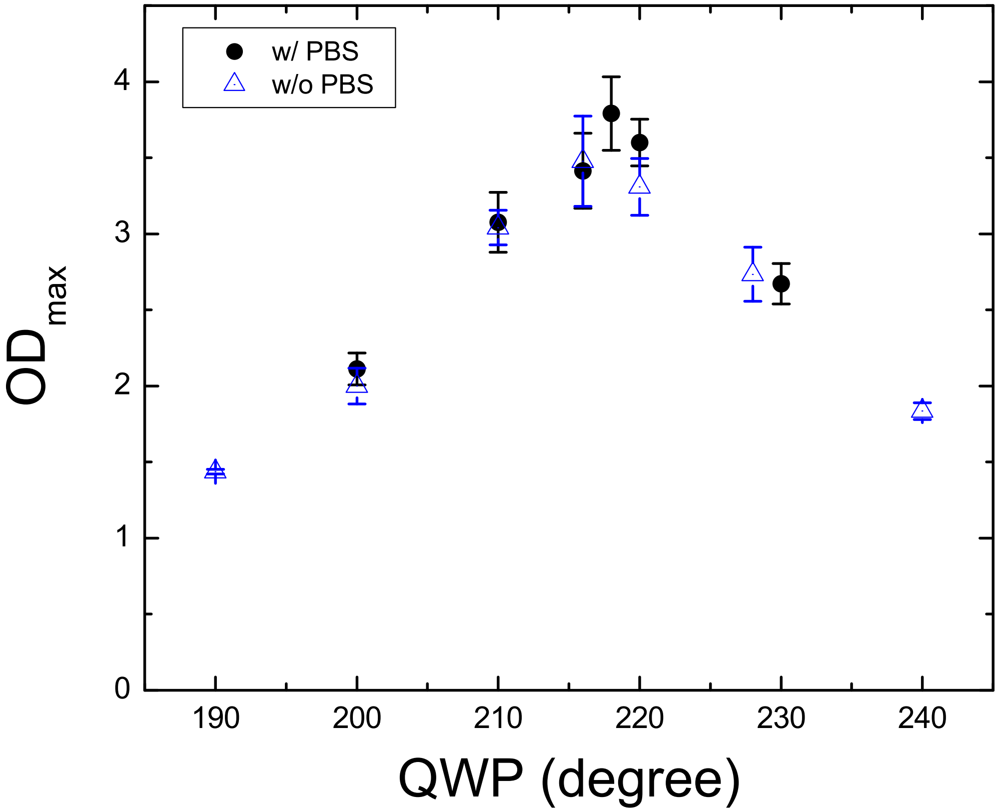

Figure 3.2: The maximum measured optical depth as a function of rotation of a quarter-wave plate. We found that adding a polarizing beam splitter (PBS) to our beam path cleaned up the polarization, allowing for a higher measured OD. With a maximum OD of 3.77, the amount of bad light is $\frac{1}{e^{3.77}+1}$, or about 2.3 %

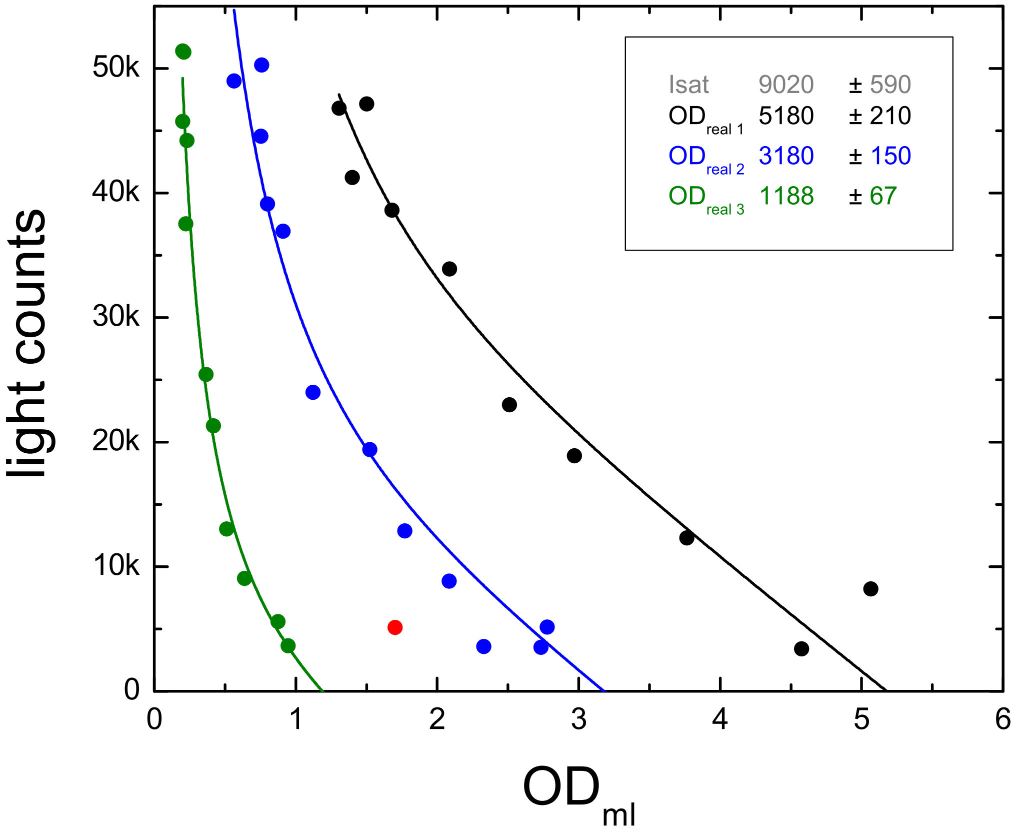

Figure 3.3: To measure $I_{\mathrm{sat}}^{\mathrm{eff}}$, we observed the measured OD_{ml} for various incident light counts for clouds of three different intrinsic OD_{real}, about 1200, 3200, and 5200 mOD. The y-axis on this plot is the independent variable, the x-axis dependent. When account for a bad light fraction of 2.3%, we see $I_{\mathrm{sat}}^{\mathrm{eff}}$ fits to 9020(590) light counts, in good agreement with our expected value of 8730.

3.2 New imaging system

3.2.1 Reasons to upgrade

There are many possible experiments that require imaging on resonance (and therefore in trap) to better understand the resonantly interacting Bose gas. Our original resolution of 6 μm seems at first good enough to image our 30 μm diameter in-trap cloud size. However, when a cloud is both small and optically dense, we observe a stifled optical depth measurements (figure 3.5) along with a larger cloud size, as if the resolution were changing. This is because our high-intensity saturation corrections break down near the resolution limit. This results in the number appearing to increase with the time-of-flight (TOF) expanded clouds, see figure 3.4.

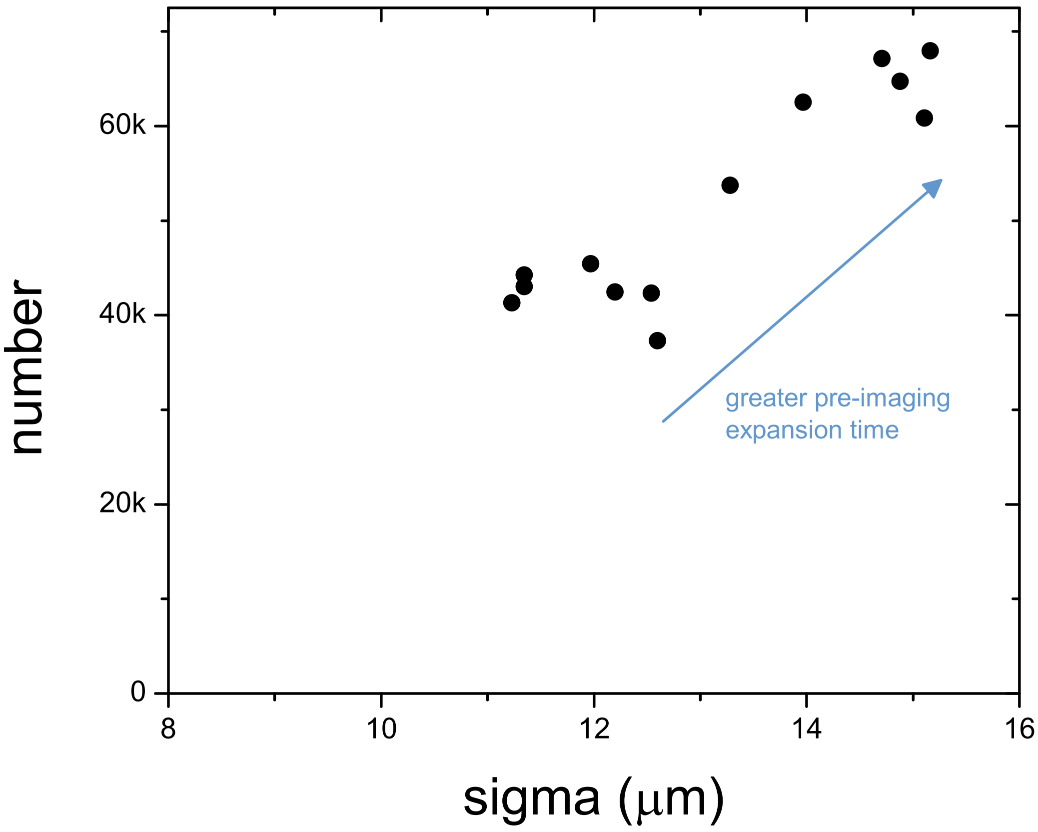

Figure 3.4: We expanded a cloud of constant N in time-of-flight (TOF). The number appears to increase nearly 40% with the cloud size because of combined saturation and resolution effects.

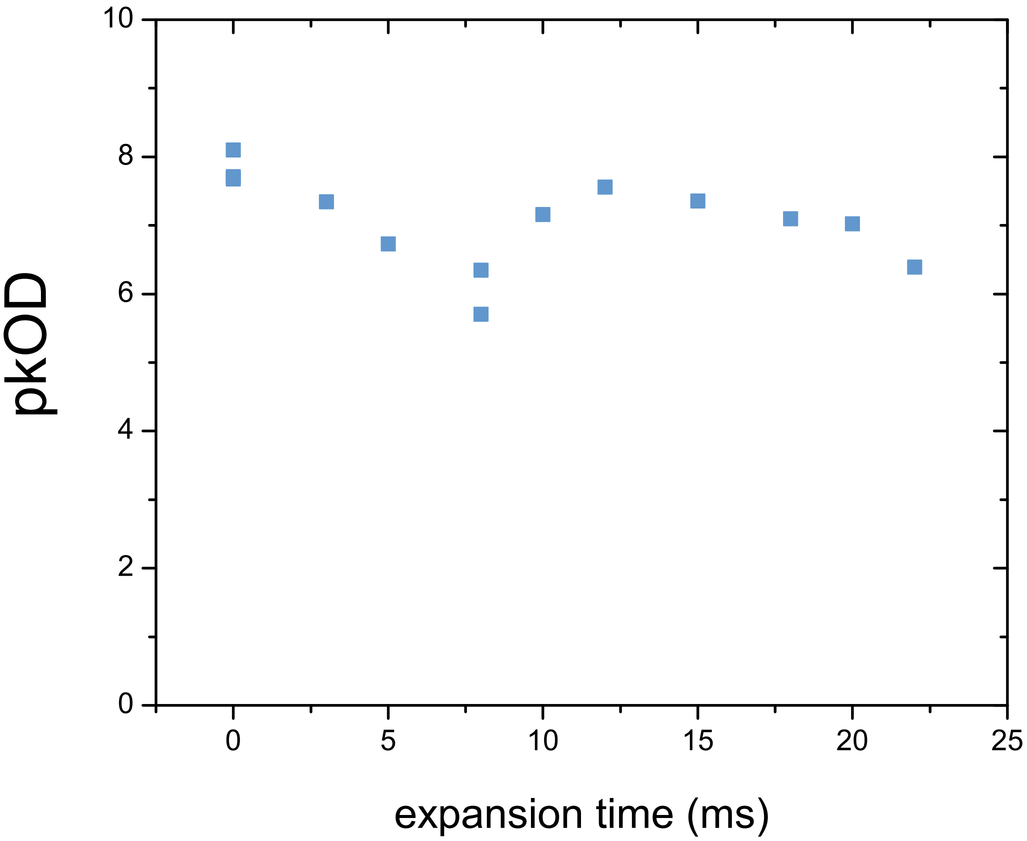

Figure 3.5: The measured pkOD as a function of cloud size for a cloud of constant N. The peak OD should decrease as the cloud expands, however it does not because the measured OD is saturated around 8, when it should be nearly 20 for the smallest cloud size (corresponding to least expansion time).

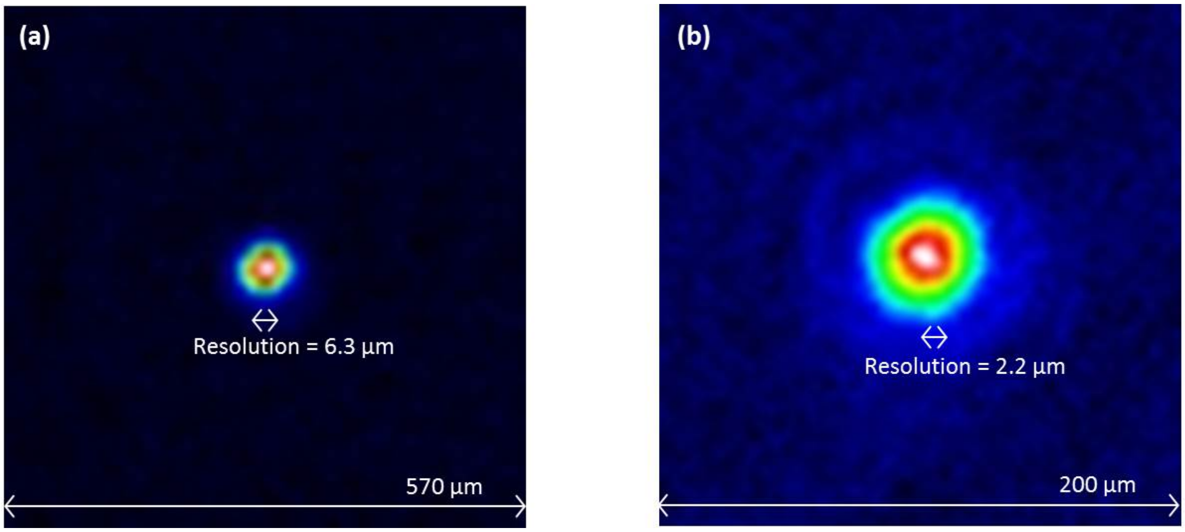

Figure 3.6: An unexpanded BEC of 70k atoms at 150 a_0 should have a pkOD of 25 and a fitted Guassian size (sigma) of 8 μm. (a) In our old imaging system this cloud was measured at 10.8 μm sigma and peak OD of 8.8, resulting in a number of 45k. (b) In the new imaging system we measure a sigma of 8.6 μm and a peak OD of 20, resulting in a calculated number of 63k.

3.2.2 New imaging lenses

The resolution of our old imaging system was limited by aberrations, specifically due to spherical aberrations, imperfect tilt and alignment, and small magnification [77]. As we saw in the previous section, this resolution worsened when we combined large optical depths with small cloud sizes near the resolution limit. We therefore sought to improve our imaging resolution. Counter-intuitively, we actually increased the diffraction-limited resolution (given by 0.61 $\lambda d/r$, where λ is the laser wavelength, d is the distance between the lens and the object, and r is the radius of the lens) by decreasing the radius of both the objective and imaging lenses to a half inch. This improved our overall resolution by decreasing the aberrations caused by tilt and misalignment. The new lenses are spaced 10mm apart and have focal lengths (f) of 75 and 500mm, resulting in a magnification of 6.35, see figure 3.6.

This new lens system increases our diffraction-limited resolution to 1.96 um. Our actual measured resolution is close to the diffraction limit, at 2.2 +/- 0.1 μm. This is why we see diffraction rings (an airy disc pattern) around our smallest clouds, see figure 3.7. We measured the resolution by making the smallest cloud possible at $a = 6{\pm}2\ a_0$, where the cloud size is set by the trap frequency, $\sigma_{real} = 3.9$ and $3.6\ \mu$m in x and y. σ_{meas} was 4.206±0.98 and 4.20±0.94, so our resolution is then $\sqrt{\sigma_{meas}^2 - \sigma_{real}^2} = 2.27 \pm 0.01$ and 2.09 ± 0.01. We calibrate the magnification of this system with respect to the camera pixel size by watching the cloud fall and find it to be $px_{\mathrm{calib}} = 1.996 \pm 0.002$ μm/px.

Because of the larger magnification, we can now throw more incident light onto our condensate. Our camera pixels saturate about 65k light counts, so we aim to keep the laser light at or below 50k light counts. 50k light counts corresponded to only 0.5 mW of incident light on the atoms with our previous magnification (when $t = 5\,\mu$s, constant for all future experiments). With our new magnification that same amount of incident light expands to only 7k light counts per pixel at the camera. We can therefore increase the incident light to 2 mW before the camera pixels near saturation. Increasing the amount of light incident on the atoms improves the maximum measurable pkOD and reduces saturation effects. We were unable to measure the $I_{\mathrm{sat}}^{\mathrm{eff}}$ of the new

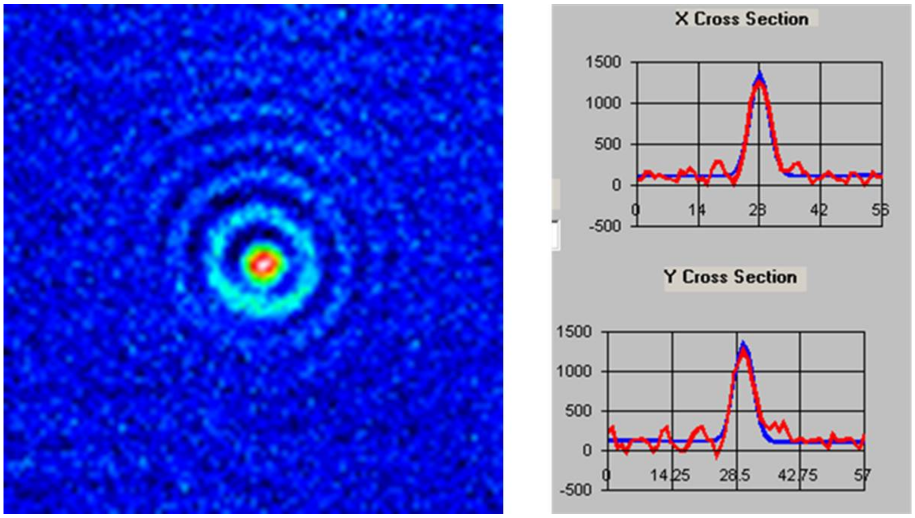

Figure 3.7: We created a very small cloud at $a = 6 \pm 2\,a_0$. On the right are the x and y cross-sections across the center of the cloud, the red lines are the data, the blue a Gaussian fit. There are visible diffraction rings, or Airy discs, around this cloud because we are near the diffraction resolution limit. The size of this cloud is set by the harmonic oscillator length of our harmonic trap, $a_{\mathrm{osc}} = 3.9(3.59)\ \mu$m in the x(y) imaging directions. By comparing this predicted size to the measured size we deduce an average resolution of 2.2 ± 0.1 μm.

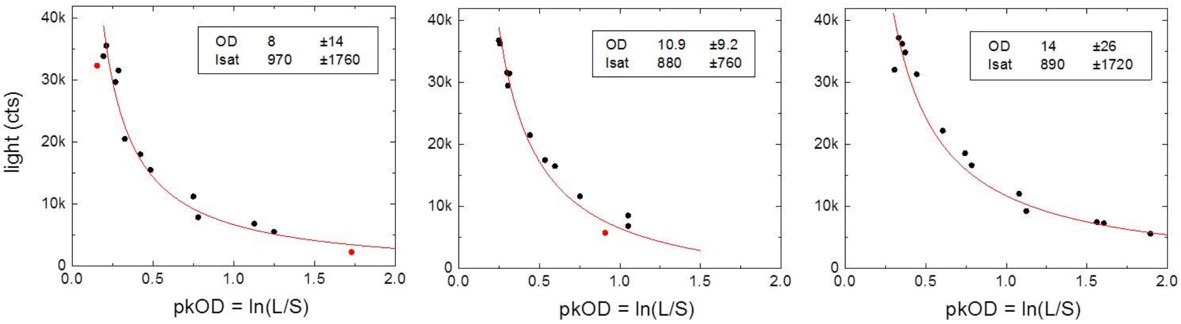

Figure 3.8: Because the magnification of our system has changed, $I_{\rm sat}^{\rm eff}$ also changes. We sought to measure $I_{\rm sat}^{\rm eff}$ at several optical depths, however dependencies between $I_{\rm sat}^{\rm eff}$ and OD dramatically increased the error bars. We do see that an $I_{\rm sat}^{\rm eff}$ of about 900 light counts produces good fits, believable OD values, and is close to our predicted value of 1074 light counts.

lens system because of dependencies in the fitting function between OD and $I_{\rm sat}$. We did see that an average fit of 900 light counts (see figure 3.8) produced good fits, believable OD measurements, and was very close to our prediction of 1074. The fractional intensity of the incident light, $I/I_{\rm sat}^{\rm eft}$, is therefore over 50, a very good ratio when using high-intensity imaging.

3.2.3 De-mag system

While the large magnification of the new lenses means that we can now measure a very small, optically dense cloud, it also means that we can no longer image very large clouds. Of particular interest for apparatus-tuning and debugging purposes is imaging the hot ^{87}Rb cloud suspended in the magnetic trap during the initial evaporation stages - this cloud could be up to 400 μm in Gaussian σ. To accommodate this large cloud we implemented de-mag lenses into our imaging system. The de-mag lenses are two additional lenses that can be flipped into the imaging beam path, see figure 3.9. The de-mag lenses are 2 inches in diameter with focal lengths of 100 and 60 mm.

With the de-mag system in place, the total magnification of the system is expected to be 1, therefore $px_{\rm calib}$ should be 10.25 μm/px. We measured this as 10.5 μm/px by measuring the same cloud with both the de-mag system in and out of the system, see figure 3.10. See [77] for more

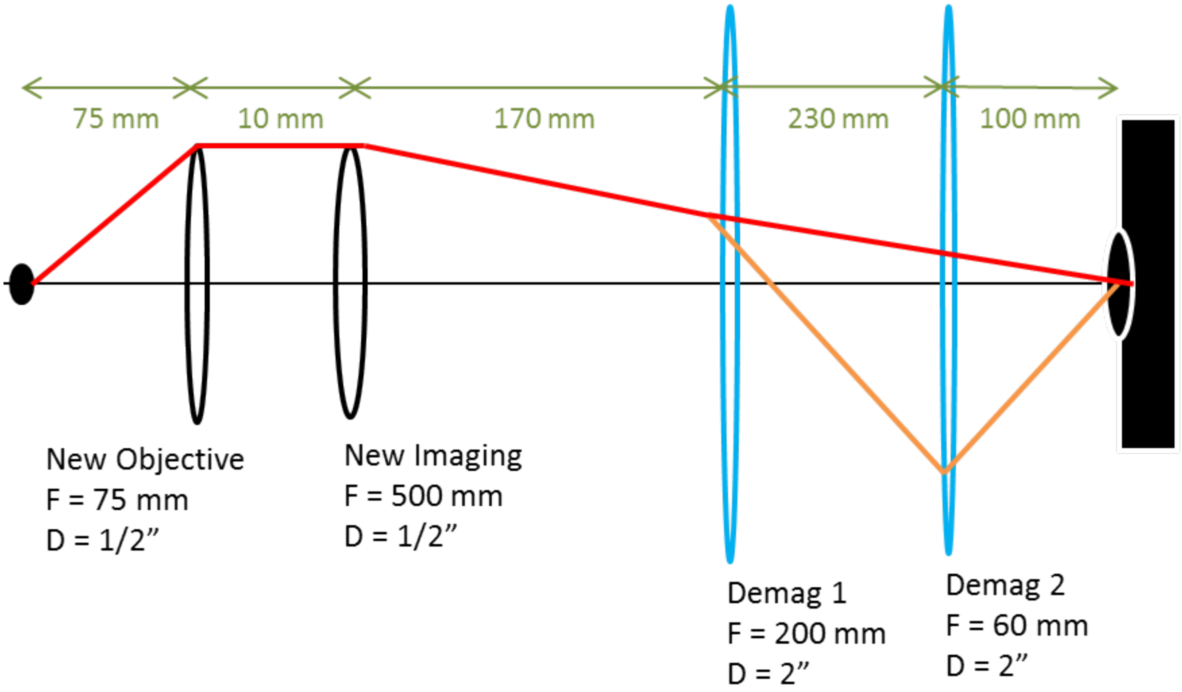

Figure 3.9: The de-mag lenses (in blue) are two large lenses that when flipped into the imaging beam path reduce the magnification from 6.35 to 1. Not to scale, figure borrowed from [77].

information on the de-mag lens system.

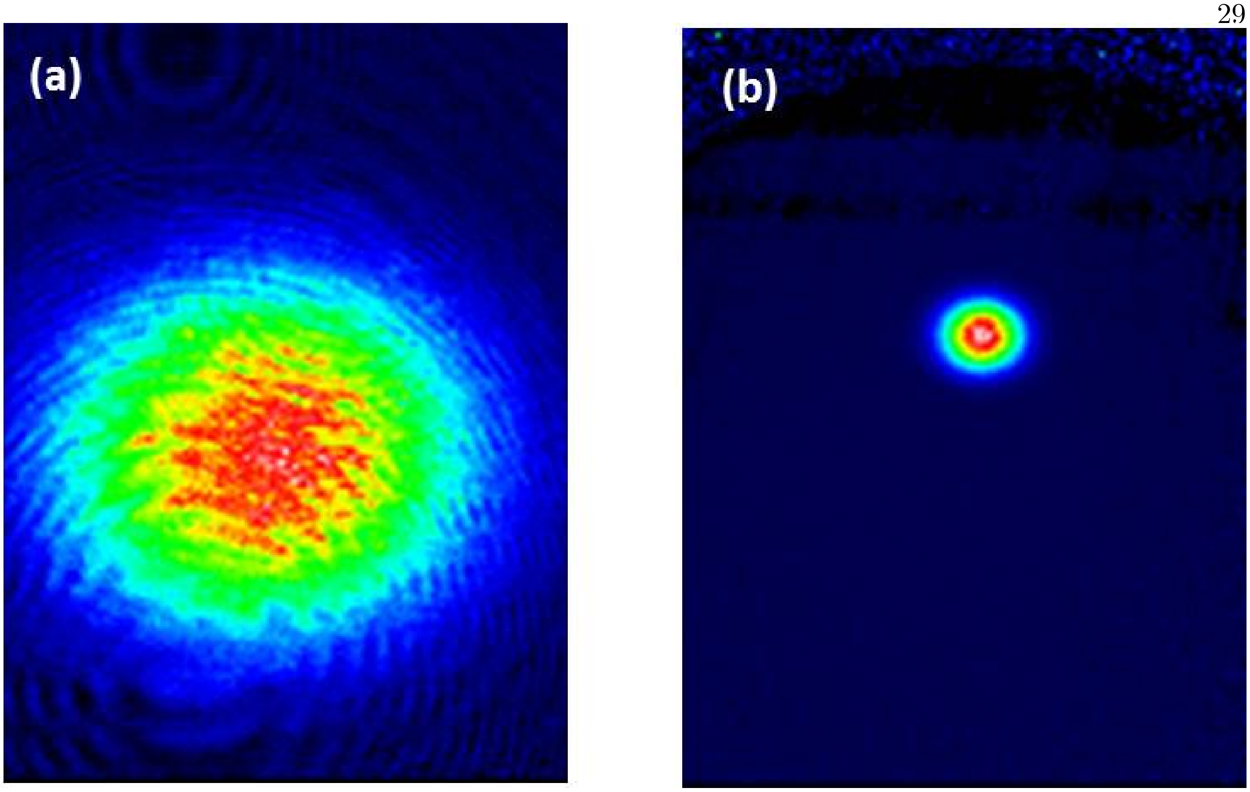

Figure 3.10: The same cloud imaged with and without our de-mag lenses. (b) Without the de-mag lenses the measured cloud size is 142.5 and 122.5 px in x and y, corresponding to 285 and 245 μm. (a) With the de-mag lenses the measured cloud size is 27.1 and 23.25 px, corresponding to a 10.5 μm/px calibration.

3.3 New OD range and expansion data

With our new imaging system (sans de-mag lenses) we find that the number no longer changes with sigma for most cloud sizes, see figure 3.11. This is because the measured optical depth (OD_{high}) is no longer saturated at 8, and can increase with smaller cloud sizes (smaller expansion times), up to about 20, see figure 3.12. We do see a 10% reduction in cloud size when the optical depth is above 15, we therefore conclude that we can trust our new imaging system up to clouds with optical depths up to 15.

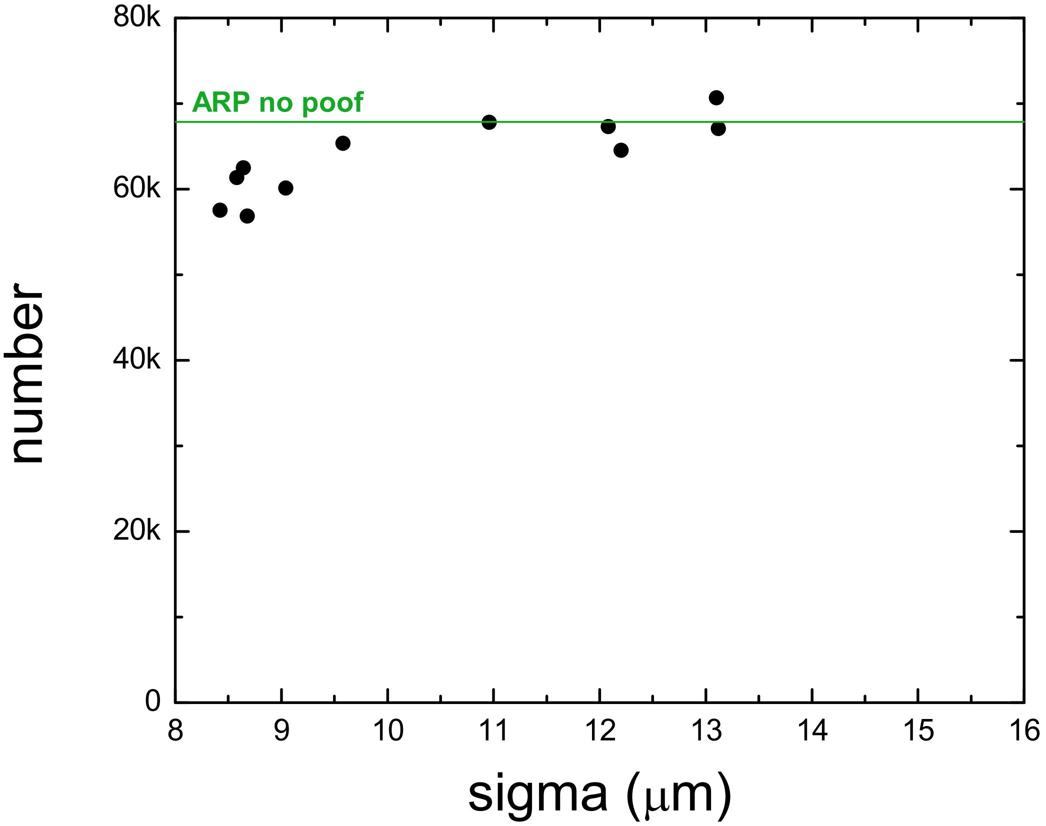

Figure 3.11: The measured number as a function of cloud size - the number of each cloud is held constant while the cloud size is expanded with TOF imaging. This atom number is transferred to the imaging state with a 9 dBm microwave pi-pulse. We compare this number to a cloud transferred to the imaging state with an ARP, the green line, our trusted “real number”. We see that the number no longer changes significantly with size. except by about 10% at the smallest sizes. These data correspond to the OD_{real} 15, we therefore conclude that we can trust our new imaging system up to optical depths of 15.

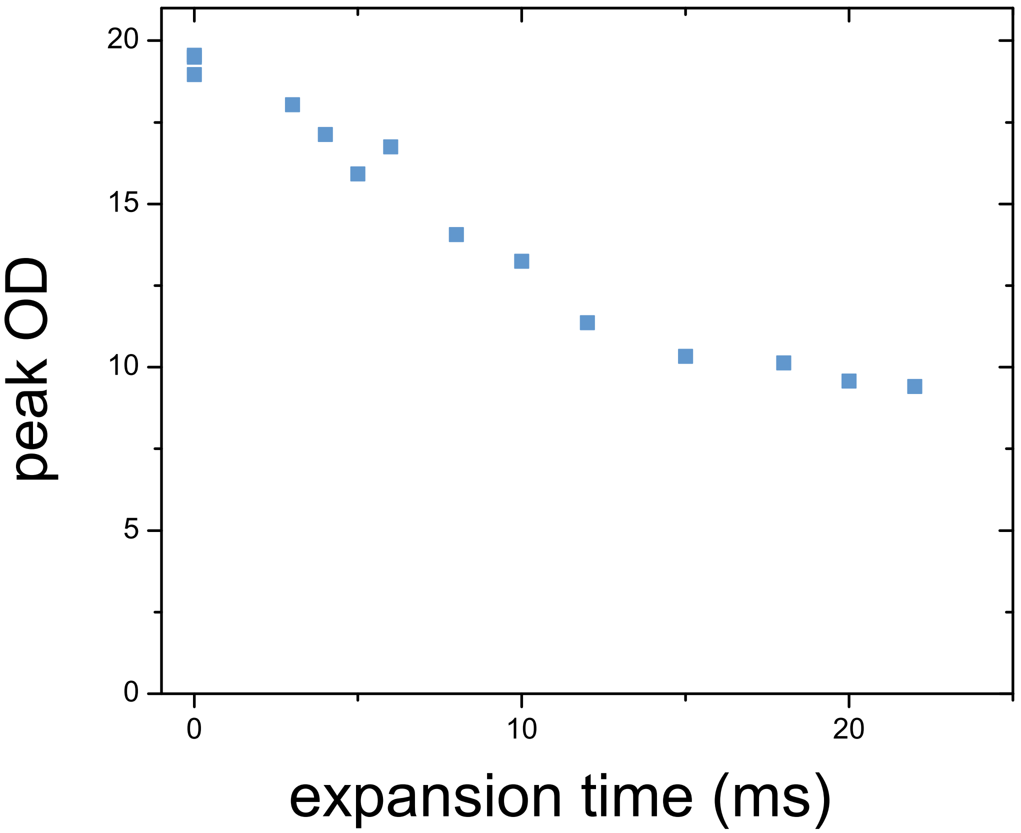

Figure 3.12: With our new imaging lenses we see that for a constant-N cloud the peak optical depth changes with cloud size, as expected! This measured optical depth reaches a maximum value of 20, the expected value given the cloud size. This data is the same data as plotted in 3.11 However, the data below 5 ms expansion time correspond to a peak OD greater of equal to 15, and this results in a reduced measured number of about 10%. Therefore we only trust our new cloud images up to a peak optical depth of 15.

3.4 Imaging analysis

In addition to correcting for the effective saturation intensity and the small percentage of bad light in our system, there is a third imaging systematic in need of correction: uneven probe pulses, i.e. the light and shadow frames having not exactly the same amount of light. This effect is caused by the AOM warming up - a warm AOM has slightly better alignment than a cold AOM. This is a problem because the incident light on the atoms is not constant across the imaging frame, see figure 3.13(a). Therefore when we subtract the shadow frame from the light frame, we see small remnants of this laser pulse in the background, when we should only see the round atom shadow, see figure 3.13(b).

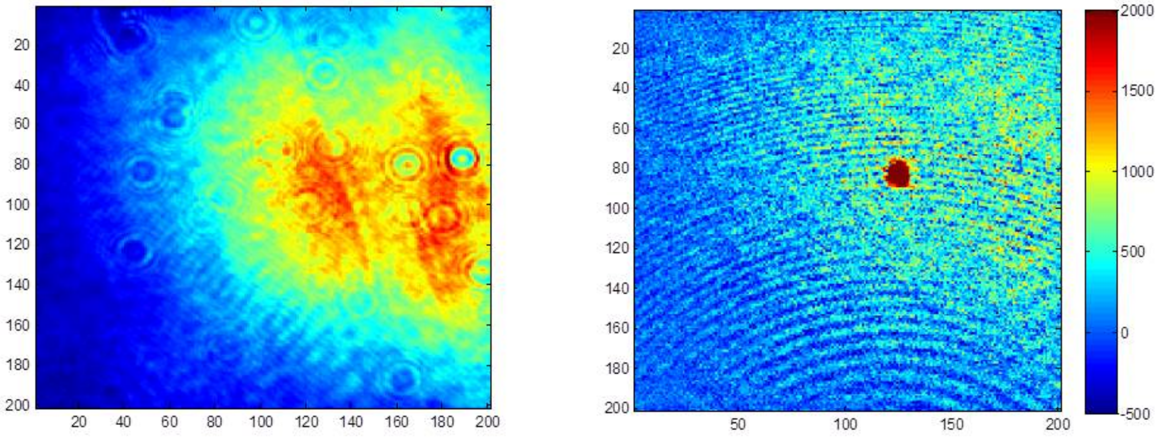

Figure 3.13: (a) the light frame, I_{L}. (b) the light frame minus the shadow frame, $I_{\mathrm{L}} - I_{\mathrm{S}}$. The dark red spot is a cloud of atoms while the remaining light stuff is laser remnants caused by the increased incident light in the light frame. We also see fringes across this frame subtraction because the two frames do not completely overlap - the small change in position is due to shaking optics, most likely caused by the cart, a coil that physically moves across our table to transport our atoms to the science cell.

3.4.1 Epsilon correction

Rather than correct this systematic by altering the AOM output, we find it easier to account for it during post-imaging analysis. The variation in incident laser light varies by, on average, only half a percent, see figure 3.14. This small percent is not a large issue for low-intensity imaging and the subsequent standard absorption optical depth analysis. If we defined a correction value ϵ as the average of the incident light in the shadow frame over the average of the incident light in the light frame, $\langle I_{\mathrm{L}}\rangle/\langle I_{\mathrm{S}}\rangle$, this correction value would become a constant term added onto the standard optical depth, as $\ln(\epsilon)$. This value becomes a very small (0.5%) constant added to the background, see image 3.15(a) to see how negligible.

In the high OD equation (3.3) however, the ϵ correction does not reduce to a constant. It is

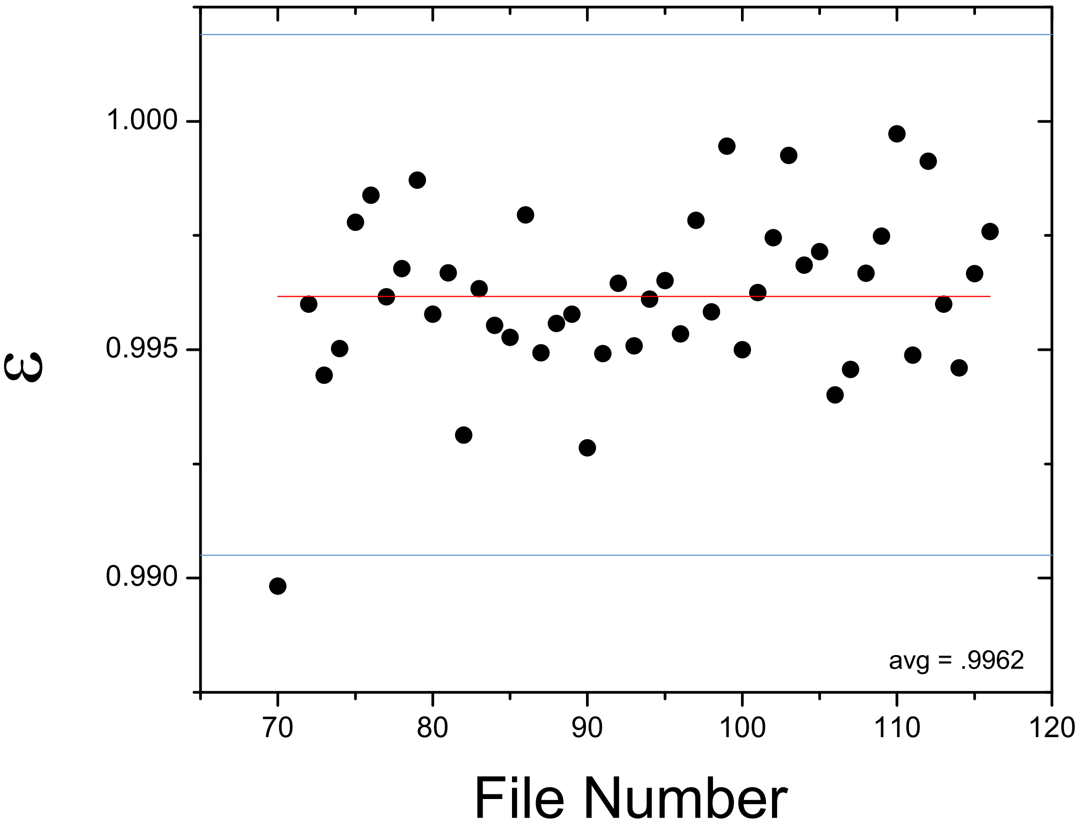

Figure 3.14: The average value of ϵ, evaluated with a 75 pixel box; the lines represent ± 3 σ. The average value of ϵ is about 0.996, meaning that 99.6% of the incident light in the light frame is also present in the shadow frame.

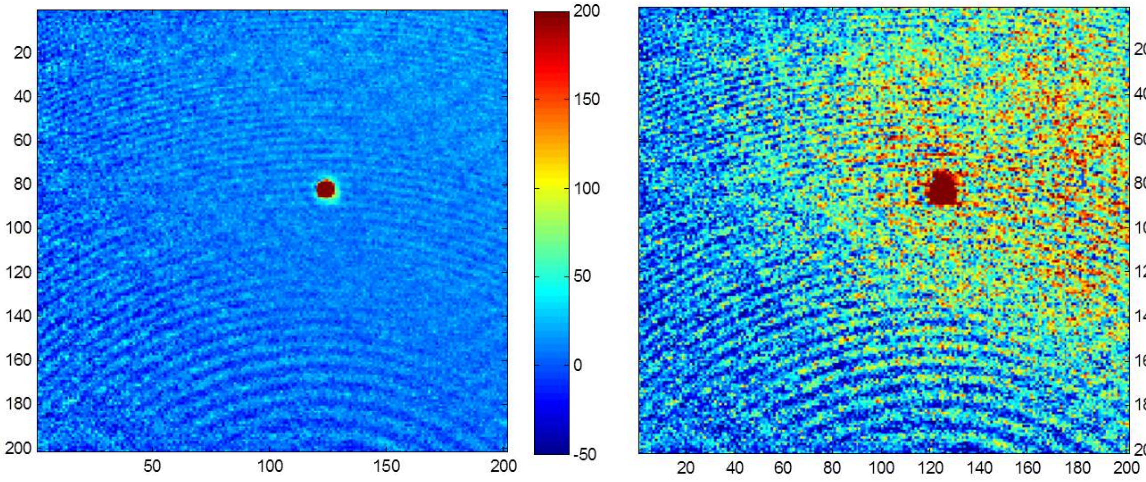

Figure 3.15: (a) The OD from the from figure 3.13 evaluated using equation 3.1; the laser remnants are too small to discern. (b) The OD from the same figure now evaluated using equation 3.3 - now the background becomes significant.

correctly accounted for in the optical depth as

$$OD \approx \ln\left(\frac{\epsilon\, I_i}{I_f}\right) + \frac{\epsilon\, I_i - I_f}{I_{\mathrm{sat}}^{\mathrm{eff}}}, \tag{3.9}$$

If ϵ is far from 1 and not correctly accounted for, a large non-linear background appears, see figure 3.15(b). To account for (remove) this background, we measure ϵ for each shadow/light frame pair.

Because the shadow frame has a dark spot due to the atoms, taking an average over the entire frame would incorrectly result in a much lower average light count for the shadow frame. We therefore define a box around the center of our cloud and only consider the light counts outside of this box. If this box too small, we might artificially lower ϵ by including atom dark spots; if this box too large, there will be too little incident light to calculate a trustworthy ϵ, see figure 3.16(a) and (b) for an example of each of these situations. We find that a box size of 75 pixels is best, see figure 3.16(c). Note that these pixel values were determined with the old imaging system, and the box size was adequately adjusted with the new imaging magnification.

To best illustrate how correction with ϵ improved our images, we need to define cumulative distribution functions (CDFs). CDFs are generated by azimuthally averaging the optical density

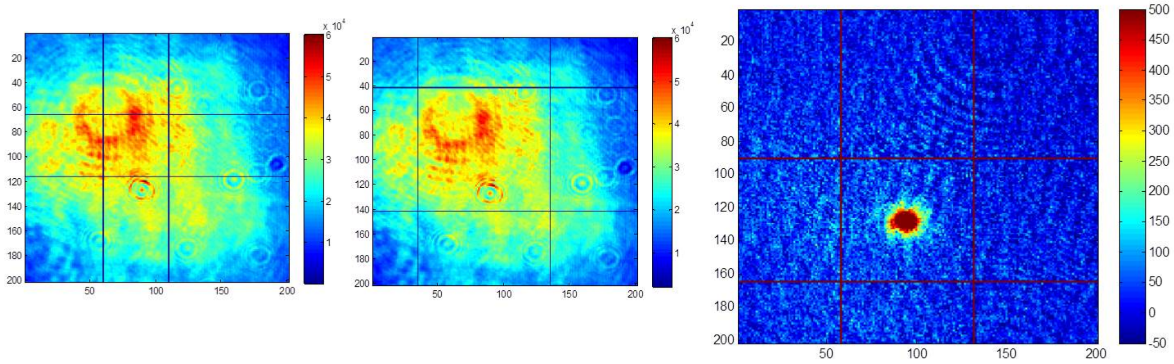

Figure 3.16: (a) is light frame with 50px box centered around the condensate center, (b) is with 100px box (c) is raw OD with 75px box, after a 12ms expansion.

then integrating from the cloud center to a specific radius r . The CDF is a plot of the number included within the radius r: the value of CDF(r) represents the number of atoms within that radius. We expect our CDFs to increase quite rapidly within the condensate radius, but then become flat.

Before accounting for ϵ our CDFs continued to increase at large radii (see figure 3.17) because the background of our images was slightly positive. This indicates that the number obtained from integrating the optical densities would change depending on the radius integrated out to. Including the ϵ correction flattened the CDFs at large radii (see figure 3.18), ϵ therefore removes most error due to our warm AOM alignment drifts. There are still a few outliers however, and for those we need to look into more corrective imaging analysis.

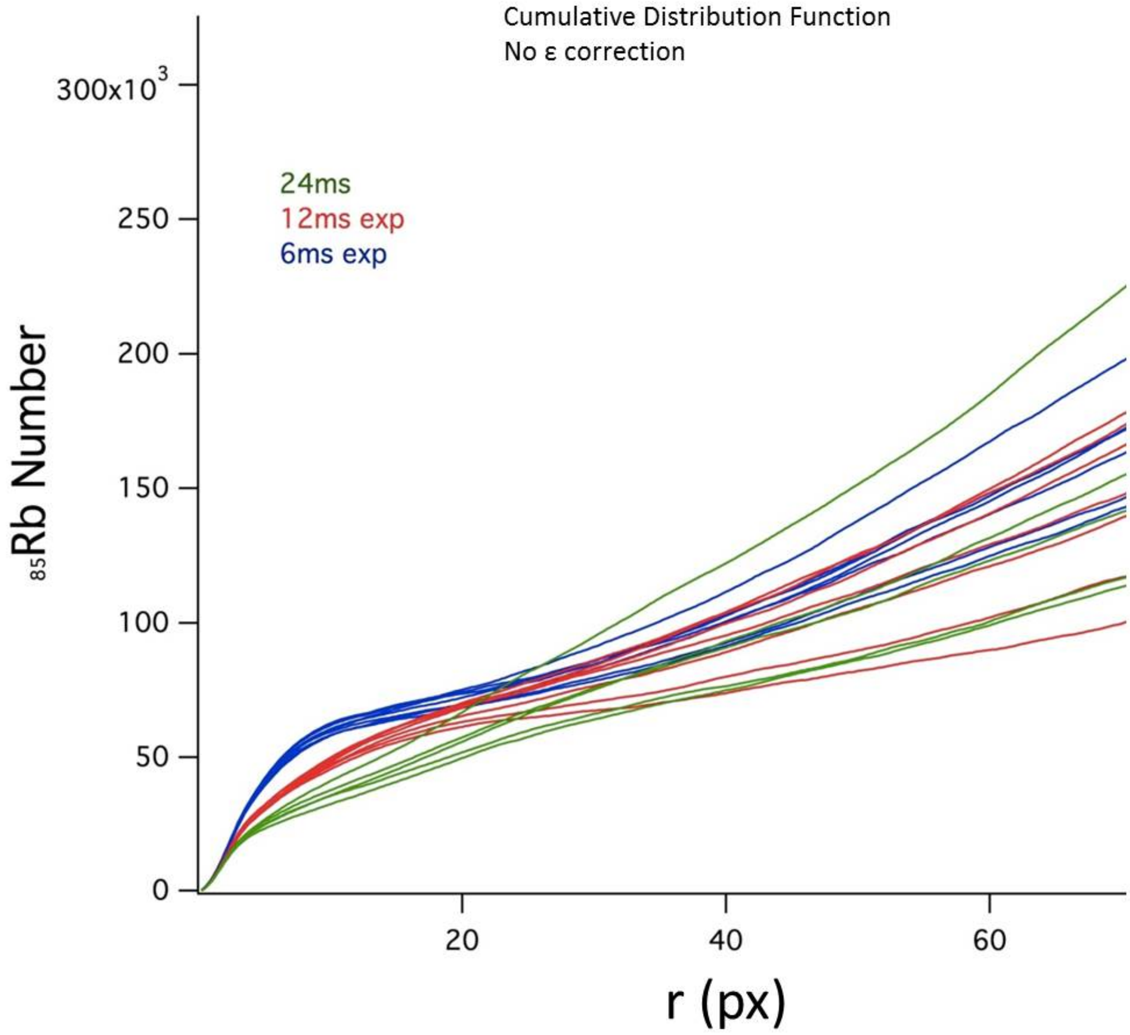

Figure 3.17: The cumulative distribution functions (CDFs) of many condensates after a 5-100-5 μs resonance jump. The clouds were expanded in TOF for 6 (blue), 12 (red) or 24 (green) ms. With no ϵ correction, we see that the CDFs continue to increase at large radii, indicating that the optical density images have a positive background.

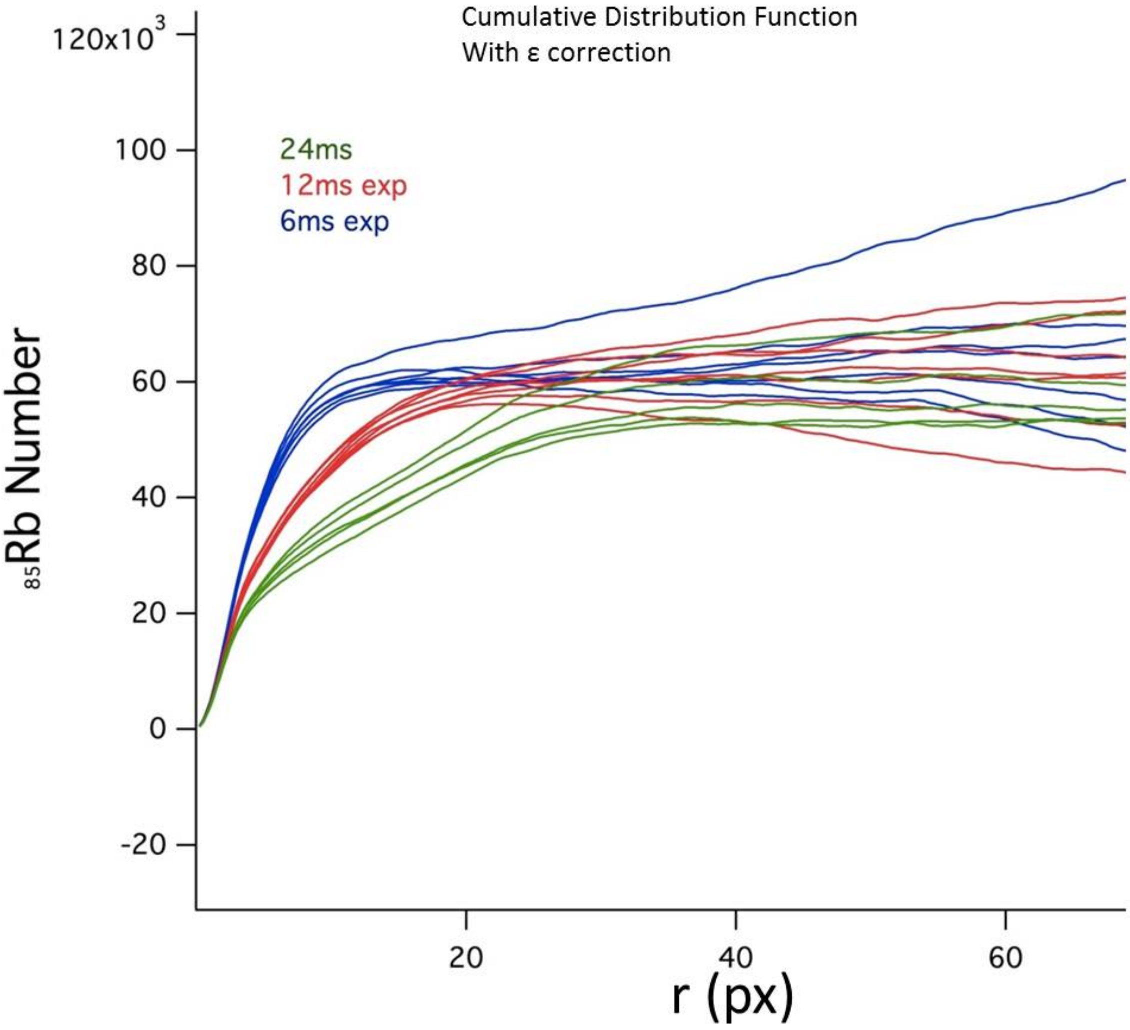

Figure 3.18: The same data that was presented in the previous figure, but analyzed with the ϵ correction. The ϵ correction enables the CDFs to flatten at large radii, indicating an optical density background of zero. There are minimal outliers after the ϵ correction that still have non-zero background.

3.4.2 Residual background subtraction

The ϵ correction does not zero-out the background of all images. Plotting more CDFs, we see that maybe 5% do not have zero slopes are large radii, see figure 3.19. We find that the images not corrected by ϵ tend to have large fringes in their frames, which may skew the ϵ calculation.

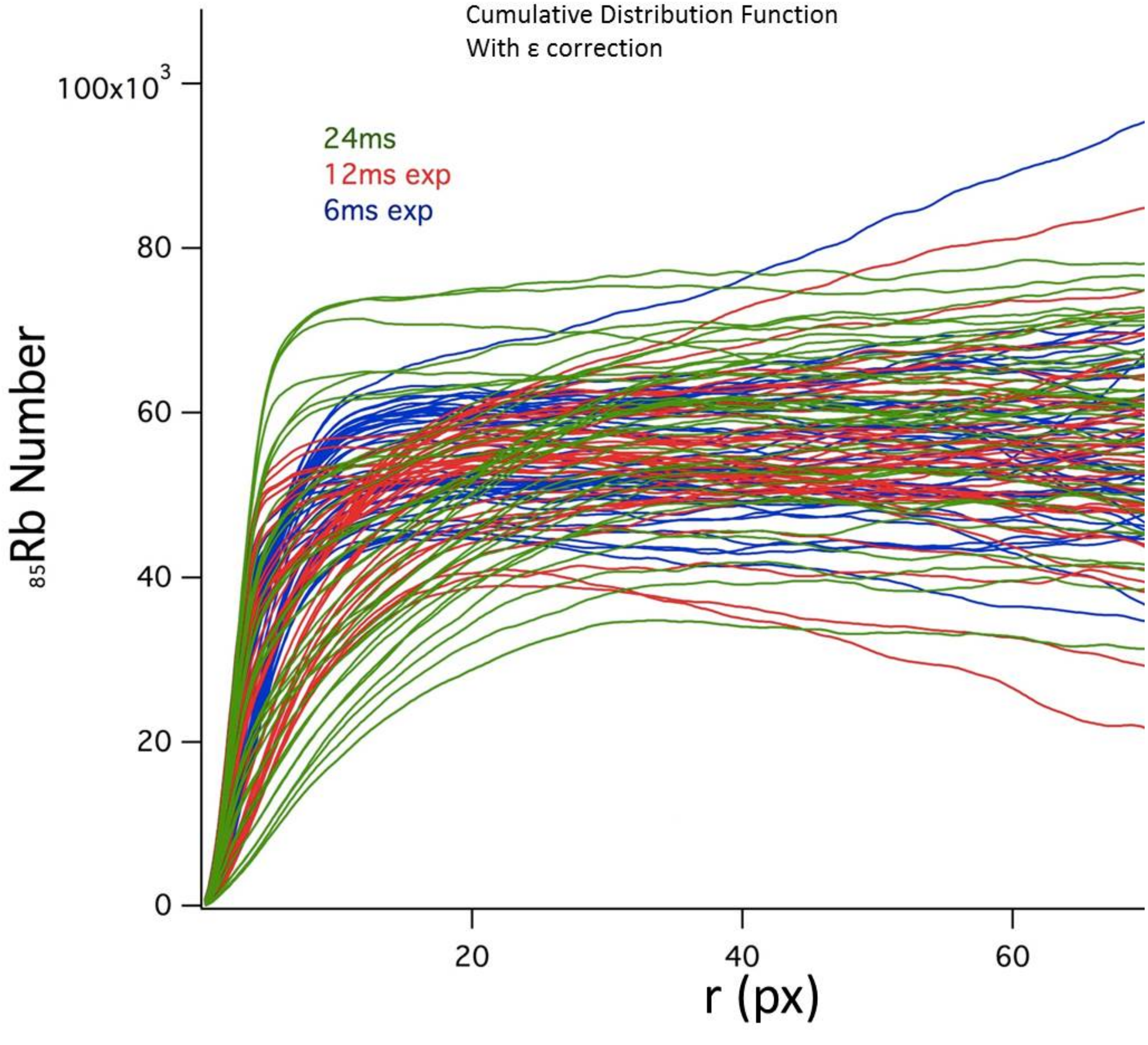

Figure 3.19: More cumulative distribution functions of condensates after various resonance jumps and TOFs. We see that maybe 5% of the CDFs continue to have a non-zero background after the ϵ correction. We expect these data to have varying total number, this is not noise.

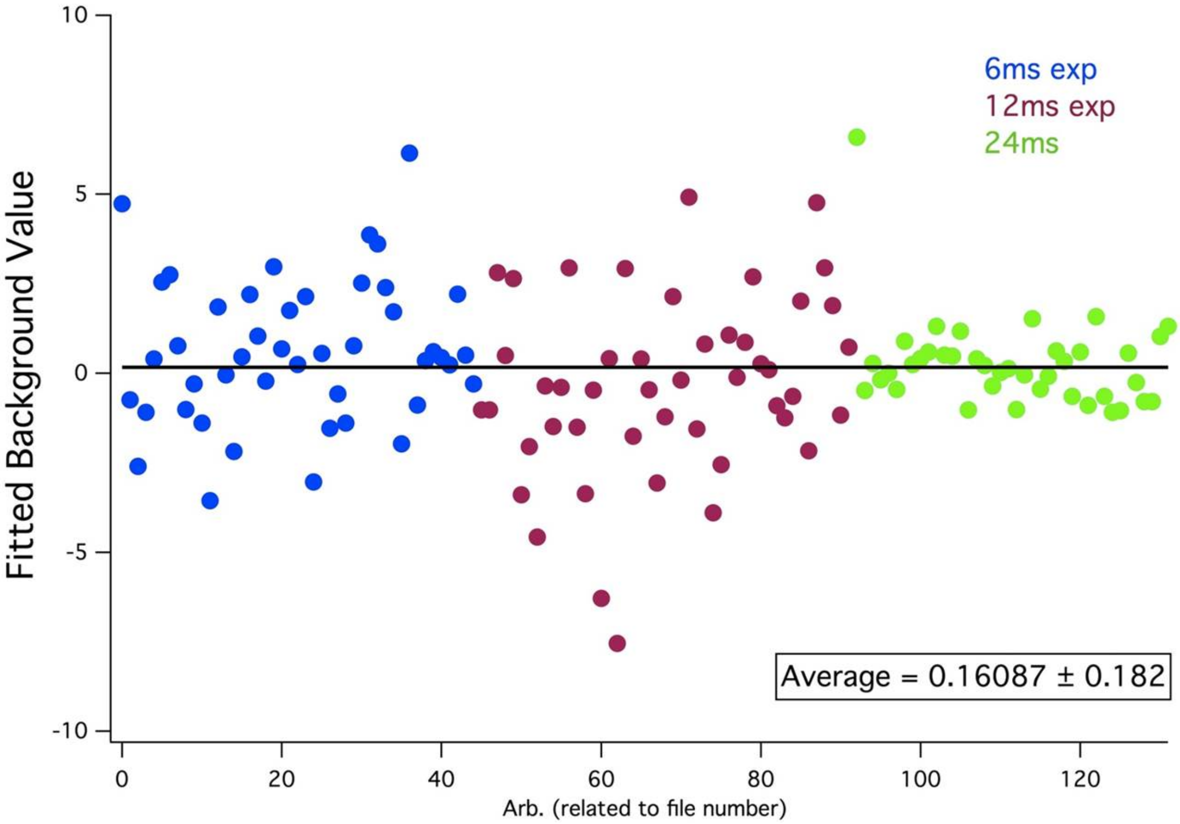

Figure 3.20: The fitted values of the residual background (B.G.) for various file numbers. The blue, purple, and green points correspond to TOFs of 6, 12, and 24 ms. Larger expansion times have larger cloud sizes and smaller optical depths. The fitted residual background appears to be independent of the cloud size and optical depth, and appears to be random noise.

We fit these CDFs at large radii with

$$N + \mathrm{B.G.} \cdot r^2, \tag{3.10}$$

where N is the fitted atom number and B.G. is the fitted slope defining the residual background. The residual background fits have a standard deviation of 0.18, see figure 3.20. Subtracting the fitted residual background from the OD drastically improves the flatness of the CDF at large radii, see figure 3.21, and works nearly consistently for all images, see figure 3.22.

To measure the number of atoms in our system, we could integrate the optical depth out to a certain radius - this is equivalent to a single point of $\mathrm{CDF}(r)$. However, there are small wiggles in our CDFs due to the OD fringes, these wiggles translate into number noise that varies with r. We find that the fitted number N from equation 3.10 has much less noise than the integrated number, see figure 3.23. We therefore use the fitted N to define the atom number in all future resonant measurements.

It is worth mentioning that later in this thesis we begin imaging molecules. As the molecular clouds have much lower optical depth, we do not use high-intensity imaging, and therefore the ϵ correction is not necessary. We found no significant different in our molecule number when azimuthally averaging the data and fitting N with the residual background as compared to taking N from a 2D Gaussian fit, and we therefore use the latter (simpler) approach to define molecule

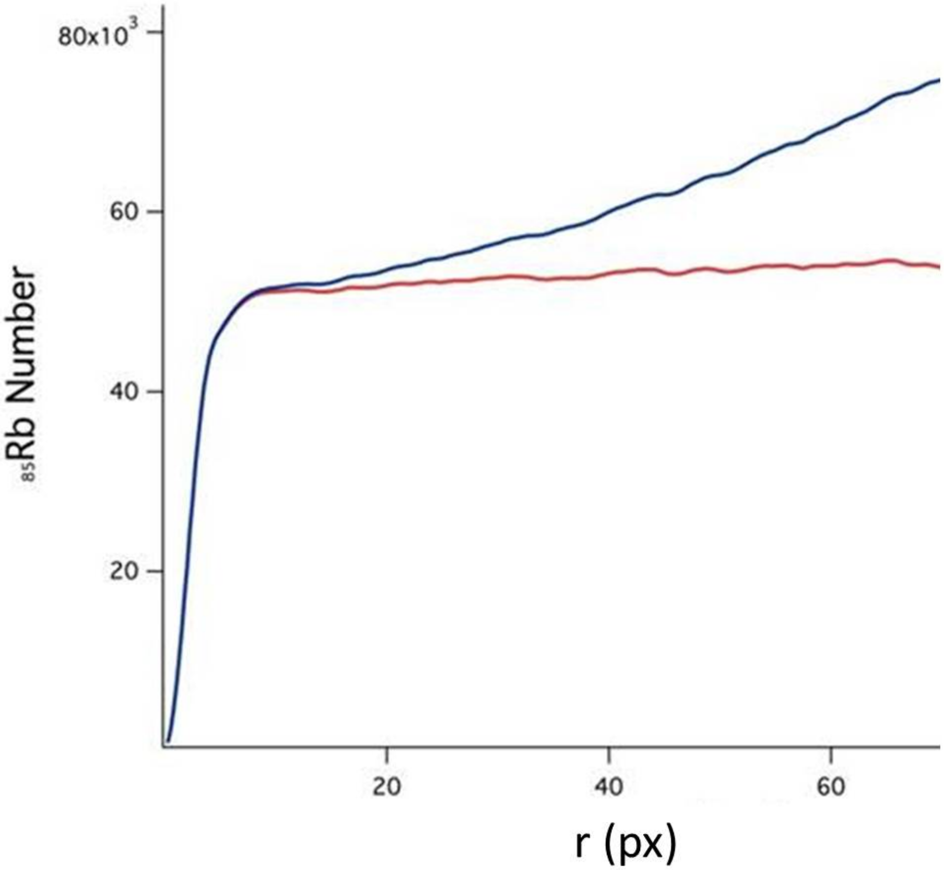

Figure 3.21: Subtracting out the residual background of the original CDF (blue) results in a CDF that is much flatter at large radii. This particular CDF is of a non-resonant condensate expanded for 6 ms TOF.

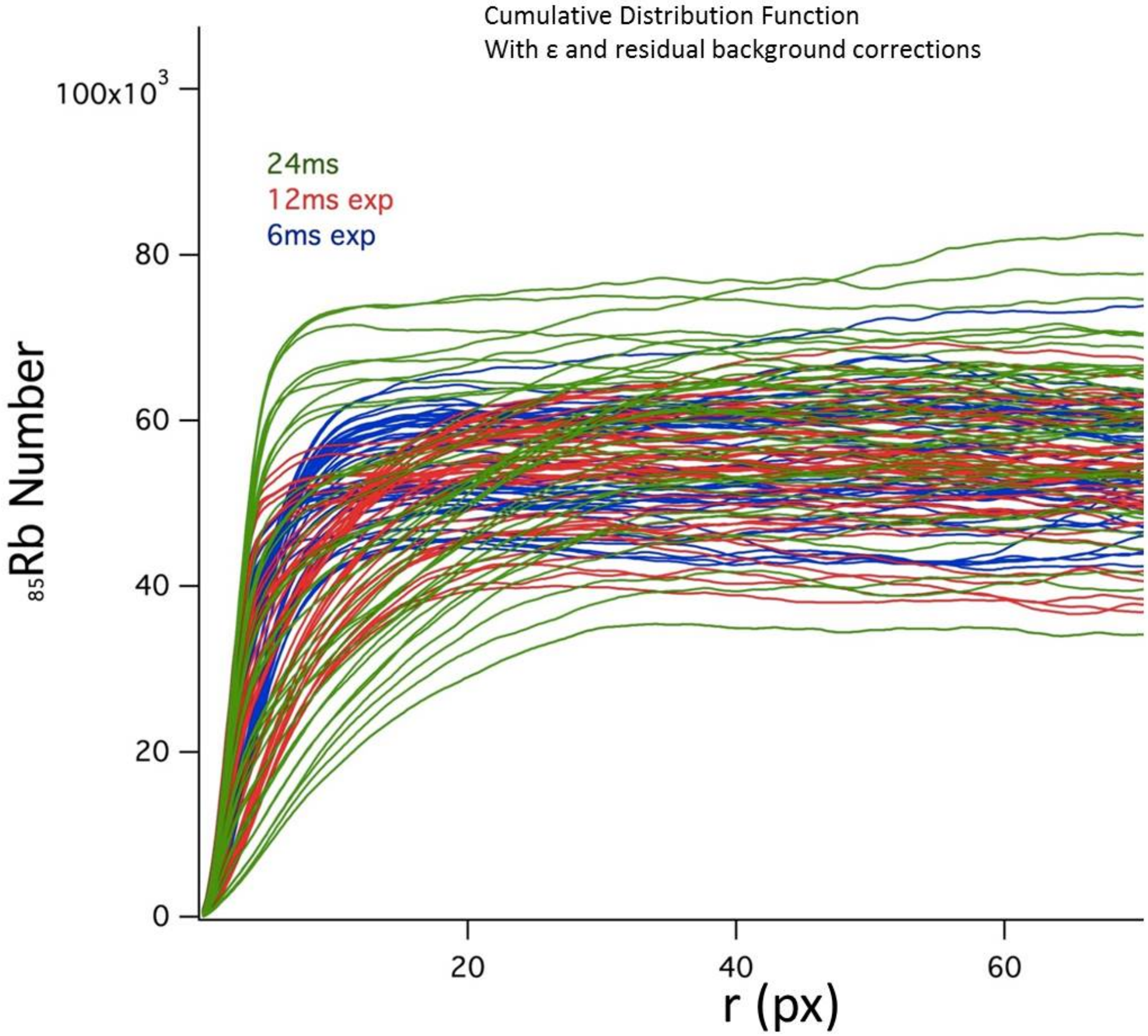

Figure 3.22: CDFs from the same condensate images as figure 3.20. We subtracted the fitted residual background (B.G.) from the optical depth for each CDF. This results in the outlier CDFs finally flattening at large radii.

number in all future resonant measurements.

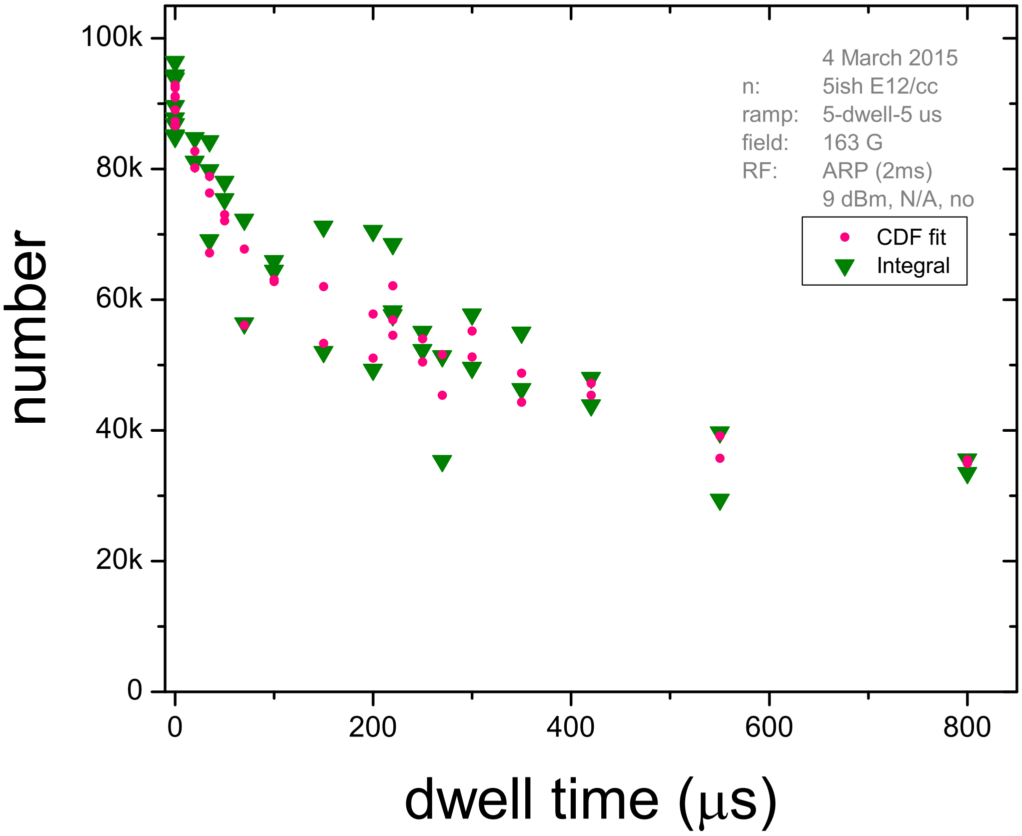

Figure 3.23: The number of atoms as a function of dwell time at unitarity after evaluated by radially integrating optical density (green triangles) or CDF fit using equation 3.10 (pink points). The latter technique reduces the noise due to background fringes.

Chapter 4

Density

Most of the experiments discussed in this thesis involve ramping to resonance, allowing the system to evolve on resonance, then ramping back out to weak interactions. Details of these ramps and definitions of the time scales used to characterize the experiment are discussed in Chapter 5. In these experiments we vary many knobs, including the resonant evolution times, the ramp in / out times, and the initial density of the gas. The density of the gas changes on resonance, due to both loss and expansion. We therefore always report the "initial" density, meaning the density of the condensate just before we begin the sweep to resonant interactions. We reference this density in units of E12/cc, more commonly seen as $\times 10^{12}$ cm^{-3}. In this chapter we discuss how we vary the initial density of our system by over two orders of magnitude.

4.1 Density-averaged density

When we colloquially say density (n), we are referring to the density-weighted density, i.e. the density averaged by the density distribution. The density of our harmonically trapped condensate varies from a peak density (n_{pk}) at the center to 0 at the very edges. Other ultracold atomic experiments avoid this large variation in density by either a box trap [80] or a donut beam [81].

We calculate the relation between the density-weighted density and peak density for a condensate in a spherically symmetric harmonic trap of frequency ω. Because the number of atoms in our condensate is large, we use the Thomas-Fermi approximation to describe the wave function of our system as

$$\psi(r) = \sqrt{\frac{\mu - V(r)}{U_0}}, \tag{4.1}$$

where μ is the chemical potential given by $\frac{\hbar\omega}{2}\left(\frac{15\,N\,a}{\sqrt{\hbar/(m\omega)}}\right)$, $V(r)$ is the harmonic trapping potential equal to $m\,\omega^2\,r^2/2$, and U_0 is the interaction energy, $4\pi\,a\,\hbar/m$ [17]. The peak density occurs at the center of this wave function, $n_{\text{pk}} = |\psi(0)|^2 = \frac{\mu}{U_0}$. The size of a Thomas-Fermi condensate, defined where $V(r) = \mu$, is called the Thomas-Fermi radius and is given by $R_{\text{TF}} = \sqrt{\frac{2\,\mu}{m\omega^2}}$ [17].

The density-weighted density is defined as

$$\langle n \rangle \equiv \frac{\int n^2(r)\ \mathrm{d}^3r}{\int n(r)\ \mathrm{d}^3r}. \tag{4.2}$$

This can be rewritten as

$$\langle n \rangle = \frac{\int |\psi(r)|^4\ \mathrm{d}^3r}{N}. \tag{4.3}$$

Plugging in equation 4.1 to equation 4.3 and evaluating the integral from 0 to R_{TF} yields

$$\langle n \rangle = \frac{4}{7}\frac{\mu}{U_0}. \tag{4.4}$$

We therefore conclude that for a harmonically trapped Thomas-Fermi condensate, $\langle n \rangle = \frac{4}{7}\,n_{\text{pk}}$ and is related to ω, N, and a by

$$\langle n \rangle = \frac{(15Na)^{2/5}}{14\pi\,a}\left(\frac{m\omega}{\hbar}\right)^{6/5}. \tag{4.5}$$

.

4.2 Perez-Garcia model

We change the density over two orders of magnitude by changing the size of our condensate. We vary the size of our condensate by jumping the scattering length to larger or smaller values (a_{jump}). This sudden change in interaction strength causes the atoms to either push away from or fall towards each other. When the cloud is in a harmonic trap, this sudden change in scattering length induces an oscillatory size change called a breathe. The dynamics of these breathes are modeled using a variational technique to solve the Gross-Pitaeveskii equation in [82]. In the case of positive scattering lengths they derive an analytic solution describing the axial and radial condensate widths:

$$\ddot{w}_r + f_r^2\, w_r = \frac{\hbar^2}{m^2}\left(\frac{1}{\omega_r^3} + \sqrt{\frac{2}{\pi}}\frac{a\,N}{w_r^3\,w_z}\right), \tag{4.6}$$

$$\ddot{w}_z + f_z^2\, w_z = \frac{\hbar^2}{m^2}\left(\frac{1}{\omega_z^3} + \sqrt{\frac{2}{\pi}}\frac{a\,N}{w_r^2\,w_z^2}\right), \tag{4.7}$$

where w_i relates to the 2D Gaussian-fit widths by $w_i = \sigma_i/0.78$. We call these equations the "Perez-Garcia model".

The three trapping frequencies of our nearly symmetric trap were measured to be 10.46, 9.47, and 10.56 Hz, see figure 4.1. We therefore set our radial and axial trapping frequencies (f_r and f_z) to 10.5 and 9.5 Hz, and this predicts a breathing oscillation period (roughly a half-trap cycle) of about 44 ms. We can therefore expand or contract our cloud by jumping the field to larger or smaller a_{jump} and allowing the cloud to breathe for a quarter trap cycle (i.e. 22.5 ms), at which point the size reaches a maximum or minimum, see figure 4.2. We will now explore the limitations of this method in both the high and low density limits.

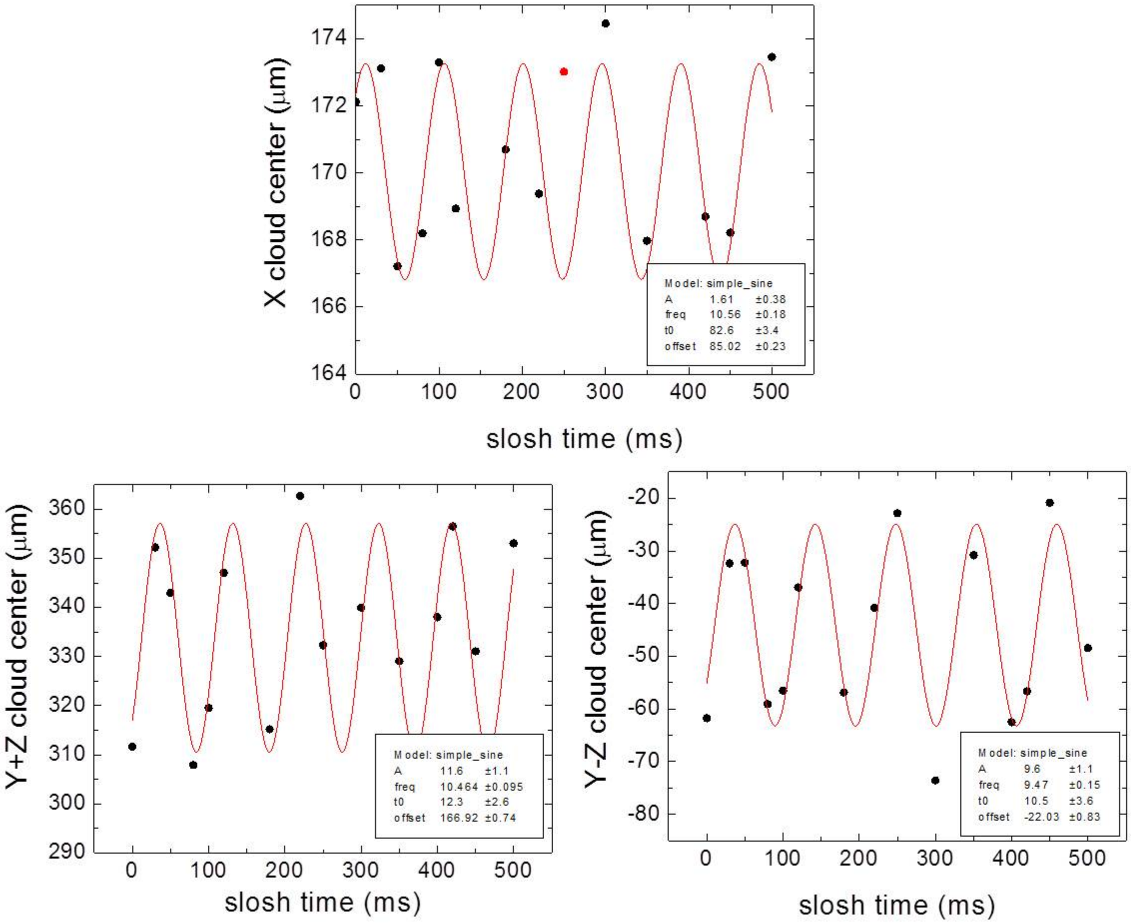

Figure 4.1: We measured the magnetic trapping frequencies by purposefully loading our cloud from a misaligned optical trap to induce a slosh. We add or subtract the measured z and y cloud centers because the axes of our trap are 45 degrees from our imaging axes [74]. We measure trapping frequencies of 10.46(9), 9.47(14) and 10.56(0.18) Hz. These trap frequencies were measured several years earlier in [74] to be 10.41(4), 9.39(7), and 10.21(5), and have not drifted significantly.

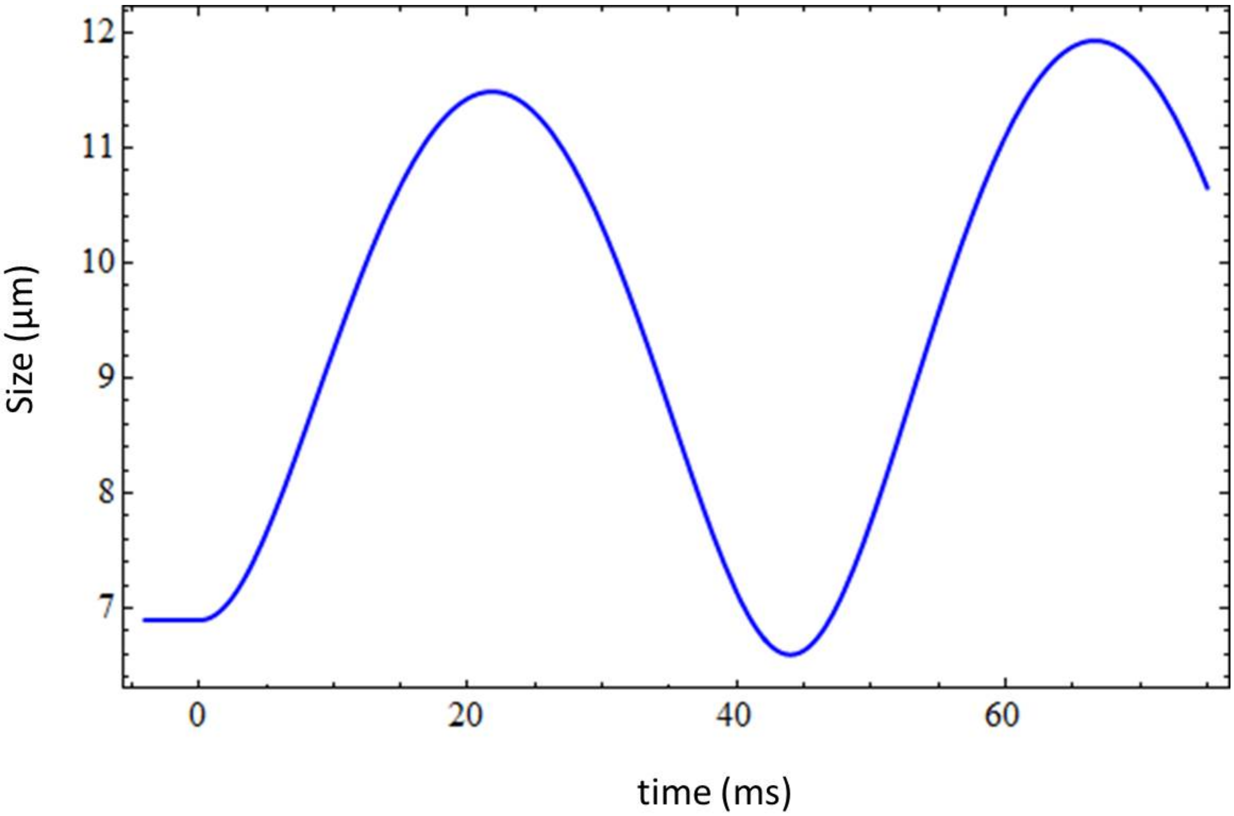

Figure 4.2: The predicted axial size of a condensate in a 9.5 x 10.5 Hz as a function of time after jumping to 500 a_0 at time 0. The cloud returns to its original size around 44 ms (equal to a half-trap period) and reaches a maximum size around 22 ms.

4.3 High density limit

High densities are achieved when $a_{\text{jump}} < a_i$. We measure a_{jump} to within $\sim 5\,a_0$ using microwave spectroscopy. This uncertainty is fine for large values of a_{jump}, however when a becomes on the order of 5 a_0 itself, it transfers into large uncertainties in density. We therefore set our minimum a_{jump} to 15 a_0, for which we expect densities of over 12 times our original density.

The real limitations on our high density however come from the speed of our fast-B coils. As will be explored in Chapter 5, our fast-B coils ramp our condensate to and from resonance and have a maximum speed of about 8 Gauss in 5 μs. More importantly, the fast magnetic ramps have a turn-around time that sets the minimum time spent on resonance to about 10 μs (this minimum time depends on the density of the cloud, as resonance is defined by $na^3 > 1$). For experiments in which we want to set $t_{\text{dwell}} \sim 1\,t_n$, this sets our maximum density to about 60 E12/cc, where t_n is 11.5 μs.

4.3.1 Actual high density limit

We want to image the clouds in trap to compare their sizes to the predicted values to ensure that the density is changing as expected. However, the smaller sizes of the high density clouds make it difficult to image without expansion. So we instead jump back to a_i and allow the cloud to expand before imaging. We are therefore comparing our clouds to a two-jump Perez-Garcia prediction, see figure 4.3. The accuracy of the high density predictions is limited by trap frequency uncertainties, as ω becomes more important in equations (4.6) and (4.7) at low a. Based on the measurement comparisons in figure 4.4, we can trust that our high density clouds are correct when we jump down to as low as 19 a_0. This corresponds to a density of 35 E12/cc.

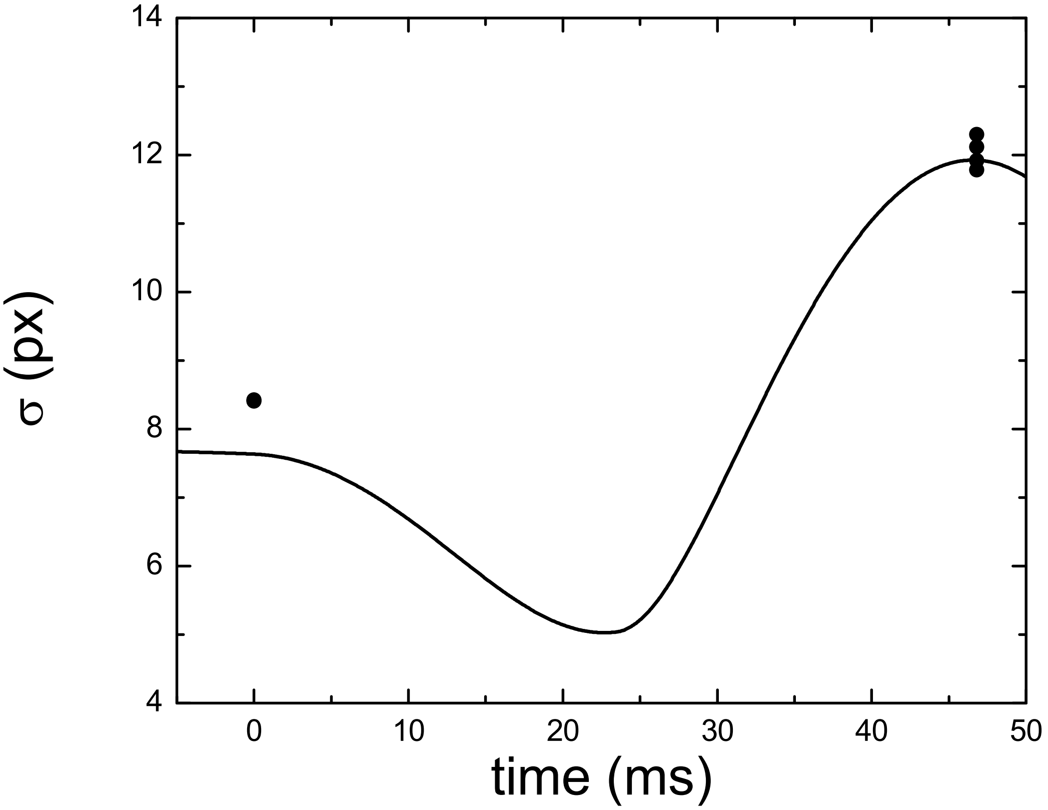

Figure 4.3: After creating a condensate at $a_i = 146.25\, a_0$, we jump to $a = 54.71\, a_0$ at $t = 0$ ms and allow the cloud to compress to high density over a quarter trap period. Because the high density cloud is difficult to reliably image, we then jump back to a_i to expand the cloud for another 22.5 ms. The black points represent measurements of our condensate size, in 2D Gaussian σ, at 0 time and at 45 ms, transferred to the imaging state with a microwave π-pulse . The solid line represents the expansion predicted by the Perez-Garcia model. We see good agreement between the predictions and our measurements.

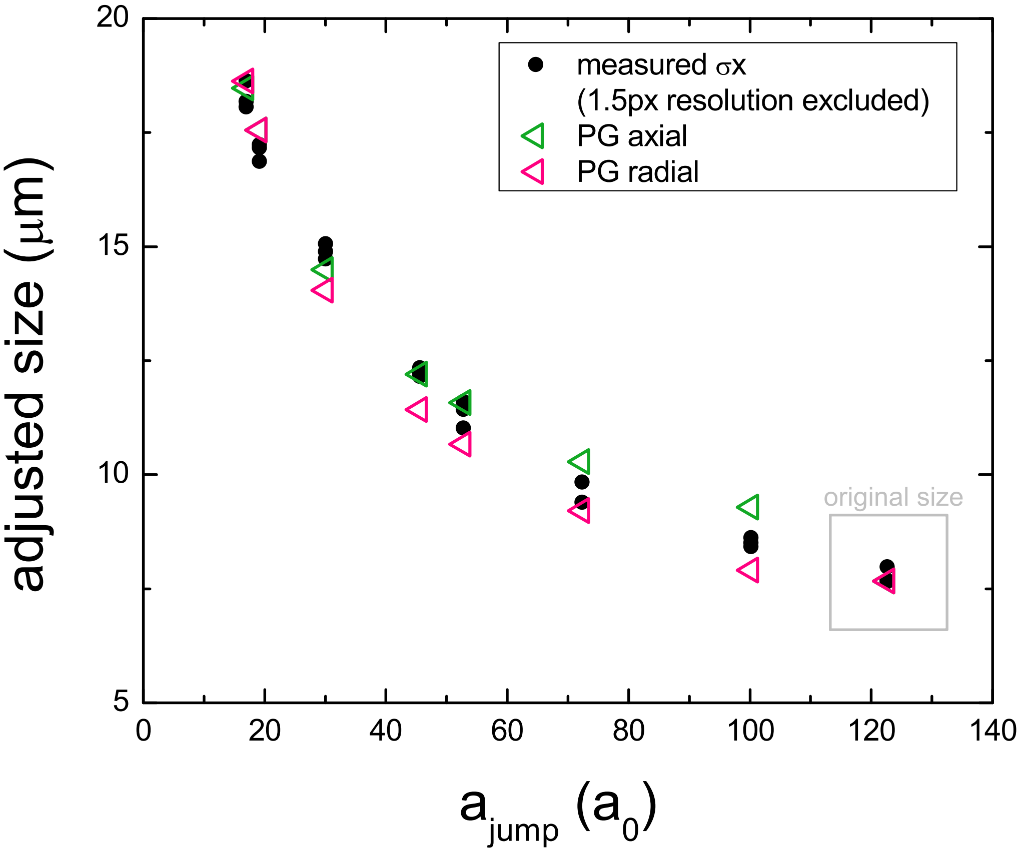

Figure 4.4: The black points represent the adjusted (i.e. resolution subtracted) measured size, in 2D Gaussian σ, at $t = 45$ ms after an $a_i \rightarrow a_{\text{jump}} \rightarrow a_i$ jump sequence with quarter trap expansions, where a_i is 122.6 a_0. The green and pink triangles represent the axial and radial predictions from the Perez-Garcia model. The points at 122.6 a_0 are the original cloud size (no jump to 500 a_0). We see good agreement with the model when jumped to as low as 19 a_0, with only minor discrepancies in cloud size beginning to emerge.

4.4 Low density limit

The density is lowered when $a_{\mathrm{jump}} < a_i$. There are two mechanical limitations to our lower density: the magnetic field gradient and heating of the Fast-B coils. There is also an interaction-based limit that we extend by a double-jump method.

4.4.1 B-field gradient

To hold our ^{85}Rb atoms in the $|2, -2\rangle$ state against gravity we apply a magnetic field gradient of $F_g = 22.4$ G/cm. This vertical field gradient sets the top and bottom ends of our condensate at different magnetic fields - the larger the condensate radius, the larger difference in magnetic field. There exists a large enough cloud then that the B-field gradient across it results in one end no longer in the resonant regime of $na^3 > 1$.

We define our initial cloud as having a density of n_0 and a radius of R_0. A cloud whose radius expands by a factor of ΔR then has a density of $n = \frac{n_0}{(\Delta R)^3}$. Assuming that the center of the cloud sits at the magnetic field corresponding to the peak of the Feshbach resonance, the change in scattering length across a cloud of this size is $\Delta a = a_{\mathrm{bg}}\left(1 - \frac{\Delta}{\Delta_B}\right)$, where Δ is the width of the Feshbach resonance (10.7 G) and Δ_B is the variation in magnetic field across a cloud of original radius R_0 expanded by Δ_R, $\Delta_B = F_g\,\Delta_R\,R_0$. Given these assumptions the resonance criteria that $na^3 > 1$ can be rewritten as

$$\frac{n_0^{1/3}}{\Delta_R}\,a_{\mathrm{bg}}\left(1 - \frac{\Delta}{F_g\,\Delta_R\,R_0}\right) > 1. \tag{4.8}$$

Solving this for Δ_R we obtain a limitation on the maximum expansion size:

$$\Delta_R \leq \frac{n_0^{1/3}a_{\mathrm{bg}}}{4}\left(1 \pm \sqrt{1 - \frac{4\Delta}{n_0^{1/3}\,a_{\mathrm{bg}}\,F_g\,R_0}}\right). \tag{4.9}$$

Assuming an initial size of 17 μm and an initial density of $n_0 = 5$ E12/cc, the maximum ΔR is 3.39; this corresponds to a lower density limit of 0.14. If we set more stringent conditions on our resonance condition and instead require $na^3 > 10$, the lower density limit rises to 0.4. We can overcome this limitation, however, by turning off the vertical B-field gradient that holds the cloud up against gravity.

4.4.2 Fast-B heating

The second mechanical limitation to our low density achievements is the heating of the Fast-B coils. A little more than 8 Amps of current is required to jump our field from a_i to $1/a \rightarrow 0$. Unlike the IP and bias coils, the fast-B coils are not water-cooled. We therefore have limited time before the coils heat enough to warp our science cell or cause general mayhem. The fast-B coils have a resistance of about 0.018 Ohms, this generates 1.2 Watts with 8.2 Amps. This corresponds to about a heating of about 6.7 deg C after a 1 second pulse. We use a very conservative estimate of keeping the cumulative temperature below 5 deg C when experiments are repeated on a 90 second duty cycle in a confined environment (i.e. little air flow). This limits the amount of time the fast-B coils can be running at full current to about 2 ms. If one is doing an experiment with dwell times of about 1 t_n, this limits the lower density to about 0.03 E12/cc.

4.4.3 Lee-Huang-Yang limit

Ultimately our low density achievements are limited by interactions, specifically when the interactions increase out of the mean-field limit. When we first jump to a large scattering length, both the density and scattering length are not small and therefore na^3 can be large. This is a problem because a large na^3 is indicative of strong interactions in the system, and these strong interactions could modify the energy of our system. We want to keep our cloud in the weakly-interacting regime, where losses and interactions are minimal. We define the weakly-interacting regime as where the Lee-Huang-Yang (LHY) correction to the energy density is below 10 %. The LHY correction was discussed in detail in Chapter 2 and the first order term was

$$\frac{128}{15\sqrt{\pi}}\sqrt{na^3}. \tag{4.10}$$

The correction term is equal to 10% when na^3 is equal to 0.000431.

We see that when we jump our cloud from its initial $a_i = 150\,a_0$ to $a_{\mathrm{jump}} = 2000\,a_0$, the LHY correction jumps up to as high as 38% and remains above 10% for nearly 10 ms, see figure 4.5. During this time there may be significant heating in the cloud, as well as loss due to three-body recombination. The largest scattering length that we can jump with our initial density cloud while keeping the LHY correction below 10% is 780 a_0. After 22 ms expansion at 780 a_0, the cloud density will fall to only 0.71 E12/cc. While this is a lower density than our original density, it is preferable to reach even lower densities.

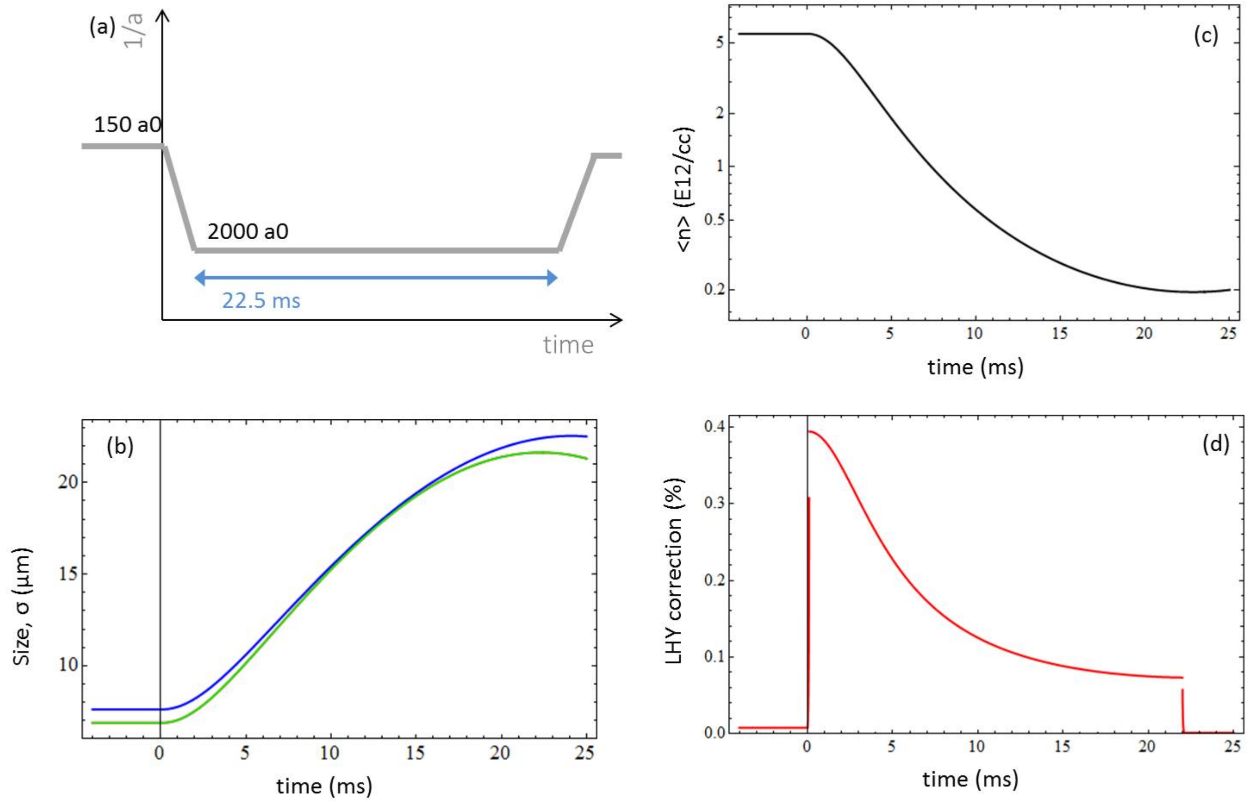

Figure 4.5: (a) Our original method to create a low density cloud involved jumping to a single large scattering length. To achieve a density of 0.195 E12/cc, $a_{\text{jump}} = 2000\, a_0$ for 22 ms. (b) The predicted axial (green) or radial (blue) size of the cloud, in Gaussian σ, as a function of time, after we jump to a_{jump} at 0 ms and return to a_i at 22 ms. (c) The density of the cloud in E12/cc as a function of time, following the same timeline. (d) The LHY correction in % as a function of time, following the same timeline. We see that the density does not decrease quickly enough after the jump to large scattering length, and the LHY correction becomes very large as a result.

4.4.4 The double-jump method

We are able to reach lower densities while still keeping the LHY correction below 10% by jumping to a smaller scattering length (a_{jump1}) before jumping to a larger scattering length (a_{jump2});

we call this the double-jump method, see figure 4.6. This technique works because the cloud shrinks when we jump to the smaller scattering length, and the decreased interparticle spacing causes the atoms to push against each other with much more force when the scattering length is increased, see equations (4.6) and (4.7).

The lowest density achievable with the double-jump method is limited by the minimum value of a_{jump1} - the lower the initial scattering length, the lower the final density. As discussed in the high density section, the minimum scattering length we trust our jump to is 15 a_0. After allowing the cloud to compress at $a_{\text{jump1}} = 15\ a_0$ for 22 ms, we can jump to $a_{\text{jump2}} = 350\ a_0$ to expand the cloud while still keeping the LHY correction below 10%. The Perez-Garcia model predicts that this particular double jump would create a cloud of density 0.075 E12/cc, nearly ten times lower than the single-jump limit.

We compared two clouds (one of density 0.195 E12/cc created with a single jump to $a_{\text{jump}} = 2000\ a_0$, the second of density 0.258 E12/cc created with a double jump to $a_{\text{jump1}} = 50$, $a_{\text{jump2}} = 500\ a_0$) to see if our conservative efforts to keep the LHY correction low were worthwhile. The single-jump cloud has a peak LHY correction of 38% and is above 10% for nearly 10ms; the double-jump cloud never strays into the strongly-interacting regime of LHY $> 10\%$. We compared both of these low density clouds' sizes to their predicted sizes, as well as the number of atoms remaining in the condensate, see figure 4.7. We saw that the single-jump cloud was both larger than its predicted size and had lower number than the original condensate. This is indicative of cloud heating and enhanced losses, both due to the strong interactions. The double-jump cloud was not larger than the predicted size and did not have any number loss. We therefore conclude that the low LHY correction associated with the double-jump method is important for keeping strong interactions out of our cloud pre-resonance.

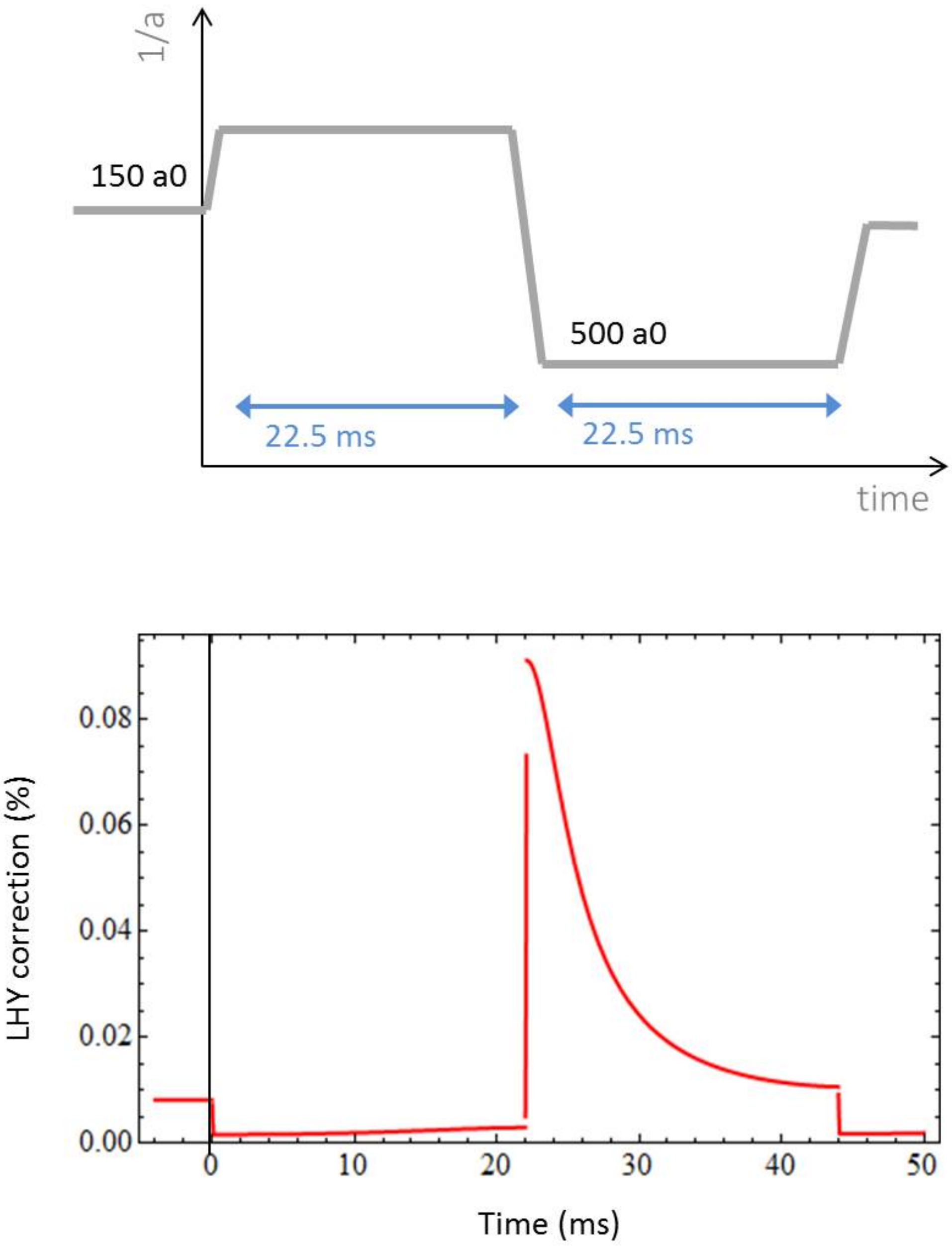

Figure 4.6: (a) We can achieve a density of 0.258 E12/cc by first jumping to a lower scattering length of $a_{\mathrm{jump1}} = 50\,a_0$ for 22 ms, then jumping to a higher scattering length of $a_{\mathrm{jump2}} = 500\,a_0$ for another 22 ms. (b) The LHY correction in % as a function of time following the same timeline. We see that this correction is below 10% at all times. This double-jump method is therefore able to achieve low densities without creating strong interactions.

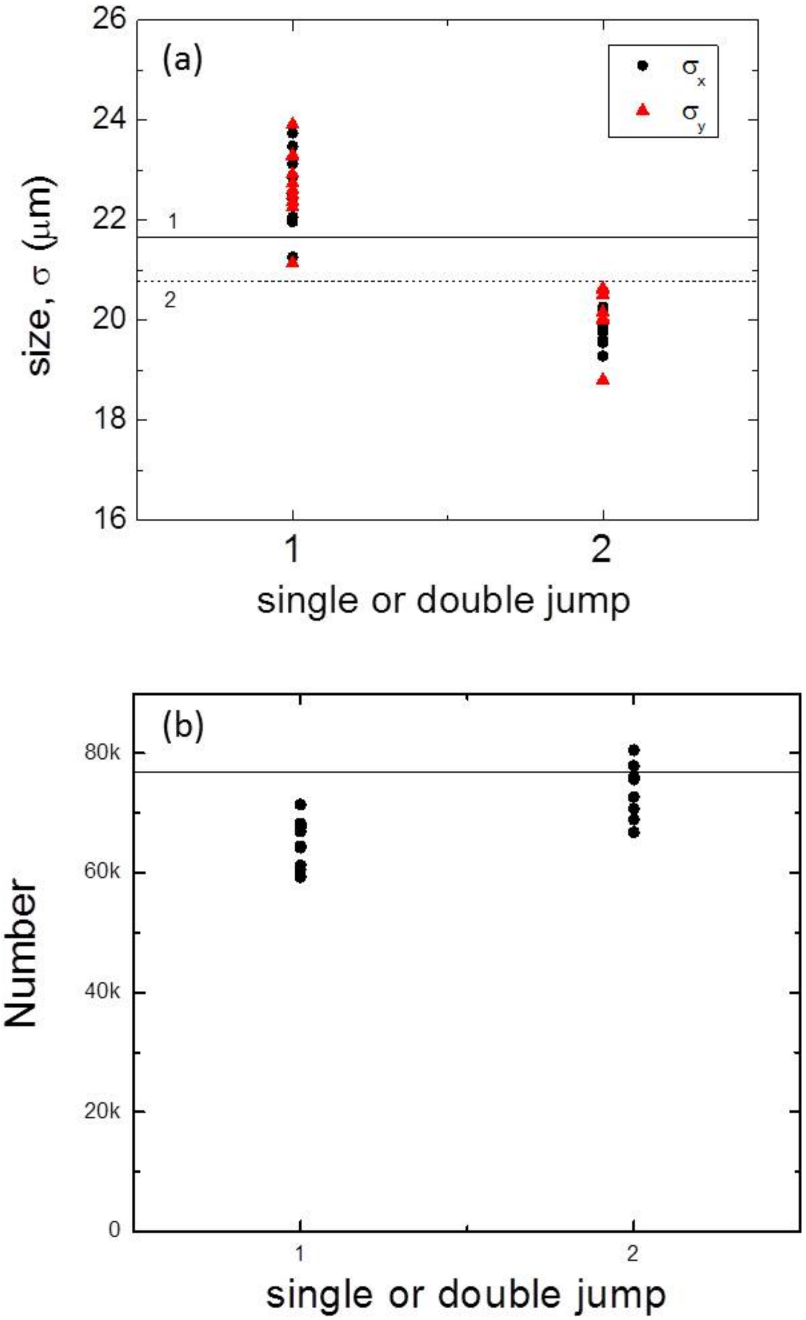

Figure 4.7: We examined the (a) size and (b) number of atoms remaining in our condensate after both a single jump to 2000 a_0 and a double jump to 50 then 500 a_0. The solid lines represent the expected values (a) calculated by the Perez-Garcia model or (b) measured by a 28 ms expanded cloud transferred to the imaging state. The single-jump cloud is both larger than expected and has less number. We believe this is due to heating and three-body recombination that is enhanced in the strongly-interacting regime. The double-jump method yields a cloud that maintains the initial condensate number and yields smaller than expected sizes; we believe the latter is due to trap frequency uncertainties.

4.4.5 Actual low density limit

While we calculated the lower density limit as 0.075, in practice we found that these low densities were not achievable in our system, see figure 4.8. We measured the sizes of clouds after jumping to various scattering lengths, see table 4.1 for a list of the scattering lengths, corresponding predicted densities, and maximum LHY correction. As we only want to work in density regimes properly predicted by the PG model, we compared the measured and predicted sizes as a test of the actual density. We found that when a_{jump1} was as low as 16 a_0, the final cloud did not fully expand. We attribute this error to trap frequency uncertainties, which magnify at low scattering lengths as ω becomes more important. We found that the actual lowest a_{jump1} value that produced reliable final cloud sizes was 44 a_0. The lowest robustly estimated density achievable with the double-jump method seen here is 0.218 E12/cc, achieved with an initial jump to 44 a_0 followed by a second jump to 486 a_0. The lowest robustly estimated density reported in this thesis is 0.18 E12/cc - the slight variance in density is caused by a different initial scattering length, a_i.

Table 4.1: The predicted final densities, and the maximum LHY correction, for clouds that are expanded at a_{jump1} for 22 ms, then a_{jump2} for another 22 ms .

a_{jump1} (a_0)	a_{jump2} (a_0)	$\langle n \rangle$ (E12/cc)	LHY (%)
43.9	220	0.678	0.03
43.9	366	0.328	0.06
43.9	486	0.218	0.10
26.9	408	0.135	0.10
26.9	486	0.123	0.13
16.2	220	0.162	0.05
16.2	366	0.076	0.11

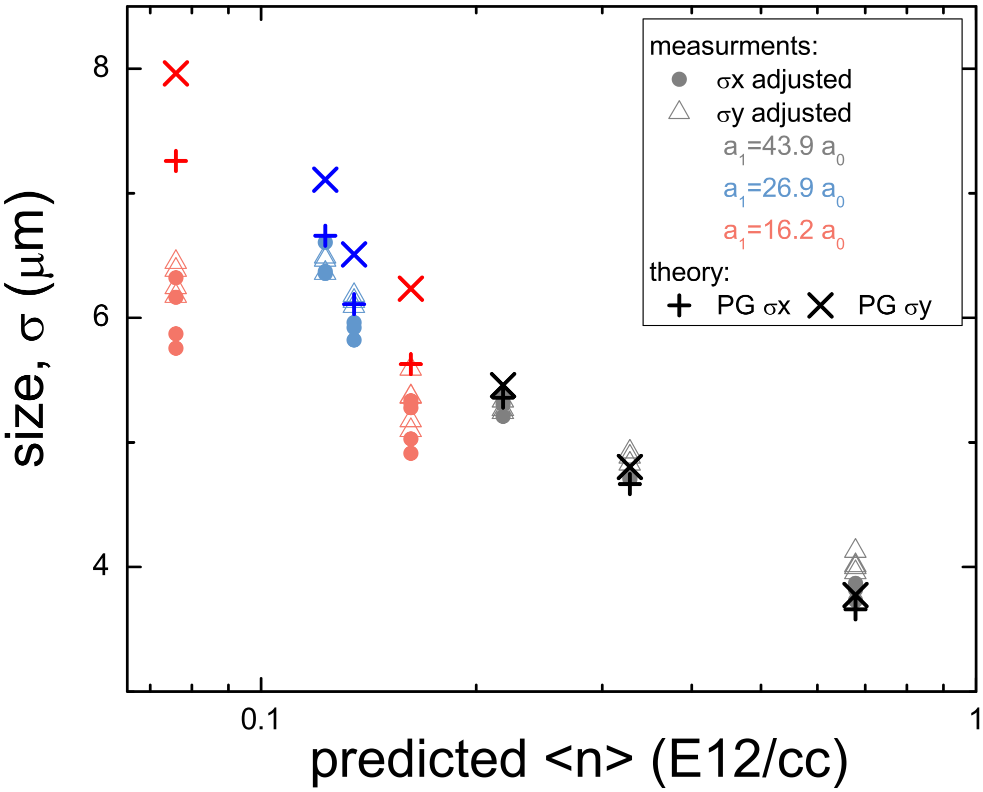

Figure 4.8: By comparing the measured cloud sizes to the predictions made by the Perez-Garcia model, we are able to quantify our actual lowest density. Gray represents data with a first jump of 43.9 a_0, blue with a first jump of 27 a_0, and pink, 16 a_0; these specific points can be found in table 4.1. The filled circles and open triangles represent the measured sizes, in Gaussian sigma, in the x and y direction, while the + and x represent the Perez-Garcia predictions in each direction. Although initially jumping to a lower scattering length allows us to achieve much lower densities without increasing the LHY correction, we see that the model over predicts the expansion of the clouds when we jump to lower initial scattering lengths.

Chapter 5

Ramp to resonance

5.1 Creating fast magnetic ramps

Thus far we have discussed how to image our BEC and to create BECs of varying densities. While these are necessary components of our experiment, the real novelty is our ability to take our BEC to resonant interactions. Resonant interactions occur near the Feshbach resonance, described in detail in Chapter 2. We recall that the scattering matrix becomes unity, this regime is also referred to as "unitarity", and the interactions as "unitary".

This regime is historically a difficult place to explore with a zero-temperature Bose gas because the three-body recombination rate, which scales as a^4 in the mean-field regime, becomes very large as a diverges, effectively destroying the condensate before it reaches resonance. We have overcome this challenge by using a fast magnetic coil, aptly named the Fast-B coil, to get the condensate to resonance before appreciable loss occurs (the "b" in magnetic is silent).

5.1.1 Fast-B coil review

Specifications of the Fast-B, including the coil size, servo circuit diagram, eddy-current theory and measurements, can be found in Makotyn's thesis [36]. In this thesis I will expand on the actual shape of our Fast-B magnetic ramps that preemptively correct for eddy currents, as this shape is important for later data analysis.

The small inductance of our Fast-B coils allows us to achieve a 10-90% current step in 2.1 μs [36]. However, eddy currents in both the Fast-B coils and two parallel coils (the Bias coils and pinch coils) slow the time to step the total magnetic field to about 10 μs. To speed up the change in magnetic field, we send a Fast-B current that, once combined with the eddy currents, results in a fast, almost-square magnetic pulse. To do this, we first characterize the eddy current constants that determine the coupling between the coils, the characteristic decay time, and the second-order effects. We determine these empirically by sending out a square pulse to the Fast-B coil and measuring the resulting magnetic field, see figure 5.1(a) for example, and Makotyn thesis [36] for the measured values. With the eddy current constants in hand, we can then work backwards to create an over-shooting Fast-B current that will, when combined with the eddy currents, produce an almost square magnetic pulse that reaches resonance in 5 μs, see figure 5.1(b).

“Working backwards” is easier said than done - as shown in [36], the eddy currents are represented by second-order differential equations. Solving these equations for the ideal current requires an iterative approach in Mathematica due to computing limitations. Most importantly, the commanded magnetic ramp must have no sharp corners, otherwise the derivatives become unbound, causing our iterative calculation to diverge. Because of this, we command a piecewise magnetic ramp (with soft edges) rather a sharp, square pulse.

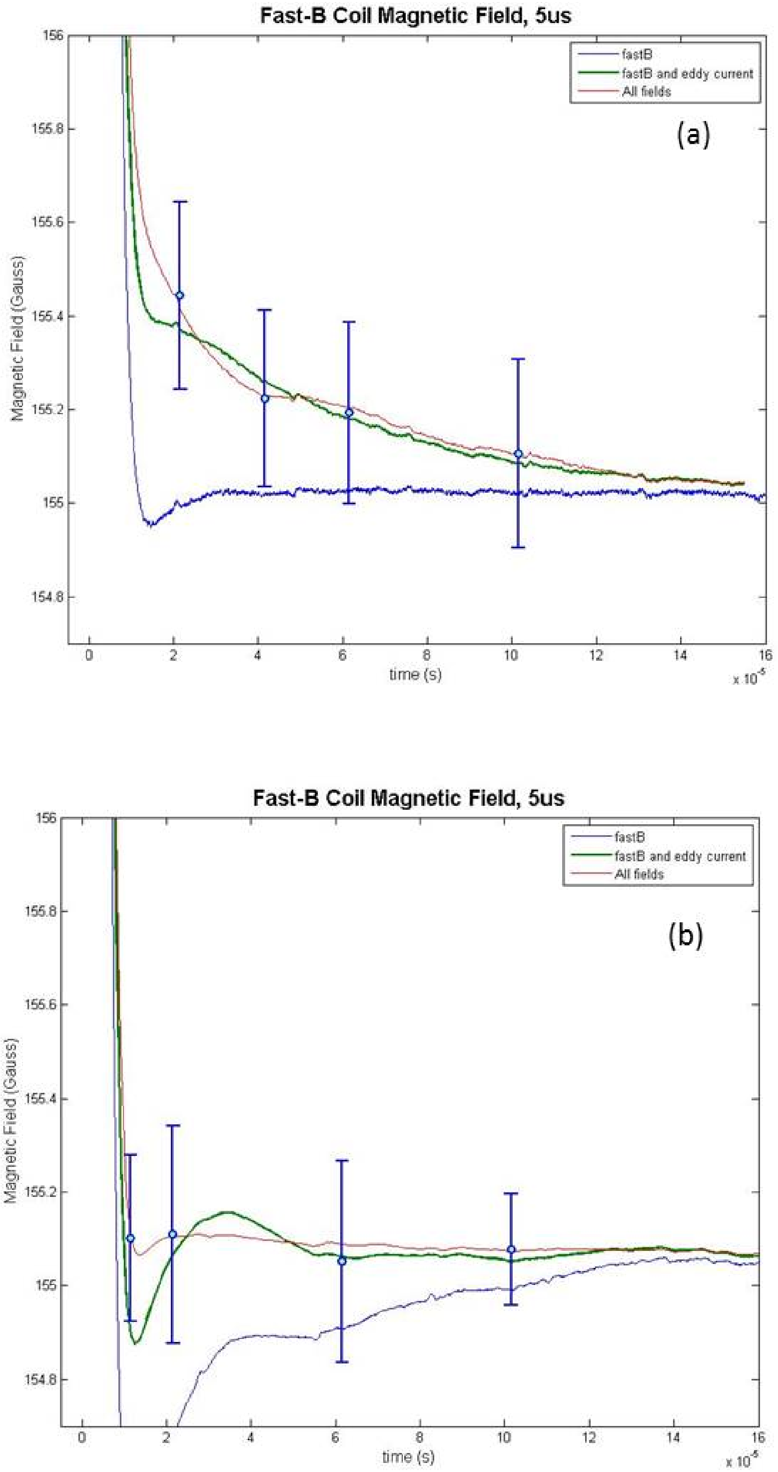

Figure 5.1: (a) We characterize the eddy currents by sending a square current pulse (blue line) through the Fast-B coils and the measuring the resulting magnetic field using RF spectroscopy(blue circles). We estimate the Fast-B correction constants by empirically matching the calculated combined magnetic fields (red line) to the magnetic field measurements. The green line represents the predicted magnetic field account for only the eddy currents in the fast-B coil, and neglecting the external eddy currents. (b) By sending out a non-square Fast-B current pulse (blue line) that corrects for the predicted eddy currents in our system, we are able to produce a nearly perfect magnetic square pulse (red line).

5.1.2 Magnetic ramp shape

Our soft-edged magnetic ramp is described by the following equation and is plotted for two different ramp rates in figure 5.2:

$$B(t) = \begin{cases} \Delta_B \, \frac{125}{6} \frac{t^3}{\mathrm{rt}^3} & : 0 < t \leq 0.1\,\mathrm{rt} \\ \Delta_B \left(\frac{-125t^3}{6\,\mathrm{rt}^3} + \frac{25t^2}{2\,\mathrm{rt}^2} - \frac{5t}{4\,\mathrm{rt}} + \frac{1}{24} \right) & : 0.1\,\mathrm{rt} < \mathrm{t} \leq 0.2\,\mathrm{rt} \\ \Delta_B \left(\frac{5t}{4\,\mathrm{rt}} - \frac{1}{8} \right) & : 0.2\,\mathrm{rt} < \mathrm{t} \leq 0.8\,\mathrm{rt} \\ \Delta_B \left(\frac{-125t^3}{6\,\mathrm{rt}^3} + \frac{50t^2}{\mathrm{rt}^2} - \frac{155t}{4\,\mathrm{rt}} + \frac{253}{24} \right) & : 0.8\,\mathrm{rt} < \mathrm{t} \leq 0.9\,\mathrm{rt} \\ \Delta_B \left(\frac{125t^3}{6\,\mathrm{rt}^3} - \frac{125t^2}{2\,\mathrm{rt}^2} + \frac{125t}{2\,\mathrm{rt}} - \frac{119}{6} \right) & : 0.9\,\mathrm{rt} < \mathrm{t} \leq \mathrm{rt} \\ \Delta_B & : t \geq \mathrm{rt}. \end{cases} \tag{5.1}$$

rt is the total time to ramp from B_{initial} to B_{final}, and $\Delta_B \equiv B_{\text{final}} - B_{\text{initial}}$. The ramp is defined in such a way that the linear portion of the ramp covers 75% of Δ_B in 60% of rt. The first and second (as well as the 5th and 4th) portions of the ramp cover the first (last) 2 and 12.5 percentages of Δ_B, respectively. The entire jump to resonance consists to a ramp to resonance, a dwell time on resonance (with no change in the magnetic field), and finally a ramp away from resonance.

As can be seen in equation (5.1), the initial rate of the magnetic field, dB/dt, is much smaller than the first approximation of Δ_B/ramptime. This has major implications during the ramp away from resonance, which will be discussed further in Chapter 7. Also of note is the linear $B(t)$ regime, which composes 75% of the total Δ_B, has a slope of $\frac{5}{4}\Delta_B/\mathrm{rt}$.

Now that we have discussed the creation and shape of our magnetic ramps, it is useful to define some experimental terminology in regards to our resonant ramps.

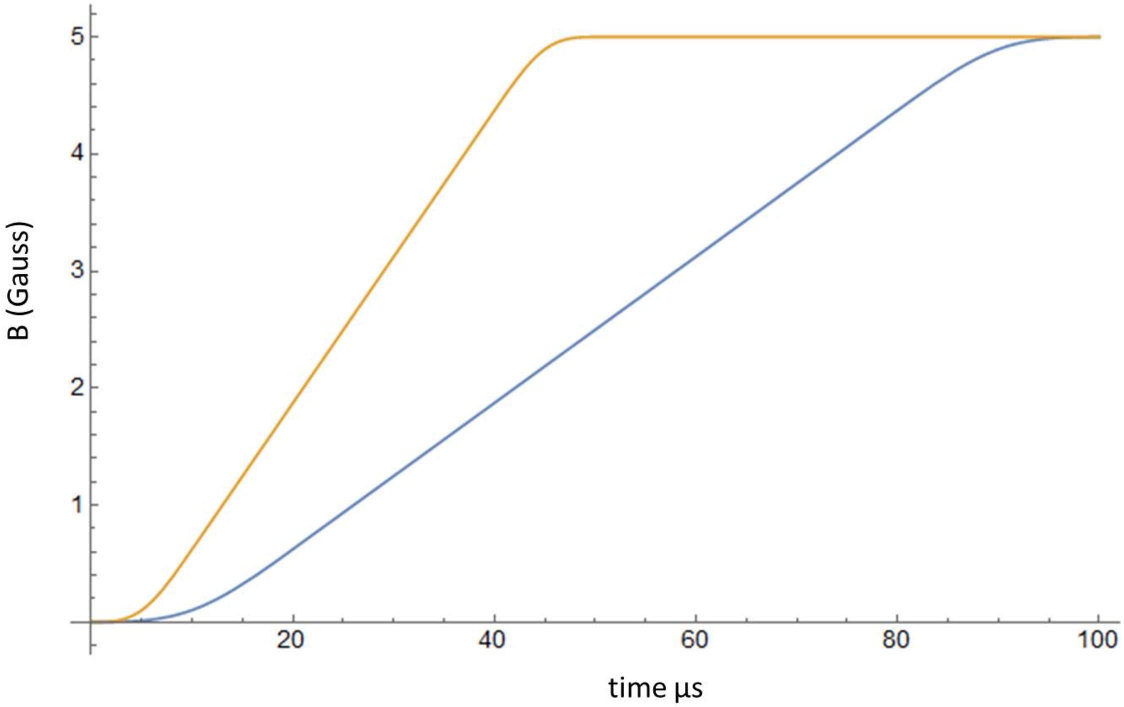

Figure 5.2: B(t) for a 50 μs ramp (orange) and a 100 μs ramp (blue).

5.2 Magnetic ramp terminology

5.2.1 Experimental parameters

The blue labels in figure 5.3 are experimental parameters. The "dwell time" is the amount of time we hold the magnetic field at resonance. r_{out} is defined as the amount of time it would take to ramp from $1/a = 0$ to a_i, our initial scattering length, such that $\mathrm{rt} = \mathrm{r}_{\mathrm{out}} \cdot \frac{\Delta_{\mathrm{B}}}{\mathrm{B}(\mathrm{a}_{\mathrm{f}})-\mathrm{B}_0}$. The actual value of a we ramp to for imaging is called a_f, and is sometimes greater than a_i; for this reason r_{out} is actually a unit of rate rather than time (although we report its value in units of μs due to its definition). This contrived definition may seem unnecessarily confusing at first, but is in fact very useful when comparing data sets probed at different values of a_f.

After we ramp away from resonance, we hold the field at a_f for a time "hold time" before transferring atoms to the imaging state. For most of the data presented in the remainder of this chapter, $a_f = a_i$ and hold time is relatively short. In later chapters, hold time becomes appreciable (on the order of 2 ms) and a_f varies between a_i and 1000 a_0.

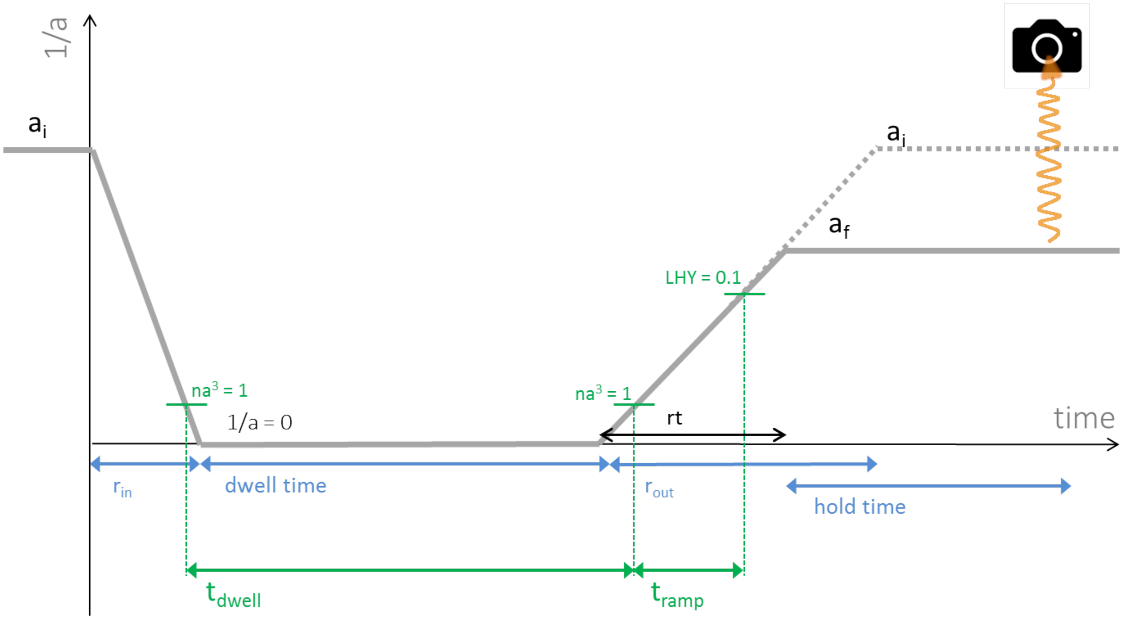

Figure 5.3: ramp definitions. The labels in blue are the experiment-set parameters, while the labels in green are density-dependent parameters. rt (in black) is the time set for the ramp definition in Eqn 5.1.

5.2.2 Density parameters

The green labels in figure 5.3 are the density parameters. t_{dwell} is defined as the amount of time the condensate spends above magnetic field values associated with $na^3 > 1$, our rough estimate of the fuzzy edge between the resonant regime and the strongly-interacting regime. t_{ramp} is defined as the amount of time the gas spends between the magnetic field values associated with $na^3 = 1$ and $na^3 = 0.000431$, the latter of which is the value where the Lee-Huang-Yang correction to the energy density of the BEC is 10% [1, 25]. The magnetic fields (and subsequent values of a) associated with these defining points are given in Table 5.1.

We empirically calculated t_{dwell} as a function of our experimental parameters by converting the Fast-B current into magnetic field, $B(t)$, for various t_{dwell} dwell times and r_{out} rates. These

Table 5.1: Magnetic field and scattering length values associated with the defining interaction strengths for three densities, in units of E12/cc.

$na^3 =$		0.000431		1	
$\langle n \rangle$ (E12/cc)	t_n (μs)	a (a_0)	$B(G)$	a (a_0)	$B(G)$
35	16.5	435	160.43	5800	155.802
5.5	56.5	810	158.83	10.7 k	155.465
0.2	515	2440	156.685	32.3 k	155.185

results were combined into linear equations for three densities:

$$t_{\text{dwell}} = \begin{cases} -0.65 + 0.18 \times (r_{\text{out}} + r_{\text{in}}) + \text{dwell time} & \text{if } n = 35 \text{ E12/cc} \\ -4.0 + 0.1385 \times (r_{\text{out}} + r_{\text{in}}) + \text{dwell time} & \text{if } n = 5.4 \\ -1.5 + 0.1 \times (r_{\text{out}} + r_{\text{in}}) + \text{dwell time} & \text{if } n = 0.2. \end{cases} \tag{5.2}$$

Note that due to both t_{dwell}'s dependence on ramp times, as well as the curvature of our ramps, it is impossible to spend zero time on resonance, see figure 5.27.

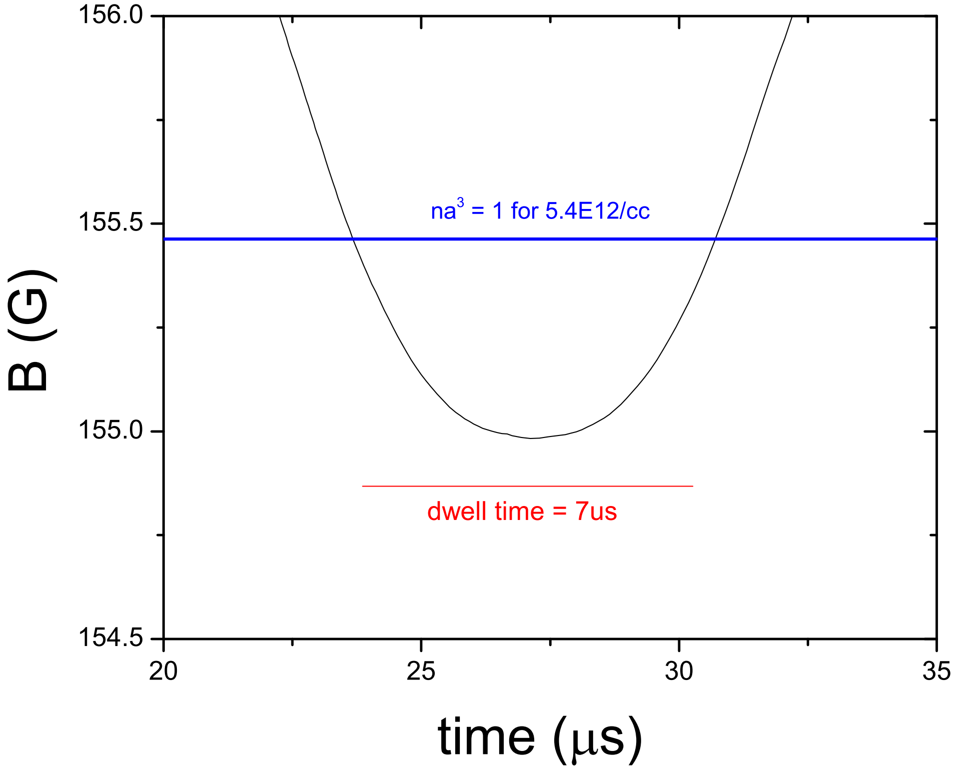

Figure 5.4: Due to both t_{dwell}'s dependence on ramp times, as well as the curvature of our ramps, it is impossible to spend zero time on resonance. In the plot above, dwell time = 0 and both the r_{in} and r_{out} = 25 μs, yet a standard density condensate would still spend 7 μs in the resonance regime (where $na^3 > 1$ for a standard density of 5.4E12/cc). This 7 μs is 12.5% of the standard density's characteristic evolution time, t_n.

5.3 Ramping in

As we have covered, our Fast-B coils and eddy current correction allow us to jump our cloud to resonance very quickly, in 5 μs. We believe this speed is necessary because the increased interaction strengths associated with a slow ramp to resonance may result in significant condensate loss. However, while we believe 5 μs to be "infinitely fast", as in so fast that the atoms act as if they were projected onto untarity, we have not yet proven this. We therefore set out to test the effects of various r_{in} rates. When the r_{in} rate is not infinitely fast, cloud characteristics such as the number and size will develop a dependence on the r_{in} rate.

We ramped a low density condensate to unitarity with various r_{in} rates while correcting the dwell time such that $t_{\text{dwell}} = 0.5\, t_n \approx 250$ μs. The results of such an experiment are shown in figure 5.5. Even for our slowest r_{in} rates of 1500 μs ($\sim 3t_n$) there was very little change in our cloud; we could not make r_{in} slower due to coil heating limitations. The lack of loss is surprising, as 1500 μs does not seem "infinitely fast". However, it is comforting that there is no size or number loss dependence on the r_{in} rate for the shortest times and therefore no reason to believe that a 10 μs r_{in} is not infinitely fast. We keep r_{in} at 5 or 10 μs for most experiments in this thesis as the fast-B coils have a finite amount of time they can be on without heating the system, and therefore a fast ramp-in time allows for more time to evolve at or ramp away from resonance.

In a later experiment where both atoms and molecules were imaged after fast (10 μs) and slow (250 μs) r_{in} rates we again saw ramp-in independence, see figure 5.6. This experiment further confirms that there is no r_{in} dependence.

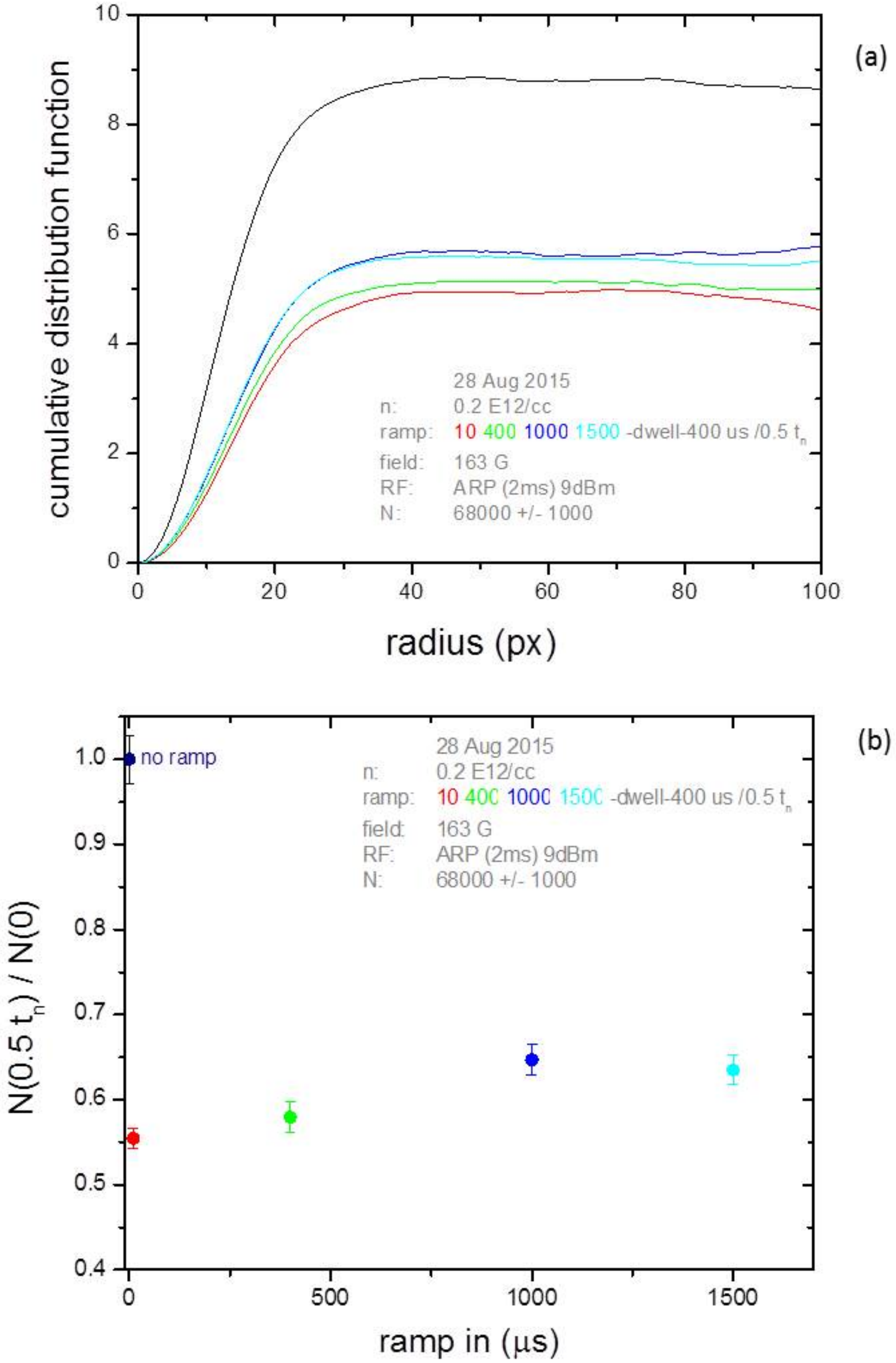

Figure 5.5: (a) The azimuthal averages for the r_{in} data show that both the number and size of the clouds are not significantly affected by the r_{in} times. See Chapter 3 to learn more about the azimuthal averages. Each color represents a different r_{in} rate to resonance, with black representing a normal BEC with no jump to resonance. (b) A plot of the number vs r_{in}, we see very little effect of the r_{in} rate on the overall loss at unitarity.The abbreviated legends in the bottom and upper right corners are explained in Appendix A.

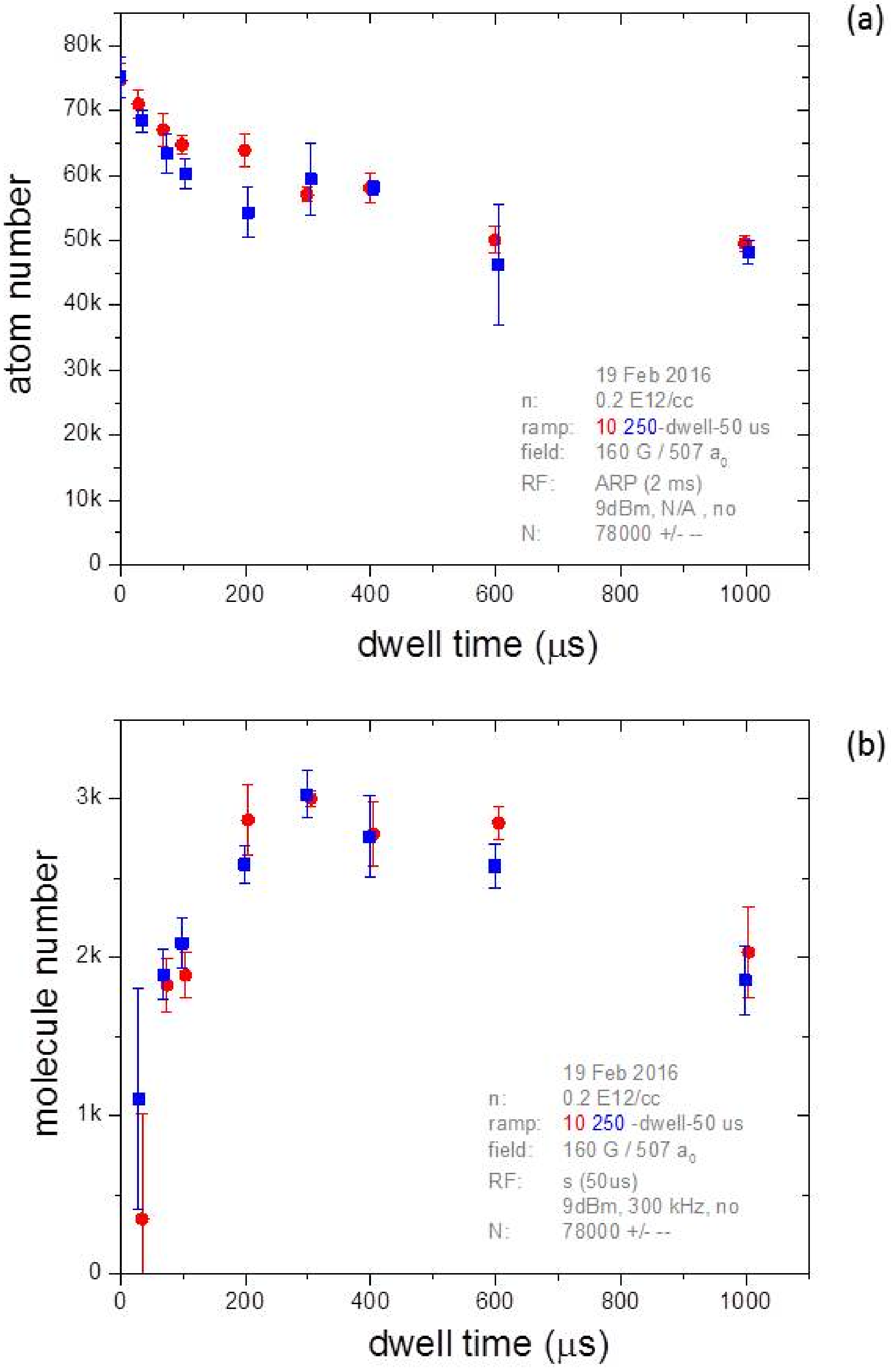

Figure 5.6: (a) The number of atoms as a function of dwell time for both a fast r_{in} (red circles) and a slow r_{in} (blue squares). We see no significant difference between the two datasets. (b) The number of molecules as a function of dwell time for both a fast r_{in} (red circles) and a slow r_{in} (blue squares). We see no significant difference between the two datasets. The density in both (a) and (b) is 0.2 E12/cc, which has a corresponding evolution time of $t_n = 510$ μs.

5.4 Evolving at unitarity

Knowing that we can project a condensate onto resonance infinitely fast, we are free to ponder the next logical, yet much more exciting question: what happens to a BEC at resonance? To best answer this question, it is ideal to image resonant BEC while it is on resonance, in action!

Imaging on resonance has many difficulties: (1) the cloud is evolving quickly, in both size and number; this means that a long imaging pulse, such as the 2ms ARP we employ when imaging off of resonance, would blur the information together and essentially be too slow to catch the fast dynamics. (2) While at unitarity the cloud is in trap and we cannot expand it, therefore it is very small, meaning that is only about 30 μm across. Though we improved our imaging resolution down to 2.2 μm, we are still unable to trust measurements when optical densities are greater than 15, as beyond this depth our diffraction-limited resolution worsens. For our typical BEC of 70k atoms, we expect optical depths of up to 20 when in-trap. (3) Noise in our magnetic field, while small enough that our atoms remain in the resonance regime, translate into RF noise that distorts imaging. Our magnetic fields vary at both fast times (due to ringing faster than our servo bandwidth) and slow times (due to thermal drifts and our cloud falling through a slight vertical magnetic gradient).

In our first attempt to overcome these difficulties we used a 6 μs square microwave pulse to transfer the atoms from the $|2,-2\rangle$ science state to the $|3,-3\rangle$ imaging state (once in the imaging state, the atoms are no longer under resonant interactions and imaging can proceed as normal). At 6 μs, this microwave pulse is faster than the characteristic evolution time at unitarity, t_n, which for our standard density of 5 E12/cc is about 50 μs. We set the pulse power to 5 dBm, this transfers about 70% of the atoms, keeping the maximum optical depth of the cloud below 15, see figure 5.7.

Unfortunately, the 6 μs pulse is narrow in frequency space, about 25 kHz, and this risks translating the magnetic field noise into number noise. We account for small drifts in magnetic field by measuring the microwave center for various dwell times, however we cannot account for the magnetic field varying more than 25 kHz in 6 μs. A variation on this order would make our atoms invisible to the microwave during transfer, thereby artificially lowering the measured number.

Unfortunately, our magnetic field at short dwell times was found to vary up to 80 kHz in a 6 μs time span (ignoring the initial 5 μs dwell measurement which varies several MHz, see figure 5.8 and table 5.2. This variation resulted in artificial lower number at short times, as evident in figure 5.9, we also found an artificial drop in size at short times due to the microwave noise.

By shortening our microwave pulse to 3 μs we can effectively double the frequency width to about 50 kHz. This results in substantial improvement in the cloud size measurements at short time, see figure 5.11. However, shortening the pulse length reduces the number of atoms transferred to the imaging state if the power is not adequately increased. We are able to send less than 30% of the atoms to the imaging state with a 3 μs 12 dBm pulse; beyond 12 dBm out microwave amplifier output saturates. As we had only a 10 watt amplifier in place, we tried placing a 16 watt amplifier to gain more power, but saw little to no improvement, see figure 5.12. Because our coil's reflectance at 2.6 GHz is -7.2 dB (not great), we determined that trying an even larger amplifier would not yield significantly larger power. We therefore settled for less than 30% transfer fraction. While this approach has low signal to noise, it is beneficial that the low optical depth never pushes our imaging resolution, regardless of cloud density, see figure 5.10.

dwell time (μs)	dB/dt (mG/μs)	Δf (6μs)
5	534	7.7 MHz
10	5.8	83 kHz
20	2.0	30 kHz
40	>-1	-15 kHz
50	>1	15 kHz
80	0.7	10 kHz

Table 5.2: The variation in magnetic field and in microwave frequency as a function of dwell time at unitarity. The third column is the variation in peak microwave frequency over $\pm 3\,\mu$s centered at the dwell time.

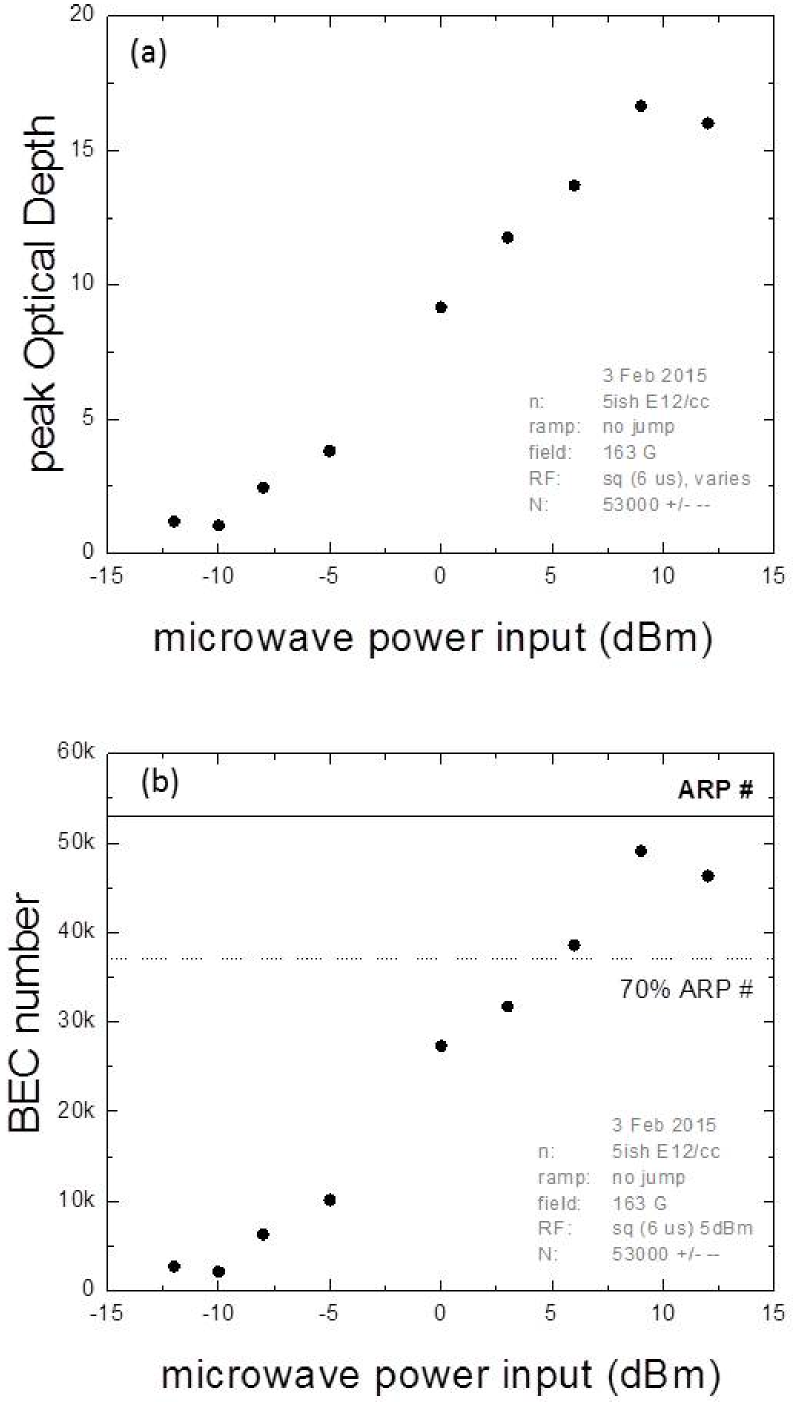

Figure 5.7: (a) The peak optical depth (OD) of a standard density cloud as a function of microwave power used to transfer the atoms from the science state, $|2,-2\rangle$, to the imaging state, $|3,-3\rangle$. We only trust our imaging system up to an OD of 15, therefore we set the microwave power to 5 dBm. (b) The BEC number as a function of the microwave power. The flat black line represents the trusted (expected) BEC number, measured with a 9 dBm, 2 ms ARP. We see that with a 5 dBm, 6 μs microwave pulse only 70% of the atoms are transferred to the imaging state.

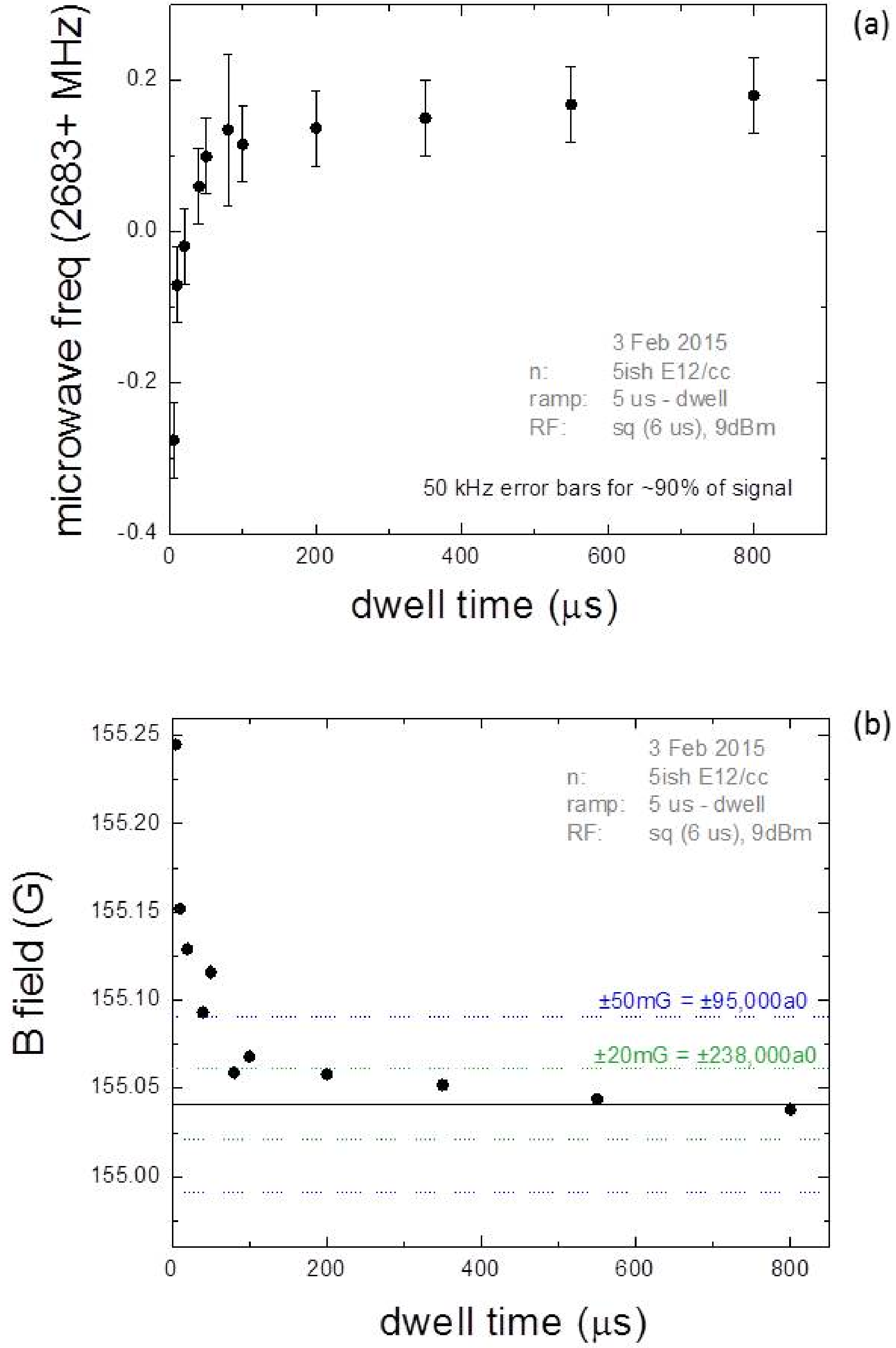

Figure 5.8: (a) The peak microwave frequency as a function of dwell time at unitarity. (b) The corresponding inferred magnetic field as a function of dwell time at unitarity. The field varies most during short times.

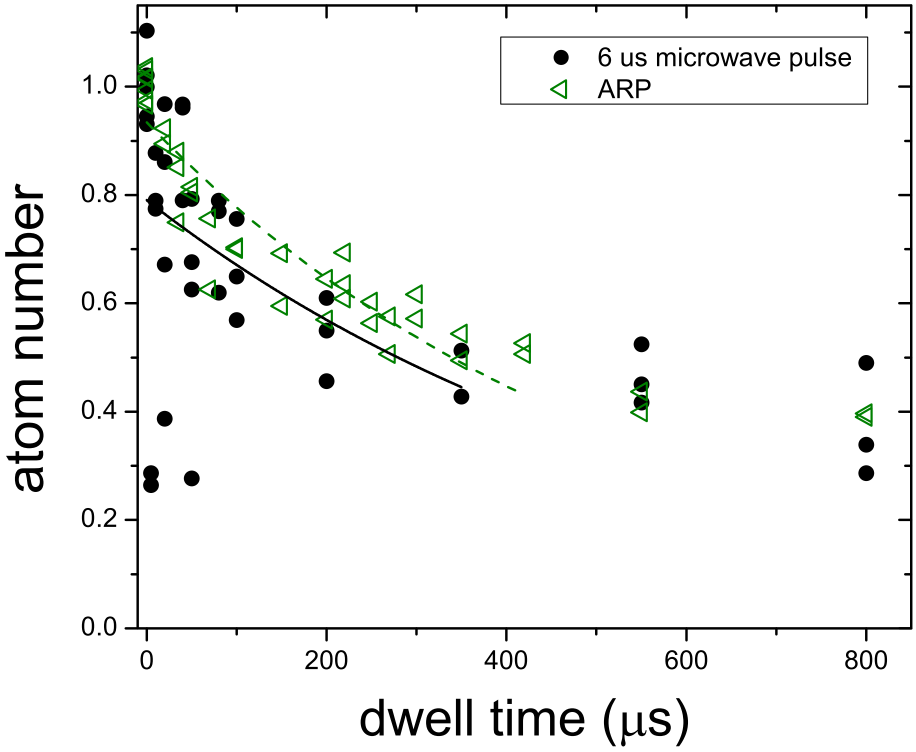

Figure 5.9: The number of atoms transferred to the imaging state via a 6 μs square microwave pulse on resonance (black circles) or a 2 ms ARP after a 5 μs ramp back to weak interactions (open green triangles) as a function of dwell time. We trust that the ARP transfers all of the surviving atoms to the imaging state, yet the ramp back to weak interactions may itself lose atoms. The ARP number is therefore a minimum number expectation. Because the on-resonance 6 μs microwave pulse transfers less atoms at short dwell times, we conclude that this imaging method is compromised by field noise.

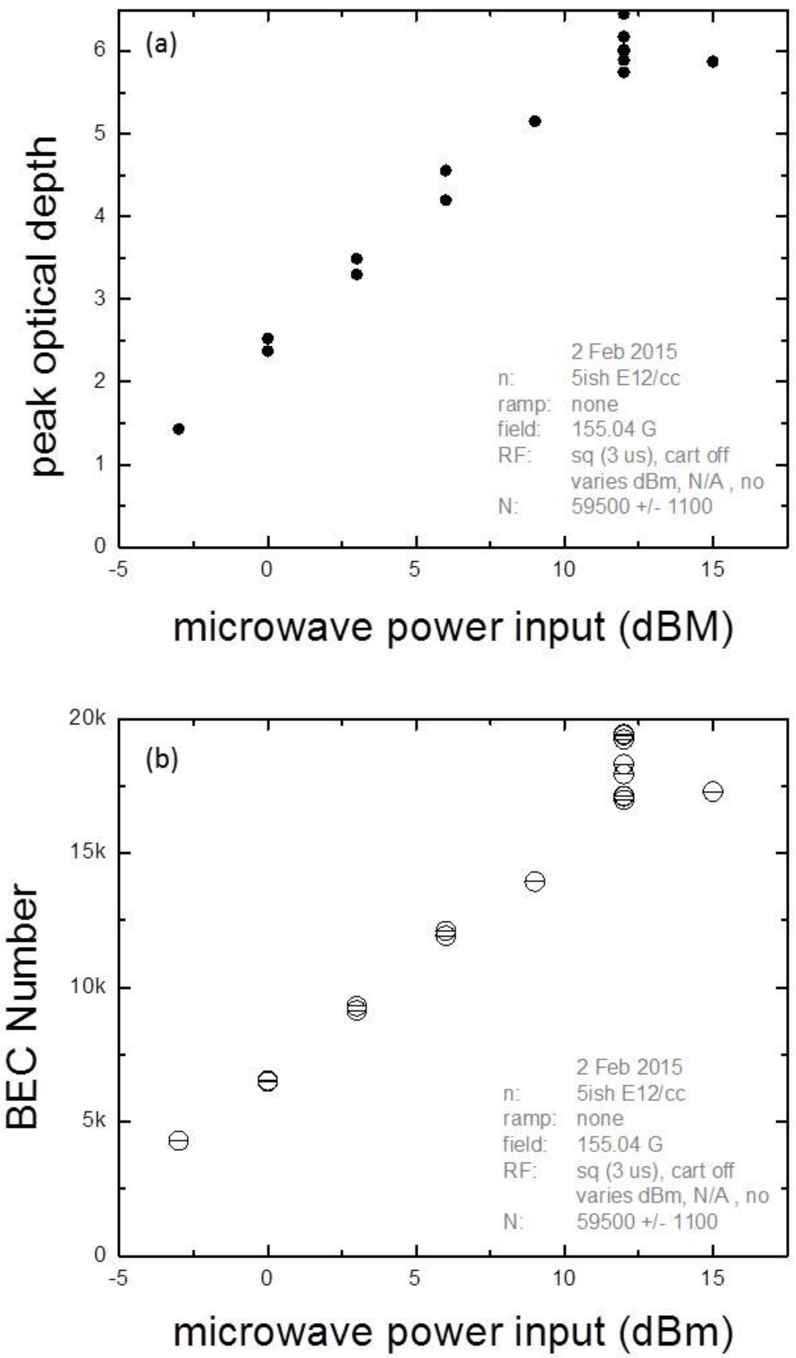

Figure 5.10: (a) The peak optical depth (OD) of a standard density cloud as a function of microwave power used to transfer the atoms from the science state, $|2,-2\rangle$, to the imaging state, $|3,-3\rangle$. Because the maximum OD is no greater than 6, we trust the number data for all microwave powers. (b) The BEC number as a function of the microwave power. We see that with a 12 dBm, 3 μs microwave pulse, less than 30% of the atoms are transferred to the imaging state.

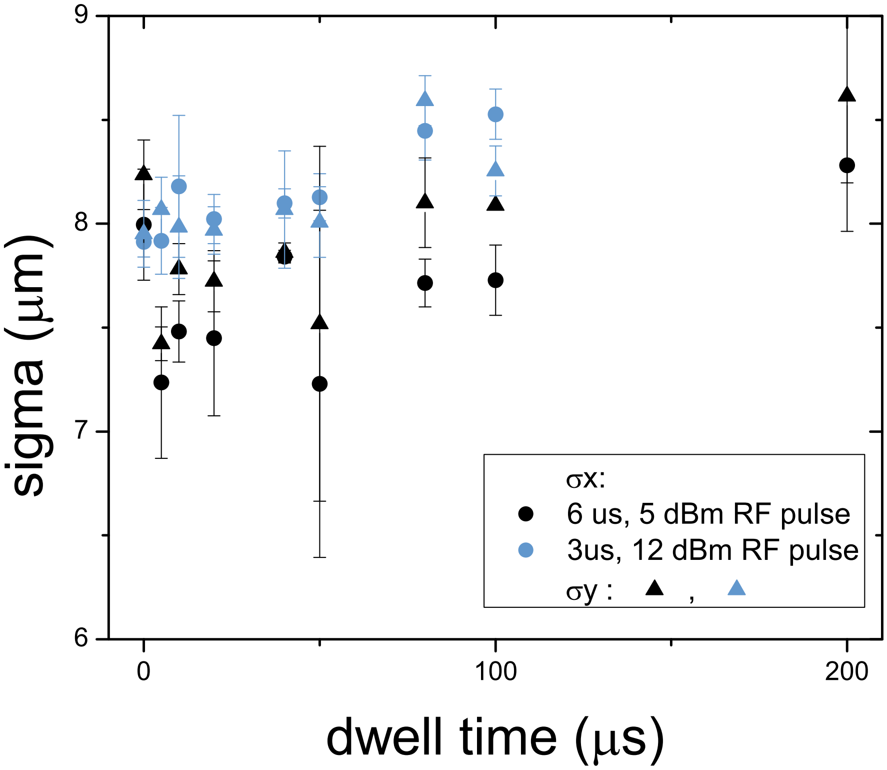

Figure 5.11: The size (Gaussian-fitted sigma, in pixels) of a standard density cloud as a function of dwell time for a 6 μs square microwave pulse (black circles and gray triangles) and a 3 μs square microwave pulse (blue circles and light blue triangles). Plotted at 0 time is the initial cloud size (before resonance). While both transfer protocols image identical clouds at 0 time, at the shortest dwell times beyond 0 the 6 μs dataset shows a decrease in the cloud size while the 3 μs dataset does not. We believe this drop in cloud size is not real and is caused by the field noise's effect on the 6 μs microwave transfer.

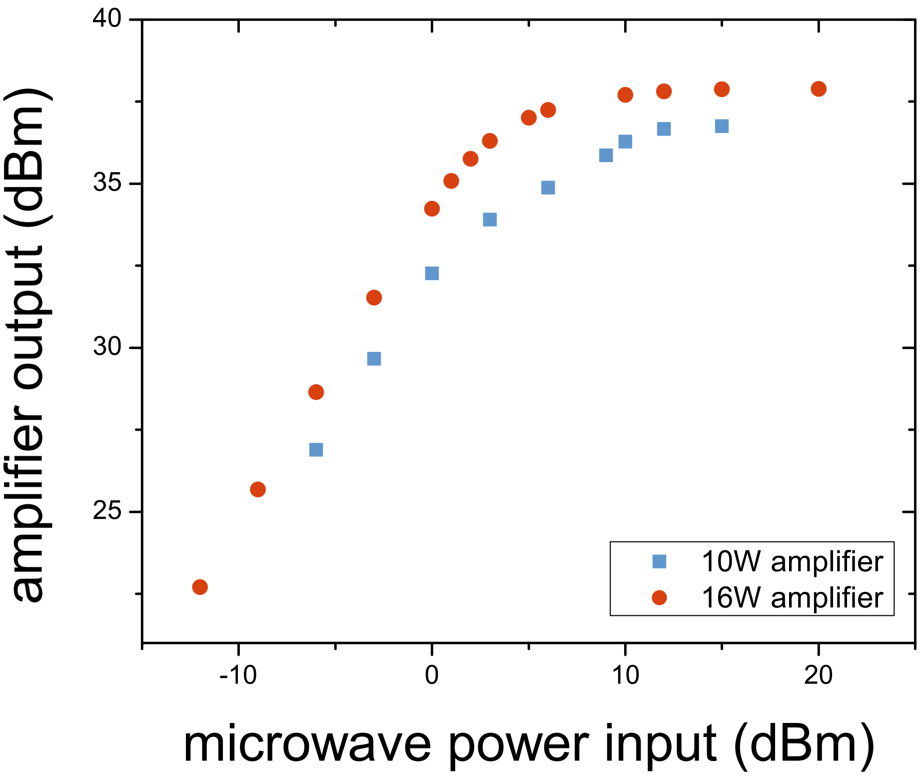

Figure 5.12: The measured power output from the microwave amplifier as a function of the microwave power input. Around 12 dBm (microwave power input), we see the output of our original 10 watt amplifier saturate. While there is a small improvement in power output from the 16 watt amplifier, we ultimately decided to forgo permanent installation.

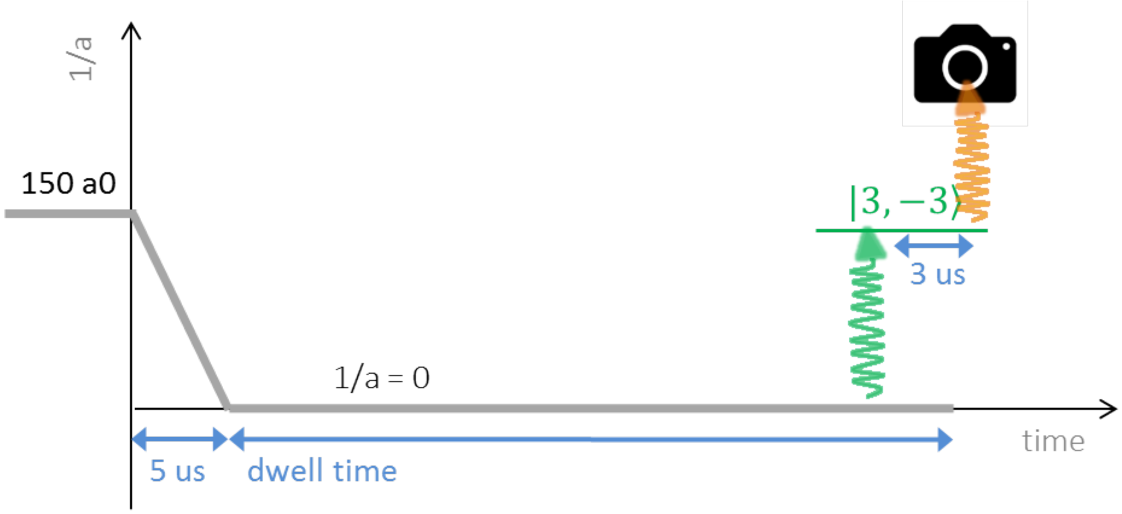

Figure 5.13: The timeline for our size measurement experiment (not to scale). Not noted in this timeline: we shut off the vertical magnetic field gradient that holds the condensate against gravity 3 ms before we jump to unitarity.

5.4.1 Expansion of a resonantly interacting BEC

Using a 3 μs microwave pulse we measured the expansion of a BEC as a function of dwell time on resonance. From this expansion we can deduce the density dynamics at resonance, which are necessary information while searching for universal density scaling. Figure 5.14(a) shows the expansion of a standard density cloud and figure 5.14(b) and (c) show the expansion of higher and lower densities clouds.

For this data the size is plotted as sigma in the x and y coordinates (σ_x and σ_y), which are defined as the 3-D Gaussian RMS width projected onto to a 2-D image: $Ae^{\frac{-x^2}{2\sigma_x^2}-\frac{y^2}{2\sigma_y^2}}$. A numerical study with a simulated image shows that the 2-D Gaussian fit to a imaged 3-D Thomas-Fermi cloud yields a conversion factor of $\sigma_x/R_{\mathrm{TF}} = 0.4368$, where R_{TF} is the Thomas-Fermi radius. For this experiment we centered the microwave pulse for each dwell time to account for small drifts in the magnetic field. The standard density cloud more than doubles in volume within 400 μs; the lower density cloud expands much slower, achieving only a 50% increase in volume by 400 μs, while the higher density cloud expands faster, doubling in size by 250 μs.

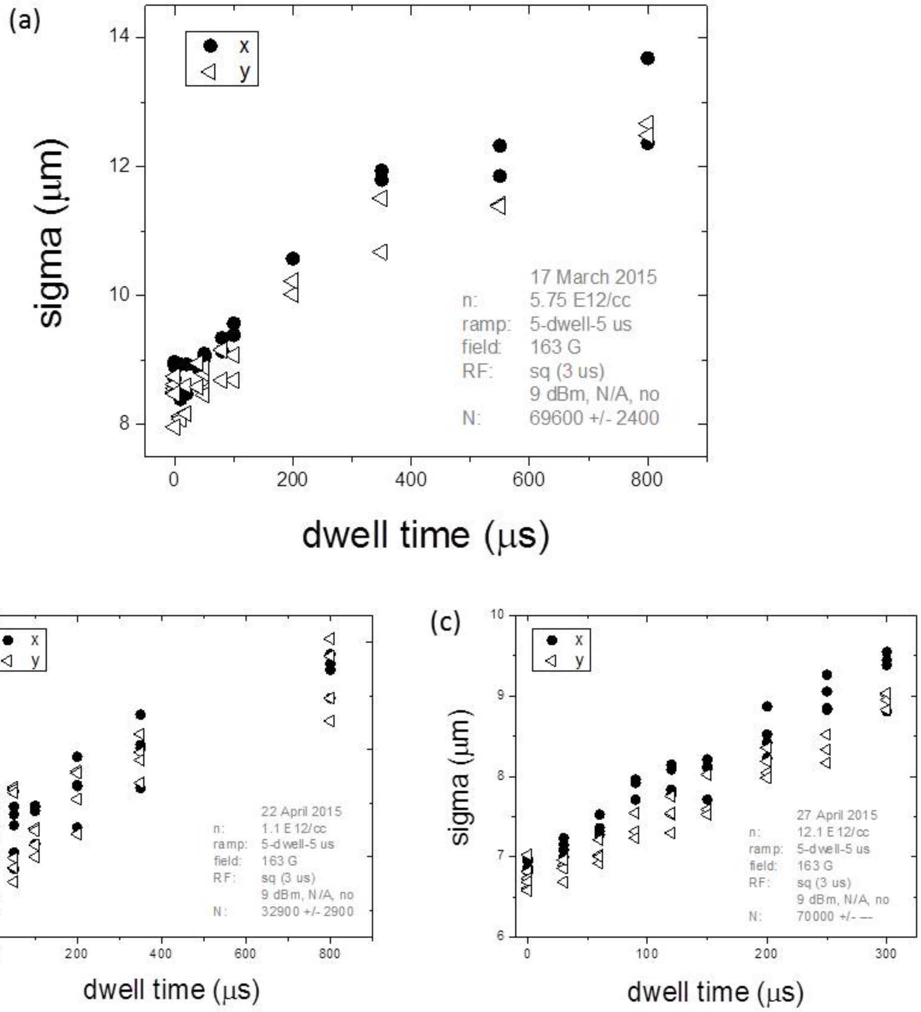

Figure 5.14: (a) Expansion data for a condensate of standard initial density. Sigma is the gaussian fitted cloud width in pixels, with a 1.1 px resolution correction. The atoms were transferred from the resonantly interacting science state to the imaging state using a 3 μs 9 dBm square microwave pulse. We see that the cloud grows, but this growth slows around 400 μs unexpectedly. (b) Expansion data at a lower density of 1.1 E12/cc, with a 1.1 px resolution correction. (c) Expansion data at a higher density of 12.1 E12/cc, with a 1.1 px resolution correction.

After substantial expansion at unitarity however, the clouds are no longer well described by a Gaussian fit [see figure 5.15(b)]. Attempting to fit the clouds with a Gaussian fit yields erroneous results for two reasons : (1) the expanded cloud is no longer well-described by a 3-D Thomas-Fermi distribution because the center of the cloud loses density faster than the edges of the cloud, and

(2) a bump in the optical depth (at 30 microns) could cause a Gaussian to fit artificially larger; this bump is present in our images of non-resonant condensates, we therefore conclude it is not an artifact from resonance.

This bump at 15 pixels is not real, it is an artifact of diffraction. By imaging clouds of various condensate fractions (see figure 5.16) we determined that this bump is not a halo of thermal atoms. We varied the condensate fraction, or percentage of atoms in a cold condensed form as opposed to a hotter thermal gas, by varying the frequency of the RF knife used to spin-flip the hot atoms during our final stage of evaporation. For example, an RF knife of 81.78 MHz yields a condensate fraction of only 20%, whereas any knife of 81.725 MHz or below yields a pure condensate. The bump becomes less pronounced when imaging a condensate surrounded by a large thermal component and more pronounced when imaging a more pure BEC, this result confirms out hypothesis that the bump is a result of diffraction. Further confirmation was had after reducing the amount of incident light on the atoms and seeing the bump become less pronounced, see figure 5.17.

Because the Gaussian approximation is unfit to describe a resonant condensate, we instead use the full-width-half-max (FWHM) of the optical density (OD), defining FWHM as the radius at which the OD has dropped to half its peak value. In the case of a Thomas-Fermi distribution, $R_{\mathrm{TF}} = \sqrt{2}\mathrm{FWHM}$ and $\sigma_i = 0.618\ \mathrm{FWHM}_i$. With this new size definition the standard density cloud now expands by less than 50% its initial volume by 400 μs, see figure 5.18.

We return now to our goal of determining the density dynamics of a resonant condensate by combining the expansion of the cloud with the number loss. While we can measure the condensate number with the 3 μs on-resonance transfer pulse, the small signal to noise (due to only transferring less than 30% of the atoms to the imaging state) is undesirable. These measurements are also difficult because each dwell time requires an individual line shape, and the process of taking these lineshapes can take hours, over which the magnetic fields experience small thermal drifts, introducing more noise. For these reasons we opt instead to ramp away to a weaker scattering length before imaging the cloud with a long ARP'd pulse that gaurantees 100% transfer.

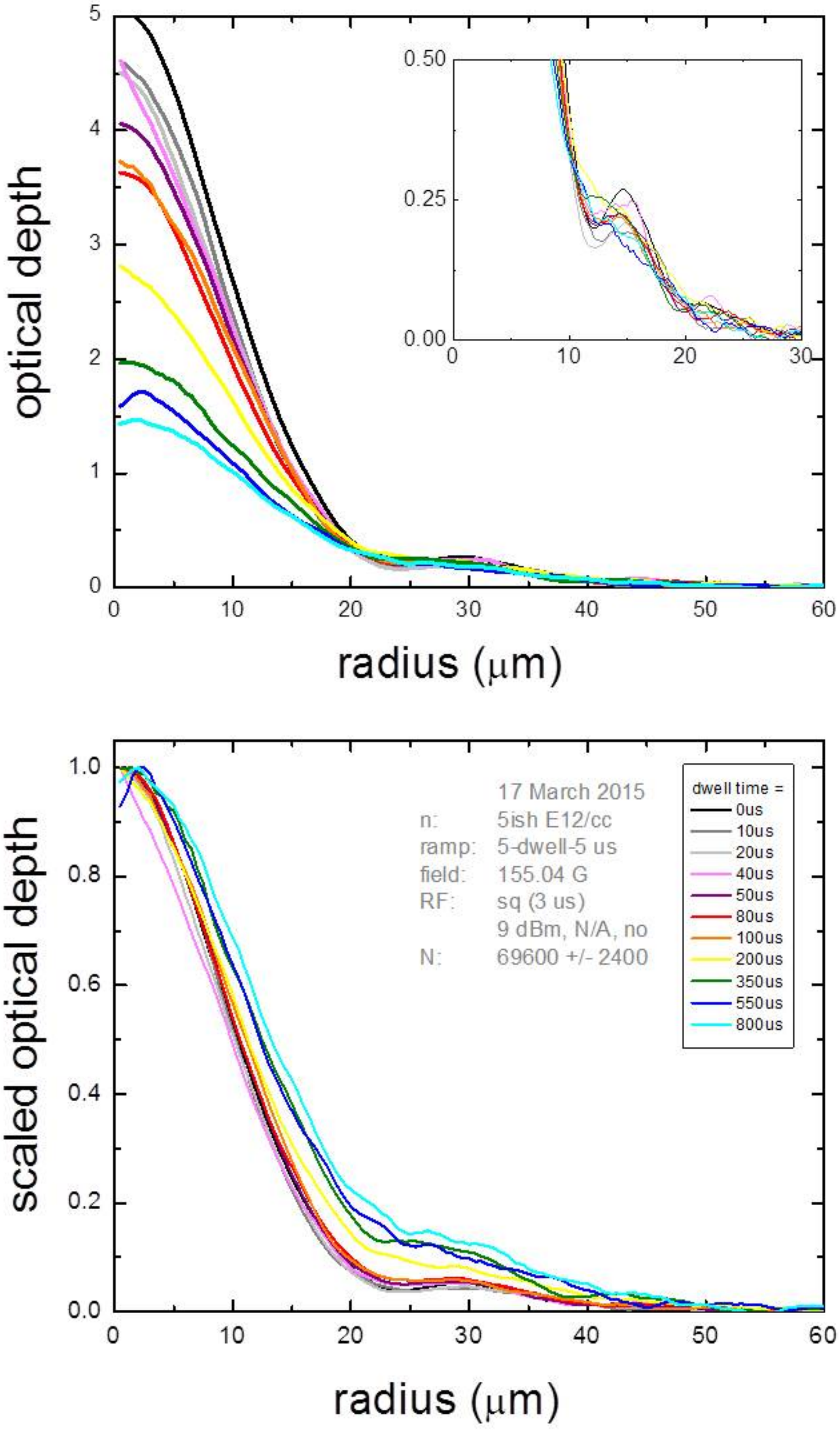

17 March 2015
n: 5ish E12/cc
ramp: 5-dwell-5 us
field: 155.04 G
RF: sq (3 us)
9 dBm, N/A, no
N: 69600 +/- 2400

Figure 5.15: (a) The azimuthal averages for the standard density expansion data. The data were azimuthally averaged before clouds with common dwell times were averaged together. The most striking characteristic that evolves with dwell time is the drop in peak optical density. The inset zooms in on the bump that occurs in all datasets around 15 pixels (px = 1.996 μm) (b) The azimuthal averages scaled by their peak optical depth. This scaling emphasizes how the tail at large radii grows over time, causing the cloud to deviate from a typical Gaussian shape .

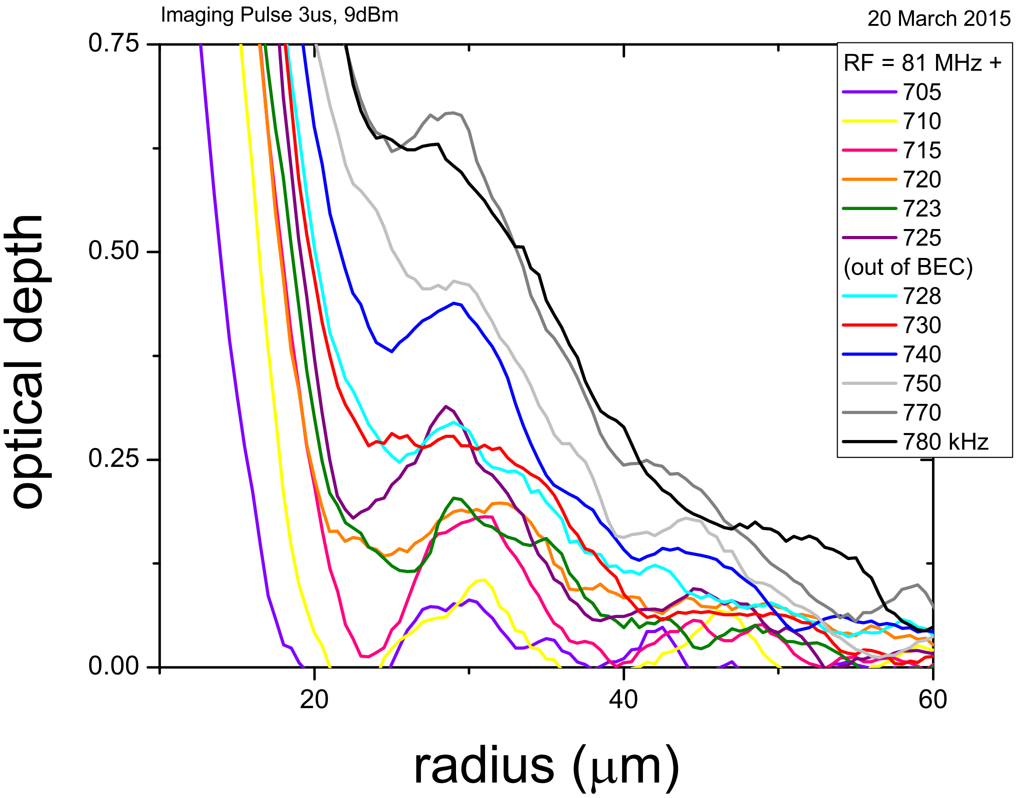

Figure 5.16: The cumulative distribution functions of clouds with various condensate percentages. For the least-invasive RF knives, such as the black curve, the cloud is almost 80% thermal atoms and only 20% cold condensate. These larger, hotter clouds wash away the bump at 15 pixels. For the nearly 100% condensates, i.e. any curve that has an RF knife of 81.725 MHz and below, the bump becomes pronounced. The bump only begins to shrink again for the closest RF knives, such as 81.710 and 81.705 MHz, yet this corresponds with an overall drop in peak optical depth, see inset. This bump behavior is consistent with diffraction around the condensate.

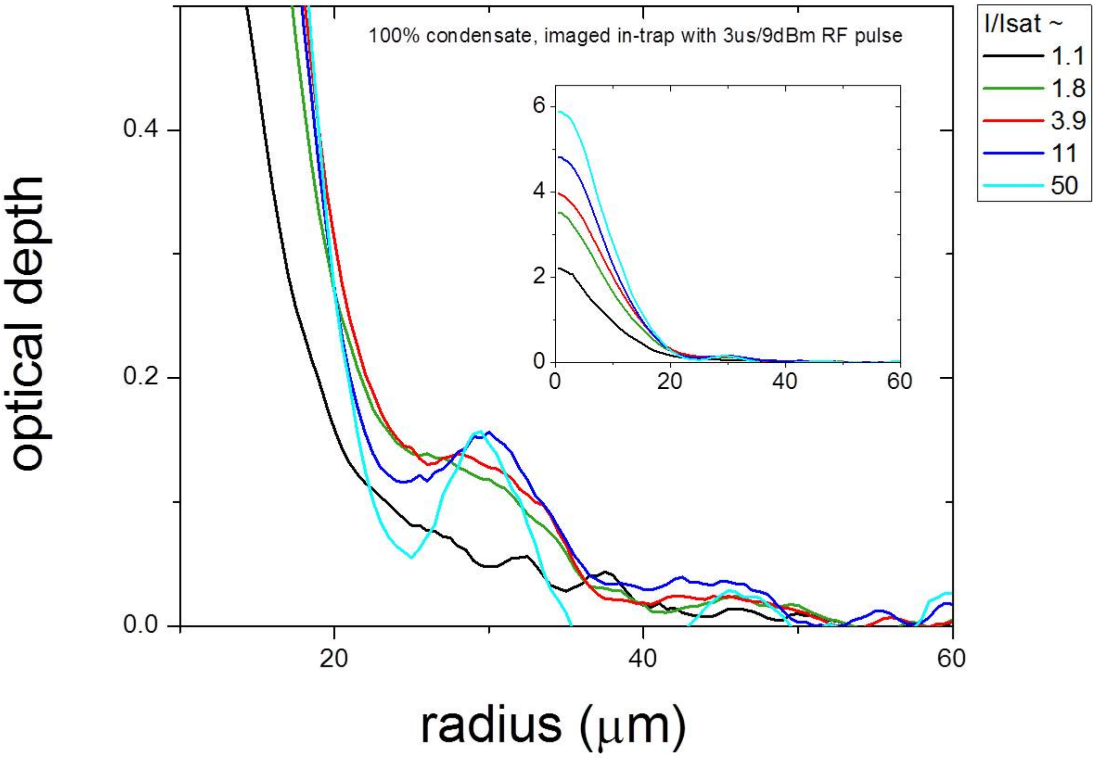

Figure 5.17: The azimuthal average of a pure condensate for various intensities of incident light. In order to properly image our high optical density condensate, we employ high-intensity imaging techniques (see Chapter 3) that involve using about 50 times more incident light than normal absorption imaging. This increase in light increases the amount of light diffracted around the condensate, thereby increasing the size of the artificial diffraction bump. We see that by lowering the intensity of the light we are able to minimize this bump. However, the lower light intensities are unable to fully image the large optical depths of our condensate, resulting in artificially low peak optical depths, see inset.

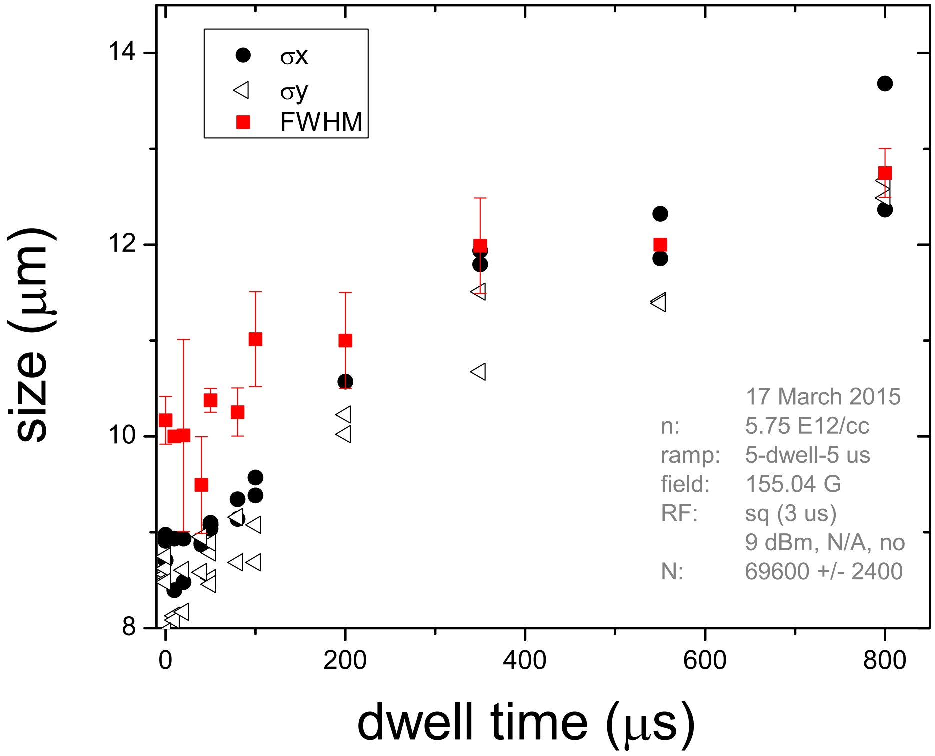

Figure 5.18: The expansion of a standard density condensate as a function of dwell time at resonance. The red squares are the size as described by FWHM, and the black points and open triangles are x and y sizes described by the Gaussian RMS width, σ. For a perfect Thomas-Fermi distribution, σ should be 0.618× FWHM, however σ at all times appears to be greater than this value, this is most likely due to artificial expansion due to fitting a cloud with a bump at 15 pixels. At later times, σ becomes almost the same value as FWHM, most likely because of the non-gaussian expansion of the cloud. We opt instead to use the FWHM to describe the size our cloud.

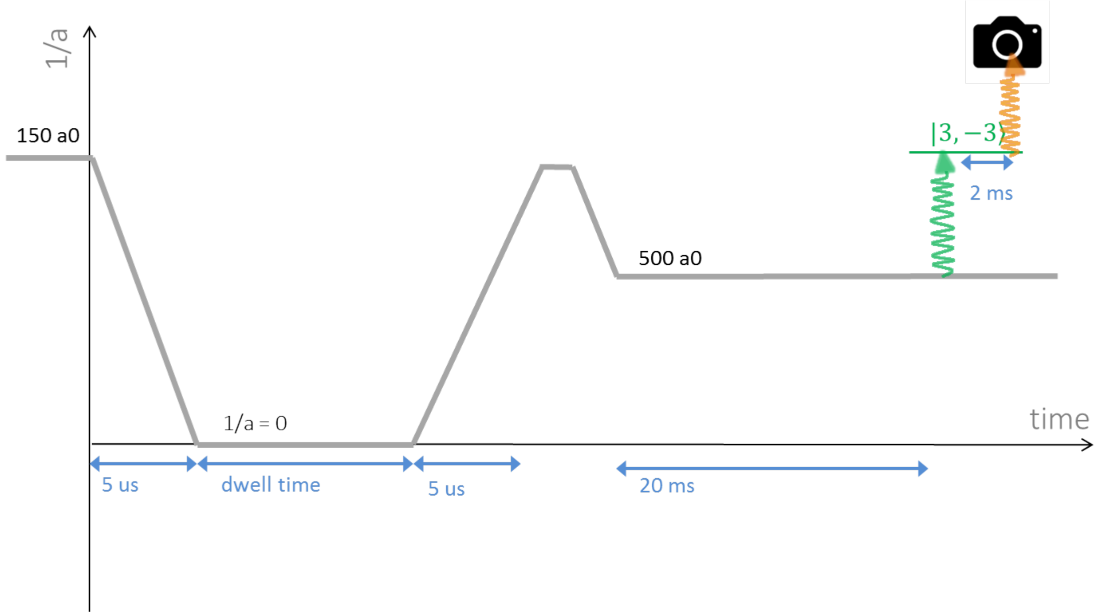

Figure 5.19: The timeline for our number measurement experiment (not to scale). We ramp away fast (in 5 μs) from resonance to weak interactions, then expand the cloud at 500 a_0 for 20 ms to lower the peak optical depth of the cloud for imaging. Because field gradients do not affect ARP transfers, we do not turn off the vertical magnetic gradient in this procedure.

5.4.2 Ramping away before imaging

Ramping away from resonance very quickly before imaging with a long, 2 ms adiabatic rapid passage (ARP) transfer to the imaging state yields almost the same number as our on-resonance 3 μs RF pulse method, see figure 5.20. While the ARP method allows us to obtain data much faster (because a line shape for each dwell time is no longer necessary) it does lose size and shape information about the cloud, and is therefore only useful for obtaining number data.

Combining the ramped-away ARP number data with on-resonance short-pulse size data we obtain the density as a function of dwell time at unitarity, see figure 5.21. The density initially drops off very quickly, falling to 85% in 50 μs ($\sim 1\,t_n$) and 61% in 100 μs ($\sim 2\,t_n$). The number loss is the main cause of the drop in density, accounting for about 70% at both the shortest and longest dwell time measurements.

The significant change in density of the cloud while at resonance makes searching for density

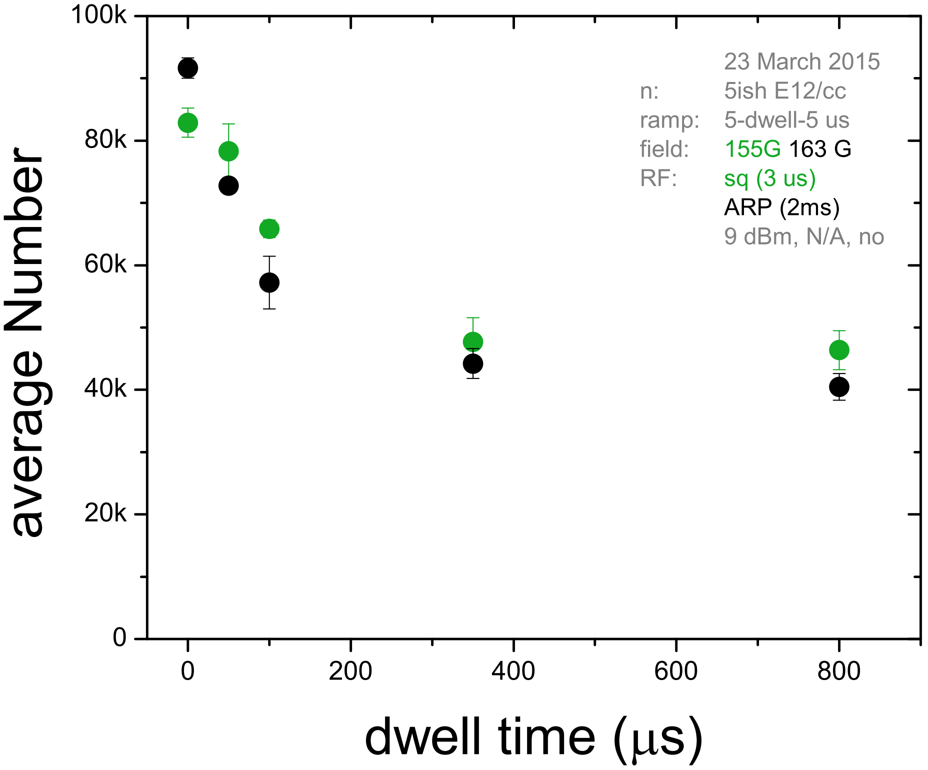

Figure 5.20: The number of atoms as a function of dwell time on resonance after imaging on-resonance with a 3 μs square RF pulse (green points) or ramping away to weak interactions in 5 μs, expanding at 500 a_0 for 20 ms, and then imaging with a 2 ms ARP (black points). We conclude that the latter measurement technique results in similar number with reduced noise. And most important to a graduate student, data taken with the latter technique is much faster to procure, meaning more data, happier advisors, and a less stressed student.

dependent universality more challenging. While many experiments exploring Bose gases on resonance are interested in testing the predicted $n^{2/3}$ dependent loss rates [37, 39, 70, 83], the changing densities complicate this analysis. As can be seen in figure 5.22, the number over time does not follow a simple exponential loss rate.

The exponential in figure 5.22 assumes no density dependence in the loss rate, assuming the three-body loss rate, Γ_3, is constant, i.e. assuming the density does not change. This non-density

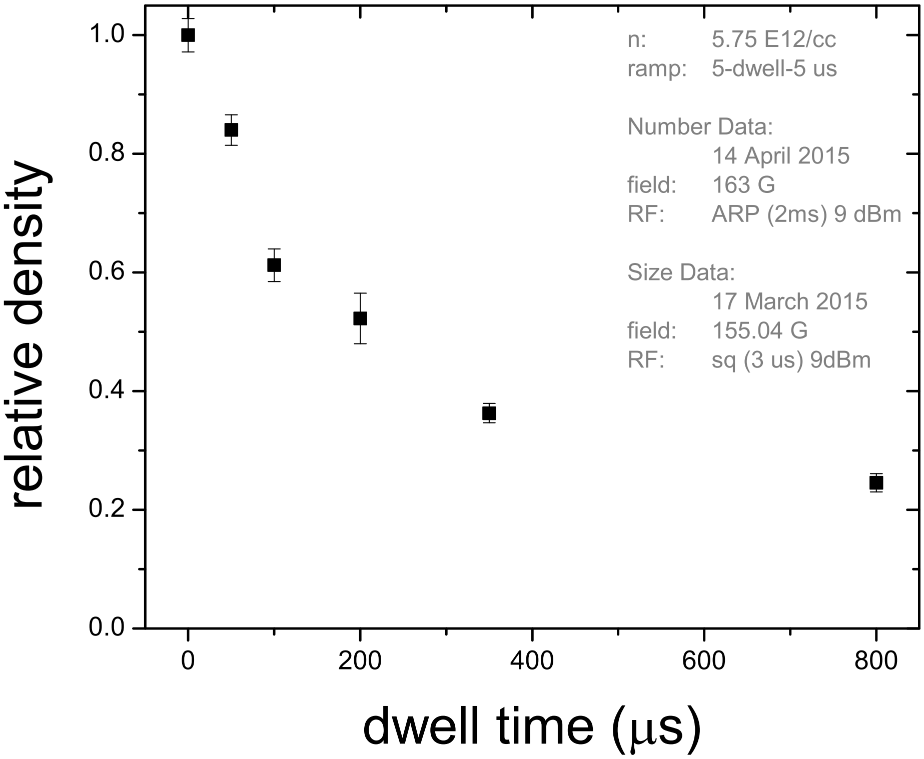

Figure 5.21: The relative density of a standard density condensate as a function of dwell time at density. This data was calculated by combining the ARP number data and 3 μs RF size data. We see an initial fast drop in density, with the condensate density dropping to 85% in 50 μs and 61% in 100 μs, which correspond to roughly 1 and 2 t_n. The point at 0 dwell time corresponds to the initial density of the cloud (1) before the resonance jump.

dependent loss rate, given in equation (2.15) can be rewritten as

$$\ln\left(\frac{N(t)}{N(0)}\right) = -\Gamma_3 N, \tag{5.3}$$

and therefore the linear fit in 5.23(a) has a slope of Γ_3.

If the density dependence of the loss rate was as simple as $n^{2/3}$, we could correct for the changing density while the cloud evolves at unitarity as a test of the loss rates' density dependence. To include the $n^{2/3}$ dependence, Γ_3 can be rewritten as $L_3' \times \langle n^{2/3} \rangle$, where L_3' is the adjusted three-body loss rate constant and $\langle n^{2/3} \rangle$ is the mean density to the two-thirds, $= \frac{\int n \cdot n^{2/3}\, \mathrm{d}^3 r}{\int n \, \mathrm{d}^3 r}$; for a

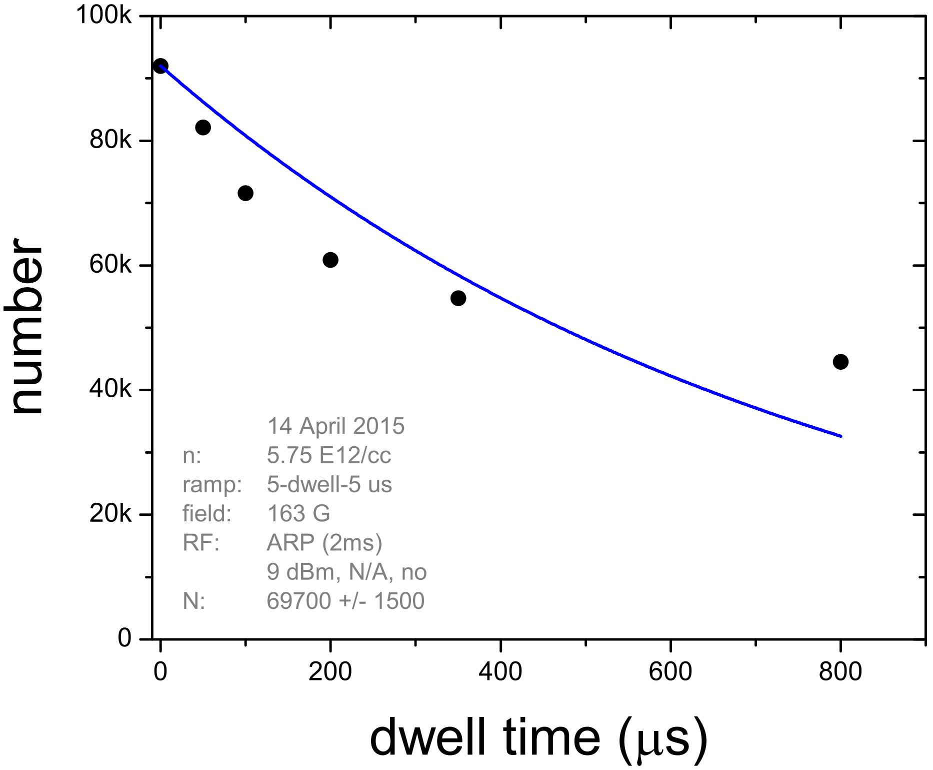

Figure 5.22: The number of atoms in our standard density condensate as a function of dwell time at resonance. We see a poor fit to the exponential, this is due to the changing density of the cloud while it evolves at unitarity.

Thomas-Fermi distribution, $\langle n^{2/3} \rangle = 0.259 \langle n \rangle$. We can then rewrite

$$\dot{N} = L_3 \times \langle n^{2/3} \rangle N \tag{5.4}$$

as

$$\ln\left(\frac{N(t)}{N(0)}\right) = -C \cdot L_3 \int_0^t \left(\frac{N(t')}{w(t')^3}\right)^{2/3} \mathrm{d}t'. \tag{5.5}$$

we now define $G(t)$ as $L_3 \int_0^t \left(\frac{N(t')}{w(t')^3}\right)^{2/3} \mathrm{d}t'$ and plot the log of the change in number as a function of $G(t)$ in figure 5.23(b).

We see that an $n^{2/3}$ dependence does not properly describe the resonant loss. This could be true for a variety of reasons, such as the loss rate has a universal scaling other than $n^{2/3}$, there is a nearby Efimov state that is perturbing this loss, but most likely we are losing vital information by defining our cloud size by the optical depth FWHM. Essentially, we have assumed that the actual density, $n(r)$, can be approximated by $n \propto \frac{N(t)}{\mathrm{FWHM}(t)^3}$. But the actual density of the cloud varies from n_{pk} to 0 across the radius of the cloud, and if the loss rate goes locally as $n^{2/3}$, there will be more number loss in the center of the cloud than at the edges. This could change the function of $n(r)$, and therefore the local decay could goes as $n(r)^{2/3}$, but this would not be equal to $\left(\frac{N}{\mathrm{FWHM}^3}\right)^{2/3}$ loss. If this were the case, the decay in terms of $\left(\frac{N}{\mathrm{FWHM}^3}\right)^{x}$ would still be the same for different initial densities.

Being unable to extract the density dependence of the loss rate by examining the loss as a function of dwell time, we instead look at the loss at short times where the change in density is still small and the expansion nearly negligible. If we examine four datasets, with initial densities spanning from 1.1 to 12.5 E12/cc, we see that the short time loss roughly agrees with $n^{2/3}$ scaling, see figure 5.24.

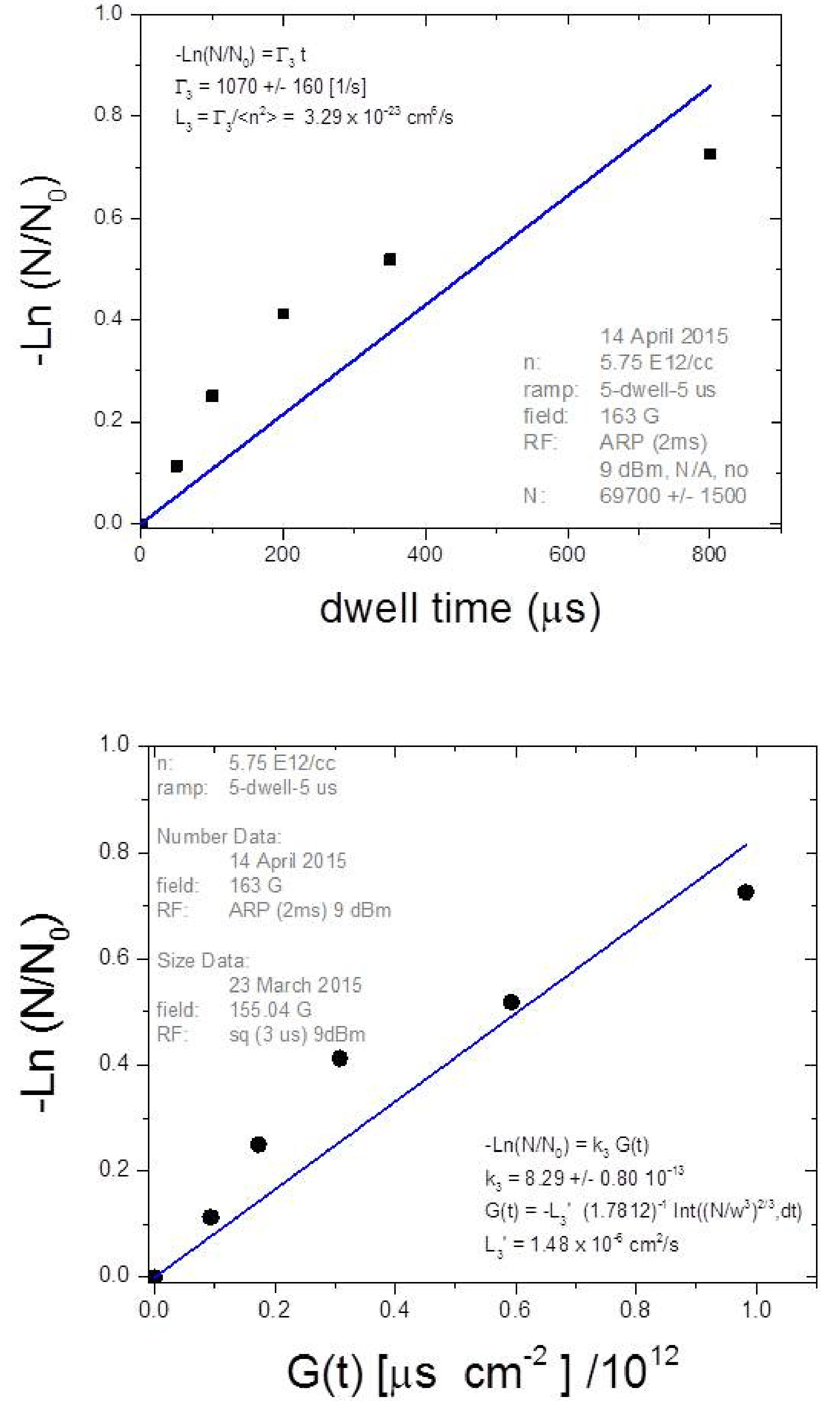

Figure 5.23: (a) The same data from figure 5.22, now plotted as the log of the number of atoms in our standard density condensate as a function of dwell time at resonance as the natural log of the change in number. In this plot, a perfect exponential decay would appear as a straight line. We can see that the data has a poor fit to the exponential decay as it deviates from the fitted straight line. (b) The same data as in (a), however the x-axis is now the function G(t), given by equation 5.5. In this plot, a perfect exponential decay that accounts for an $n^{2/3}$ dependence would follow a straight line. We see that while this data follows a straight line better than that in (a), it is far from perfect. We conclude from this that we do not see $n^{2/3}$ density dependence in the loss rate as a function of dwell time on resonance.

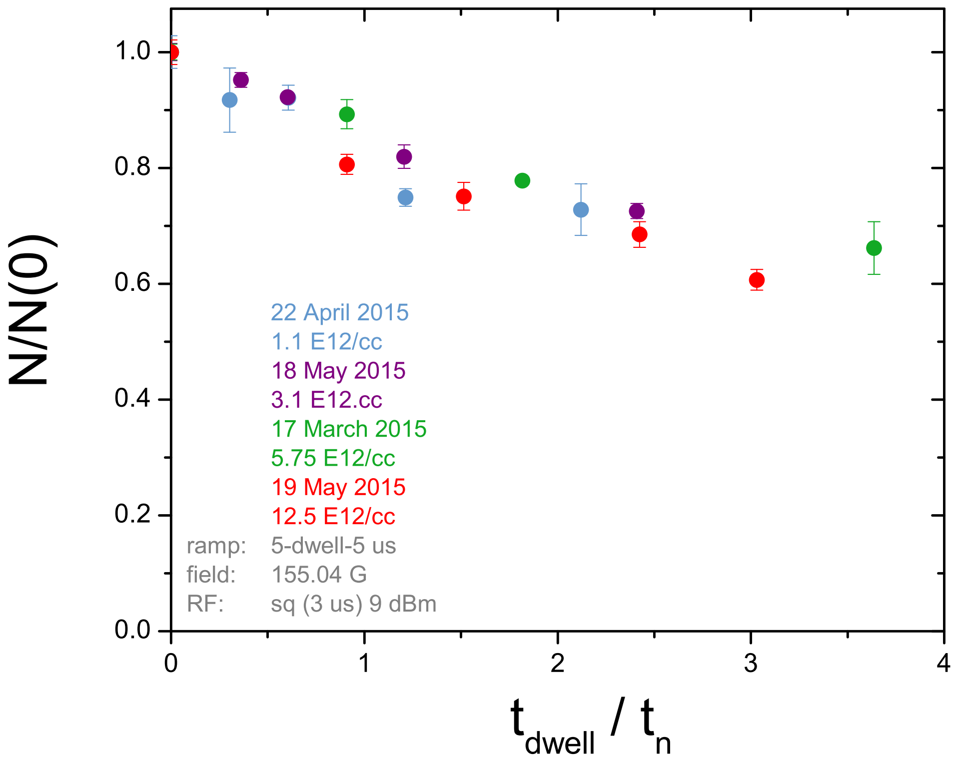

Figure 5.24: The relative change in number vs t_{dwell}, scaled by the density-dependent units of t_n. The four initial densities seem to have the same loss rate in units of t_n, hinting at an $n^{2/3}$ dependence in the loss rate.

5.4.3 Atom loss at Unitarity

The next experiment involves ramping to resonance in 5 μs, dwelling on resonance for 1 t_n, then ramping away in 5 μs. We varied the density by over a factor of 250 using techniques outlined in Chapter 4. The recorded loss is plotted as a function of density in figure 5.25. We see very good agreement with the $n^{2/3}$ scaling, however there is some slight deviation from this scaling at the larger densities, and for a single point at the smallest density. To examine further, we replot this data as $\Gamma_3/n^{2/3}$, see figure 5.26. From this replotting we see that this small deviation is actually quite large and could fit to a log-periodic curve, which is an Efimov smoking gun. If these deviations in the loss rate were due to the presence of the Efimov states, they would be correcting the loss rate by more than 50%. In [83] the oscillations in loss rate due to the Efimov effect in a thermal Bose gas at unitarity were theorized to be $0.022\mathrm{e}^{-2\eta^*}$. For ^{85}Rb, η^* is 0.057 [34], yielding an expected amplitude correction of only 2%. In any case, these calculations were for non-degenerate gases in which T is varied, not a degenerate gas in which n is varied. There is preliminary work by José P. D'Incao which predicts larger oscillations [84].

There are a myriad of ways to kill a BEC, and therefore many other possibilities to explain this deviation in $n^{2/3}$ loss rate scaling. It is suspicious that the least loss occurs near our standard density of 5 E12/cc. While we verified that no loss was occurring during the density expansion / compression procedures, it is possible that the densities at the far ranges of the spectrum could be slightly off from their calculated values (see Chapter 4 for more details). An incorrect density would lead to an incorrect value of t_n, and if t_n was smaller than calculated, the cloud would spend a longer time at unitarity. However, for this to explain both the deviations at high and low densities it would require that our actual densities were *always* lower than calculated, when in reality it is more likely that errors in our density calculations would lead to either overshooting or undershooting the change in density regardless of an expansion or compression. This paranoia could be disproved by taking loss data across an even larger density range, beyond the predicted turning point, to confirm that the deviation is log-periodic and not just coincidentally increasing.

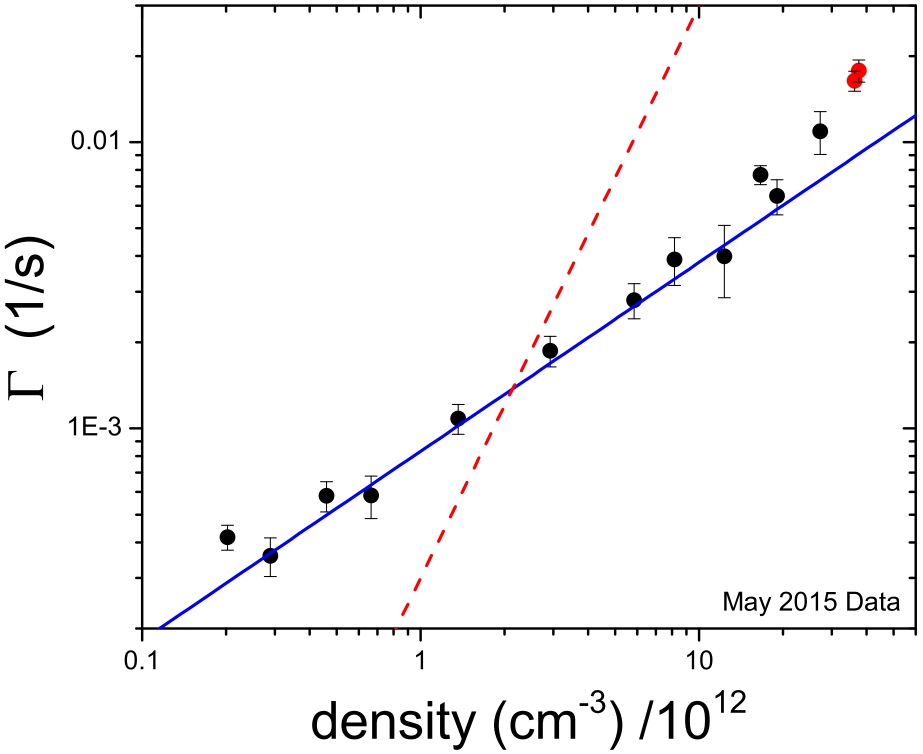

Figure 5.25: The measured loss rate, $\Gamma_3 = (1 - N(t)/N(0))/1\, t_n$, as a function of initial condensate density. The solid blue line represents the predicted universal $n^{2/3}$ scaling and the red dashed line represents the mean-field loss rate n^2 scaling. The red points at large n have a density larger than 35 E12/cc, the highest verified density, see Chapter 4.

Another controlled variable to scrutinize is the r_{out} rate to weak interactions. In this experiment the r_{out} was always 5 μs. We naively assumed that the number of atoms before and after the jump were practically the same. However, further investigation reveals that the r_{out} has a larger effect on the system than one might assume at first glance. Whether the ramp to weak interactions in this experiment should be consistent in units of r_{in} or t_{ramp} in order to probe only the effects of t_{dwell} was (is still?) hotly debated in our lab.

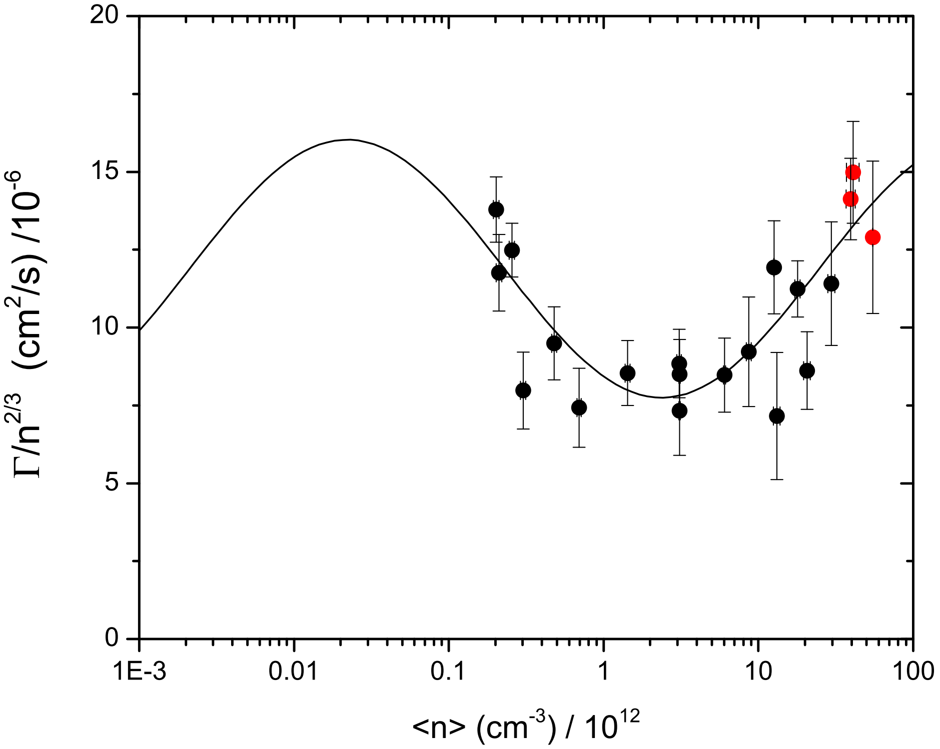

Figure 5.26: The measured early-time loss rate, $\Gamma_3 = (1 - N(t)/N(0))/t$ $(t = 1t_n)$ divided by $n^{2/3}$, plotted as a function of density. This data has the same data that was plotted in figure 5.25, with some additional measurements. The red points at large n have a density larger than 35 E12/cc, the highest verified density, see Chapter 4. If there was perfect $n^{2/3}$ scaling the data would appear as a flat line, however there is a deviation from this scaling that appears to be sinusoidal. The solid line is a log-periodic function representing the Efimov states: offset $+ A\sin^2[s_0 \ln(n^{-1/3}/a_*) + 0.19]$, based loosely on the three-body recombination rate derived in [4, 50] with $a \to n^{-1/3}$. The frequency of this line is set by the Efimov period, the offset and amplitude were fit. The fitted amplitude is 107% of the offset value, suggesting an Efimov correction to the three-body loss rate of more than 50%. In the text we discuss experimental issues that could cause increased loss rate at smaller and larger densities and therefore diminish our confidence in this data.

5.5 Ramping away: the effects

5.5.1 Vary r_{out}

To test the effects of the ramp away from resonance we varied the r_{out} rate while keeping t_{dwell} constant for a low density cloud (n = 0.2 E12/cc), see figure 5.27 for an example of magnetic field ramps with constant t_{dwell} for a high density cloud. The resulting number loss is shown in figure 5.28. We find that after a 0.5 t_n dwell on resonance, r_{out} alone can drop the return atom number by an additional 30%. r_{out} therefore has as much influence over the perceived loss as dwell time.

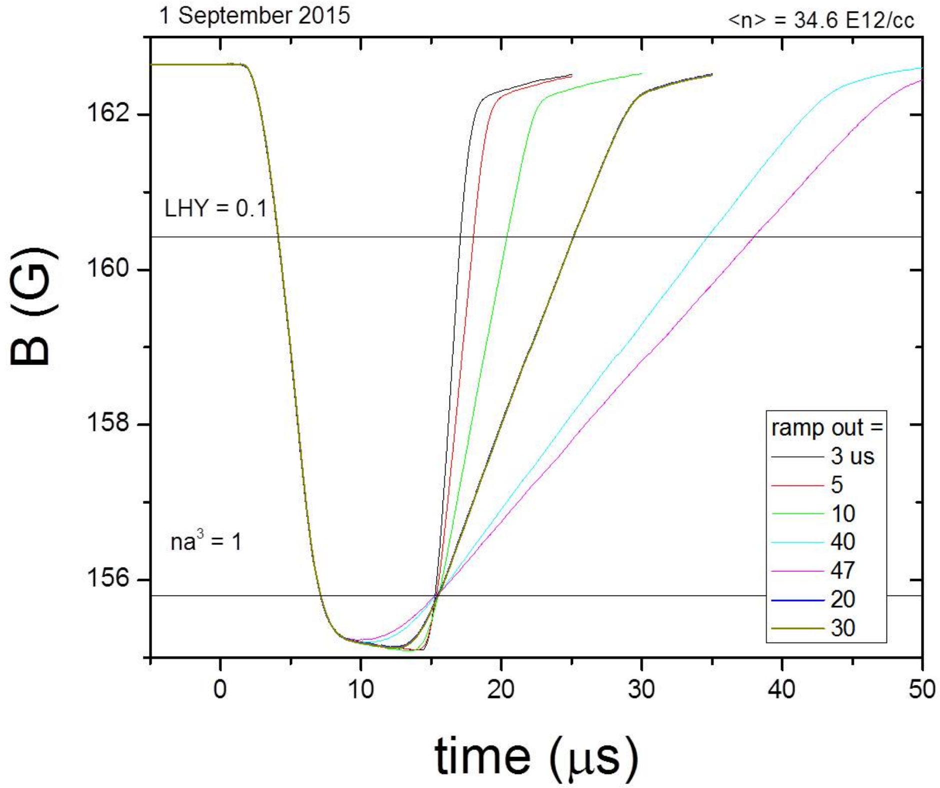

Figure 5.27: Jumps to resonance with varying r_{out} times. The dwell time was set to keep t_{dwell} the same for a density of 34.6E12/cc.

While seeking to prove solely the effects of t_{dwell} (and not t_{ramp}) we questioned whether the ramp to weak interactions should be held constant in units of r_{out} (the rate of the ramp from 155 $\rightarrow$ 163 G in units of μs) or t_{ramp} (the rate of the ramp from $na^3 = 1 \rightarrow 0.000431$ in the universal units of t_n). Holding the ramp rate constant in units of t_{ramp} maintains density universality by keeping the rate between two universal values of interaction strengths scaling in units of $n^{2/3}$. Our universal values of interaction strength were defined as $na^3 = 1$ (roughly where the resonant

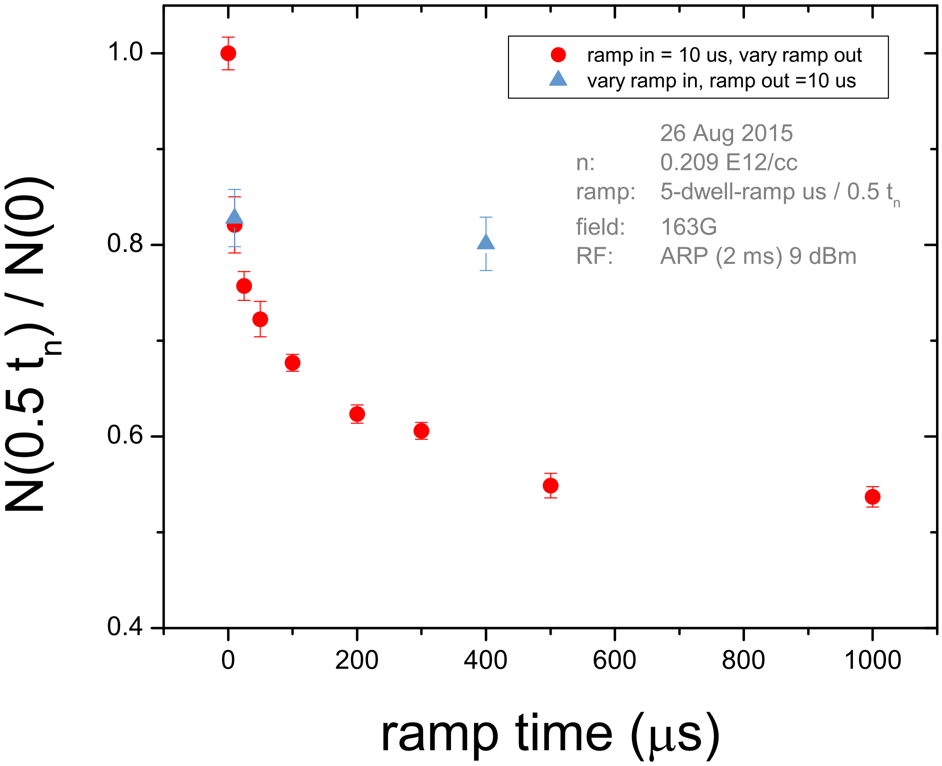

Figure 5.28: The relative number of atoms that returned after $t_{\text{dwell}} = 0.5\, t_n$ on resonance as a function of r_{out} while the r_{in} is held constant at 10 μs (red points). Two points that instead vary the r_{in} time and keep r_{out} constant at 10 μs are included for comparison (blue triangles). From this data we see that r_{out} has significantly more influence in the perceived atom loss than the r_{in}. r_{out} influences the perceived atom loss by nearly 30% (from over 80% at 10 μs to over 50% at 1000 μs) in this dataset.

interactions begin) and $na^3 = 0.000431$ (where the LHY correction to the energy density = 10%, below which is comfortably in the weakly-interacting regime).

To test the universal ramp hypothesis we measured the number of atoms that returned after $t_{\text{dwell}} = 0.5\, t_n$ on resonance for two different densities, 0.209 and 5.4 E12/cc. This data is plotted in both standard units and universal units, see figures 5.29 (a) and (b). We see much better agreement between the two density datasets when scaled in standard units of time, i.e. r_{out}.

The lack of universal density scaling in the ramp away could be due to many reasons. Ar-

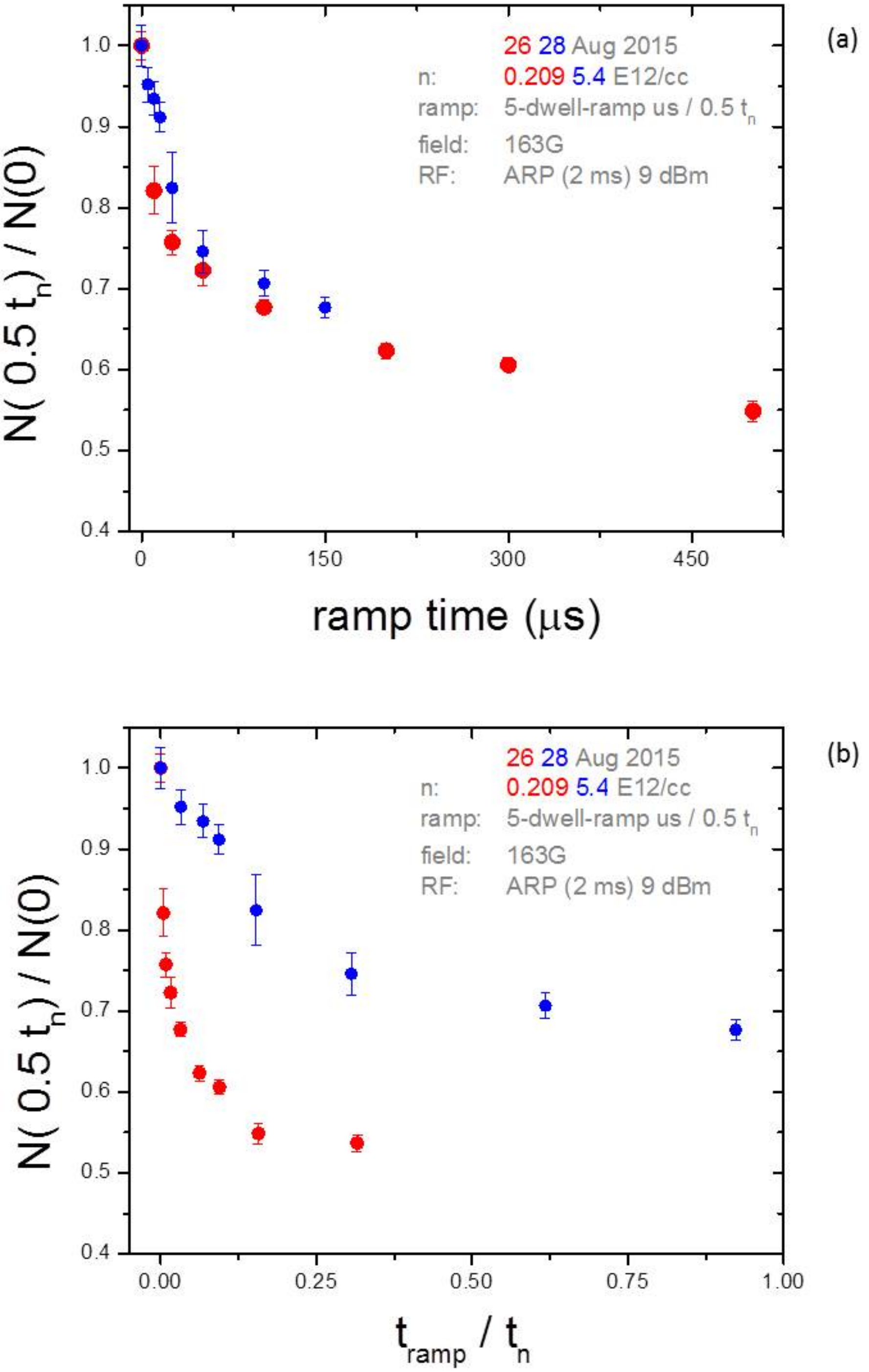

Figure 5.29: The number of atoms to return after $t_{\mathrm{dwell}} = 0.5\, t_n$ on resonance plotted as a function of (a) r_{out} in standard units and (b) r_{out} in universal units, t_{ramp}/t_n, for a low density of 0.209 E12/cc (red points) and a standard density of 5.4 E12/cc (blue points).

guably the most important component of the ramp away is the very beginning of the ramp, when the atoms cross from the resonant to strongly-interacting regime. As discussed earlier, our ramp is a piece-wise function with curved edges. The first 12.5% of the ramp (1 Gauss of the total 8 in this case) is in the non-linear regime, and this is also where the critical crossing out of the resonantly interacting regime occurs for all densities. It is possible that the non-linear ramp at $na^3 = 1$ is the cause of our ramp's non-universal behavior. So we instead rethought the problem and found a way to test it:

We know that the ramp up to and beyond $na^3 > 1$ is non-linear and therefore not well characterized by our theory. r_{out} to $na^3 = 0.000431$ is linear for all densities. Our universal ramp-away theory assumes that the ramp rate between only $1 \leq na^3 \leq 0.000431$ determines the atom loss. If this were true, a two-component ramp that was at first "slow" and then for $na^3 < 0.000431$ "fast" should produce the same loss as an entirely "slow" ramp. The results of such an experiment are shown in figure 5.30.

The two-component ramp loss not only disagrees with the single-component "slow" ramp loss, its disagreement seems to vary with the dwell on resonance, which is very unexpected. For example, the two-component ramp seems to yield identical results to the slow ramp at the shortest dwell time of $t_{\text{dwell}} = 84$ μs, however beyond this dwell time the two-component ramp proceeds to match the linear decay of the fast ramp while the fast ramp has a non-linear loss that accelerates and then stabilizes. This suggests that there is more happening at unitarity than simple loss to deeply bound states.

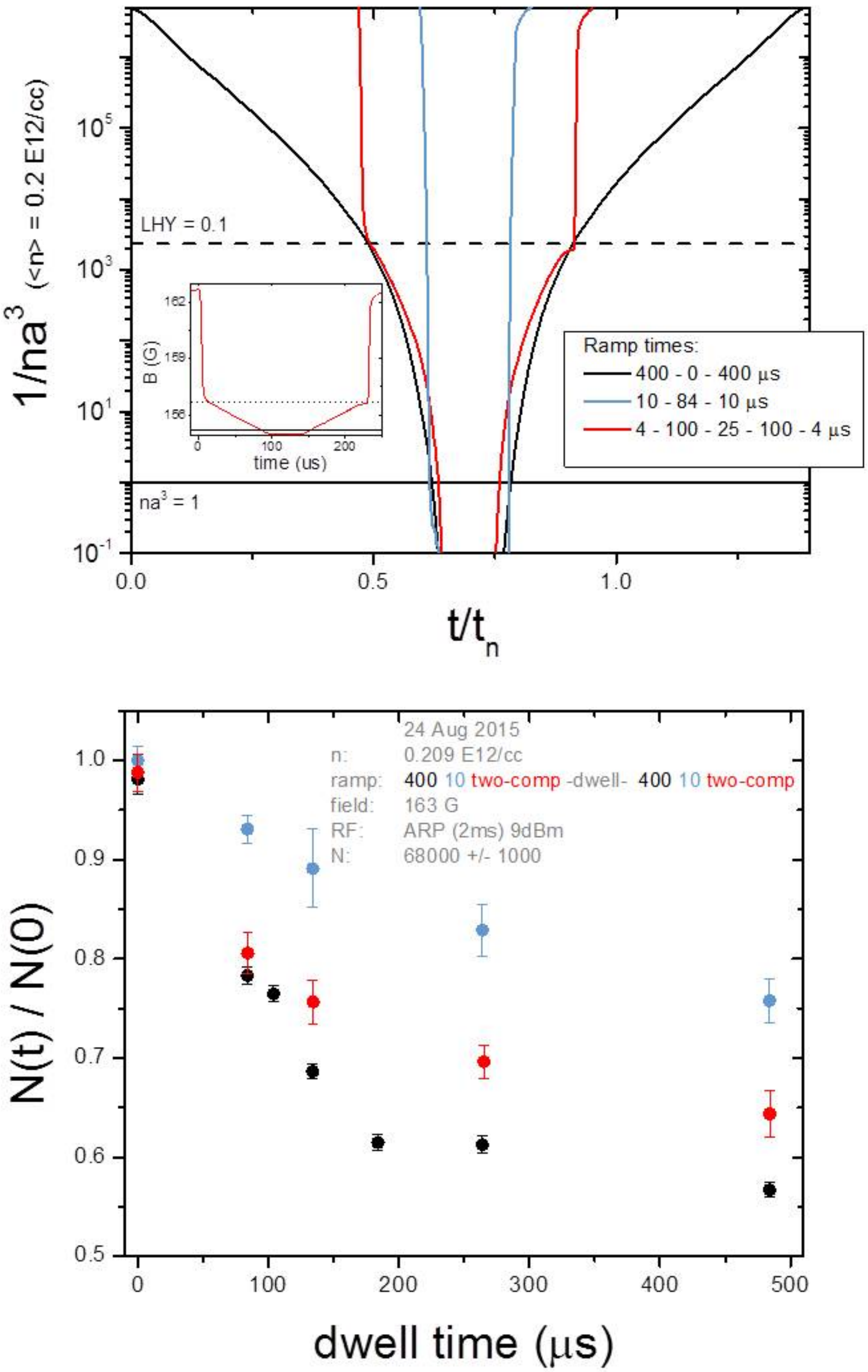

Figure 5.30: (a) There are three ramps in this experiment: two were single-component ramps characterized as 10 μs“fast ramp” (blue) and a 400 μs “slow ramp” (black) and the third ramp was a two-component ramp (red) that matched the “slow” ramp for $na^3 \geq 0.000431$ and the fast ramp for $na^3 < 0.000431$. The inset shows this two-component ramp on a linear scale. (b) The number of atoms that returned as a function of dwell time for each respective ramp.

5.5.2 Understanding the loss

Understanding the loss associated with the ramp away requires a shift in our patterned thinking. Suspicious that the increase loss associated with slower ramps away from resonance was caused by Fesbach molecule production (atoms in a superposition of unbound and bound molecule states have previously been observed in a similar system after pulsing to large a, see [85]), we theorized that we could sweep these molecules back into atoms. If we then jumped back to weak interactions quickly, we could image the return of the missing atoms, see figure 5.31 for the magnetic ramps. In figure 5.32 we see that such an experiment resulted in nearly all the atoms returning, with the exception of the the farthest magnetic ramp (we attribute the increased loss in this point to finite Feshbach molecule lifetime).

Having confirmed the creation of Feshbach molecules, further investigation requires another shift in patterned thinking: we should image the molecules directly.

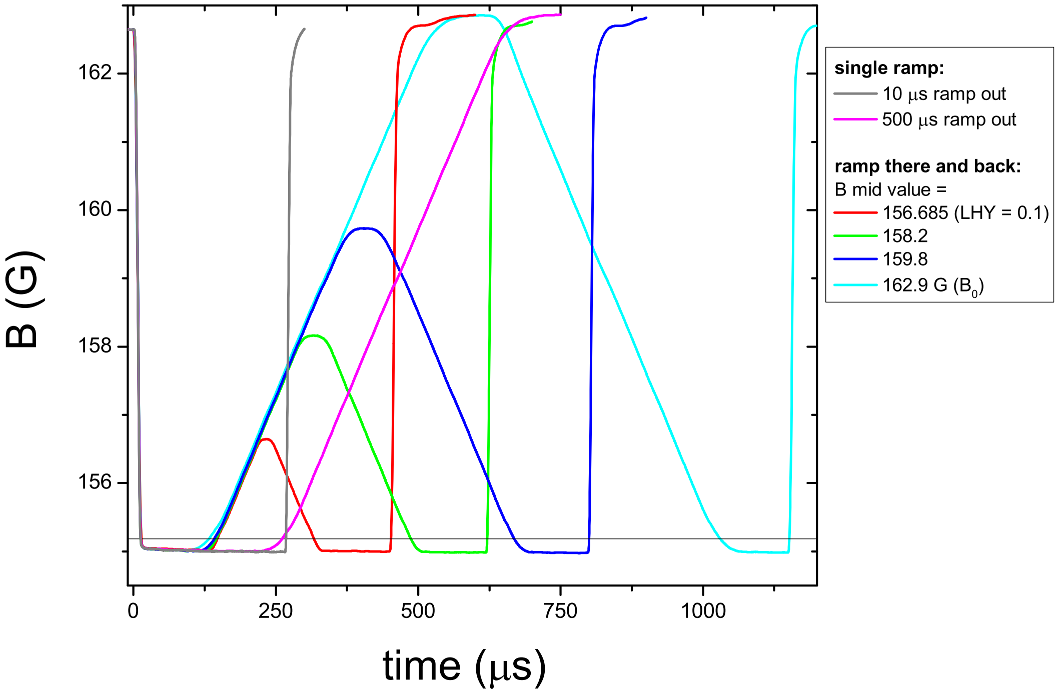

Figure 5.31: There were two single-component ramps used as reference points for this experiment: a fast 10 μs ramp (gray) and a slow 500 μs ramp (magenta). Four ramps ramped away first at the slow ramp rate to various values of magnetic field before ramping back in at the same rate; they later jumped back (at the fast ramp rate) to the initial magnetic field for imaging. The total dwell time on resonance was around $t_{\rm dwell} = 0.5\, t_n$ (for a $n = 0.2$ E12/cc cloud) and was split between the first and second time at resonance for the double ramps; the measured values of $t_{\rm dwell}$ were 255, 249, 268, 260, 266, and 240 μs for the ramps in the order of the legend, respectively.

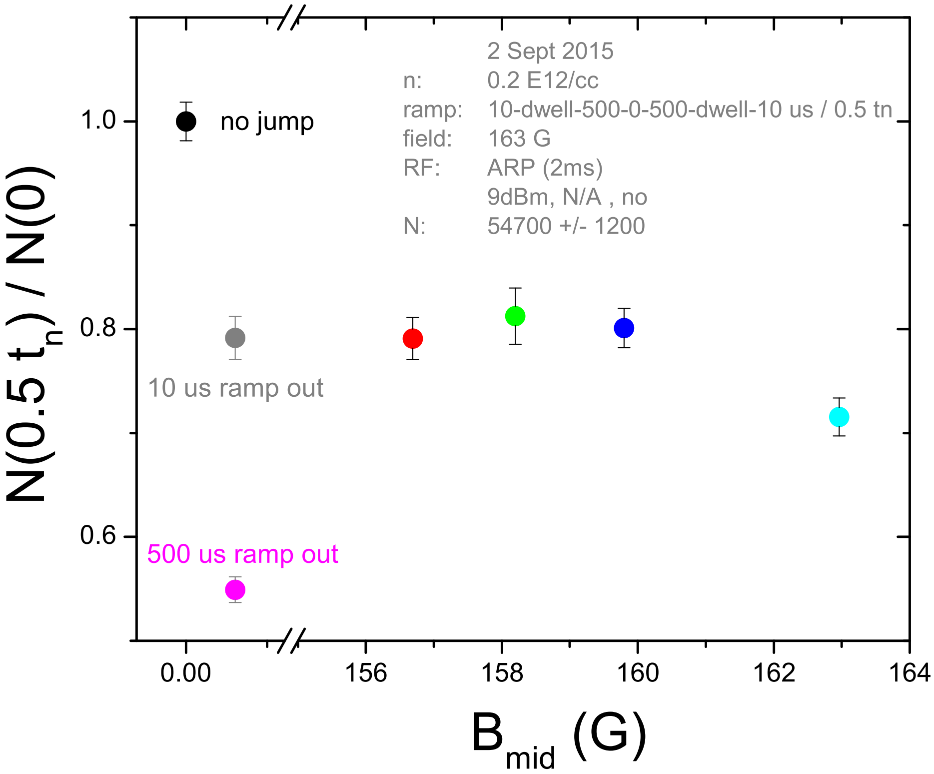

Figure 5.32: The number of atoms measured after the final jump back to the initial magnetic field for the ramps shown in figure 5.31. By ramping back to resonance slowly and then jumping out quickly we were able to see a return of almost all of the atoms , with the exception of the cyan point which ramped all the way back to the initial magnetic field - while it certainly had more final atoms than if we had only just ramped away slowly, not all of the atoms were able to return. We attribute this loss to loss of the molecules due to finite molecule lifetime at our initial magnetic field.

Chapter 6

Dissociating molecules for imaging

To image molecules directly, we use a microwave pulse to simultaneously dissociate the molecule and spin-flip one of the molecular atoms from the $|2,-2\rangle$ science state to the $|3,-3\rangle$ imaging state. In this chapter we will discuss the relevant binding energy of the molecules as well the three microwave pulses we can use to spin flip molecules into the imaging state.

6.1 Molecular binding energy

6.1.1 Theory

A simple analytic formula for the excitation rates and lineshapes of the molecular dissociation spectra was derived based on the scattering theory in the threshold regime in [86]. Because our imaging state has a negative scattering length of $a' \approx -500\,a_0$, the pulse excites a bound-free transition that results in molecule dissociation. In this event only one atom in the molecule is excited to the imaging state. The minimum energy required for this pulse (E_{rf}) is equal to the $|2,-2\rangle \rightarrow |3,-3\rangle$ energy difference E_0 (around 2.6 GHz for our conditions) plus the additional binding energy of the molecule E_{b}, typically on the order of 100 kHz, but molecules can also be dissociated in this manner with microwave pulses of greater energy. The peak of the dissociation spectra occurs with an additional $(1/3)E_{\text{b}}$, or $E_{\text{rf}} = E_0 + (4/3)E_{\text{b}}$. The dissociation effectiveness of the microwave pulse is related to many factors, including the intensity and the duration of the pulse, however we will focus mainly on the detuning of the microwave pulse from the atom resonance, δ.

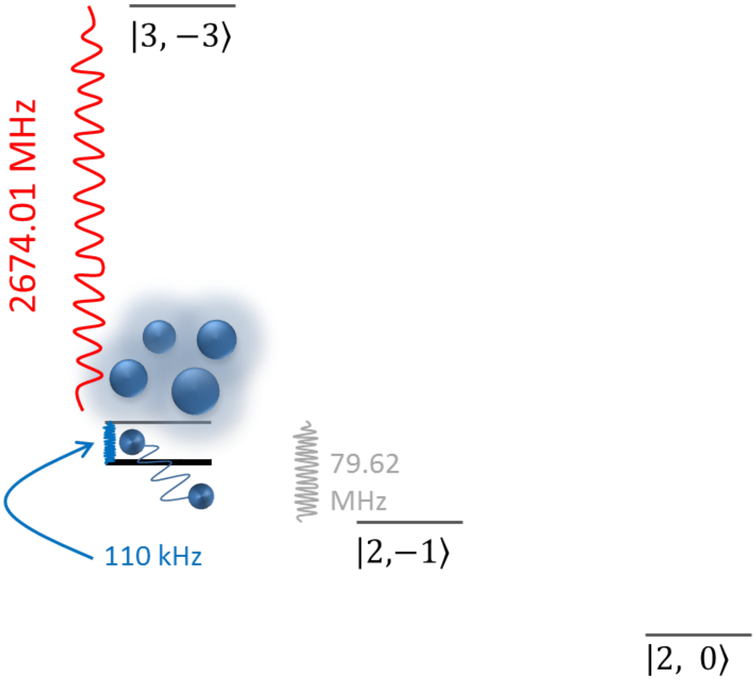

Figure 6.1: The energy diagram of ^{85}Rb at 159.5 G. Our atoms begin in the science state $|2,-2\rangle$, the Feshbach molecules are bound by 110 kHz. Our imaging state, $|3,-3\rangle$, is 2.674 GHz away from the science state when $B = 159.5G$. We can transfer molecules to the imaging state by applying an RF with a frequency greater than 110 kHz + 2.674 GHz.

In the small Rabi frequency limit, the bound-free transition rate is given by

$$\Gamma_f(K) = \frac{h\Omega^2}{2} F_f(K), \tag{6.1}$$

where Ω is the rf Rabi frequency and $F_f(K)$ is the bound-free Franck-Condon factor per unit energy, and K is the kinetic energy of the outgoing wave with wave number k, $K = \hbar^2 k^2/m$. The Franck-Condon lineshape is derived in [86] to be

$$F_f(K) = \frac{2}{\pi}\left(1 - \frac{a'}{a}\right)^2 \frac{K^{1/2} E_{\mathrm{b}}^{1/2} E'_{\mathrm{b}}}{(K + E_{\mathrm{b}})^2 (K + E'_{\mathrm{b}})^2}, \tag{6.2}$$

where $E'_{\mathrm{b}} \equiv \frac{k^2 a'^2}{K}$, and a' is the scattering length of our imaging state. Defining the microwave offset energy as $E \equiv E_{\text{rf}} - E_0 = K + E_b$, we can rewrite equation (6.2) as

$$F_f(E) = \frac{2}{\pi}\left(1 - \frac{a'}{a}\right)^2 \frac{E'_{\text{b}}\, E_{\text{b}}^{1/2}\, (E - E_{\text{b}})^{1/2}}{E^2\,(E + E'_{\text{b}} + E_{\text{b}})}. \tag{6.3}$$

We have plotted these lineshape as a function of microwave detuning ($\delta = E/h$) from the atomic resonance, E_0, for initial scattering lengths of $a = 1000$, 700, and 500 a_0 in figure 6.2. We observed the molecular lineshape with microwave spectroscopy and saw good agreement with this theory, see figure 6.3.

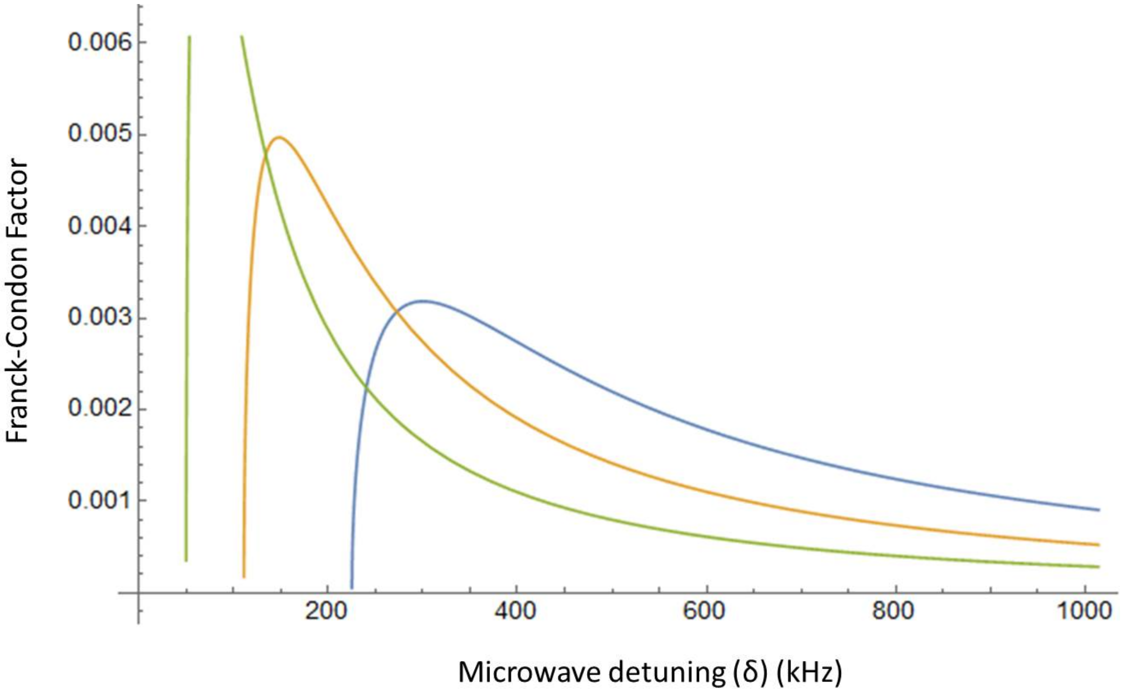

Figure 6.2: The Franck-Condon factor as a function of microwave detuning from the atomic lineshape for initial scattering lengths of $a = 1000$ (green), 700 (orange) and 500 (blue) a_0 to $a' \approx -500\, a_0$ represents the the bound-free dissociation spectra of our Feshbach molecules. The binding energies of the molecules at these scattering lengths are 50, 110, and 240 kHz respectively. As is shown in this figure, molecules can be dissociated by microwave pulses with energies equal to or greater than their binding energies, and the peak of the dissociation rate occurs at $(4/3)\, E_{\text{b}}$.

Due to their close proximity, the bound molecular atoms have large uncertainty in momentum. This momentum is released during dissociation, thereby causing them to fly apart. For this reason, our molecular atoms are not at risk for reassociating into molecules with continued microwave exposure. Therefore we can dissociate all of the molecules with a long microwave pulse without

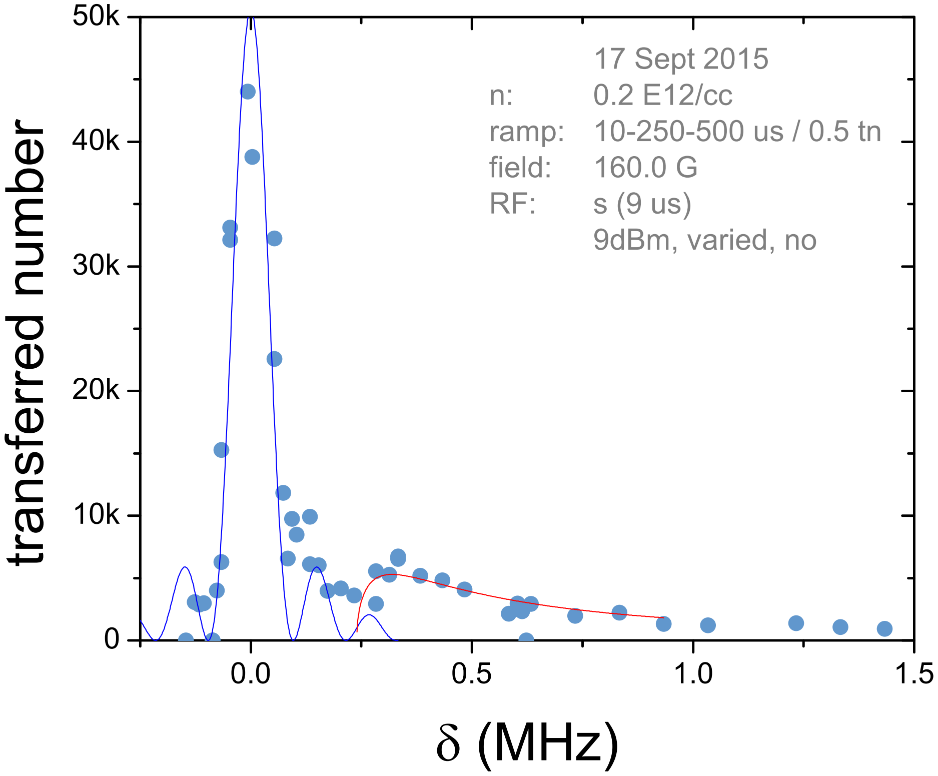

Figure 6.3: The number of atoms and molecules transferred to the imaging state as a function of microwave frequency detuning (δ) from the atomic resonance. The abbreviated legend in the upper right is explained in Appendix A.

the concern of Rabi flopping. We define the "saturation time" as the time to dissociate more than 95% of the molecules for a given microwave detuning and power. This saturation time is inversely proportional to the Franck-Condon factor: the saturation time when $a = 500\ a_0$ at the peak of the lineshape ($\delta = 320$ kHz) is much shorter than with a very large microwave detuning, such as 1 MHz, see figure 6.4.

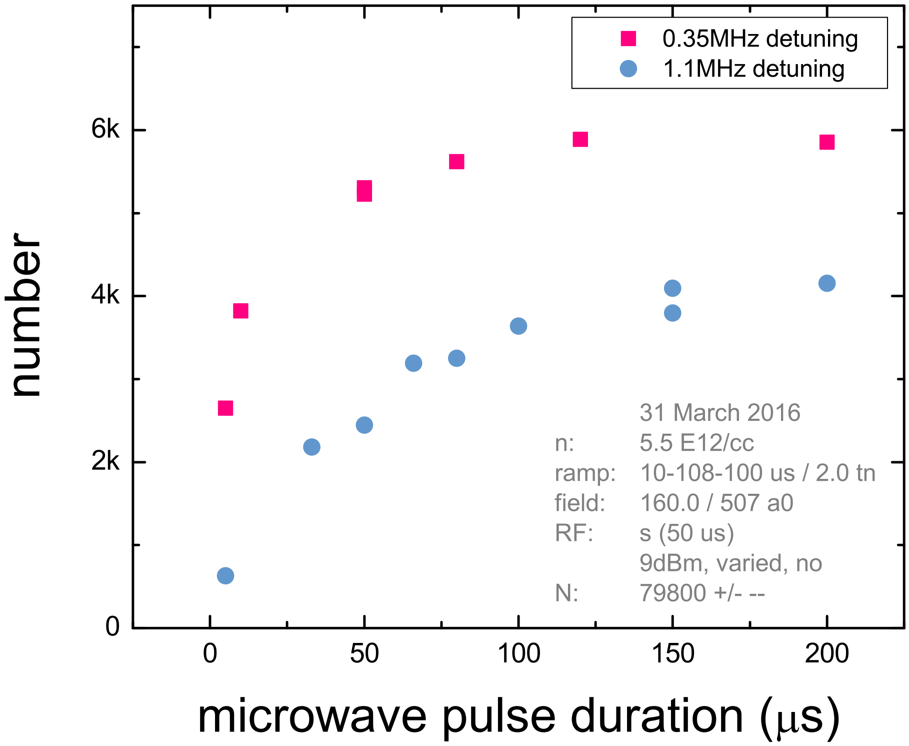

Figure 6.4: The number of molecules measured as a function of microwave pulse duration for two microwave detunings : $\delta = 350$ kHz (pink squares) and 1.1 MHz (blue points). The former is close to the peak of the molecular lineshape while the latter is far away, therefore we expect the former to saturate faster. And indeed, we see the $\delta = 350$ kHz data saturate in about 50 μs, and the $\delta = 1.1$ MHz data saturate after 150 μs. These numbers are not equal, possibly because the molecular atoms dissociated by the large detuned pulse fly apart with much more energy.

6.1.2 Experimental considerations

Because the dissociation rate of the molecules depends on the detuning from the atomic resonance, and the exact frequency of the atomic resonance is sensitive to the magnetic field, the dissociation of the molecules could be sensitive to magnetic field noise. However, as long as our microwave pulse is equal to or longer than the saturation time, small changes in the magnetic field will not translate into number noise.

Because in the future we will probe temporal molecular dynamics, we wish to keep the microwave pulse length constant and greater than the saturation time. We therefore find that we need to adjust the microwave detuning as we vary the scattering length a at which we probe the molecules. By changing the microwave detuning such that the Franck-Condon remains the same, we find that the saturation time does not vary. For example, a microwave detuning of 400 kHz at 500 a_0 has the same Franck-Condon as 315 kHz at 700 a_0 and 214 kHz at 1000 a_0 (see figure 6.5) therefore the saturation times at these detunings are also equal (assuming constant intensity of the microwave pulse), and are about 50 μs, see figure 6.6.

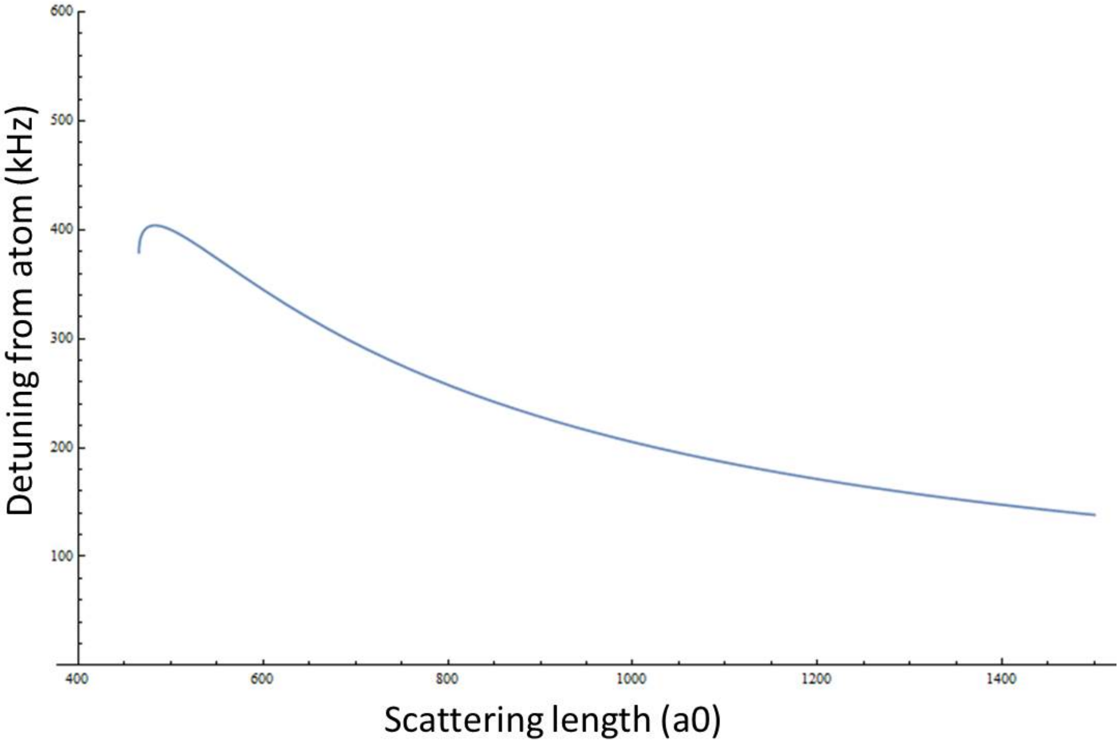

Figure 6.5: A curve representing a contour of constant Franck-Condon factor for detuning from the atom resonance as a function of scattering length. We see that 400 kHz detuning at 500 a_0 spin flips as many molecular atoms as a 315 kHz detuning at 700 a_0 and 214 kHz at 1000 a_0.

Because a 50 μs square pulse is very narrow in frequency space (relatively speaking in comparison to the other energy scales), it is necessary to turn off the vertical magnetic gradient that holds the atoms up against the gravity . The cloud then falls for a few ms during the experiment,

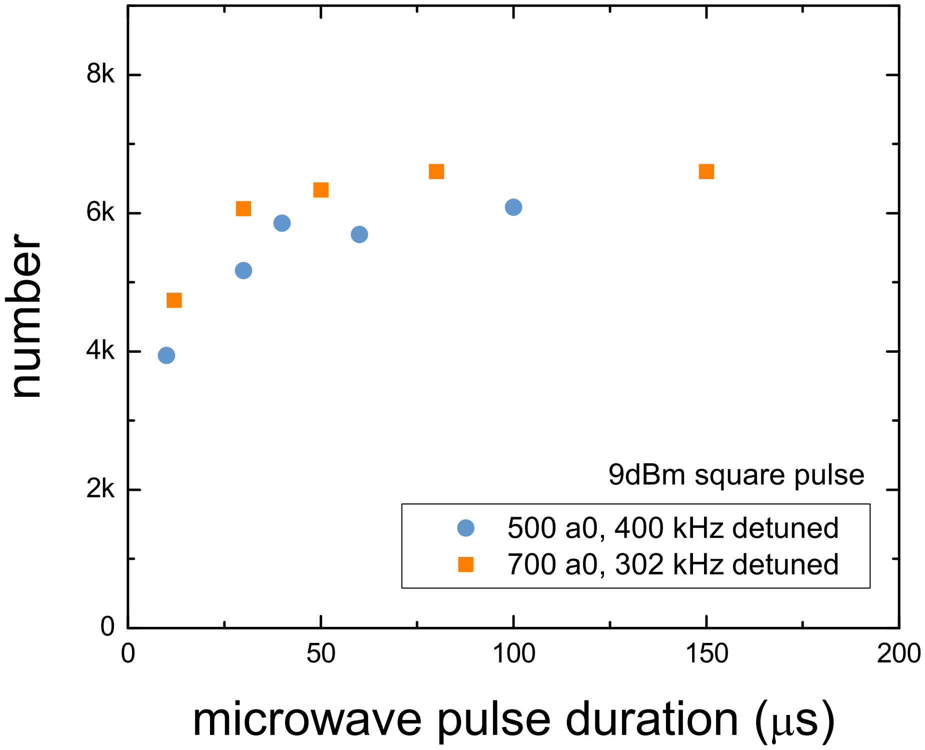

Figure 6.6: The number of molecules as a function of microwave pulse duration for a square microwave pulse at 9 dBm nominal power. The molecules at 500 a_0 were probed with 400 kHz detuning (blue points), the 700 a_0 at 302 kHz (orange squares). The saturation times are both roughly 50 μs, and the total molecule number appears to be about the same.

traveling less than 100 μm, or about three cloud diameters, see figure 6.7.

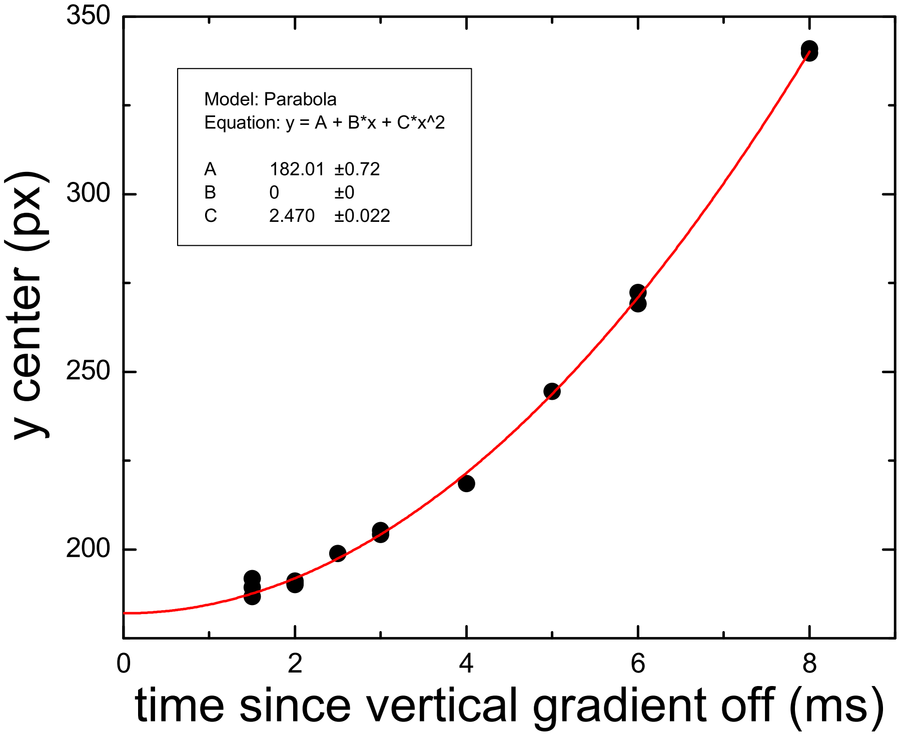

Figure 6.7: The vertical position of the cloud center as a function of time after turning off the vertical magnetic gradient. We see that within 4 ms the cloud falls less than 100 μm. There remains a small field gradient despite turning off the applied field gradient. This is evident by the acceleration of the cloud, measured to be just slightly less than gravity's pull. From this discrepancy we infer a residual field gradient of 1 G/cm in the vertical direction.

6.2 Square RF pulses

6.2.1 Atoms, atoms everywhere

While many atoms are bound into molecules by our ramp away from resonance, the majority of atoms in our system remain unbound. For the atoms, the 50 μs, 9 dBm square microwave pulse corresponds to a 6-π pulse from $|2,-2\rangle \rightarrow |3,-3\rangle$, see figure 6.8. At 400 kHz detuning from the atom resonance (so 290 kHz beyond the dimer binding energy) this 6-π pulse transfers over 1% of the atoms (and even more at smaller detunings). These atoms show up in the background of our molecule images (I colloquially refer to images of the previously molecular-bound atoms as molecule images, and the atoms contaminating these molecule images are atoms that were never bound in a molecule). The presence of the atoms is a very large experimental problem for us, as the number of atoms flipped into the imaging state is extremely sensitive to magnetic field noise, which introduces noise into our measurements rather than simply a constant background. We first attempt to fully understand that transfer of these atoms so we can correctly subtract them from our molecule images.

A standard 6-π lineshape predicts oscillation of the atom transfer from 0 to 2.5% near 400 kHz detuning, see figure 6.8(b). Our data however do not show oscillations but instead a nearly (but not completely) flat transfer of atoms of about 1%. This discrepancy can be explained by the small residual field gradient in our system, measured by our cloud acceleration (figure 6.7) of 1 G/cm. Across a 30 μm cloud this corresponds to 7 kHz. To model this field gradient, we convolve our predicted atom transfer with a 10 kHz-wide gaussian, see figure 6.9. We see that including this field gradient minimizes the predicted contrast such that the number of transferred atoms is never zero. This means that within our current system we can not avoid transfering atoms when also imaging molecules. While removing this magnetic field gradient is possible (but not easy), the gain from the endeavor would be minimal, as the frequency of the oscillations is large enough that small changes in the magnetic field would still introduce atom noise into our measurements, even if we parked at a detuning corresponding to zero atom transfer.

We instead move forward, accepting the transfer of atoms during our molecule measurements, and trying to remove them with post-imaging analysis. We first explore the possibility of using the small magnetic field gradient to our advantage in the post-image analysis by identifying the atoms by a marked stripe pattern. This technique proves promising, but only for low density (large radius) clouds. We then attempt to estimate the number of atoms present in our molecule images and subtract this constant number, and we find that this technique works significantly better when we track the microwave frequency to account for the cloud falling through the small field gradient. We eventually grow tired of trying to remove the atoms with post-image analysis and instead study two shaped (not-square) microwave envelopes that transfer nearly zero atoms to the imaging state.

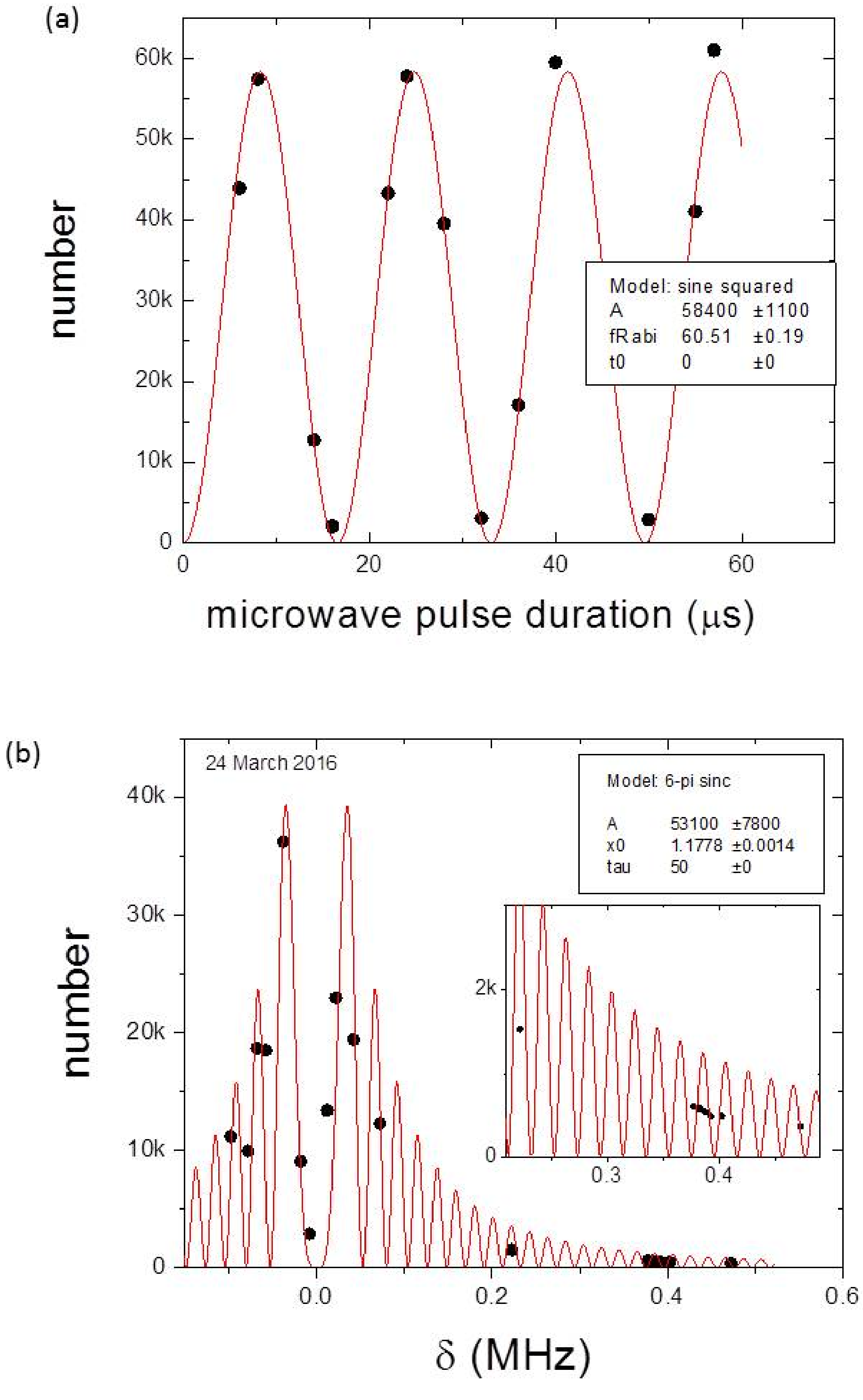

Figure 6.8: (a) The number of atoms transferred to the imaging state by a 9 dBm microwave pulse centered on resonance as a function of pulse duration. The red line is a fit sine squared function. We see that a 8 μs pulse corresponds to a π-pulse, meaning that all of the atoms are transferred to the imaging state. At 50 μs, we have a 6-π pulse. (b) The number of atoms transferred by a 9 dBm, 50 μs microwave pulse as a function of microwave frequency. Zooming into the signal (inset), we see that there are roughly 600 atoms transferred to the imaging state when 400 kHz detuned, this corresponds to about 1.2% of the atoms.

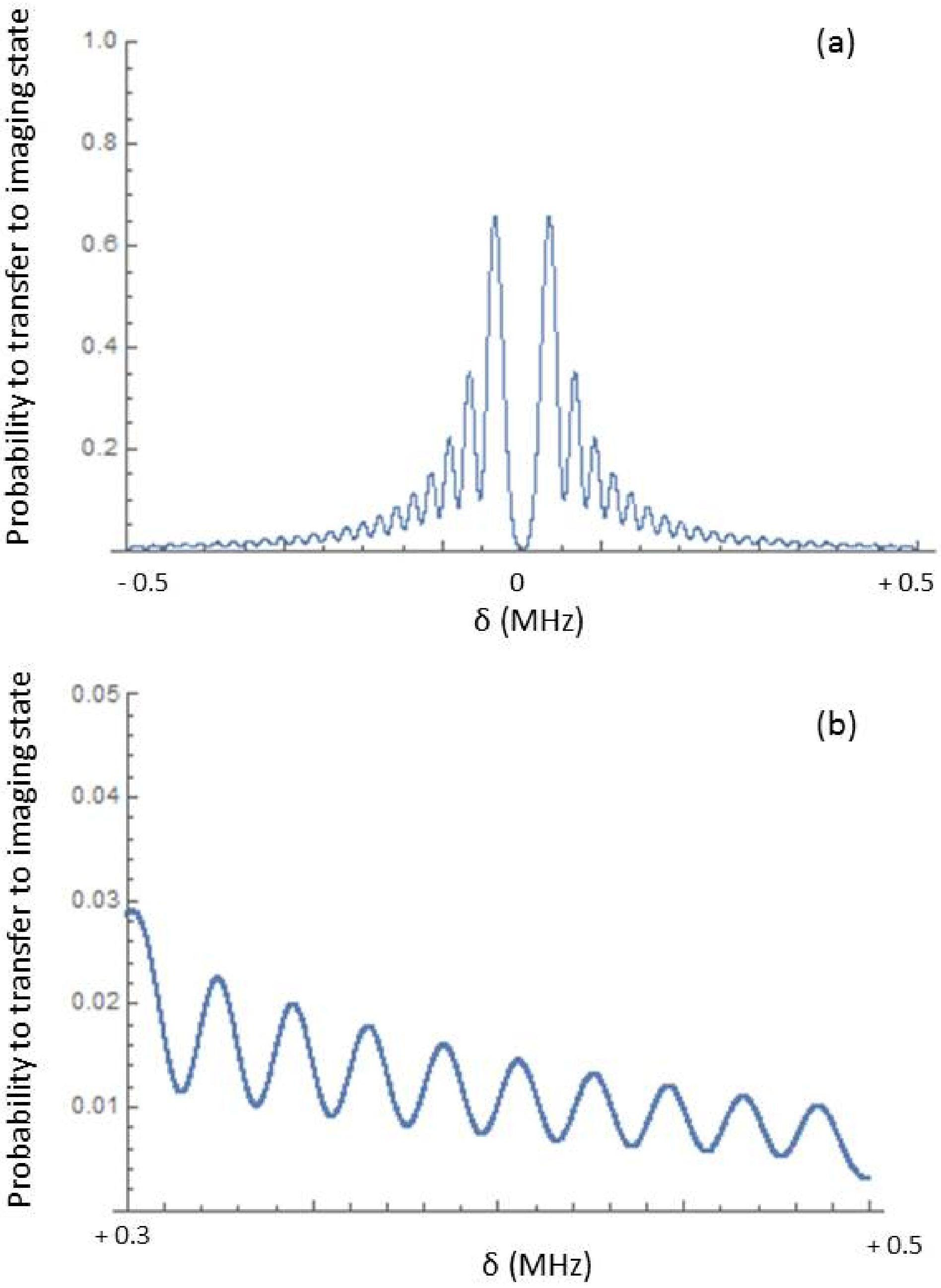

Figure 6.9: (a) The probability to transfer atoms to the imaging state with a 6-π pulse as a function of RF detuning after considering the residual field gradient across our cloud. (b) Zooming in from 300 to 500 kHz, we see a reduced contrast, confirming our suspicion that the residual field gradient is the cause of the flat number seen in figure 6.8. While a 10 kHz convolution does not completely dampen out the predicted oscillations, a larger convolution (of around 20 kHz) does, and we believe that a combination of the field gradient, cloud size, and imaging analysis account for the oscillation-less measurements in figure 6.8(b).

6.2.2 Atom stripes

Having accepted that our standard microwave pulse transfers unbound atoms the imaging state when we only wish to image molecular atoms, we attempted to remove the atoms from our molecule signal with post-imaging analysis. Fortunately, we found the task of separating atom from molecule signal was simplified for us by the small magnetic field gradient - this gradient created strips in our atom clouds, but not our molecule clouds.

The total field gradient across the cloud depends on the size of the cloud; our low density clouds are large enough that the total field gradient is larger than the oscillation frequency of the transfer function. This results in stripes across an imaged atom cloud. From these stripes we can determine that the field gradient is at a small angle with respect to the vertical axis, see figure 6.10(a). These stripes are not present in the molecular clouds because, unlike the atoms, they do not Rabi-flop between the states.

We can use these stripes to discern the atom signal from the molecule signal. We fit the combined optical depth with a two-Gaussian sum including stripes:

$$\begin{aligned} OD(x,y) =& A_a \mathrm{e}^{\left(-(x-x_c)^2/2\sigma_{xa}^2\right)} \mathrm{e}^{\left(-(y-y_c)^2/2\sigma_{ya}^2\right)} \left(1 + A_s \sin(k_x\, x + k_y\, y + \phi)\right) \\ &+ A_m \mathrm{e}^{\left(-(x-x_c)^2/2\sigma_{xm}^2\right)} \mathrm{e}^{\left(-(y-y_c)^2/2\sigma_{ym}^2\right)} + C. \end{aligned} \tag{6.4}$$

The first term represents the atom signal with stripes and the second term represents the molecule signal: x_c, y_c are the cloud centers; σ_{xa}, σ_{ya}, and σ_{xm}, σ_{ym} are the x and y widths of the atom or molecule cloud; k_x and k_y determine the frequency of the stripes, ϕ the phase; A_s is the stripe contrast ($0 \leq A_s \leq 1$) and A_a, A_m are the peak optical of atomic and molecular components.

With this fitting function we are able to fit both the atom and molecular components of the cloud, see figure 6.10. After a dwell time of 500 μs ($\sim 1 t_n$) and $r_{\mathrm{out}} = 100\,\mu$s to 700 a_0, our fit claims 3000 molecular atoms and 1660 unbound atoms transfer to the imaging state.

Repeating this technique at larger densities has issues due to smaller cloud sizes. When the cloud is less than two stripes across, it becomes impossible to fit the atom signal solely by the stripes. Fixing the stripe frequency, cloud size, and/or atom number does not produce a reliable fitting function for molecular number. We also tried increasing the frequency of the stripes across the smaller clouds by increasing the magnetic field gradient in our system but the results were subpar.

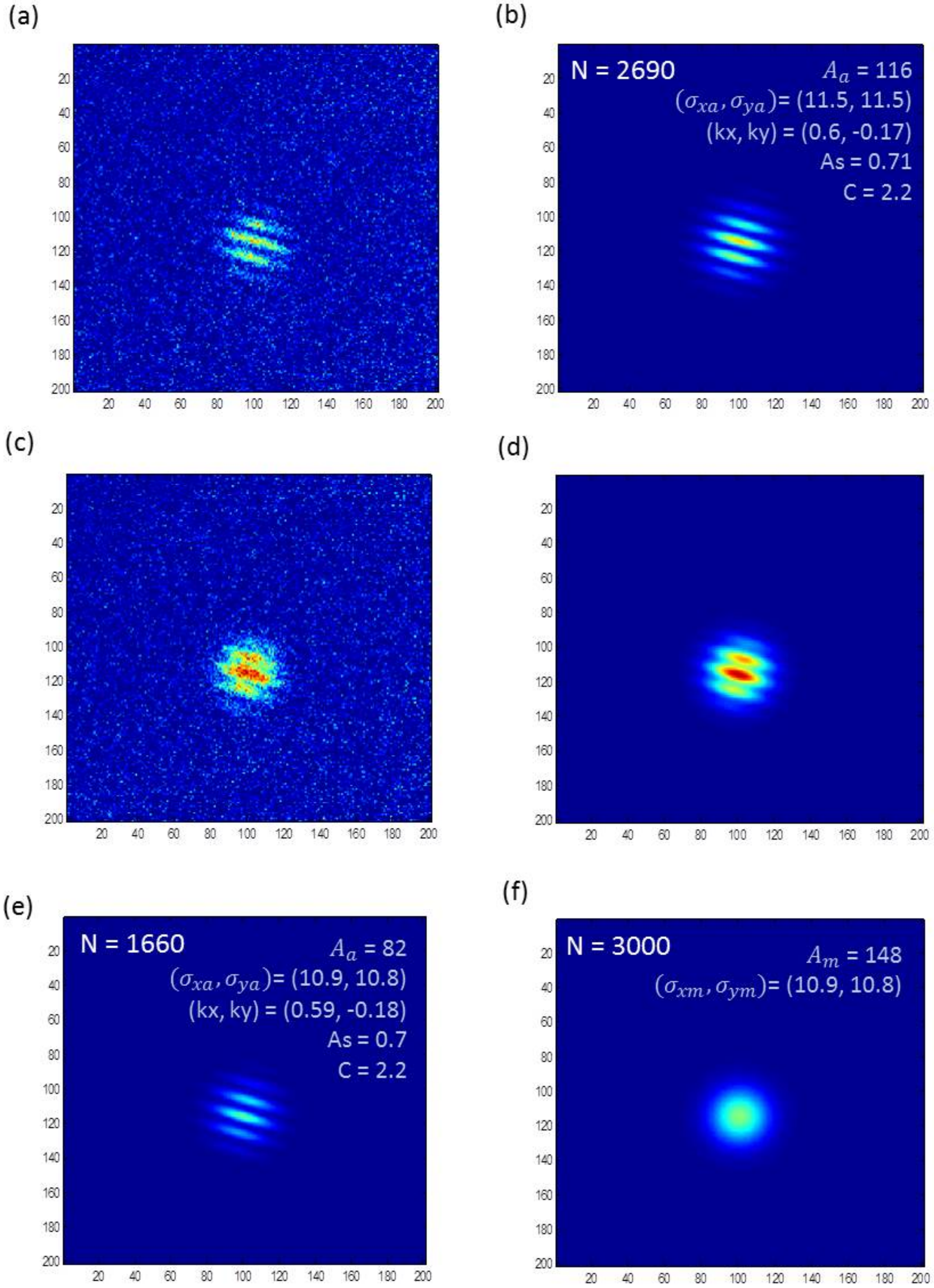

Figure 6.10: (a) The stripes across an atom (no molecules) cloud at 700 a_0 after a 9 dBm, 50 μs microwave pulse detuning 300 kHz from resonance. (b) A fit to the atom cloud shows that 2690 atoms were transferred to the imaging state. (c) Atom stripes appear across a cloud of both atoms and molecules, created by a 510 μs dwell time ($\sim 1\, t_n$ for n =0.2 E12/cc cloud) on resonance and a ramp time = 100 μs to 700 a_0 . (d) A fit to the molecule + atom cloud. (e) The atom contribution to the atom+molecule fit predicts 1660 atoms. After accounting for loss at unitarity we expect 65% of the original atom number. (f) The molecule contribution is about 3000 molecules.

6.2.3 Subtracting constant atom number

Because the atom stripe technique does not work on clouds of all densities, we instead attempted to filter the atoms out of our molecule signal by fitting the atom+molecule images with a single Gaussian, then subtracting the expected number of atoms. The expected number of atoms was estimated by measuring the number of atoms transferred to the imaging state from a pure atom cloud (i.e. no molecules) by a microwave pulse with the same detuning, intensity, and duration as the molecule pulse. Unfortuantely, we found that the atom transfer fraction increased with hold time, due to the cloud falling (and thereby decreasing the microwave detuning), see figure 6.12(a). This means that in order to accurately subtract the atoms out of our molecule signal, we needed to measure the transfer fraction as a function of dwell time for each dataset. Additionally, we had to calibrate the atom transfer fraction with the measured resonant atom loss, see figure 6.11 for the atom loss as a function of dwell time on resonance. We tested this new technique (dubbed "atom subtraction") with a low density ($n = 0.2$ E12/cc) cloud so we could compare results with our old fringe fit method.

The molecular number derived from this method was untrustworthy, as it at times predicted unrealistic results, such as an increase in molecule number at later times, see figure 6.12(b). This discrepancy is due to incorrect atom calibration, most likely from simplified fitting functions to describe how the transfer probability changes as the cloud falls. Easier than determining a correct functional form is to correct the microwave frequency as the cloud falls; this will keep the transferred atom number constant over all hold times. We call this correction "frequency tracking".

We measured the change in detuning as the cloud dropped by taking π-pulse lineshapes at 50 μs and 1800 μs hold times, see figure 6.13(a and b). The lineshape center shifts by 97 kHz over the 1750 μs, corresponding to 0.055 kHz / μs if we assume a linear frequency shift. While the cloud is somewhat accelerating while falling, we find that a linear correction was a good approximation and yielded constant atom number when applied to the microwave frequency, see 6.13(c). This linear correction is not zero because turning off the main vertical gradient apparently shoves the atoms

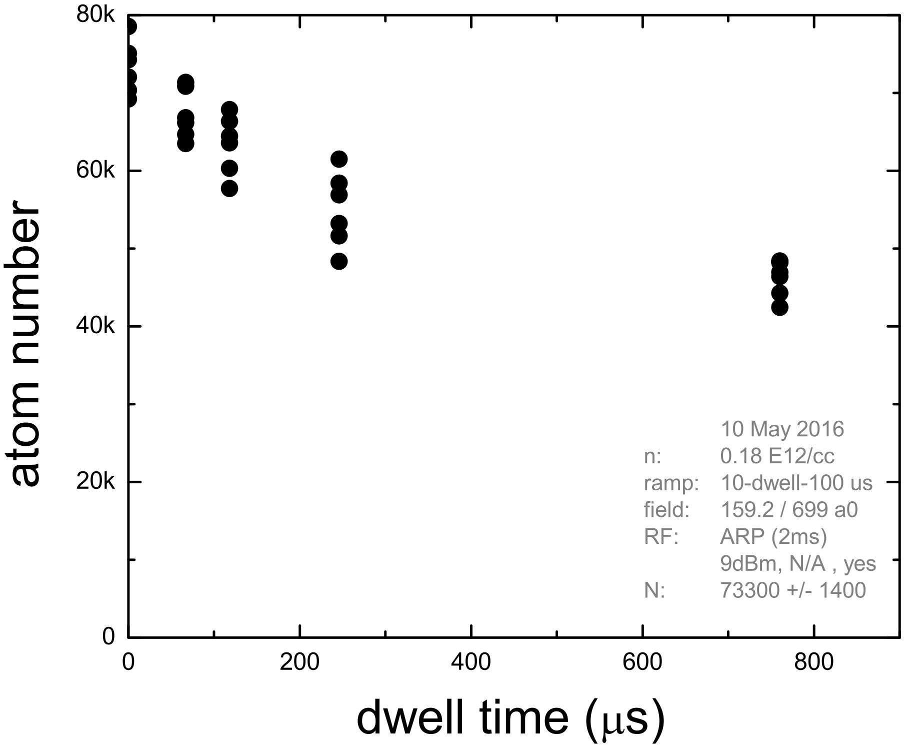

Figure 6.11: The number of atoms to return from resonance after various dwell times and a 100 μs ramp to ~700 a_0. The atoms are measured with a 2 ms ARP that transfers 100% of the atoms to the imaging state.

downwards with a small initial velocity.

Frequency tracking drastically improves our atom subtraction method, see figure 6.14. After subtracting the atom number obtained in figure 6.13(c) (with resonance calibration), we see molecule numbers nearly identical to that produced with a fringe-fit analysis. We therefore trust the atom subtraction with frequency-tracking method as much as our fringe-fit method, except atom subtraction will work equally well at all densities.

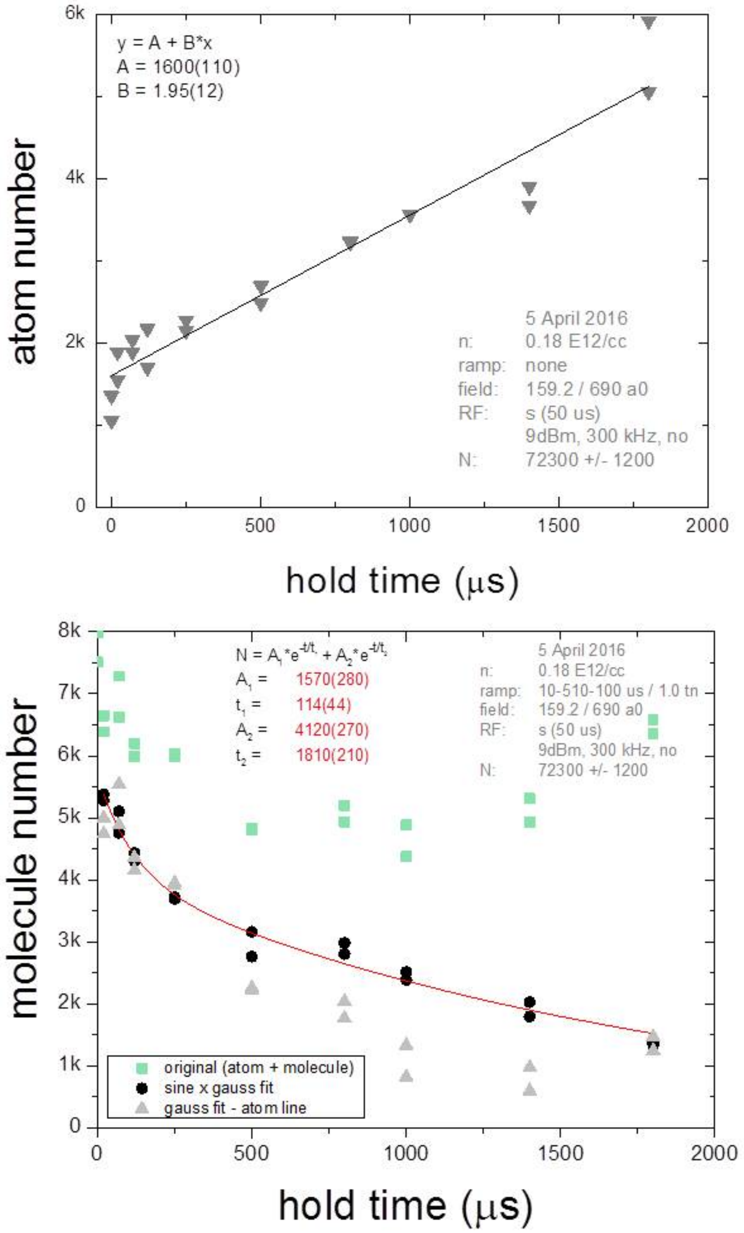

Figure 6.12: (a) The number of atoms from an atom-only (no resonance jump to generate molecules) cloud transferred to the imaging state after a 300 kHz detuned pulse at 700 a_0. The contaminating transfer of atoms increases with longer hold times because the cloud is falling through a slight residual magnetic field gradient, thereby decreasing the microwave detuning. (b) The green squares are the combined atom and molecule signal after jumping a low density (n = 0.2 E12/cc) to resonance for 1 t_n and then ramping to 700 a_0 with a 100 μs ramp. We see this signal at first decrease, due to the decay of the molecules, then later increase to nearly its original value as more atoms contaminate the background! The black points are the molecule signal determined by fitting the cloud with a fringe fit, the gray points are the molecule signal determined by subtracting the calibrated atom number from (a). The black and gray points disagree for many hold times. The gray points in particular appear to increase between 1400 and 1800 μs, which is highly unlikely if not downright impossible to be real molecule decay dynamics. We therefore conclude that time-varying contamination of atoms is not easy to filter out of our molecule signal.

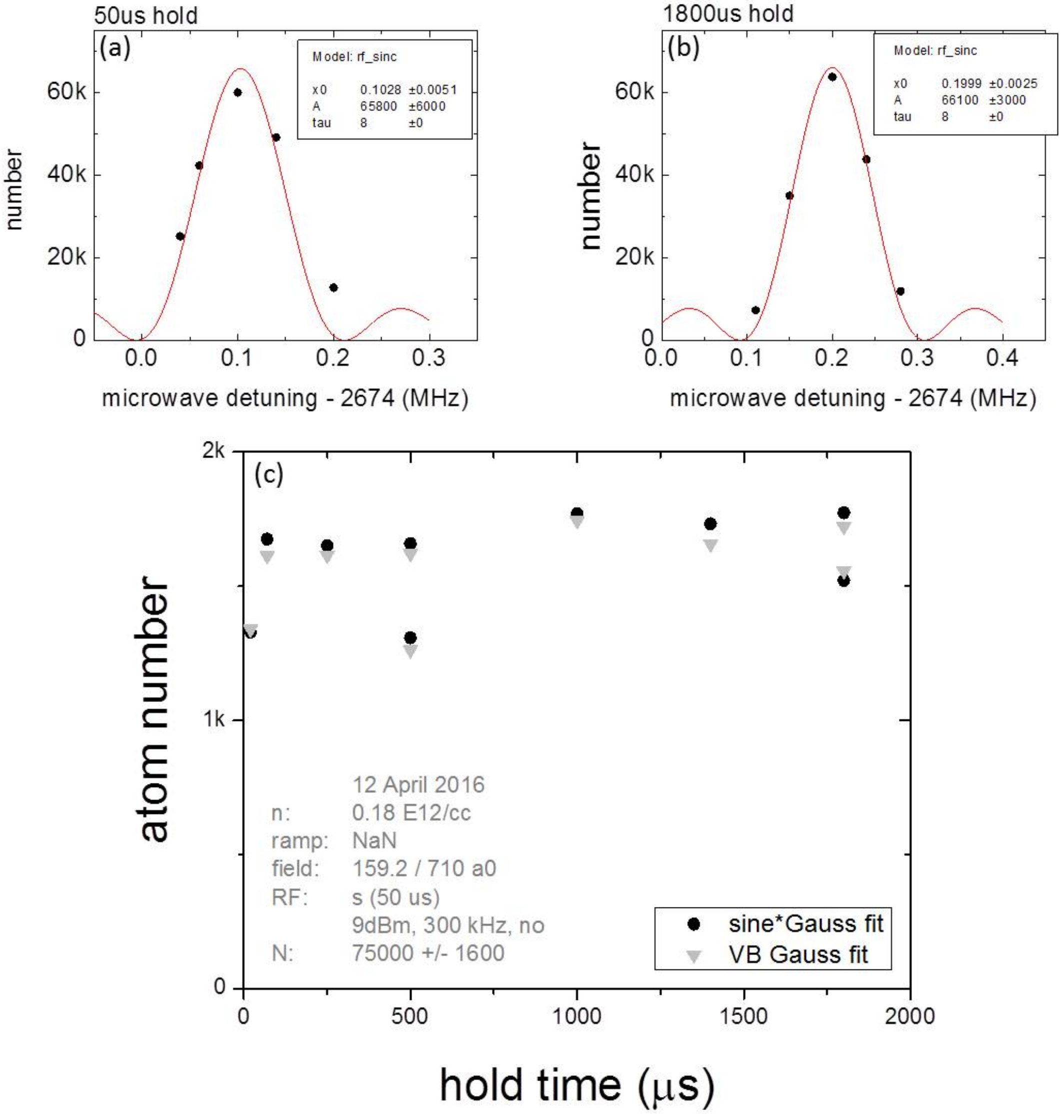

Figure 6.13: (a) Microwave lineshapes of our low-density ($n = 0.2$ E12/cc) condensate with a 8 μs, 9 dBm π-pulse after a 1 t_n dwell time on resonance and a ramp time = 100 μs to 700 a_0. Over 1750 μs the frequency changes by 97 kHz. (b) The number of atoms transferred to the imaging state by a 9 dBm, 300 kHz detuned 50 μs microwave pulse that tracked the microwave frequency by 0.055 kHz/μs. We compare a Sine×Gaussian fringe fit (black points) to a normal Gaussian fit (gray triangles) and see good agreement in number. The number is roughly constant as a function of time, therefore the linear tracking is a good approximation.

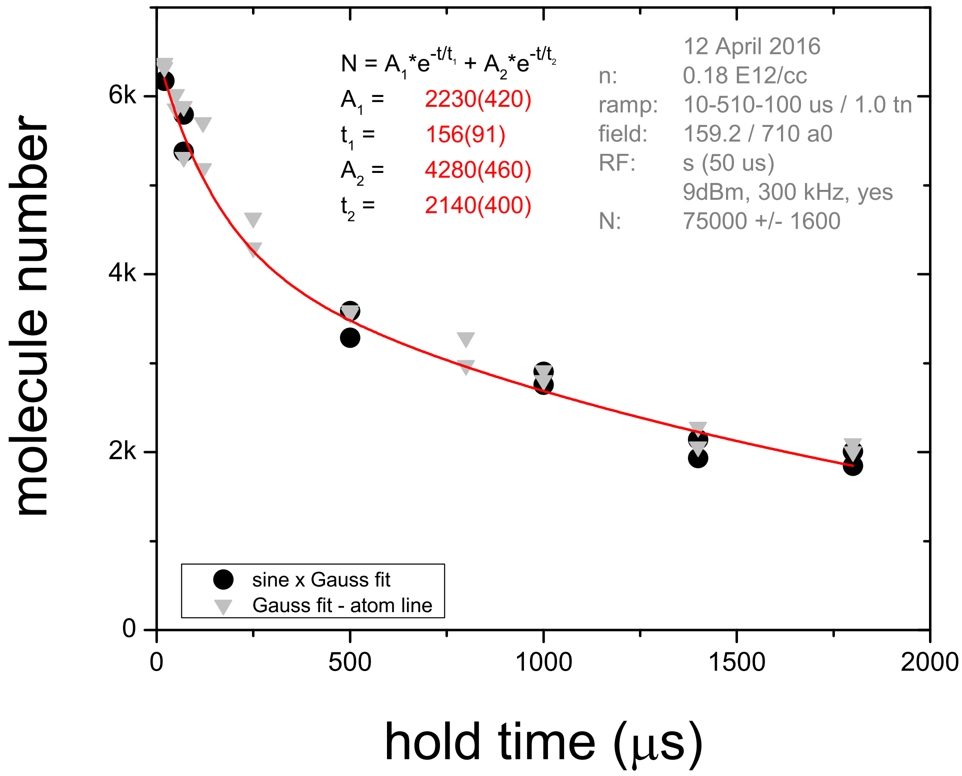

Figure 6.14: The number of molecules after a 510 μs dwell time ($\sim 1\,t_n$ for the n =0.2 E12/cc cloud) on resonance and a 100 μs ramp to 700 a_0 as a function of hold time, transferred to the imaging state with a 9 dBm, 300 kHz detuning 50 μs microwave pulse that tracked the detuning as the cloud fell. The black points represent the molecule number determined after separating the atoms from the signal using fringe fit analysis, the gray triangles represent the molecule number determined after subtracting the calibrated, constant atom number.

6.2.4 Investigation into B-field noise

Frequency tracking is necessary to keep the transferred atom number constant as the cloud falls, but it does not affect the transferred molecule number. Because the molecule signal has a broad dissociation lineshape, and the molecules do not resassociate and therefore can be saturated, the molecule signal can be made insensitive to small changes in the magnetic field. This is not true for the transferred atom number.

Frequency tracking does not protect us from fluctuations in the transferred atom number due to other magnetic field variations. Careful tuning of our coil driver current servos and meticulous eddy current corrections have minimized our magnetic field noise to less than 10 mG, see figure 6.15. However, this magnetic field noise projects into $\leq 10\%$ number noise! This projection is calculated by the slopes of the transferred atom number over microwave detuning, these slopes are 501 atoms/kHz and 145 atoms/kHz at 200 kHz and 400 kHz detuning, respectively.

Because we treat the number of atoms as a constant, this noise has huge implications for our perceived molecule signal, especially at short times when the magnetic field noise is maximum. Rather than accept the consequences of these implications, we seek to avoid them altogether. We have three options: (1) make the atoms less sensitive to the magnetic field, (2) reduce the magnetic field noise, or (3) remove the magnetic-field sensitive atoms from the imaging process.

One could reduce the field-sensitivity of the atoms by changing the state transition for imaging. Our beginning and final states must remain the same: atoms and molecules begin in $|2,-2\rangle$ and we image the molecules in $|3,-3\rangle$. The 2.6 GHz transition of $|2,-2\rangle \rightarrow |3,-3\rangle$ is sensitive to the magnetic field, hence our noise problem [75]. However, if we first transferred our molecules to the $|2,-1\rangle$ state (a 80 MHz transition that is significantly less sensitive to the magnetic field), then the molecules could be transferred $|3,-2\rangle \rightarrow |3,-3\rangle$. This is the imaging process previously employed to spectroscopically measure Tan's contact in our lab [75]. However, the fast expansion of the newly-seperated molecular atoms as they transfer through the multiple states, combined with the already low-signal, results in clouds too sparse to properly image. There are also implications regarding transferring the molecules to the $|2,-1\rangle$ state to probe their lifetime, when said lifetime is dominated by loss to the $|2,-1\rangle$ state.

Abandoning the idea of a less-sensitive state transition, our next option is to reduce the magnetic field noise. First we need to understand the cause of this noise: is it caused by a high-frequency ringing too fast for the current servo to control (fixable), or is it a base magnetic field noise in our experiment (less fixable)? Using an external magnetometer we measured the base magnetic field noise near our science well (while all of our magnetic fields and currents were off) to be $\sigma = 2.377$ mG, see figure 6.16(a). We then measured the base magnetic field noise experienced by atoms in our system by repeating microwave lineshapes from $|2,-2\rangle \rightarrow |3,-3\rangle$. We plotted the residuals of these points from the fitted line as a function of detuning [figure 6.16(c)]. The points near zero detuning represent physical number noise (due to varying MOT fill numbers, transfer-survival rates, and evaporation survival); the points at larger detunings represent both field noise and physical number noise. We measure this latter noise at 0.07465, which results in a magnetic field noise of 0.004952 MHz, or 2.153 mG. This value's agreement with the external field noise is good confirmation that the current servos driving our magnetic trap coils are not introducing noise into our system.

The magnetic field variation we saw after ramping back from resonance had a maximum of 10 mG and a σ of about 5 mG. Therefore about half of this magnetic field noise is caused by base magnetic field noise that would require great lengths to reduce. We turn instead to our third option: removing the atoms from the imaging process.

We can remove atoms from our imaging process by changing the shape of our microwave envelope from square, to something more narrow in frequency space. Before we move forward in discussing microwave envelopes, it is worth mentioning that lots of molecule lifetime data was obtained with a square microwave pulse and analyzed using either the atom stripes or atom subtraction with frequency tracking methods, see Appendix E.

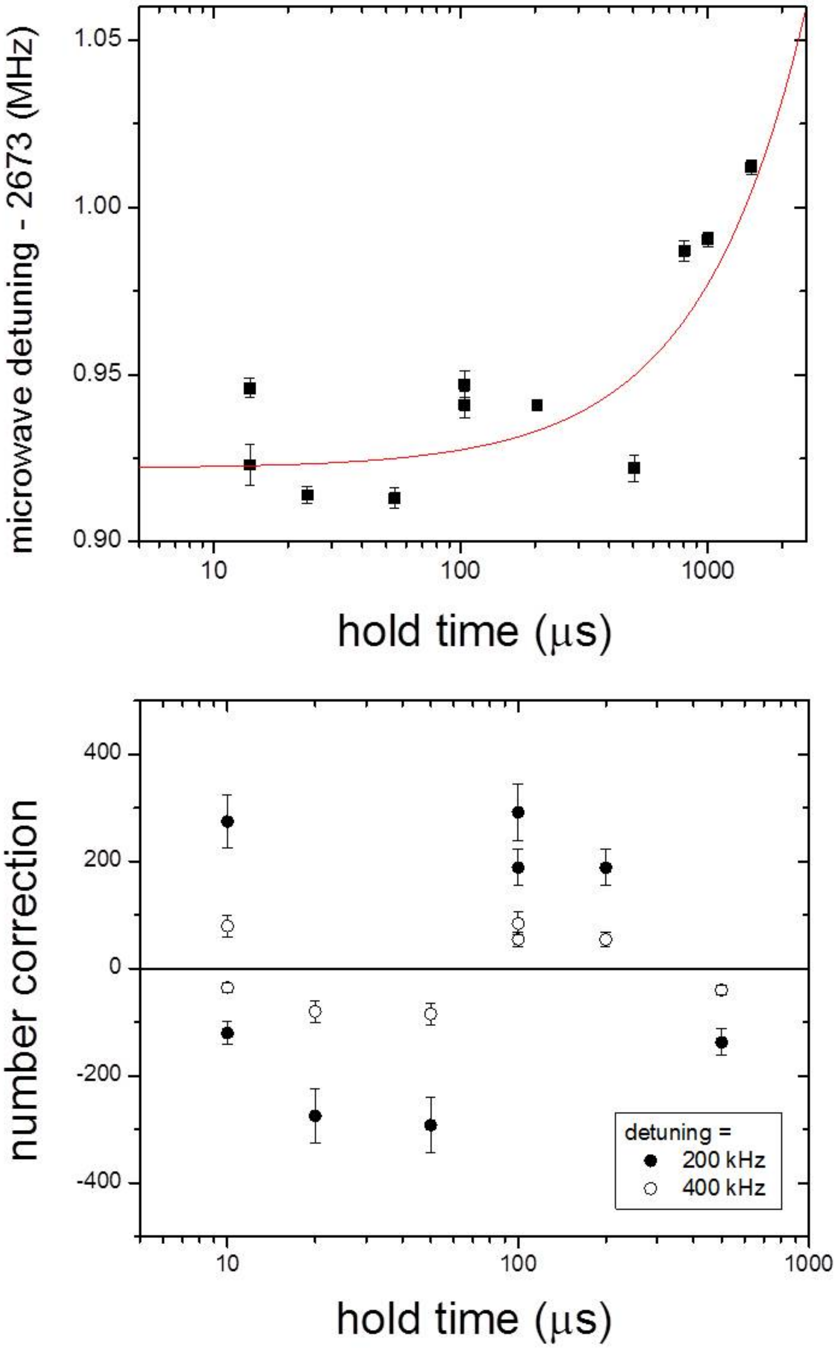

Figure 6.15: The measured magnetic field after a ramp time = 100 μs from resonance to 700 a_0. The measured microwave lineshape centers as a function of hold time at 700 a_0 after a ramp time = 100 μs back from resonance. The red line is a linear line on a lin-log plot representing the expected change due to the cloud falling. Deviation from this line is a representation of the magnetic field noise. (b) The predicted effect of the magnetic field noise on the number of atoms transferred to the imaging state as a function of hold time at unitary for 200 kHz detuning (black points) and 300 kHz detuning (open circles), which are the detunings used to image molecules at 1000 a_0 and 700 a_0, respectively. At 200 kHz detuning this magnetic field noise could transfer 250 fewer atoms, or about 10% of our overall signal.

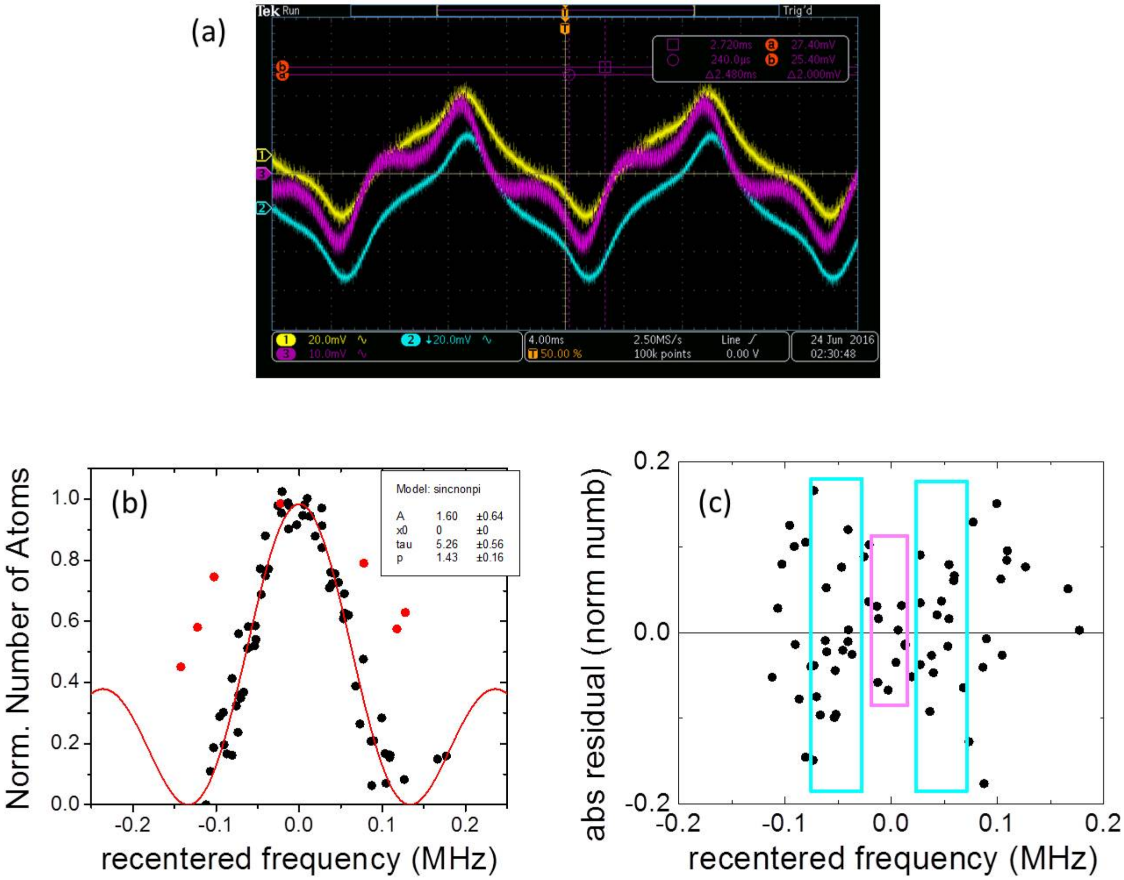

Figure 6.16: (a) The magnetic field measured in the x (yellow), y (blue) and z (pink) axes. The base field oscillates on a 120 kHz frequency (consistent with power line noise) with $\sigma = 2.377$ mG. (b) The normalized number of atoms transferred to the imaging state as a function of RF detuning. (c) The residuals from (b) vs detuning. At zero detuning this noise represents the noise in number from shot to shot, $\sigma_{\text{num}} = 0.04969$, while the noise at larger detunings represents the magnetic field noise in conduction with number noise, $\sigma_{\text{comb}} = 0.07465$.

6.3 Microwave envelopes to suppress atom transfer

Our molecule images are contaminated by atoms because the far-detuned square microwave pulse transfers off-resonant atoms to the imaging state. This transfer occurs because the corresponding instrument function (i.e. the Fourier transform) of a square pulse is a sinc function, and the oscillatory wings of a sinc function have appreciable amplitude, even at large detunings:

$$\begin{aligned} \mathrm{sq}(t) &= A\mathrm{if}(-T/2 \leq t \leq T/2) \\ F(\omega) &= \frac{1}{2\pi}\int_{-\infty}^{\infty} \mathrm{sq}(t)\mathrm{e}^{-i\omega t}\mathrm{dt} \\ &= \frac{A}{2\pi}\,\mathrm{sinc}\,(\omega/2) \end{aligned} \tag{6.5}$$

In this section we will examine two candidate envelopes for our microwave pulses whose frequency components fall off much faster with detuning than our standard square envelope.

6.3.1 Long Gaussian pulses

A Fourier-transformed Gaussian is still a Gaussian, and therefore a microwave pulse with a Gaussian-amplitude envelope is much more narrow in frequency space than a square pulse.

$$\begin{aligned} \mathrm{G}(t) &= A\mathrm{e}^{\frac{t^2}{2\sigma^2}} \\ F(\omega) &= \frac{1}{2\pi}\int_{-\infty}^{\infty} \mathrm{G}(t)\mathrm{e}^{-i\omega t}\mathrm{dt} \\ &= A\sigma\mathrm{e}^{-\omega^2\sigma^2/2} \end{aligned} \tag{6.6}$$

Chapter 4 of [75] discusses past lab procedures to create Gaussian microwave pulses using a linear variable gain amplifier to combine the outputs of a high frequency synthesizer and an arbitrary function generator. Nowadays we have combined the high frequency and envelope generation into one Agilent N5181A signal generator.

Our Gaussian pulse has a width characterized by $\sigma = 50\,\mu\mathrm{s}$. We truncate the signal at $\pm 3\sigma$, so the entire pulse is 300 μs. There is no saturation and very little delay after sending our signal through a 10 W amplifier, see figure 6.17. When detuned by $\geq$ 200 kHz this Gaussian pulse transfers practically no atoms to the imaging state, we are therefore able to discern the molecular lineshape from the atom lineshape, see figure 6.18.

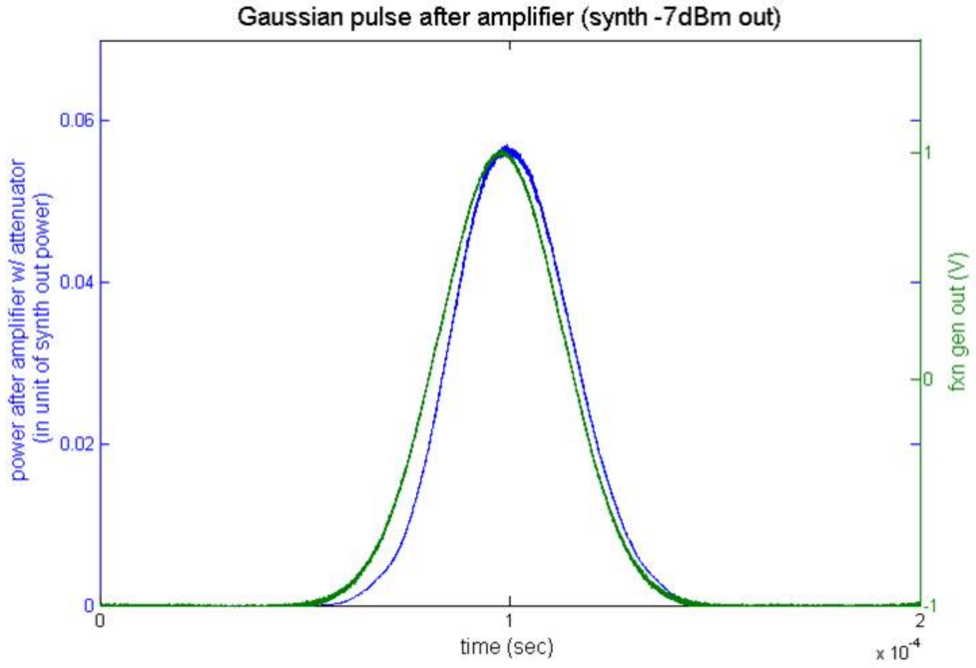

Figure 6.17: The gaussian envelope output from the function generator (green) and the signal after passing through a 10-watt microwave amplifier (blue).

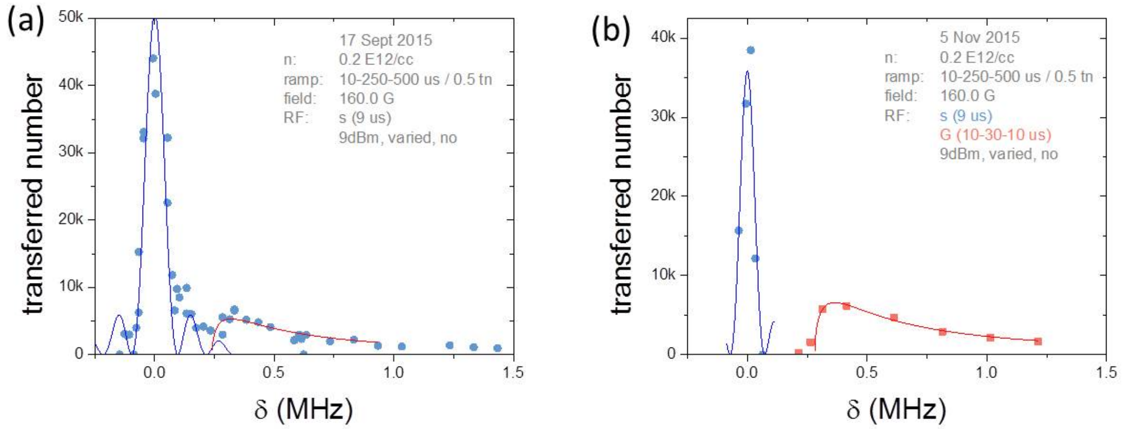

Figure 6.18: (a) The atomic and molecular lineshapes, both taken with a square microwave pulse. Because of the wide wings of the atom signal, it is difficult to see where the atom signal begins and the molecular signal begins, and the molecule signal is artificially increased by background atoms. (b) the atomic (blue circles) lineshape after a square microwave pulse and the molecular (pink squares) lineshape after a Gaussian microwave pulse. At large detunings from the atomic resonance, the Gaussian pulse does not transfer any atoms to the imaging state so we can clearly see the molecular signal go to zero at 2672.02 MHz, just below the Feshbach binding energy.

Figure 6.19 compares molecule data acquired by square and Gaussian microwave pulses as a function of the ramp rate out. We see very little difference in the data. The implications of molecular ramp out data is explored further in Chapter 7. More molecule data taken with Gaussian pulses can be found in Appendices F and G.

Because the molecular dynamics we wish to study occur on a fast time scale (order of 100 μs), the 300 μs pulse length of the Gaussian pulse makes it not ideal for molecule lifetime measurements. While we could truncate our Gaussian pulse to be shorter with only minimal effects to its width in frequency space, the Gaussian pulse does not provide enough power to saturate the molecule signal in a timely manner. Whereas the square pulse emitted full power for its entire duration, the Gaussian pulse emits full power for a small fraction of its duration. We therefore explore a second envelope that can emit more power, quickly, while still keeping frequency width low.

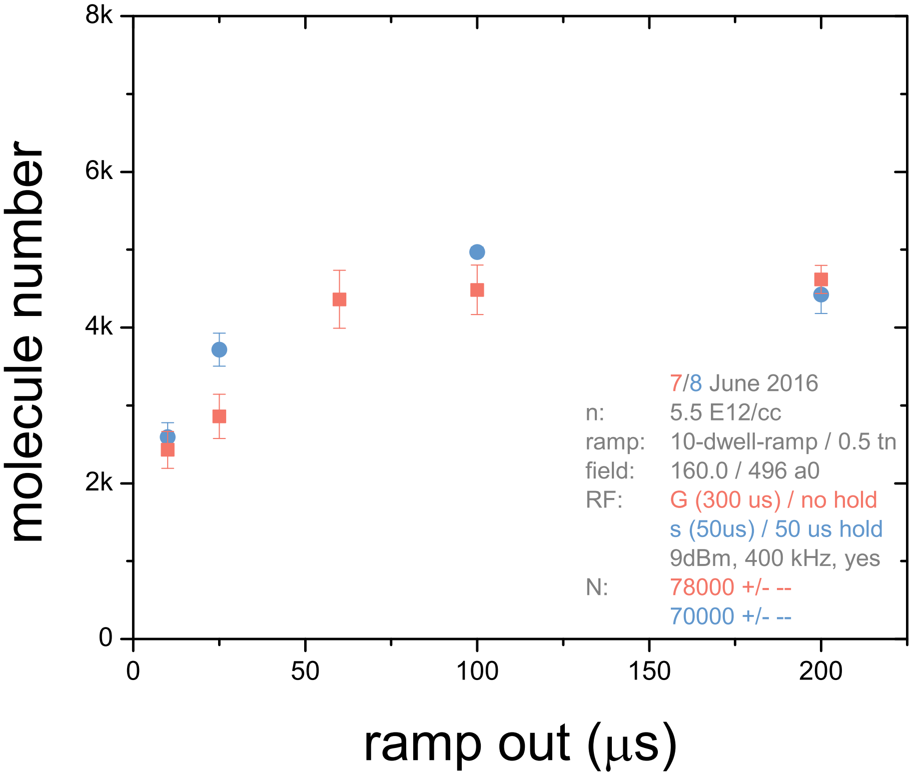

Figure 6.19: The molecule number as a function of ramp out rate after transfer to the imaging state by a square (blue circles) or a Gaussian microwave pulse (pink squares). There is very little difference between the two datasets.

6.3.2 Short curved pulses

A good compromise between the frequency-succinct yet temporally long Gaussian pulse, and the temporally-succinct yet frequency-wide square pulse, is a square pulse with curved edges. In this "curved pulse" the non-negligible duration of maximum power present in the square pulse is maintained by a flat top of maximum microwave power, yet the high-frequency components associated from the sharp, square edges are reduced, see figure 6.20(a).

The curved pulse envelope is based off the Blackman function:

$$B(t) = \frac{21}{50} + \frac{1}{2}\cos\left[\frac{\pi t}{\sigma}\right] + \frac{2}{25}\cos\left[\frac{2\pi t}{\sigma}\right]. \tag{6.7}$$

The corresponding instrument function is a sinc function divided by powers of σ up to σ^4:

$$\begin{aligned} F(\omega) &= \frac{1}{2\pi}\int_{-\infty}^{\infty} B(t)\mathrm{e}^{-i\omega t}\mathrm{dt} \\ &= \frac{a(0.84-0.36\sigma^2\omega^2)\,\mathrm{sinc}(2\pi\sigma\omega)}{(1-\sigma^2\omega^2)(1-4\sigma^2\omega^2)} \end{aligned} \tag{6.8}$$

[87]. The reduced frequency components of this function are ideal, however this function alone has a short peak, much like a Gaussian. For our purposes, we want to blast the molecules with maximum microwave power for a prolonged period in order to saturate molecule signal. We therefore defined our curved pulse envelope by the following piecewise function:

$$\mathrm{c}(t) = \begin{cases} A/10000 & \text{if } t < -(\tau_1+\tau_2)/2 \\ A\left(\frac{1}{2}\cos\left[\frac{2\pi(t-(\tau_1-\tau_2)/2)}{2} - 1\right] + 0.08\cos\left[\frac{2\pi(t-(\tau_1-\tau_2)/2)}{2} - 1\right] + 0.42\right) & \text{if } -(\tau_1+\tau_2)/2 \le t \le -\tau_2/2 \\ A & \text{if } -\tau_2/2 < t < \tau_2/2 \\ A\left(\frac{1}{2}\cos\left[\frac{2\pi(t-(\tau_1+\tau_2)/2)}{2} - 1\right] + 0.08\cos\left[\frac{2\pi(t-(\tau_1+\tau_2)/2)}{2} - 1\right] + 0.42\right) & \text{if } \tau_2/2 \le t \le -(\tau_1+\tau_2)/2 \\ A/10000 & \text{if } t > (\tau_1+\tau_2)/2, \end{cases} \tag{6.9}$$

where τ_1 and τ_2 define the rise (fall) time and persist time, A is the amplitude of the signal and $A/10000$ is effectively zero. We find that a rise time of 10 μs and a persist time of 30 μs transfers less than 1% of atoms to the imaging state for detunings $\geq$ 225 kHz (for 200 kHz, we set $\tau_1 = 15$ μs), this results in a full pulse length of 50 (60) μs. We record the times of curved pulses as (rise - persist - fall) time, e.g. the pulse described above is (10-30-10 μs).

Because this signal follows a piecewise function with a fast frequency rising time, we are unable to generate this amplitude envelope on our Agilent synthesizer. We instead generate the envelope as a voltage on a function generator (Agilent 33522A) and use a gain amplifier (ADL5330) to combine the synthesizer's microwave frequency with the curved voltage envelope. The amplifier has non-linear gain, especially at high power, that we must calibrate into our envelope. For a desired waveform voltage of c(t), the output of the amplifier is

$$0.28654 + 0.9441\mathrm{e}^{\frac{\mathrm{V(t)}-4.39056}{43.48201}} + 1.1326\cdot 10^{-7}\mathrm{e}^{\frac{\mathrm{V(t)}-4.39056}{0.27742}}, \tag{6.10}$$

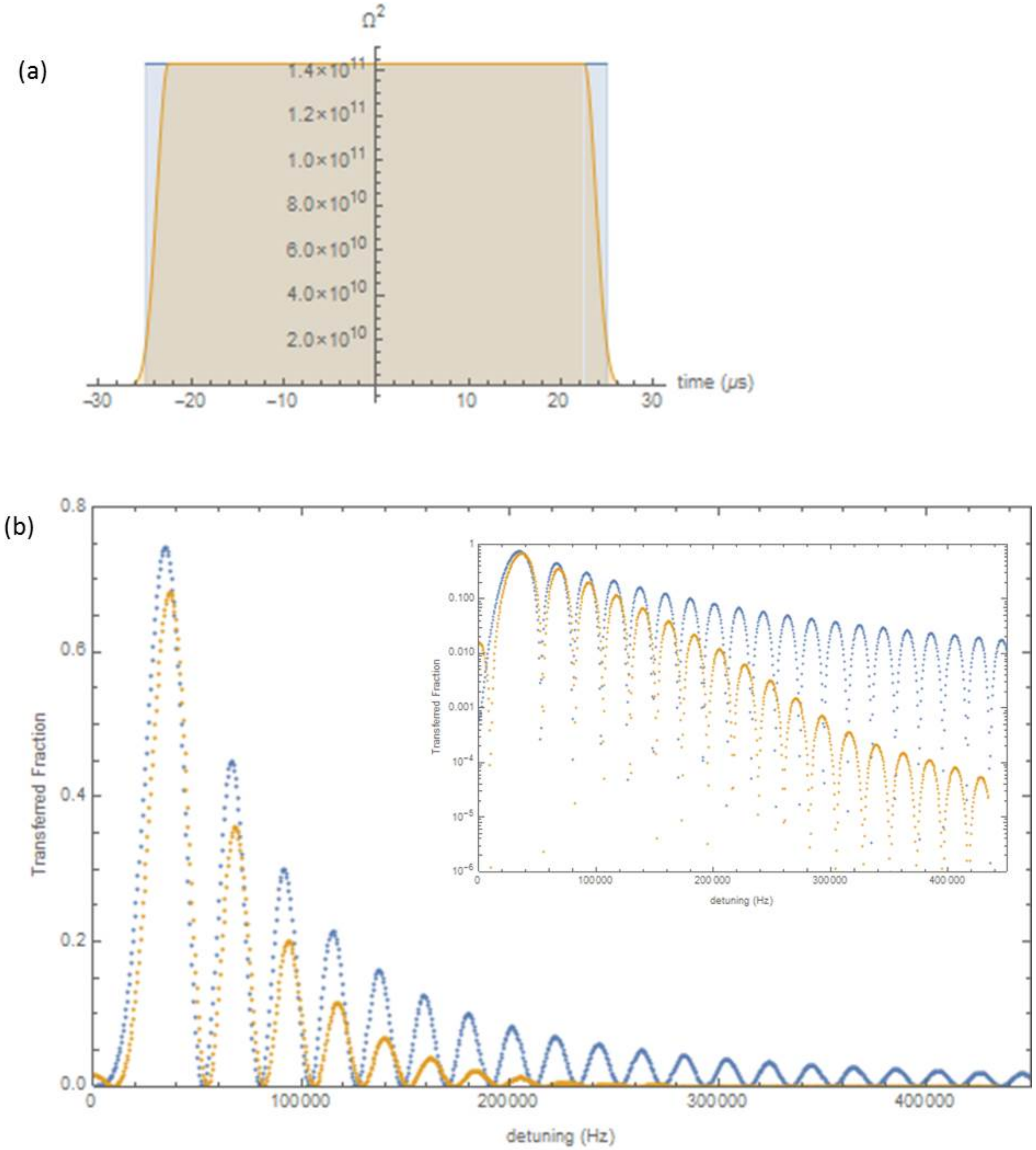

Figure 6.20: (a) Our curved pulse with an amplitude of for a (5-45-4μs) pulse (orange) compared to a 50 μs square pulse (blue). (b) The Fourier transform of our curved pulse (orange) compared to a square pulse (blue). The high frequency components of our curved pulse fall off much faster than that of a square pulse. The inset shows the same plot on a log scale, on which it is easier to see that the percentage of atoms of transferred with our curved pulse is only 1.5% at 200 kHz detuning, 0.1% at 300 kHz detuning, and 0.01% at 400 kHz. At this largest detuning this percentage corresponds to only 7 atoms, a significant decrease from the 700 atoms (1%) transferred with a square pulse.

where V(t) is the variable gain amplifier input voltage,

$$V(t) = 10 + 20\log(\mathrm{c}(t)). \tag{6.11}$$

Figure 6.21 compares molecule lifetime data taken with our curved pulse to that taken with a square pulse. The curved pulse has overall less number because, unlike the square pulse data, only a negligible number of atoms transfer to the imaging state. Without these field-sensitive atoms in the image background, the curved-pulse dataset also has greater signal to noise, resulting in smaller lifetime fit errors.

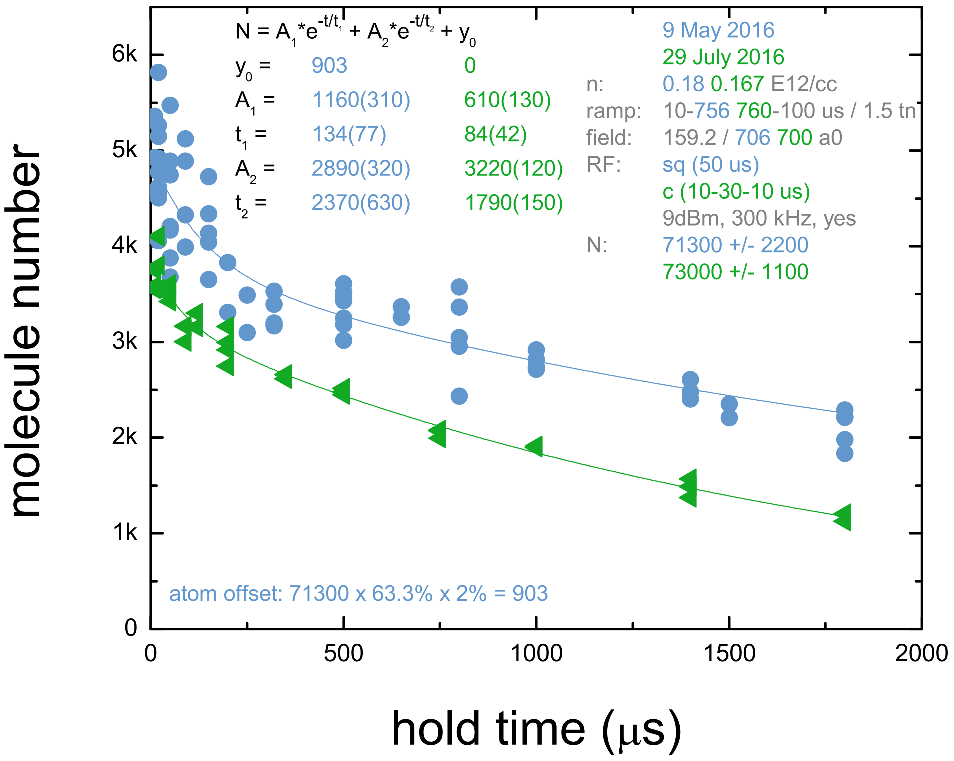

Figure 6.21: The number of molecules (and atoms) imaged after a (10-30-10 μs) curved RF pulse (green triangle) or a 50 μs square RF pulse (blue point) after a $t_{\mathrm{dwell}} = 1.5\, t_n$ evolution on resonance and ramp time = 100 μs to 700 a_0. Both datasets account for the falling cloud with frequency tracking. In addition to the molecules, there are about 900 atoms transferred to the imaging state for the square dataset.

6.4 Imaging settings for molecules

Once the molecules are spin flipped to the imaging state they are imaged using standard absorption imaging procedures. Because the optical depth of these clouds are usually lower than 2, high-intensity imaging is not needed.

Because we are not using high-intensity imaging, epsilon correction due to varying AOM power is not pronounced (see Chapter 3). We analyzed our molecule data by both (1) fast 2D Gaussian fits and (2) azimuthally averaging the 2D images then subtracting residual backgrounds, as outlined in Chapter 3. We did not see appreciable difference in the size or number of the molecule clouds, and therefore most of the remaining molecule data in this thesis is processed using 2D Gaussian fits.

Chapter 7

Molecule formation

Having realized the production of molecules, we now attempt to understand how these molecules are produced. In this chapter we will discuss a simple model to predict the number of molecules as a function of ramp out, then compare predictions to measurements. We will then discuss the more mysterious dependency on dwell time, for which we have no model. Finally we will discuss corrections and limitations to our model.

7.1 A simple ramp-out model

We present now a simple theory to explain the molecule production during the ramp back from resonance. This model is based heavily on the model developed by Altman and Vishwanath to describe the production of Feshbach molecules in Fermi systems when rapidly sweeping away from the Feshbach resonance [88]. Our system differs in that we are working with Bosons.

When applying this model to our system it is best to think of the resonant atoms as in a superposition of the two states present at unitarity, see figure 7.1. While the bound Feshbach state technically ceases to exist on resonance, this model assumes the existence of a higher momentum free atom state that we suppose is about 1 E_n higher in energy than the ground many-body state. These states are modeled as an avoided crossing.

The model supposes that fast sweeps across the resonance can be divided into two stages: a "sudden" stage and an "adiabatic" stage. The sudden stage is approximately an infinitely fast sweep, meaning that the initial state is simply projected onto the final state; during this stage the

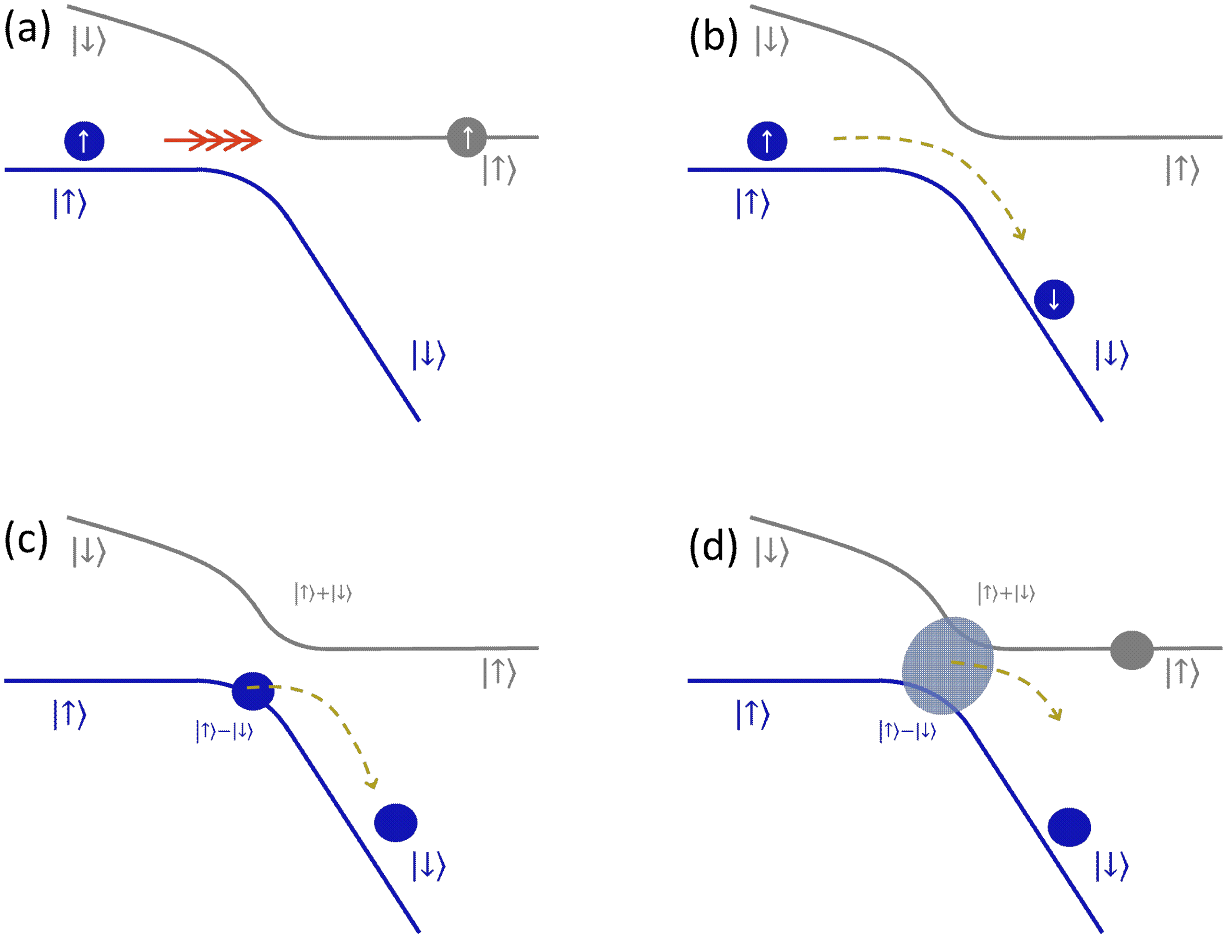

Figure 7.1: We can use an avoided crossing metaphor to explain molecular formation. We have two states, gray and blue, whose avoided crossing switches their spins; in thos metaphor, the right side of the spin up and spin down states represent our free atom and bound molecule states. (a) For an infinitely rapid jump that begins from the spin-up blue state, the system hops across the avoided crossing and maintains in the spin-up configuration. (b) A gradual adiabatic change allows the system to adapt its spin such that it can remain in the blue state. (c) If we now begin in the blue state near the avoided crossing, we begin in a superposition of spin up and spin down. An adiabatic ramp away from the avoided crossing would allow the state to adapt to spin down and remain in the blue state. (d) If we begin in a superposition of both the gray and blue states on resonance, an adiabatic ramp away from the avoided crossing would separate the cloud into blue and gray states. Likewise, a sudden jump away from the avoided crossing could result in the entire system projecting onto only the blue or gray state, depending on the phase of the superposition.

resonance wave function is projected into molecular and atomic components. Our ramp is in the adiabatic stage after $\dot{E}_\mathrm{b} < E_\mathrm{b}^2$ (E_b is defined in equation 2.9); during this stage the projected atoms and molecules are simply dragged to the final B field value, see figure 7.2.

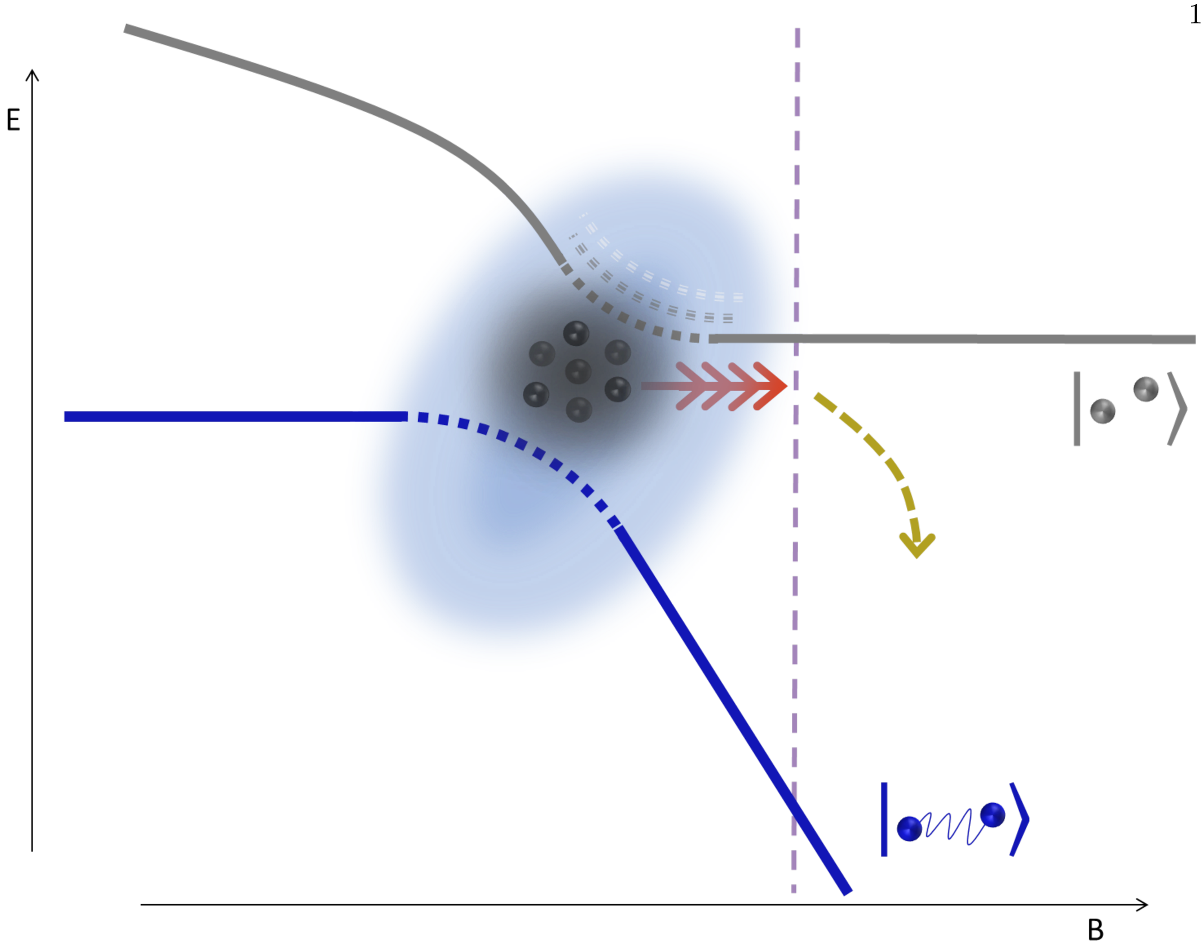

Figure 7.2: Our resonant condensate may be in a superposition of a ground and excited energy state which translate into the free atom and molecular bound state at larger magnetic fields. The ramp away from resonance is at first sudden but becomes adiabatic at $B(a_*)$, represented by the dashed line. The two-state superposition model is an oversimplification of our actual system, as there are more unbound states present on resonance. And we will discuss later how not all the resonant atoms seem to be in a superposition of the bound and unbound states, i.e. only some atoms have the propensity to be swept into molecules.

The scattering length at which the sweep converts from sudden to adiabatic is a_*, defined by $\dot{E}_\mathrm{b}(a_*) = E_\mathrm{b}^2(a_*)$. In [88], they make the linear assumption $a(B) = \frac{\alpha}{B-B_0}$, where $\alpha = \frac{mg^2}{4\pi\Delta\mu}$, g is the coupling between open and closed channels and Δ_μ is the difference in magnetic moment between the open and closed channels. This linear approximation is valid near the resonance, where α is approximately 4000 a_0 G. With the linear assumption of a, a_* becomes

$$a_* = \left(\frac{\alpha\hbar}{4m\dot{B}}\right)^{1/3}. \tag{7.1}$$

We see that the value of $a_* \propto (\dot{B})^{-1/3}$. This means that for a constant Δ_B, a longer ramp time yields a larger value of a_*, see figure 7.3. We assume a linear ramp speed of $\dot{B} = (5/4)\Delta_B\ /r_{\text{out}}$. We multiply this ramp rate by 5/4 for reasons explained in Chapter 5.

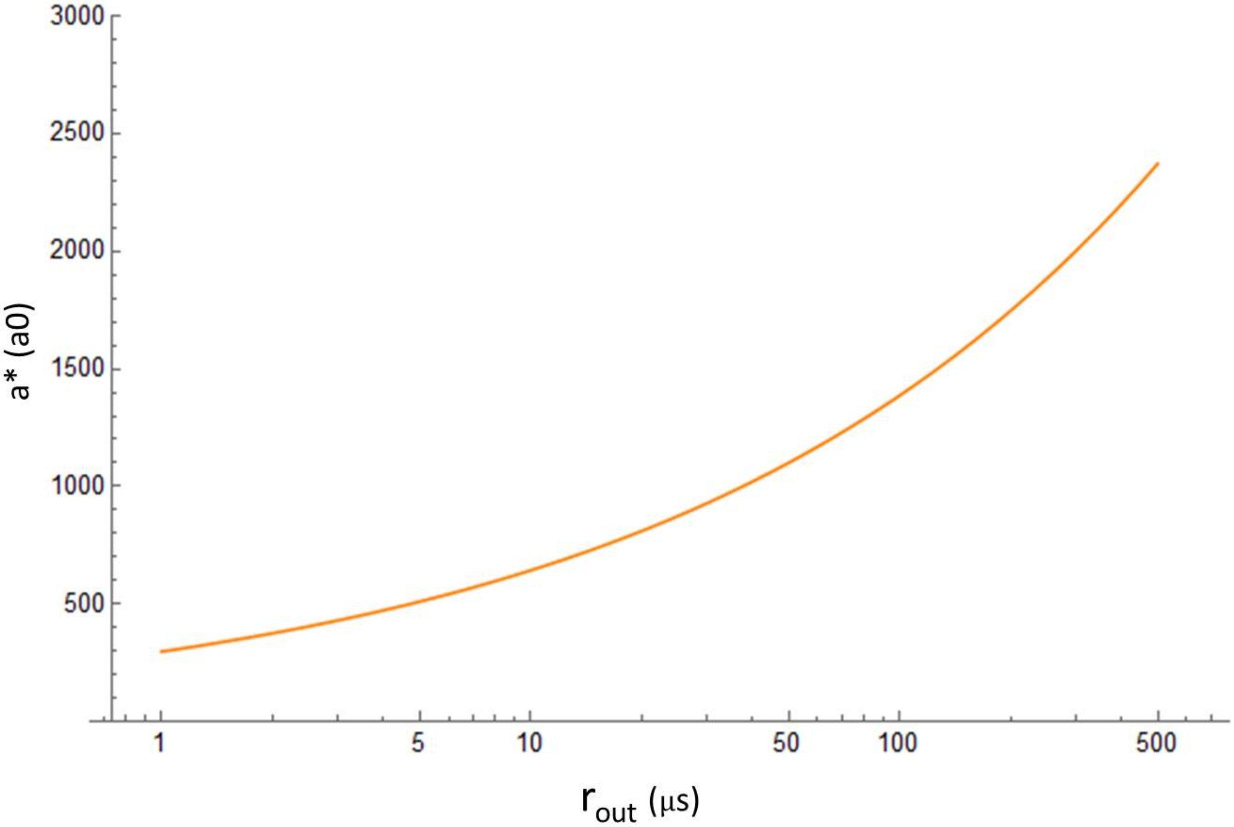

Figure 7.3: Calculations of a_* assuming a linear approximation of a(B), as a function of ramp time for constant Δ_B (because we define ramp time in relation to $B - B_0$, the actual value of Δ_B does not change this plot). a_* is larger for slower ramp times, indicating that a greater percentage of the total ramp time is adiabatic.

The sudden approximation theory dictates that the number of molecules formed is equal to the initial resonance wave function projected onto the wave function at a_*. If we assume that the wave functions are of $\mathrm{e}^{-r/a}/r$ form, the number of molecules projected is then

$$N_{\mathrm{mol}} = \frac{N}{2} \int \frac{1}{\sqrt{2\pi a_*}} \frac{\mathrm{e}^{-r/a_*}}{r} \cdot \frac{1}{\sqrt{2\pi a'}} \frac{\mathrm{e}^{-r/a'}}{r} \cdot 4\pi\, r^2 \,\mathrm{d}r, \tag{7.2}$$

where a' represents the interactions on resonance that are currently unknown. This integral simplifies to

$$N_{\mathrm{mol}} = \frac{N}{2} \frac{2\sqrt{a_*}\sqrt{a'}}{a_* + a'}. \tag{7.3}$$

If $a' \gg a_*$, as is true for very fast ramps, this simplifies further to $4a_*/a'$.

If we assume universal scaling with density in our resonant condensates, we can then suppose that the size of the molecule-like state on resonance is proportional to the inverse of universal momentum κ_n such that

$$a' = s(6\pi^2 n)^{-1/3}, \tag{7.4}$$

where s is a scaling factor that we will for now set to 1. The predicted $n^{-1/3}$ dependence in a' translates into density dependence of N_{mol}, see figure 7.4.

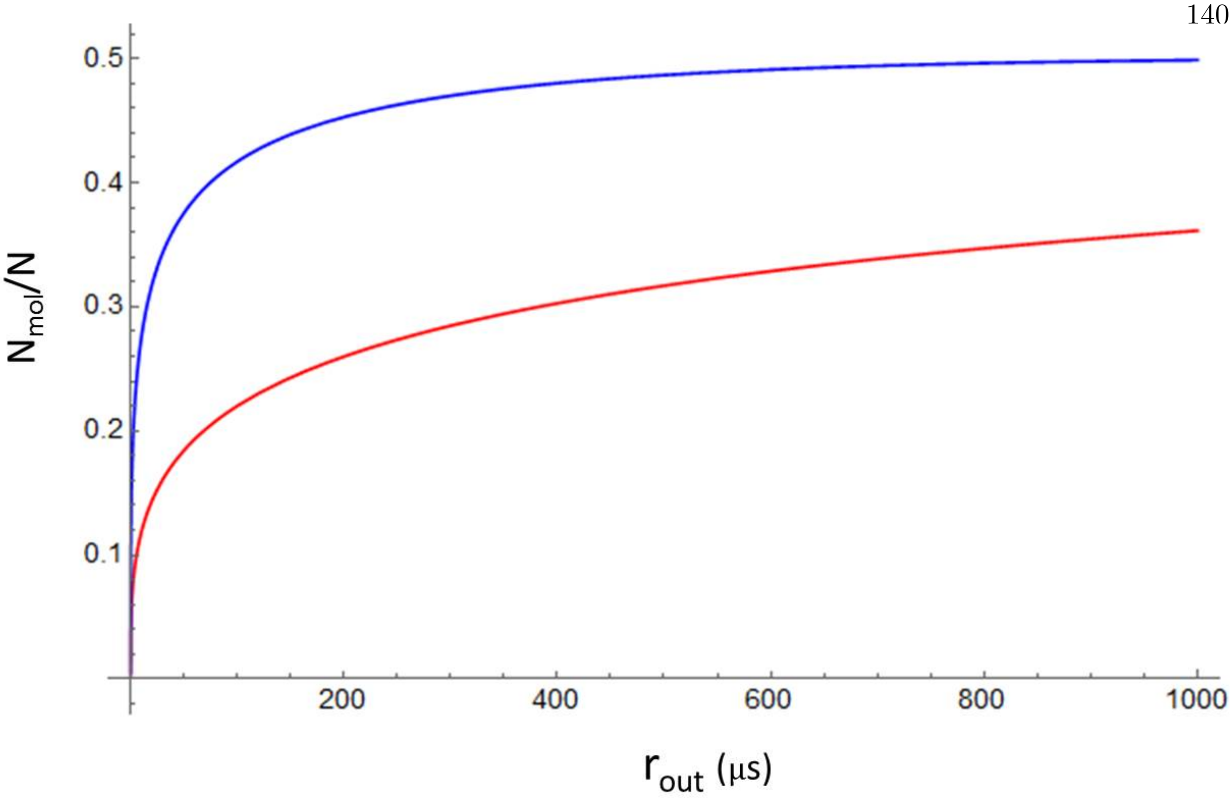

Figure 7.4: The calculated fraction projection of molecules, N_{mol}/N, equation (7.3), as a function of r_{out} for constant Δ_B. The modeled clouds have initial densities of 0.2 (red) and 5 (blue) E12/cc, using equations (7.1) and (7.4).

7.2 Data

7.2.1 Molecule number vs r_{out}

We measured the number of molecules as a function of r_{out} for clouds of initial densities of 5.5 and 0.18 E12/cc after spending $t_{\mathrm{dwell}} = 1.4\, t_n$ on resonance then ramping away to 160 G , see figure 7.5. The molecules were transferred to the imaging state by a long (300 μs) Gaussian-enveloped microwave pulse detuned 400 kHz from the atom resonance (see Chapter 6 for more information about microwave transfers). We fit this data by eye (no χ^2) with equation (7.3) (assuming equation (7.4) to be true) and including a proportionality factor of C_{fit}. We find that the data are well described by this equation when $C_{\mathrm{fit}} = 0.1$, meaning that about 10% of the resonant atoms have the propensity to be swept into molecules, or 90% of the atoms are not in the superposition resonant state of our rough model in figure 7.2. This data therefore serves as good evidence for universal scaling with density at unitarity.

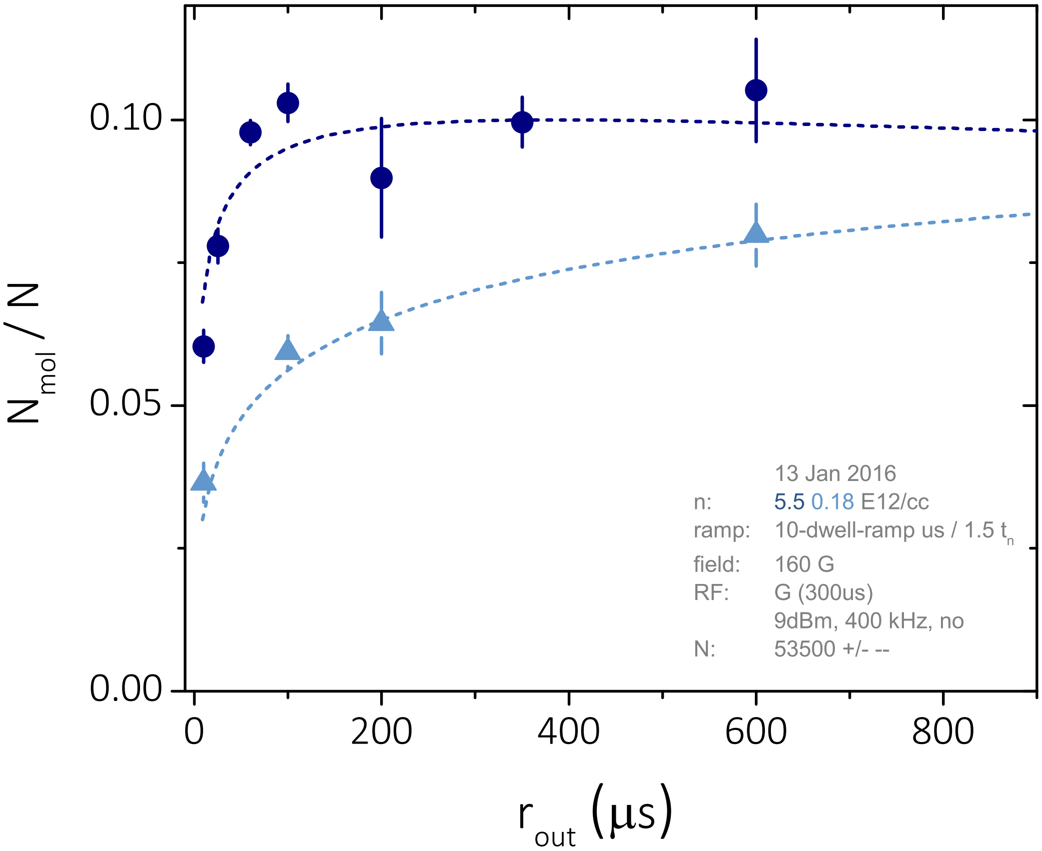

Figure 7.5: The fractional number of molecules, N_{mol}/N, measured after $t_{\mathrm{dwell}} = 1.5\, t_n$ on resonance and a ramp away to 160 G at various r_{out} rates, for initial densities of 5.5 (dark blue points) and 0.18 (cyan triangles). The dashed lines are equation (7.3) combined with equations (7.1) and (7.4) including a proportionality factor of 0.1. We see good agreement between the predictions and data, this encourages not only our application of the superposition ramp-out model but also our assumption of universal scaling with density to predict a'. The abbreviated legend in the bottom right is explained in Appendix A.

While the projection model predicts that 100% of the atoms can be swept into molecules (such that N_{mol}/N saturates to 50%, see figure 7.4), we saw our molecule signal saturate at only 10% (see figure 7.5). This begs the question of whether the time on resonance affects the propensity of the atoms to be swept into the molecule state. Unfortunately, not all data is as agreeable with our universal arguments. Ramp out data of $t_{\mathrm{dwell}} = 0.5\, t_n$ (all other experimental settings unchanged) is plotted in figure 7.6. The dashed lines are the same as in figure 7.5, using equation (7.3) and assuming equation (7.4) to be true, with $C_{\mathrm{fit}} = 0.1$. While we expect to see a change of C_{fit}, we instead find that the number of atoms projected into the molecular state no longer varies with density as expected. This indicates that the interactions on resonance are not fully explained by our simple approximation in equation (7.4) and perhaps evolve on resonance in a not fully density-universal manner. This strange behavior is explored further in Chapter 9.

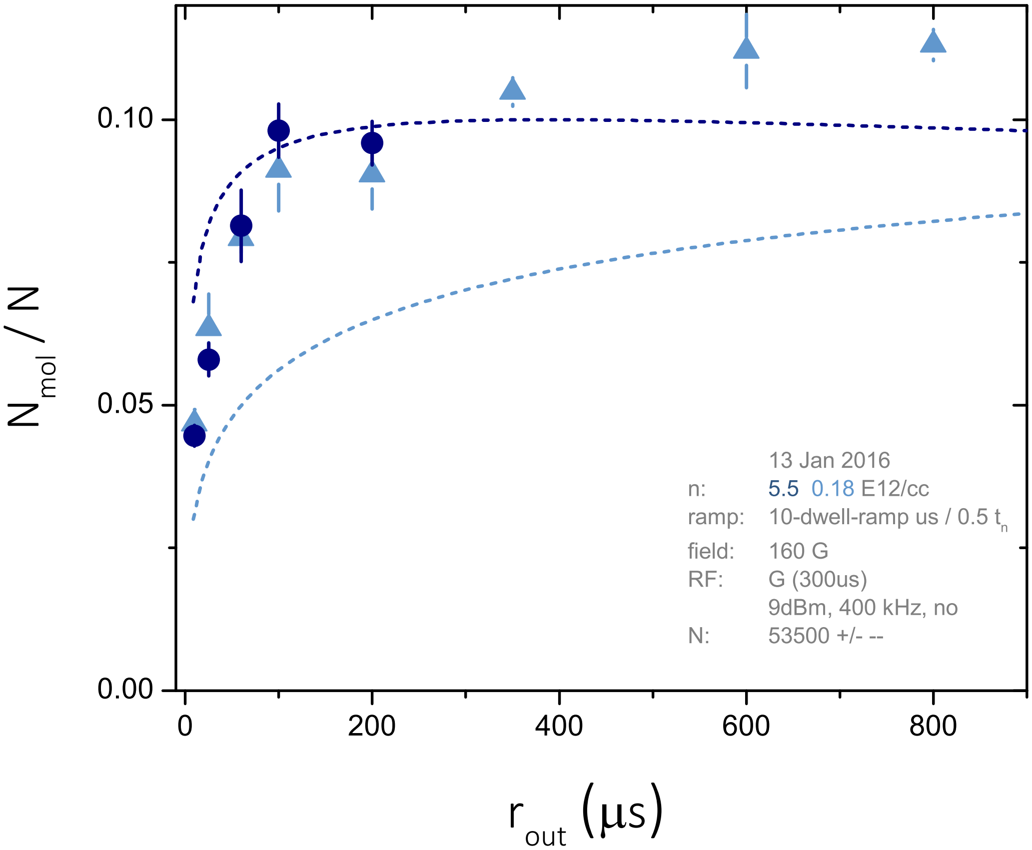

Figure 7.6: The fractional number of molecules, N_{mol}/N, measured after $t_{\mathrm{dwell}} = 0.5\,t_n$ on resonance and a ramp away to 160 G at various r_{out}, for initial densities of 5.5 (dark blue points) and 0.18 (cyan triangles). The dashed lines are the same predictions plotted in figure 7.5. We see that the projected number of molecules no longer varies with density in the expected manner consistent with universal scaling with density. This indicates that the interactions on resonance are not fully explained by our simple assumption of equation (7.4).

7.2.2 Comparing atom loss with molecule formation

From our ramp-out data we reach the unfortunate (but interesting?) conclusion that molecules are produced even for our fastest ramps away from resonance. The resonant atom loss data in Chapter 5 is therefore not purely loss during resonance, but a sum of atom loss to deeply bound dimers while on resonance and atom loss to shallow dimers during the sweep to weak interactions. While we cannot quantify the percentage of atom loss due to the shallow dimer production with an exact number, we can estimate an upper limit.

We measured the number of molecules produced out of an N = 73800 ± 4300 condensate after $t_{\mathrm{dwell}} = 1\, t_n$ on resonance and $r_{\mathrm{out}} = 10$ μs to 160 G. About 2983 ± 33 molecules formed out of an initially low density cloud ($n = 0.208$ E12/cc) and 2791 ± 173 molecules form out of a standard density cloud ($n = 5.78$ E12/cc). This corresponds to 8.1 and 7.6 % of the atoms in the low and standard density clouds being swept into shallow dimers. The atom loss reported in Chapter 5 ($r_{\mathrm{out}} = 5$ μs to 163 G) between $n = 0.211$ and $n = 0.302$ E12/cc had an average loss of 17.6 %, while data at $n = 3.07$ and $n = 6.03$ E12/cc had an average loss of 15.85%.

Comparing the 10 μs molecule ramp to the 5 μs atom ramp over-estimates the percentage of atoms swept into the molecular states. This data is also skewed by the different Δ_B (5 G for molecule data, 8 G for atom data), which affects the extent of the linear regime of the magnetic ramp, see equation (5.1). However, from this comparison we can estimate that up to 46 and 48 % of the atom loss observed in the low and standard density clouds was due to ramping molecule formation - i.e. nearly half of the atom loss was to shallow dimers! This number is large not because N_{mol} is large, but because the amount of atom loss is low. We expect this percentage to vary with dwell time both because the atom loss increases with dwell time, and because the number of molecules also varies significantly.

7.3 Dwell time dependencies

As was discussed in section 7.2.1, our simple sweep model cannot explain how the propensity of atoms to be swept into molecules is influenced by the evolution on resonance. To explore this experimentally, we measured the number of molecules produced by a $r_{\mathrm{out}} = 50$ μs to 160 G after various dwell times on resonance, see figure 7.7. We found that the number of molecules first increases with dwell time, indicating that the propensity to be swept into molecules is a feature that evolves on resonance, possibly at a universal density rate that scales with t_n. At longer dwell times however, the number of molecules begins to fall. Unlike the formation rate, this decay rate does not appear to scale with t_n, but is rather constant in absolute time units. It is unclear from this data whether this drop in molecule number arises from decay of dimer-prone resonant atoms to deeply bound states, or from the dimer-prone atoms evolving back into atoms that are not dimer-prone. While corresponding returned atom data never showed an upswing of atoms that would support the latter hypothesis, there was a flattening in the decay rate at similar times that was suspiciously close to, yet ultimately below our signal to noise, see figure 5.25.

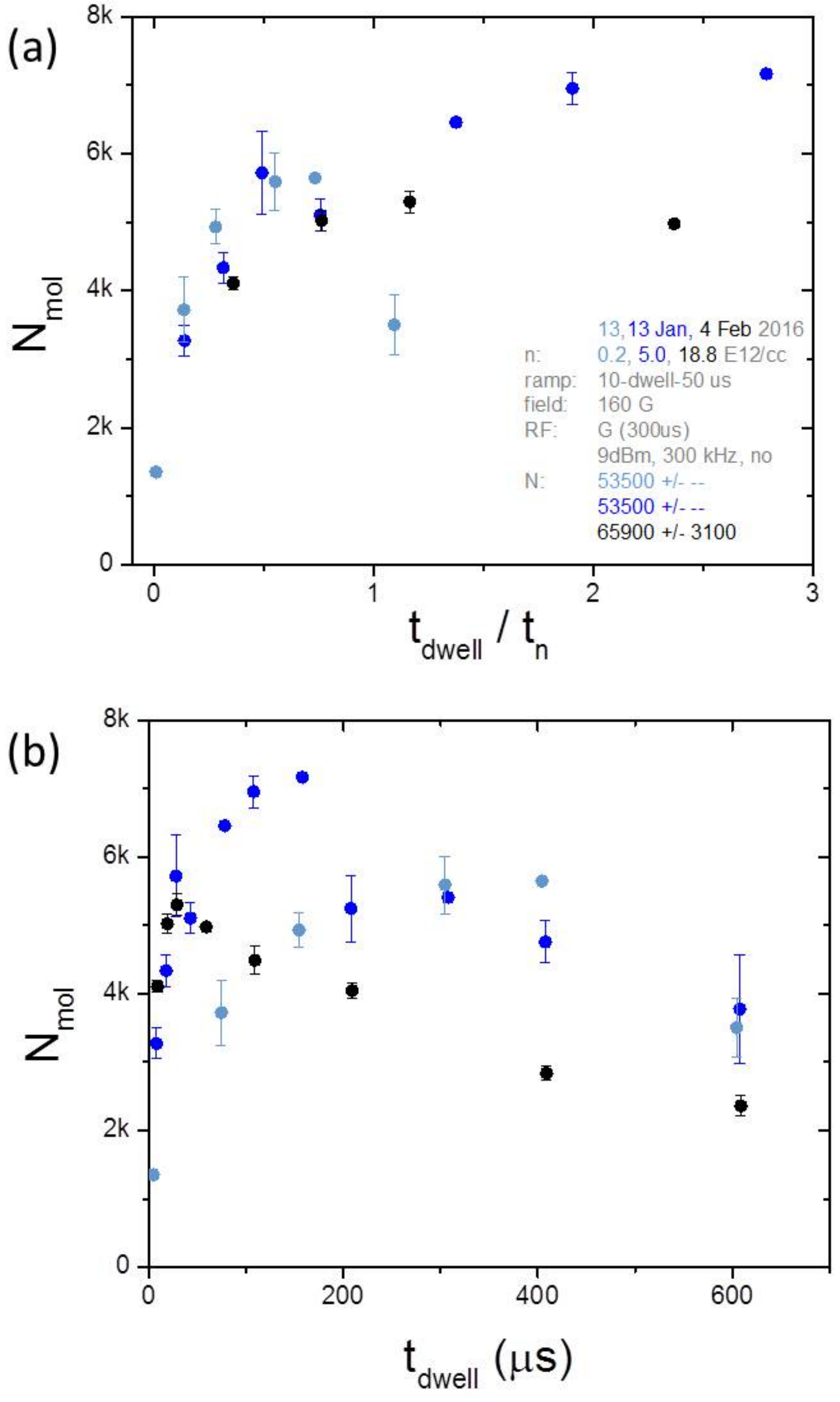

Figure 7.7: The molecule number produced after a resonant cloud of n = 0.2 (cyan), 5 (blue), and 18.8 (black) E12/cc is ramped to 160 G at $r_{\text{out}} = 50$ μs, as a function of dwell time on resonance. (a) The data plotted in universal units of t_{dwell}/t_n. (b) The same data plotted in absolute time units. The number of molecules first increases with dwell time at universal rate, but later decreases at a rate independent of density.

7.4 Corrections to the ramp-out model

Disregarding how the resonant wave function changes with dwell time, we focus again on the simple sweep model, specifically on corrections to this theory. We focus first on a simple correction to $a(B)$, and then explore more complicated corrections for $a(t)$ that ultimately conclude that a new ramp, $B(t)$, may be necessary.

7.4.1 a is not linear with B

When first discussing our ramp-out model, we made the assumption that $a(B)$ was linearly related by $\frac{\alpha}{\Delta_B}$. If we instead use the non-linear $a(B) = a_{\mathrm{bg}}\,(1 - \Delta/\Delta_B)$, where Δ with the width of the Feshbach resonance, we derive a new formula for a_*:

$$a_*^3 - 2a_{\mathrm{bg}}\,a_*^2 + a_{\mathrm{bg}}\,a_* = \frac{\hbar\Delta a_{bg}}{2m}\frac{1}{\dot{\Delta}_B}. \tag{7.5}$$

This corrected equation for a_* yields smaller values of a_* for the same r_{out}, see figure 7.8. The lower values of a_* in turn yield a lower overall projection number, as well as slower saturation times and an overall larger discrepancy between different densities, see figure 7.9.

Another correction, that is not explored in this thesis but is worth mentioning, is including the finite-range shift of E_{b} [89].

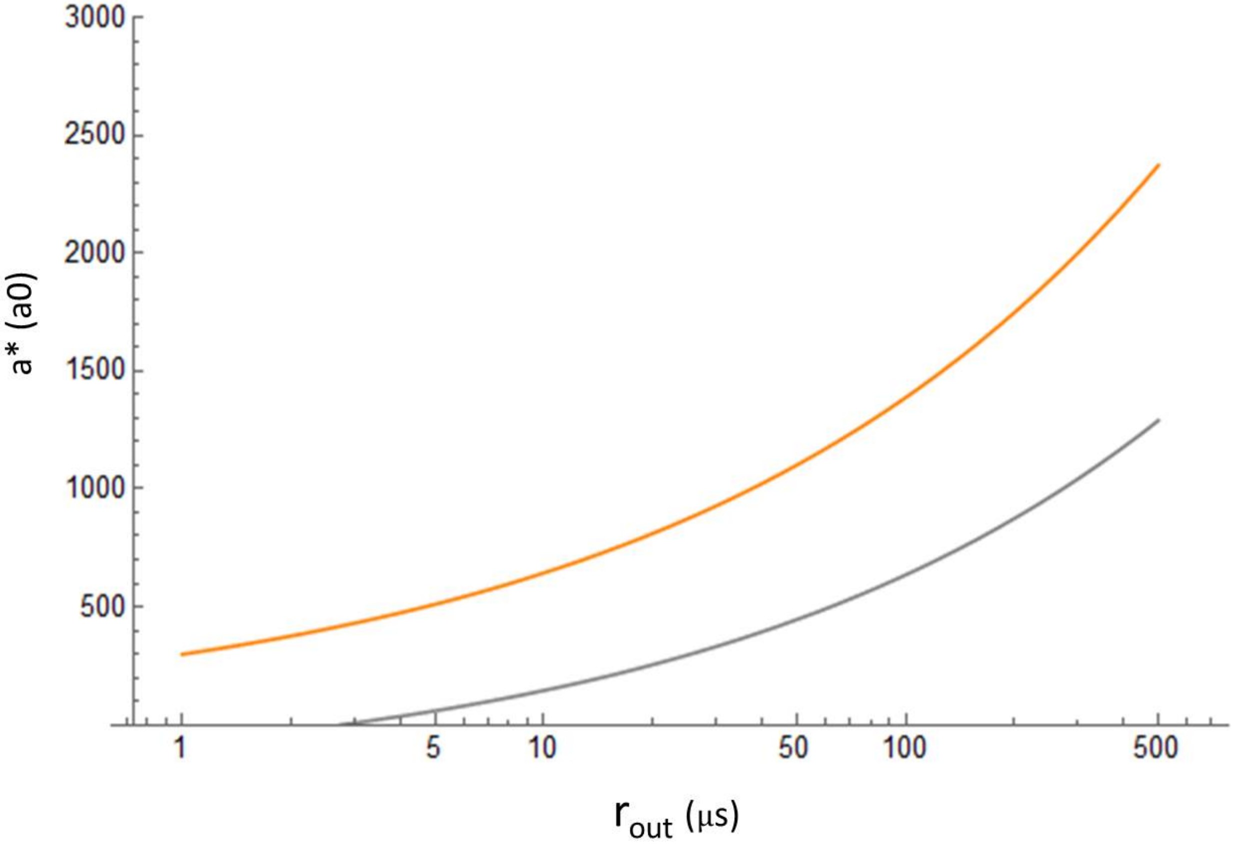

Figure 7.8: The calculated a_* as a function of r_{out} for constant Δ_B, assuming a linear $a(B)$ approximation (orange) given by equation (7.1), or a more accurate $a(B)$ relation (gray) given by equation (7.5). The latter has lower values of a_*, meaning that more of the total ramp time is adiabatic, and therefore predicts that less atoms will be swept into the shallow molecule state.

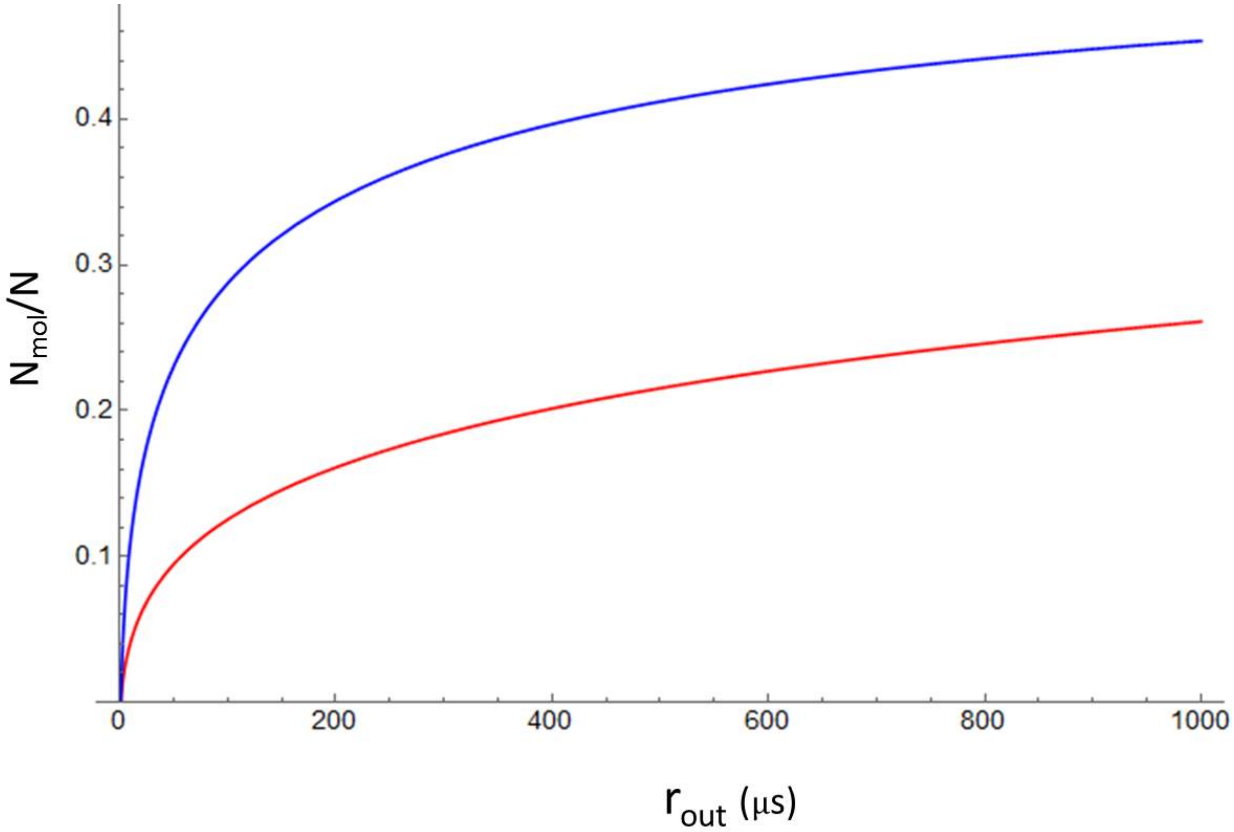

Figure 7.9: The fractional projection of molecules, N_{mol}/N given by equation (7.3), as a function of r_{out} for constant Δ_B and clouds of initial densities 0.2 (red) and 5 (blue) E12/cc, using equation (7.4) and (7.5). Note that for $r_{\mathrm{out}} < 50\mu$s, the calculated a_* is less than 500 a_0, meaning that our simple model has broken down.

7.4.2 Non-linearities in B(t)

In Chapter 5 we discussed the actual shape of our magnetic ramp, $B(t)$. Most importantly, we discussed how the linear regime of $B(t)$ exists only between 0.125 and 0.875 Δ_B. This is important now because we ramp our atom and molecule data out to different final values of B (for imaging reasons). Although we compensate r_{out} in order to keep the linear rate ($\dot{B}$) the same regardless of Δ_B, this does not properly correct $B(t)$ in the non-linear regime. For our fastest ramps, a_* can occur in the non-linear regime. The non-linear regime composes the first and last 12.5% of our magnetic ramps. When ramping from resonance to 163 G, as we do when imaging atoms, this means that only between 4560 and 240 a_0 is the ramp linear. This constrains our minimum r_{out} to only 20 μs to keep a_* in the calculable linear regime, or about 4 times slower than our maximum speed. (Note: this maximum speed was calculated using equation (7.5), if we assume the linear approximation of equation (7.1), then the minimum r_{out} is extended to a non-constraining 0.5 μs). However, when ramping to 160 G, as we do when imaging molecules, the ramp is linear only between 7040 and 650 a_0, which constrains our minimum r_{out} to only 105 μs!

It is very difficult to extract the dependency of a_* on r_{out} when $B(t)$ is non-linear. Moreover, the ramp-out model we use here is a simple approximation, and therefore changing our ramp rates to keep a_* at nearly the same value as we vary Δ_B to compare atom and molecule number is frivolous. We therefore conclude that the best course of action for further study of ramp out effects is to design a new ramp, $B(t)$, that better suits the needs of our system. We do not explore this option further in this thesis. For now, we shift our focus to the properties of the molecules that have been formed, regardless of the ramp out rate.

Chapter 8

Molecule lifetime measurements

8.1 Two-component decay

This chapter describes our studies of molecules created after spending $t_{\mathrm{dwell}} = 1.5\, t_n$ on resonance and ramping away at $r_{\mathrm{out}} = 100$ μs to a_f. We measure the lifetime by measuring the molecule number as a function of hold time at a_f. Figure 8.1 shows this number decaying at $a_f = 700\, a_0$ for clouds of two different initial densities, $n = 0.208$ and $n = 1.32$ E12/cc. Neither dataset can be described by a single exponential decay rate, as would be expected for a simple gas of Feshbach dimers. They instead fits well to a sum of two exponential decays:

$$A_1 \times \mathrm{e}^{-t/t1} + A_2 \times \mathrm{e}^{-t/t2}. \tag{8.1}$$

Spontaneous dissociation, such as spin relaxation into a lower spin state, would appear as a simple exponential decay in our data. Non-exponential decay would be present if there was also inelastic loss, such as molecule-molecule collisions. Such inelastic loss would be density-dependent, and would therefore be less pervasive at lower densities. Because figure 8.1 shows two-component loss where the fast component does not vary with density, despite the density varying by more than a factor of 6, we can safely conclude that this non-exponential loss is not due to inelastic loss mechanisms.

We investigated this loss further by measuring the molecular decay rates for more values of density and a_f; some of this data is shown in figure 8.2. When this data is analyzed by a two-exponent sum, the faster of the two loss rates is unchanged by both a_f and initial density. The

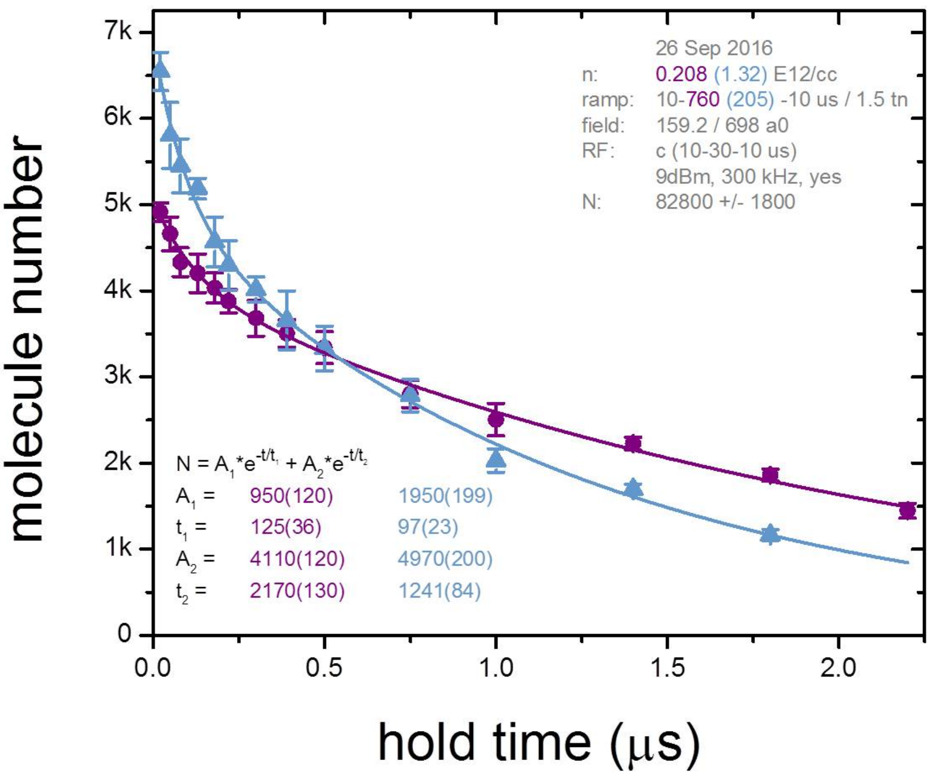

Figure 8.1: The molecule number measured as a function of hold time at $a_f = 700\ a_0$ for initial cloud densities of $n = 0.208$ E12/cc (purple points) and 1.32 E12/cc (blue triangles). This data is best fit by a sum of two exponentials, the fit values for each dataset are included in the lower left corner of the plot. The fast loss for each dataset is equal within error, while the slower loss of each dataset is slower in the lower density dataset. The abbreviated legend in the upper right is explained in Appendix A.

decay rate of the slower loss $(1/t_2)$, however, appears to decrease with larger a_f and increase with larger n. We will now investigate the dependencies of this slower loss.

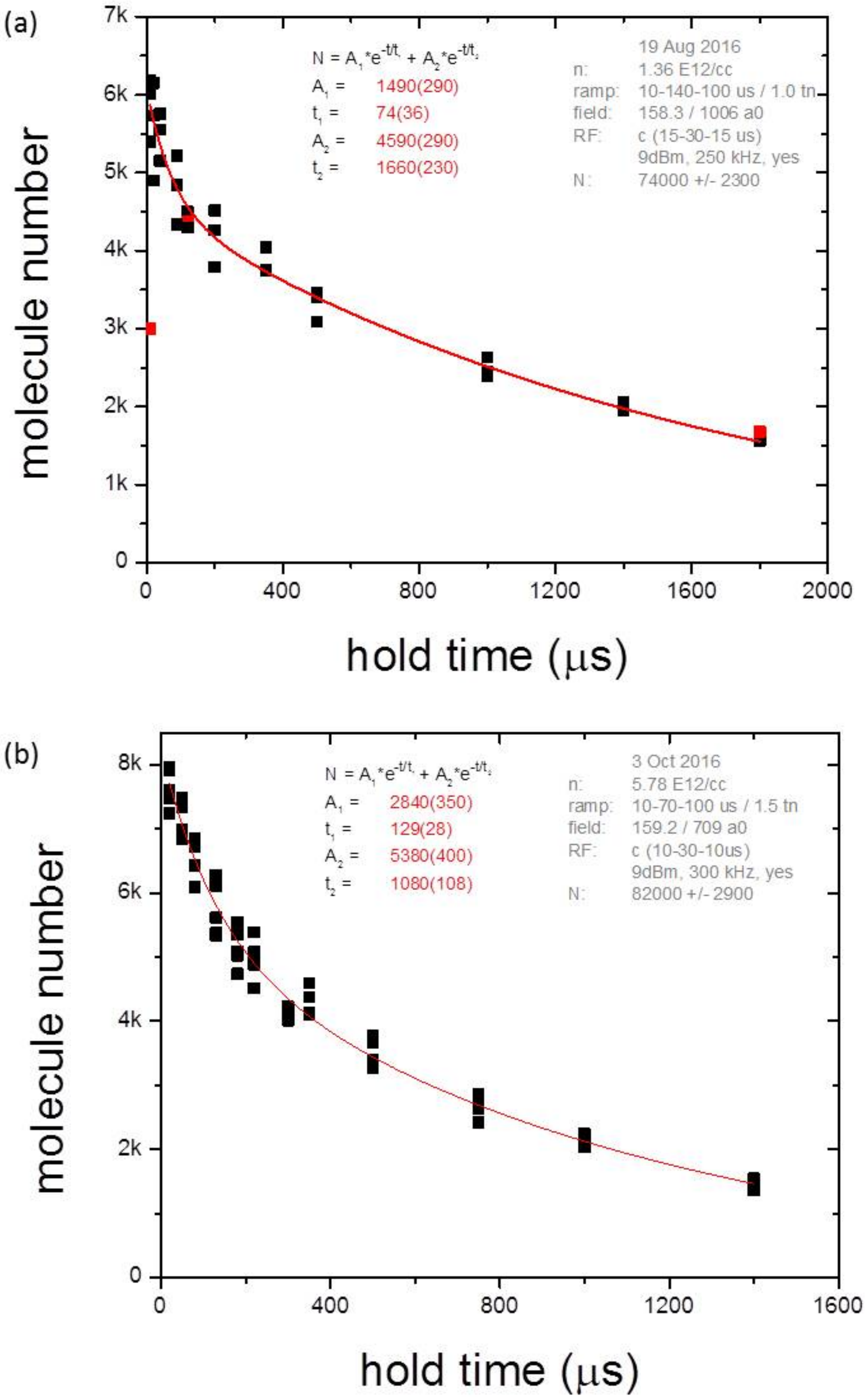

Figure 8.2: (a) The molecular loss from a $n = 1.32$ E12/cc cloud ramped out to $a_f =\sim 1000\,a_0$. Comparing the summed two exponential fit with that in figure 8.1 for the same same n, we see that the fast loss remains unchanged within error while the slower loss becomes even slower. (b) The molecular loss from a $n = 5.75$ E12/cc cloud ramped out to $a_f =\sim 700\,a_0$. Comparing this to the other $a_f = 700\,a_0$ datasets of different densities in the previous figure, the fast loss remains unchanged within error while the slow loss has a shorter lifetime at this higher density.

8.2 Dimers: the slow decay

8.2.1 Dimer lifetime predictions

At 700 a_0 the Feshbach molecules are bound by about 110 kHz in the $|2,-2\rangle$ state. These molecules can spontaneously dissociate via spin relaxation into the $|2,-1\rangle$ and $|2,0\rangle$ states [90], which are 79.62 and 75.49 MHz away, see figure 6.1. This lifetime due to this spontaneous dissociation varies with a_f but not density, and is calculated in [90] to be

$$\tau_D(B) = \tau_{\mathrm{res}} \frac{m\, a_{\mathrm{bg}}^2\, \mu_{\mathrm{res}}\, \Delta}{2\,\hbar^2} \left(\frac{B-B_0}{\Delta}\right)^2 \left(\frac{\Delta}{B-B_0} - 1\right)^3, \tag{8.2}$$

where a_{bg}, B_0 and Δ are all Feshbach resonance parameters defined in Chapter 2, $\mu_{\mathrm{res}}/h = 34.66$ MHz/mT and $\tau_{\mathrm{res}} = 32\,\mu$s. In terms of a_f, τ_D becomes:

$$\tau_D(a) = \tau_{\mathrm{res}} \frac{m\, a_{\mathrm{bg}}\, \mu_{\mathrm{res}}\, \Delta}{2\,\hbar^2} \frac{-a^3}{(a_{\mathrm{bg}} - a)^2}, \tag{8.3}$$

this decay rate is plotted in figure 8.3.

Density dependence is introduced into the predicted dimer lifetime by inelastic atom-dimer collisions. An atom-dimer scattering event occurs when an unbound atom collides with a shallow-bound Feshbach molecule, producing a deeply bound molecule and recoiling atom [66, 91]. This loss is enhanced by the presence of the three-body Efimov state, as it increases the probability for an atom to be near a dimer. This loss rate has been measured experimentally by many [58, 59, 57, 60], and is defined by the atom-dimer collisional rate coefficient, β, calculated in [92] to be

$$\beta(a) = \frac{20.3\, \sinh(2\eta_*)}{\sin^2\left[s_0 \ln(a/a_*)\right] + \sinh^2(\eta_*)} \frac{\hbar a}{m}, \tag{8.4}$$

where a_* is the scattering length at which the Efimov state intersects the atom-dimer threshold (creating a loss rate resonance), and η_* is the inelasticity parameter characterizing the width of the Efimov resonance at $a = a_*$. For ^{85}Rb, η_* was measured in [34] to be 0.057. a_* for the first-excited Efimov state was calculated in [66] to be $\sim 275\ a_0$.

The lifetime determined by the atom-dimer collisional rate is then

$$\tau_{\mathrm{AD}} = \frac{1}{n'\beta} \tag{8.5}$$

where n' is the adjusted density after calibrating for the atoms lost while on resonance. For $t_{\mathrm{dwell}} = 1.5\,t_n$, $n' = 0.7n$ for almost all densities. Because there are many more atoms than molecules in our system, the fractional atom loss is small and n' therefore remains nearly constant during hold time; this makes the density-dependent inelastic loss appear as a simple exponential decay in our systems. This loss rate is plotted in figure 8.4 as a function of adjusted cloud density, n'.

We can now define our total predicted lifetime, defined by the inverse of the loss rate, by combining the collisional and spontaneous decay rates:

$$\frac{1}{\tau_{\mathrm{Total}}(a,n)} = \frac{1}{\tau_{\mathrm{D}}(a)} + \frac{1}{\tau_{\mathrm{AD}}(a,n')}. \tag{8.6}$$

This combined inverse loss rate is plotted as a function of a_f for three *initial* densities in figure 8.5.

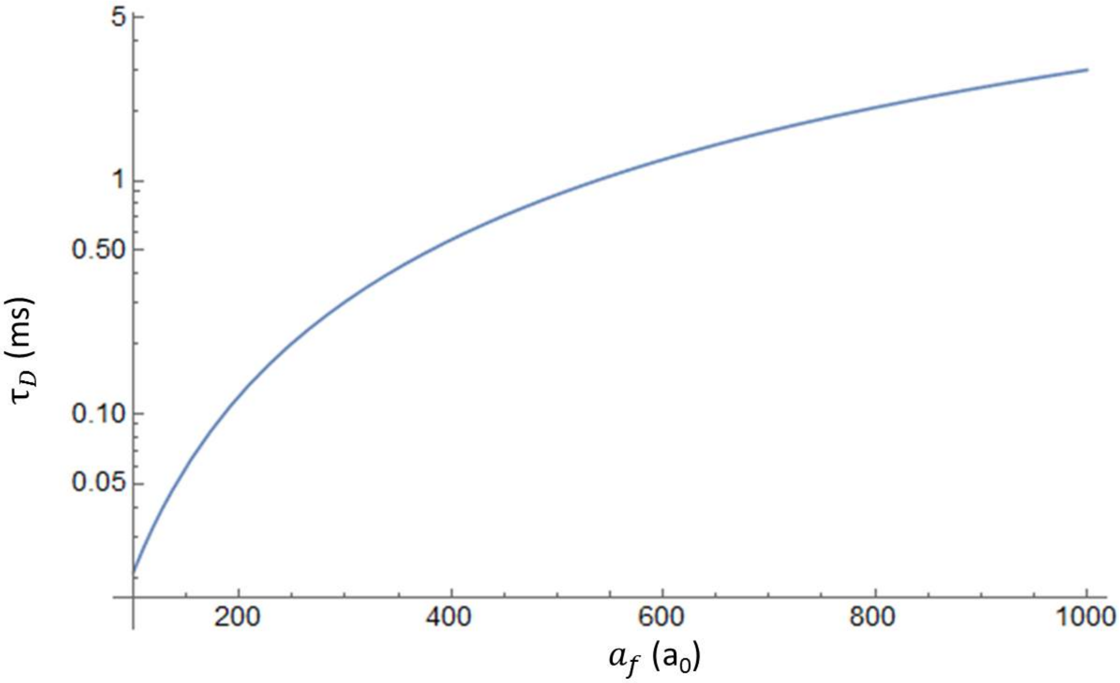

Figure 8.3: The dimer lifetime considering only loss due to spontaneous dissociation into the lower spin state as a function of a_f.

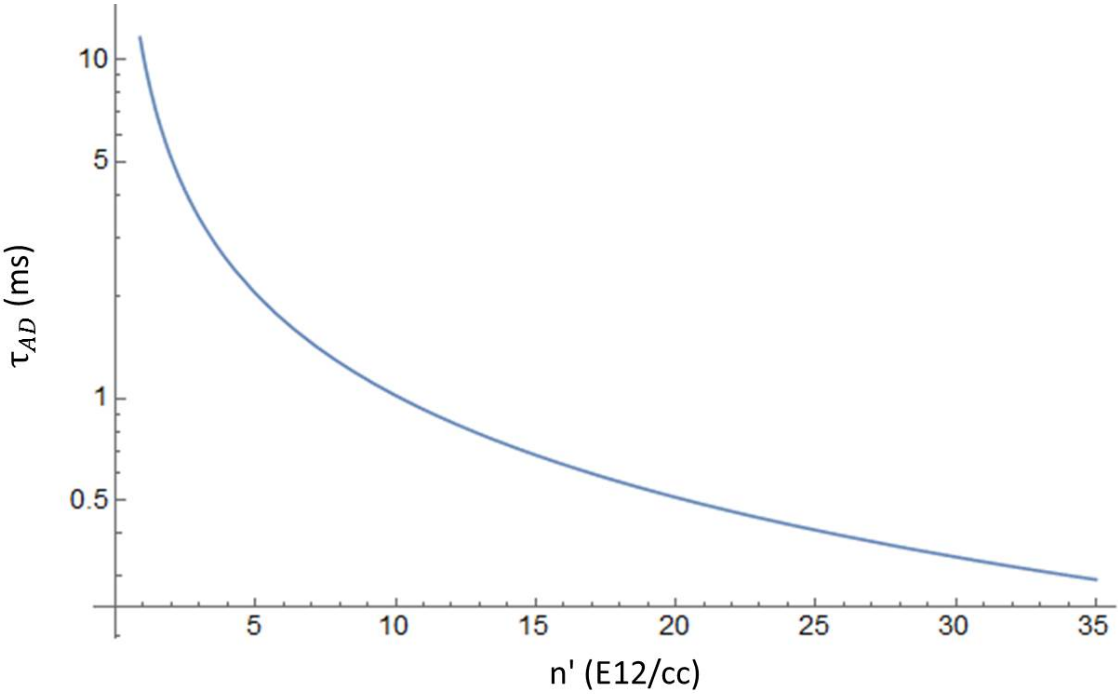

Figure 8.4: The dimer lifetime considering only loss due to inelastic atom-dimer collisions as a function of density, for $a = 700\,a_0$.

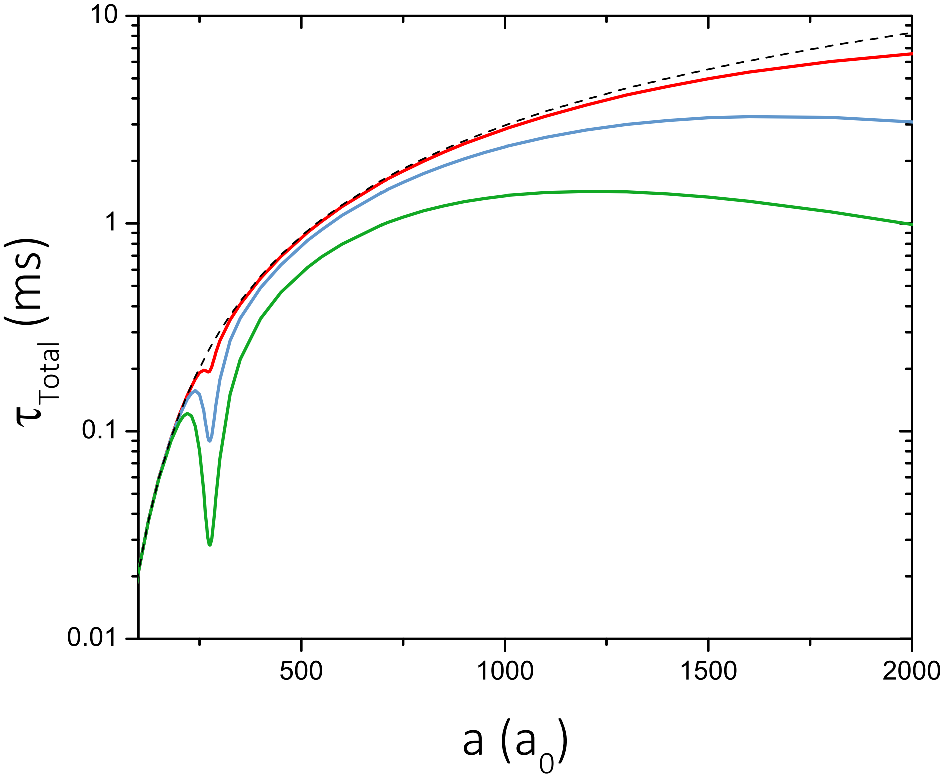

Figure 8.5: The total predicted dimer lifetime considering both spontaneous dissociation and inelastic atom-dimer collisions for atom+molecule clouds of initial density $n = 0.2$ (red), 1.3 (blue) and 5.8 (green) E12/cc. The dashed line represents the dimer lifetime predicted by spontaneous dissociation only. The lowest density curve follows the lifetime set by spontaneous dissociation because it is the least influenced by atom-dimer collisions. We that at $a_f \sim 275\,a_0$ the lifetimes decrease dramatically due to the atom-dimer collision resonance near $a*$. At larger scattering lengths we see the total lifetime again begin to decrease, this is due to the next atom-dimer collision resonance located at $22.7 \times a_*$.

8.2.2 Dimer lifetime measurements

We measured the slower lifetimes of our molecular gas at $a_f =\sim 1000\,a_0$, 700 a_0, and 500 a_0 and $n =\sim$ 0.2, 1.3, and 5 E12/cc. The raw data measurements can be found in Appendix B and the slower fitted lifetimes from this data are plotted in figure 8.6. We see qualitative agreement between our lifetime measurements and the predicted dimer lifetime, we therefore conclude that this slow loss represents the lifetime of the Feshbach dimers in our system.

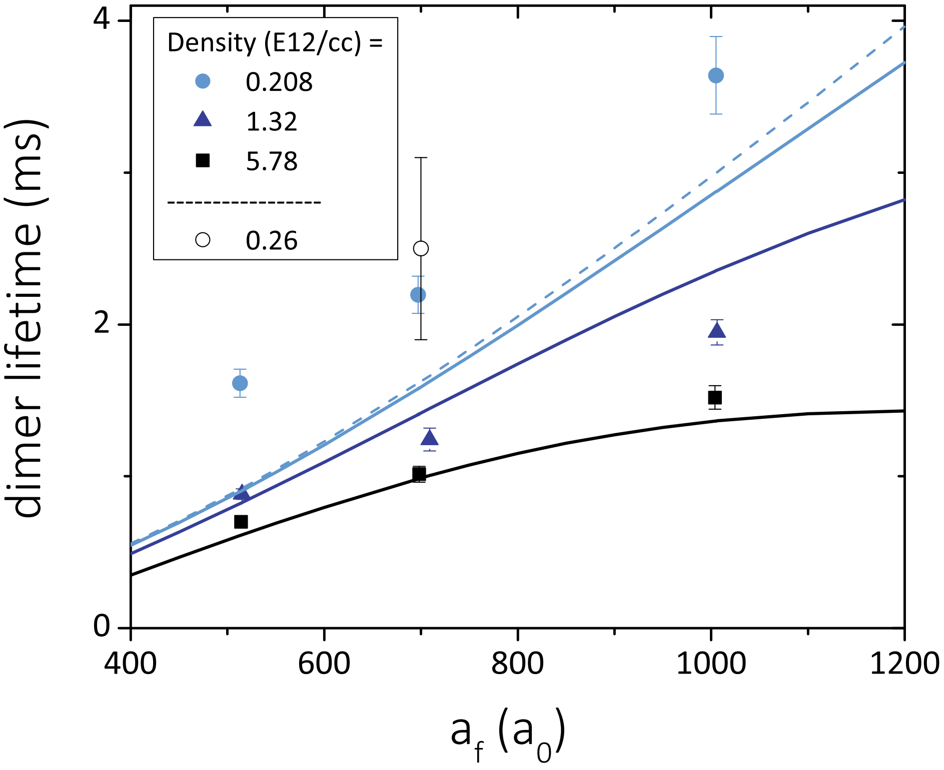

Figure 8.6: The longer of the two fitted (dimer) lifetimes as a function of a_f for initial cloud densities of n = 0.208, 1.32, and 5.78 E12/cc. The solid lines represent the predicted dimer loss rates from equation 8.6, the dashed line represents the predicted dimer loss rate neglecting density-dependent atom-dimer collisions. The open circle point is a previous measurement from [93]; we see good agreement between our lowest density measurement and this previous measurement, as well as qualitative agreement between our data and the lifetime predictions, we therefore conclude that the slower of the two losses in our molecule decay data represents the Feshbach dimers in our system.

8.3 Trimers: the fast decay

We now turn our attention to the faster of the two decays seen our molecule decay. This decay was previously seen to be independent of both a_f and n. We suspect this may be evidence of Efimov trimers in our system.

8.3.1 Trimer lifetime prediction

Because there are in theory an infinite number of Efimov states, we must use process of elimination to narrow down our focus to the relevant states. In our case, the second-excited and all higher states (3, 4, 5...) have already merged with the Feshbach dimer state at the scattering lengths we are studying, and therefore no longer exist. Only the first-excited and ground Efimov state exist in the range we study. To understand the likely population of each of these states, we must examine the energies of these states, $E_{\mathrm{T}}^{(p)}$, where p designates the Efimov state, $(p = 0, 1, 2...)$. These energies were calculated (by José P. D'Incao) by solving the three-body problem in the adiabatic hyperspherical representation [43, 8], and are plotted in figure 8.7. On resonance, the first-excited state's energy is only 600 Hz apart from the Feshbach state, while the Efimov ground state's energy is on the order of a few hundred kHz ($\sim$ 330 kHz). This large resonant binding energy means that if atoms were associating into ground state Efimov molecules during t_{dwell}, the process would happen very quickly, on the order of a few μs. However, this large resonant binding energy also makes production of these molecules during the ramp away very unlikely. Ultimately what is most relevant in our experiment is the fact that at the magnetic fields we are probing our system, the binding energy of the ground-state Efimov molecule is too far away from the Fesbach dimer's energy for our microwave pulse to dissociate both.

Having eliminated the $(p = 0)$ and $(p \geq 2)$ Efimov states from possibility, we now turn our attention to the $(p = 1)$ state. Because this state's binding energy is so close to the dimer's, we have instead plotted the difference in this energy in figure 8.8. We see that these two states are always less than 7 kHz apart. This small difference in energy means that if there were first-excited Efimov

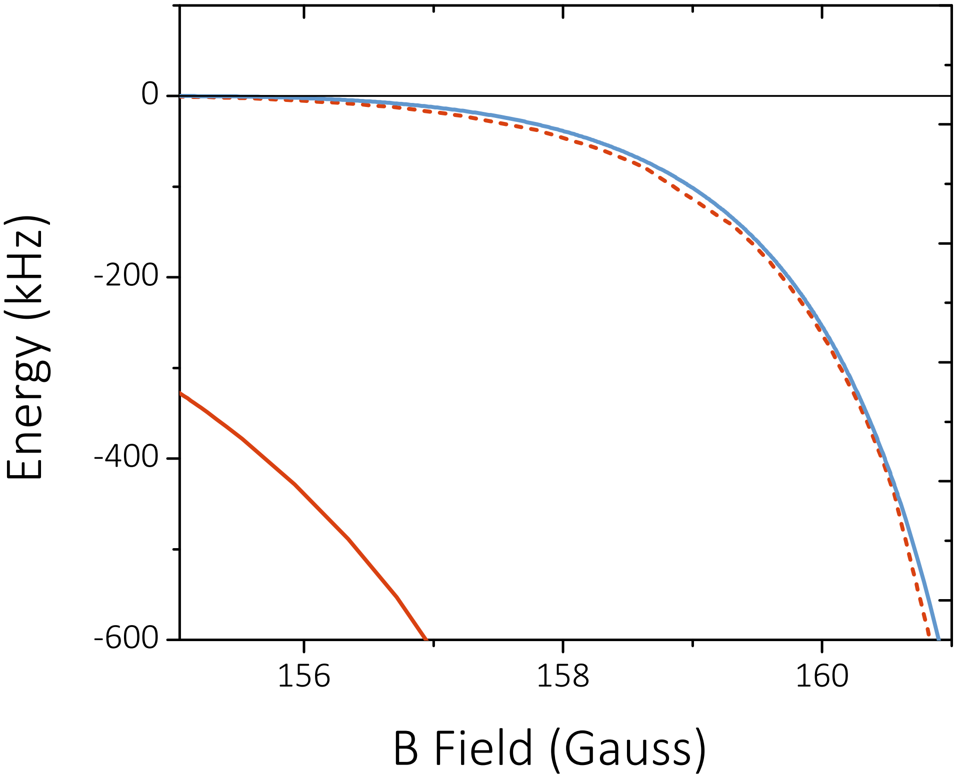

Figure 8.7: The binding energies of the Feshbach molecule E_{D}(blue solid line), the ground Efimov molecule $E_{\mathrm{T}}^{(0)}$ (red solid line) and the first-excited Efimov molecule $E_{\mathrm{T}}^{(1)}$(red dashed) as a function of magnetic field. The left most side of the plot ends at $B = B_0 = 155.04$ G, the center of the Feshbach resonance.

trimers in our system, they would be transferred to our imaging state by the same microwave pulse we use to transfer the Feshbach molecules. We also see that $E_{\mathrm{T}}^{(1)}$ at resonance is only a few hundred of Hz; this is comparable to our value of E_n in our experimental range of densities. It is therefore reasonable to expect the mechanism sweeping resonant atoms into shallow Feshbach dimers might also sweep atoms into shallow first-excited Efimov trimers. If trimers were present in our system, whether they are created during t_{dwell} or during the ramp away from resonance is then a relevant question. Given their small energies on resonance, it would be more likely that, much like the dimers, they are created during the ramp away, as population on resonance, if occurring, would take on the order of several ms to be substantial.

The shape of the first-excited trimer molecule depends on a. The distance between two of the atoms is roughly equal to the separation in a Feshbach dimer, a. The distance of the third atom however is set by $E_\mathrm{b} - E_\mathrm{T}^{(1)}$. If we treat the two closely spaced atoms are one particle ("dimer"), the third atom can be approximated to be bound to the "dimer" by

$$E_\mathrm{b} - E_\mathrm{T}^{(1)} \approx \frac{\hbar^2}{\frac{4}{3} m a_\mathrm{T}^2}, \tag{8.7}$$

where a_T is the distance between the third atom and the "dimer". This distance is at a maximum of 6.6 kHz at $a = \sim 1000\, a_0$, corresponding to $a_\mathrm{T} \approx 2200\ a_0$; the third atom is therefore separated by more than twice the other two atoms' distance. At a low density of $n = 0.2$ E12/cc, the interparticle distance ($n^{-1/3}$) is safely > 10 times larger than the trimer size, however at our standard density of $n = 5$ E12/cc, $n^{-1/3} = 10.7$ k a_0, only five times the Efimov size. If there were Efimov trimers in our system at this standard density then, many questions arise, such as what does it mean to have a three-atom molecule when it is embedded in a gas with inter particle spacing comparable to the molecular size?

The predicted lifetime of the trimers is how we analyze our system for their existence. The width of the first-excited Efimov trimer (Γ), calculated by the same method as that to calculate the binding energy, is plotted in figure 8.8. The lifetime of this state is then $1/(2\pi\Gamma)$, and is plotted in 8.9. It does not vary appreciably over our studied range of a, being 100 μs at 500 a_0 and only $\sim 130\ \mu$s at 1000 a_0.

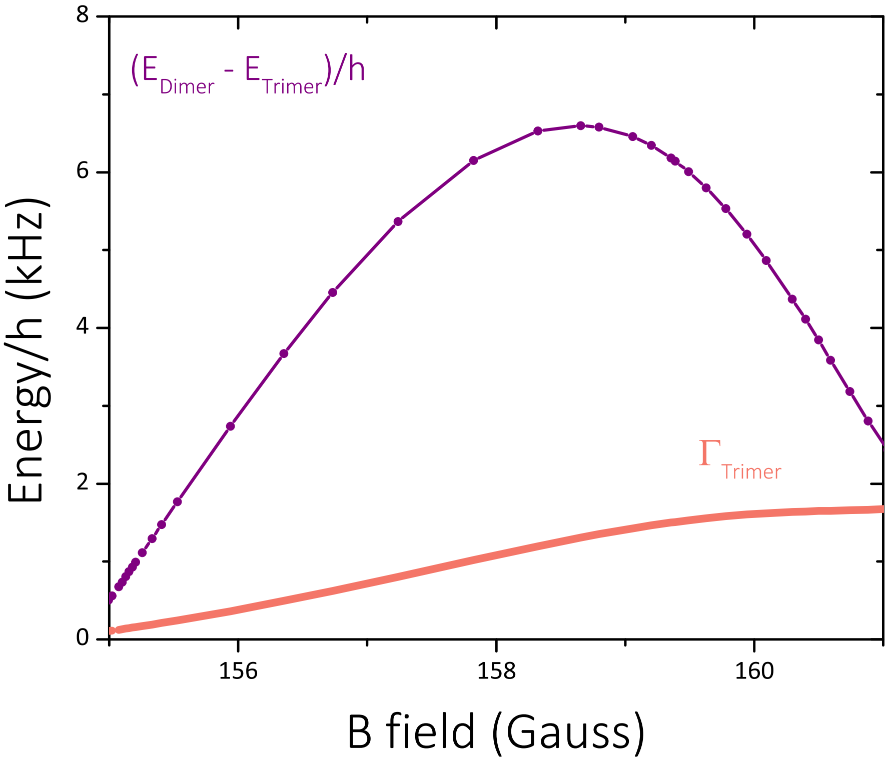

Figure 8.8: The difference between the Feshbach dimer and first-excited Efimov trimer binding energies is plotted in purple. On resonance, $E_{\mathrm{T}}^{(1)} - E_{\mathrm{b}} \sim 600$ Hz. The calculated width of the first-excited trimer state is plotted in pink.

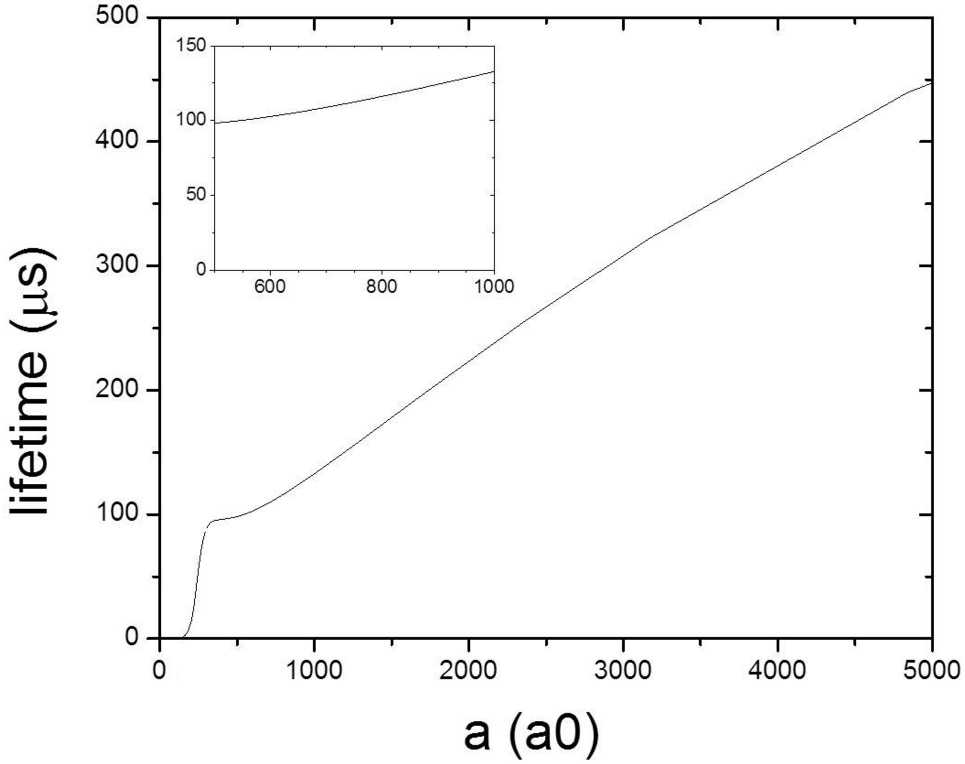

Figure 8.9: The predicted trimer lifetime as a function of a. This lifetime does not vary appreciably within our studied range of a, is 100 μs at 500 a_0 and only $\sim$ 130 μs at 1000 a_0, see inset.

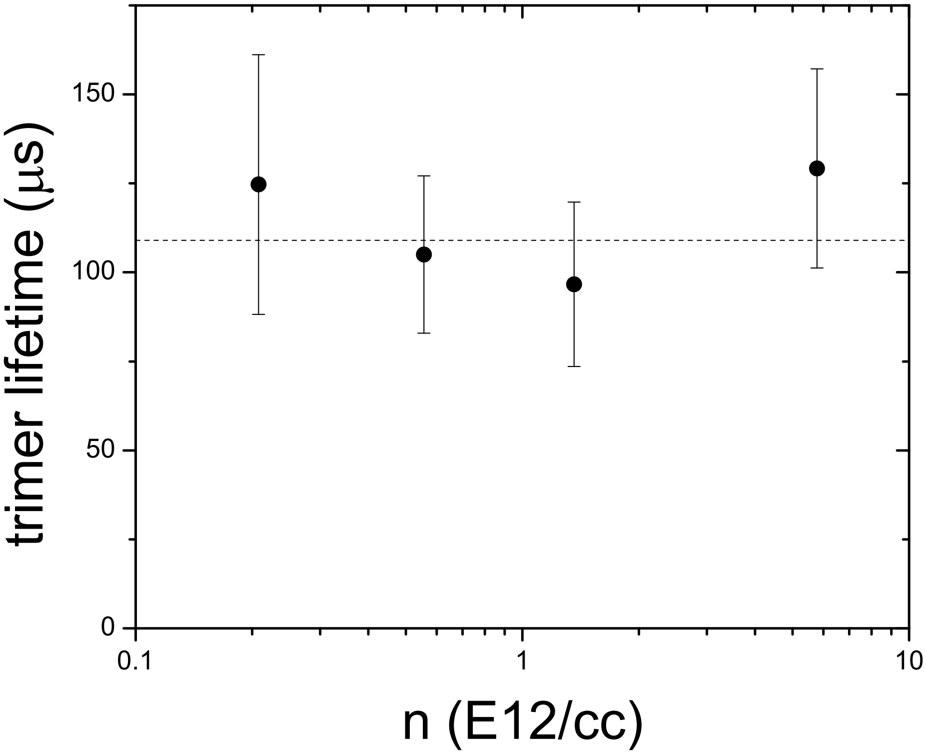

Figure 8.10: The faster of the two fitted lifetimes in our molecular gas plotted as a function of density. The system was probed at $a_f = 700\, a_0$. The predicted trimer lifetime at this scattering length is 109 μs. Our measured lifetimes average to 114 ± 16.

8.3.2 Trimer lifetime measurements

We measured the fast lifetimes of our gas created by a $t_{\text{dwell}} = 1.5\, t_n$ on resonance and a ramp time = 100 μs to 700 a_0 for various densities, the results are plotted in figure 8.10. We see that the fast lifetime does not vary with density within error, and averages to a value of 114 ± 16. This is in very good agreement with the predicted first-excited Trimer lifetime of 109 μs at $a = 700\, a_0$.

8.3.3 How many trimers?

The excellent agreement between our measured fast decay and predicted trimer lifetime, as well as the slower decay and the predicted dimer lifetimes, confirms the existence of first-excited trimers in our system. We can now surmise that the fitted amplitudes of our exponential sum represent the number of trimers and dimers in the system. Because the microwave pulse to our imaging state works by spin-flipping only one atom in each molecule to the imaging state (fun fact: the trimer atom that is sent to the imaging state in this case is one of the two closer-bound atoms), A_1 and A_2 of equation (8.1) are the number of trimers and the number of dimers, respectively. The number of atoms swept into the trimer state is then $3 \times A_1$ and into the dimer state $2 \times A_2$.

From figure 8.1 we can estimate the number of atoms that were swept into the respective molecules. The initial condensate number was 82400 ± 1600. Given the fitted values of A_1 and A_2 then, we see that $(3.46 \pm 0.44)\%$ atoms are swept into trimers, and $(9.98 \pm 0.33)\%$ into dimers for the $n = 0.2$ E12/cc dataset, and $(7.1 \pm 0.17)\%$ into trimers and $(12.06 \pm 0.54)\%$ into dimers for the $n = 1.32$ E12/cc dataset. It is expected that the number of molecules created would depend on the density, see Chapter 7 for further exploration into this idea.

Now that we are convinced that we are in fact creating molecules when we ramp away from resonance, and these molecules are both Feshbach dimers and Efimov trimers, let us now explore how the formation of these molecules is affected by dwell time on resonance.

Chapter 9

The oddities

9.1 Molecule lifetime measurements at short dwell times

We want to study how the system's evolution of resonance affects molecule production. In Chapter 7 we explored how the rate of the ramp away from resonance affected the molecule production. We briefly saw that the molecule production was also affected by the initial density of the system and the dwell time on resonance. We surmise that a minimum evolution on resonance is necessary for molecular production.

For our initial experiment, we decreased t_{dwell} from 1.5 to 0.15 t_n, and, through fitting the decay rates of the subsequent molecular cloud, hoped to extract the number of dimers and trimers produced, A_1 and A_2 (see figure 9.1). This seemingly simple experiment hit a snag when we realized that at a shorter t_{dwell} our defining lifetimes of t_1 and t_2 had changed: t_1 nearly doubled while t_2 decreased by nearly 25%, from 1250 to 950 μs.

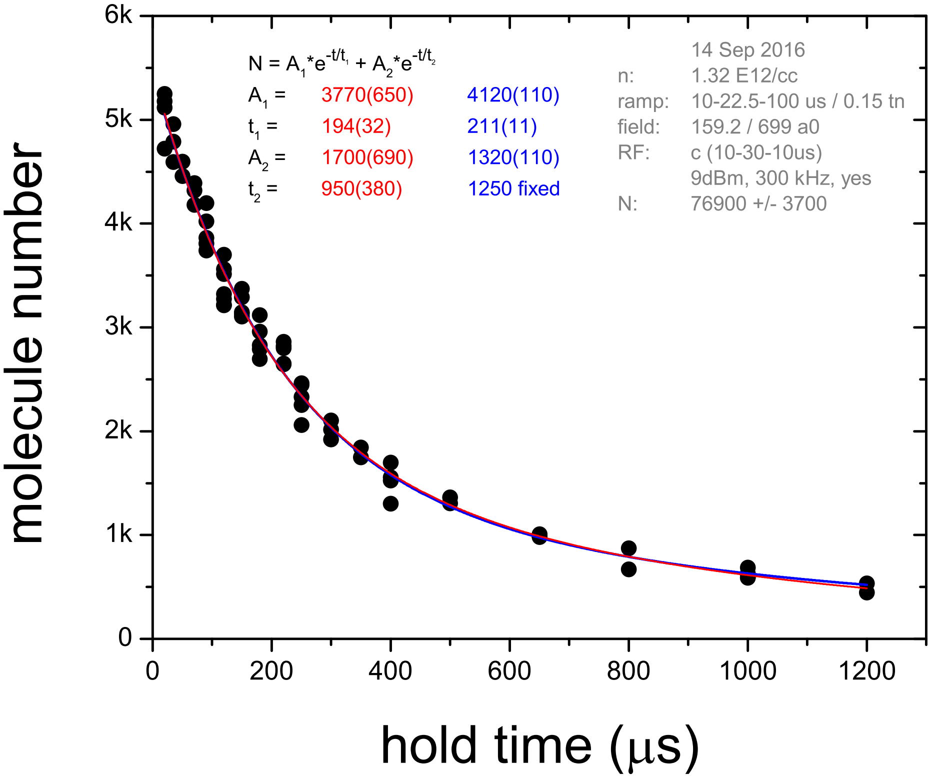

Figure 9.1: The number of molecules in a $n = 1.32$ E12/cc system, as a function of hold time at $a_f = 700\,a_0$. The molecules are generated after a $t_{\text{dwell}} = 0.15\,t_n$ on resonance and a ramp time $= 100$ μs to a_f. The data are fit with a sum of two exponentials with all fit parameters free (red) and fixing the dimer lifetime, t_2 (blue, behind red) to the predicted value based on the density and a_f, see equation (8.6). We see that the dimer lifetime fits to a 25% faster decay when allowed to float. The trimer lifetime repeatedly fits to around 200 μs, about double its expected value. The abbreviated legend in the upper right is explained in Appendix A.

9.2 Dimers: the slow decay

To study how exactly t_{dwell} affects the fitted molecular lifetimes, we took molecular decay data of an intermediate density ($n = 1.3$ E12/cc) cloud at $a_f = 700\,a_0$ for various values of t_{dwell}, see Appendix C for the raw data. Due to the perceived decrease in dimer lifetimes and increase in trimer lifetimes, our fitting function at many times had difficulty discerning two lifetimes. To simplify matters we fixed t_1 to 100 μs and have plotted the resulting fits of t_2 in figure 9.2. When $t_{\text{dwell}} \geq 0.9\,t_n$, t_2 fits to its predicted value of 1240 μs. For $t_{\text{dwell}} \leq 0.5\,t_n$, we find that t_2 is not only shorter but also seems to change with t_{dwell}.

Figure 9.2 shows that at low values ($< 0.5\,t_n$) of t_{dwell} the fitted value of t_2 does not depend on ramp out. However, in figure 9.3 we see that ramp rate does become important near the critical value of $t_{\text{dwell}} \sim 1\,t_n$. This could be due to incorrect definition of t_{dwell}, and therefore the real, actual resonant evolution time that the experiment cares about is changing as we vary ramp out near the critical value.

The molecule lifetime's perceived dependence on t_{dwell} is very unexpected and suspicious. To test our sanity, as well as any imaging systematics, we thoroughly checked our molecular decay while purposefully detuning our experimental set points, see figure 9.4. For all the things we varied, we never saw appreciable change in number at critical hold times that would change the fitted values of t_1 and t_2. We therefore conclude from these checks that this odd behavior we see from short-evolved resonant clouds is real.

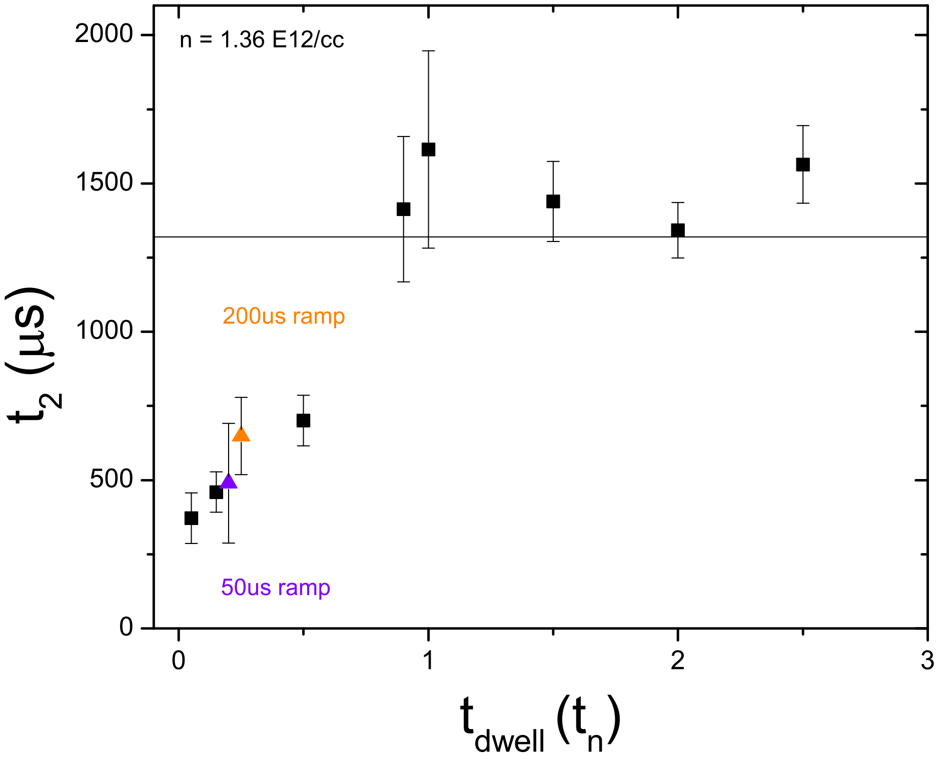

Figure 9.2: The fitted dimer lifetime measured in $n = 1.32$ E12/cc ($t_n = 146$ μs) clouds at $a_f = 700\,a_0$ for various resonance dwell times. For these fits we fixed t_1 to 100 μs. t_2 fits to its expected value of 1250 μs (solid line) when $t_{\mathrm{dwell}} \geq 0.9\,t_n$, but fits to much shorter lifetimes for smaller t_{dwell}'s. Most of the points (black squares) are taken after a ramp time = 100 μs to a_f, however we also measured the lifetime for a longer ramp out time of 200 μs (orange triangle) and a shorter ramp time of 50 μs (blue triangle), and saw no appreciable difference in t_2 behavoir.

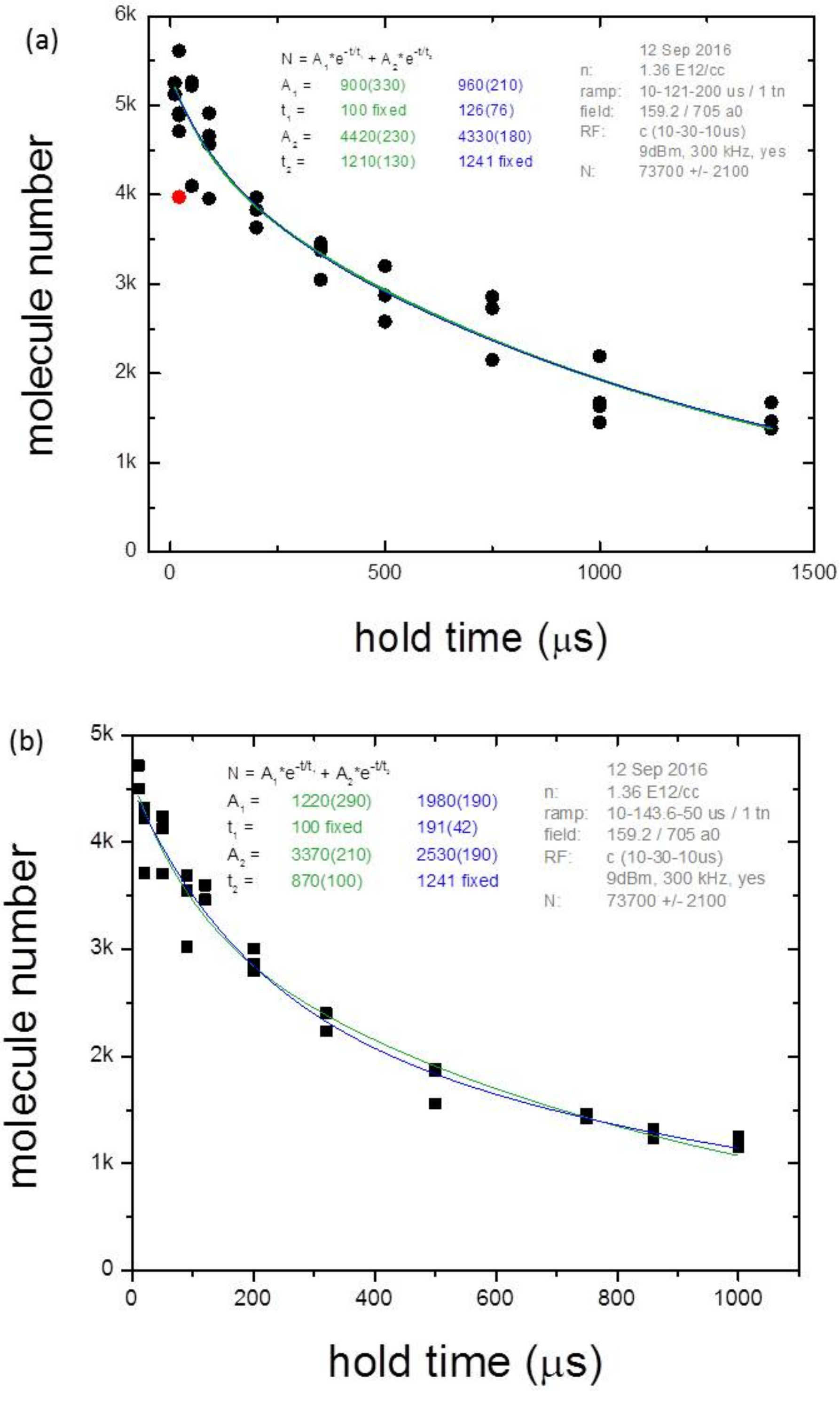

Figure 9.3: The molecule number as a function of hold time at $a_f = 700\,a_0$ for $t_{\text{dwell}} = 1\,t_n$ after a (a) a slower ramp time of (a) 200 μs, and (b) a faster ramp time of 50 μs. The data are fit with a sum of two exponentials while fixing the trimer lifetime , t_1 (green) or fixing the dimer lifetime, t_2 (blue). The slower ramp out dataset fits to normal values of t_1 and t_2, whereas the faster ramp out dataset fits either smaller values of t_2 or doubled value of t_1.

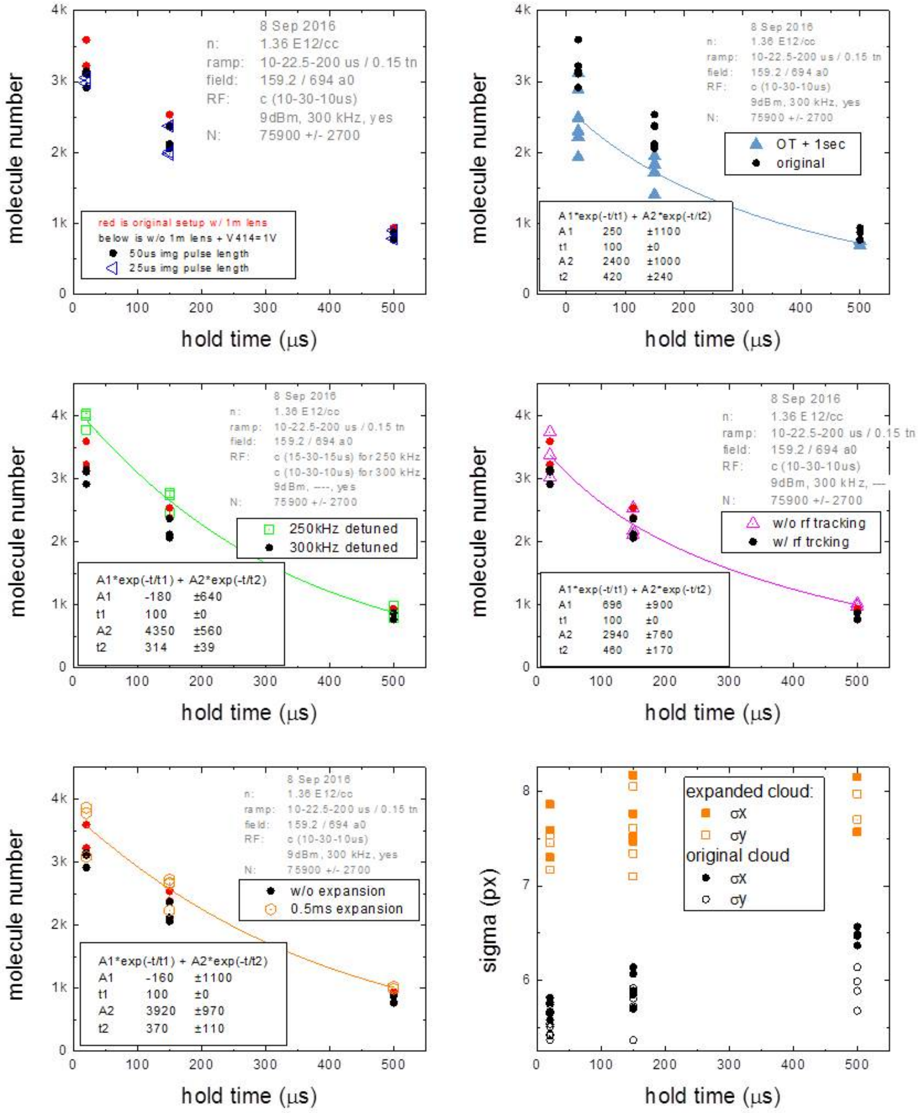

Figure 9.4: The molecule number as a function of hold time at $a_f = 700\,a_0$ for $t_{\text{dwell}} = 0.15\,t_n$ with a cloud of initial density $n = 1.36$ E12/cc. We changed various aspects of the experiment in order to see if the data was affected: (a) varied the imaging pulse length as well the amount of incident imaging light. (b) Held an extra second in our hybrid optical+magnetic trap before proceeding with the resonance-jump procedure. This checks for invisible Oort clouds that could be oscillating in our trap and later smashing into our system. We see small decrease in number after holding the extra second, most likely due to slight heating of the system, however these drop in number does not explain the short fitted values of t_2. (c) Decreased the microwave detuning, thereby introducing more field-sensitive atoms into the image background. (d) No tracking of the microwave frequency as the cloud fell. This is not expected to affect the number of molecules transferred to the imaging state as this molecule number is saturated, and the cloud does not fall so far that the detuning exceeds E_b. (e) We expanded the molecule image by delaying the time between the microwave transfer and the imaging laser. This expansion increases the size and decreases the optical depth, thereby testing for imaging errors related to background corrections or resolution effects. (f) The measured sizes of the clouds with and without expansion, we see that the new clouds are 250% their original volume. From all of these test (a-f) we conclude that the strange effects we see from our short-evolved resonant clouds are real and not an effect from experimental error.

9.3 Superposition theory

We suggest now a theory to explain why it may not be the dimer lifetime decreasing, but the perceived trimer lifetime increasing. Because the spacing in energy between the dimer and trimer states is small (< 7 kHz) while the atom state is on the order of hundreds of kHz, we speculate that the atoms swept into molecules are in a superposition of being both dimers and trimers. These superimposed molecules are partially trimers ($|T\rangle$), and partially dimers with an unbound atom, or monomer ($|d+m\rangle$). This superposition would be more likely after only a short dwell time on resonance because it takes a finite about of time for a first-excited trimer to form. The wave function of this molecule immediately following the ramp out to a_f is described by

$$|\psi\rangle = \alpha|T\rangle + \mathrm{e}^{i\phi}\beta|d+m\rangle, \tag{9.1}$$

where ϕ is the phase of the wave function. After a time t_{hold}, the wave function evolves to

$$|\psi\rangle = \alpha|T\rangle + \mathrm{e}^{i\phi}\mathrm{e}^{i\Delta_E t_{\mathrm{hold}}/\hbar}\beta|d+m\rangle, \tag{9.2}$$

where Δ_E is the energy difference between the dimer and trimer states, plotted in 8.8. When we image these superimposed molecules, we collapse the wave function. This imaging process begins when we use a microwave pulse to send two atoms to the unbound state, and a third atom to the $|3,-3\rangle$ imaging state. The molecular atom sent to the imaging state is always one of the dimer-bound atoms (or dimer-close atoms in the trimer), never the monomer in the superposition of being bound and unbound. However, the amplitude for detecting the spin-flip atom goes as $\alpha + \beta\mathrm{e}^{i\frac{\Delta_E t_{\mathrm{hold}}}{\hbar}+\phi}$, and therefore the transferred number of molecules is given by

$$N = \left|\alpha + \beta\mathrm{e}^{i\frac{\Delta_E t_{\mathrm{hold}}}{\hbar}+\phi}\right|^2, \tag{9.3}$$

or

$$N = \alpha^2 + \beta^2 + 2\alpha\beta\cos[(\Delta_E t_{\mathrm{hold}}/\hbar) + \phi]. \tag{9.4}$$

We therefore would expect to see our transferred molecule number oscillate with t_{hold}. The frequency of these oscillations is determined by $E_{\mathrm{b}} - E_{\mathrm{T}}^{(1)}$, and would therefore have a maximum frequency of 7 kHz around 1000 a_0.

To search for these oscillations, we took data with very fine time steps, see figures 9.5, 9.6, and 9.7. To the naked eye we do not see any oscillations in the molecular number. The Fourier transform of the fit residuals of each plot (see figure 9.8) still do not see clear 7 kHz oscillations.

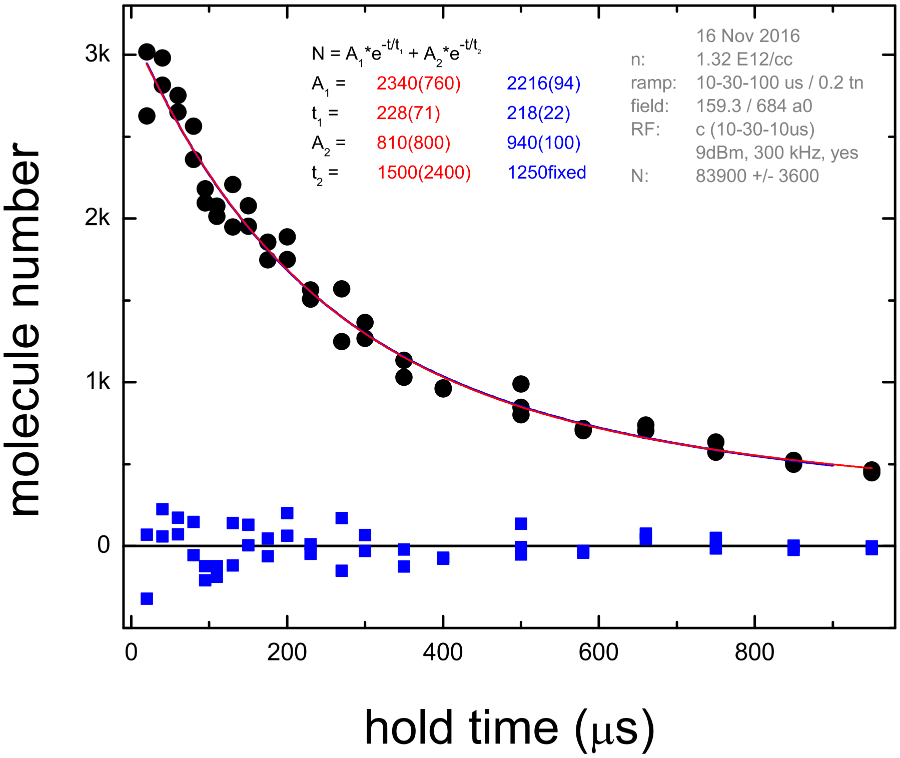

Figure 9.5: The molecule number as a function of hold time at $a_f = 700\,a_0$ for $t_{\rm dwell} = 0.2\,t_n$. The data are fit with a sum of two exponentials with all the parameters free (red) and fixing the dimer lifetime, t_2 (blue). The residuals from the latter fit are included as blue squares. We took this data with a high density of points in order to look for a 7 kHz oscillation in the molecular number

There are many reasons to explain why we would not see oscillations in the imaged molecular number even if there were superimposed molecules. First, if not every trimer were a superimposed molecule, the amplitude of the oscillations could be quite small compared to our noise. Second, various superpositions may be out of phase with each other across the cloud, thereby washing out the signal.

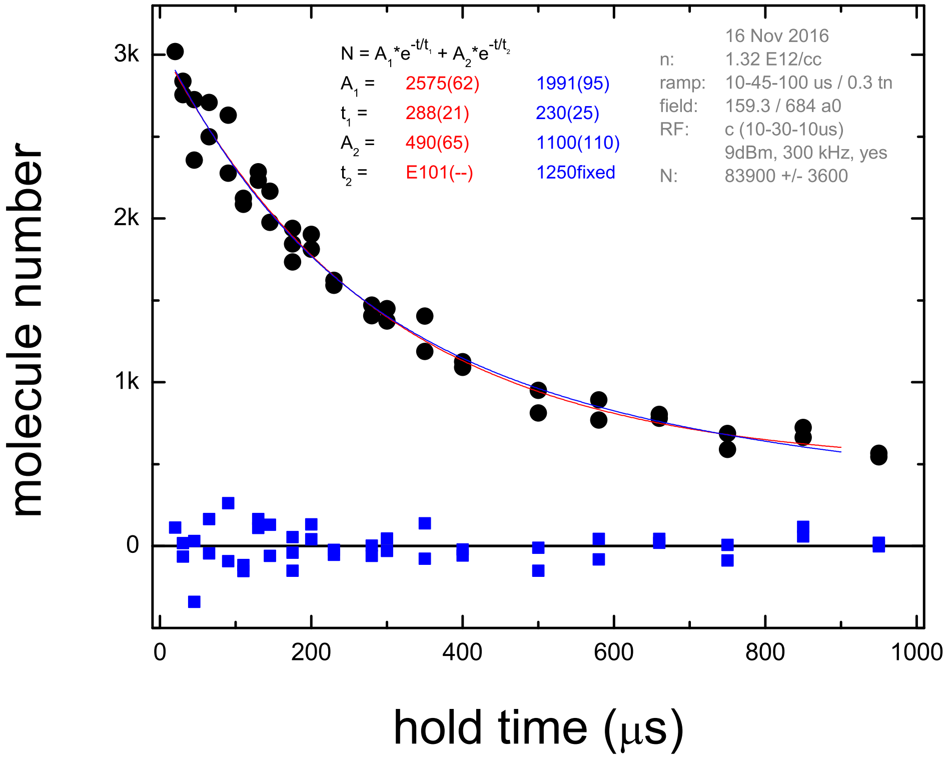

Figure 9.6: The molecule number as a function of hold time at $a_f = 700\,a_0$ for $t_{\text{dwell}} = 0.3\,t_n$. The data are fit with a sum of two exponentials with all the parameters free (red) and fixing the dimer lifetime, t_2 (blue). The residuals from the latter fit are included as blue squares. We took this data with a high density of points in order to look for a 7 kHz oscillation in the molecular number

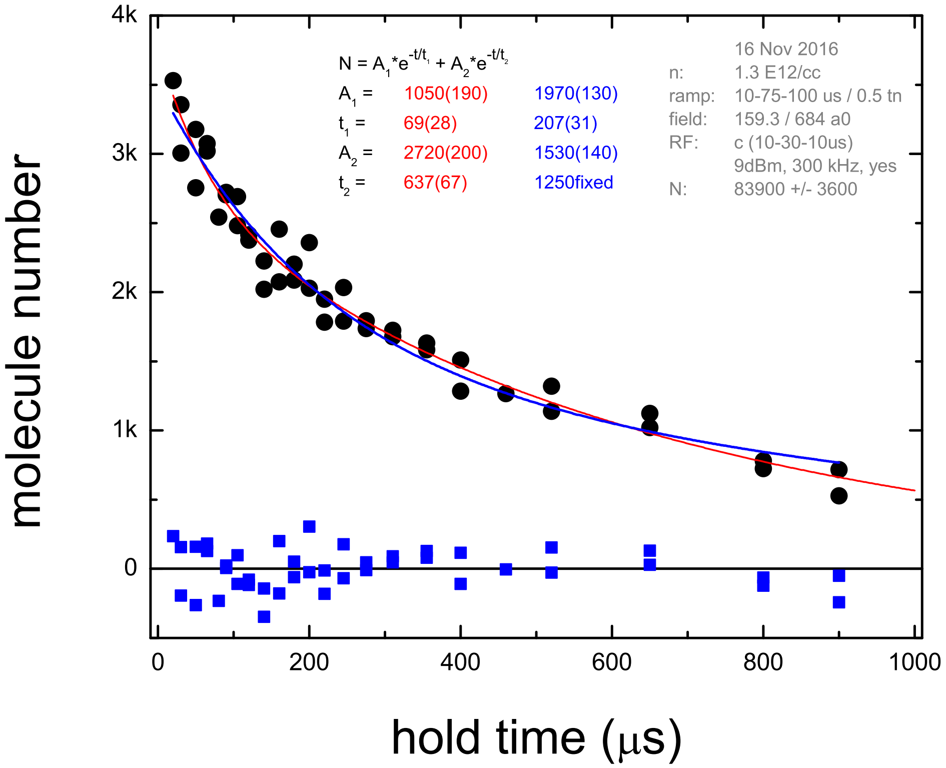

Figure 9.7: The molecule number as a function of hold time at $a_f = 700\, a_0$ for $t_{\mathrm{dwell}} = 0.5\ t_n$. The data are fit with a sum of two exponentials with all the parameters free (red) and fixing the dimer lifetime, t_2 (blue). The residuals from the latter fit are included as blue squares. We took this data with a high density of points in order to look for a 7 kHz oscillation in the molecular number

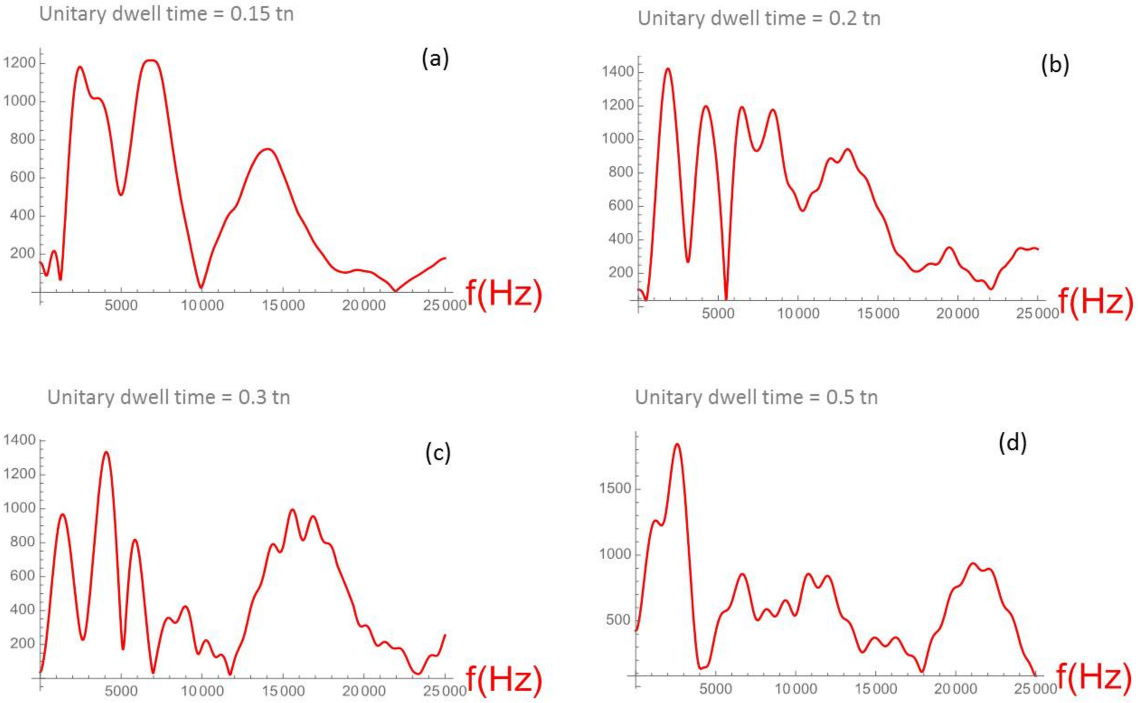

Figure 9.8: The Fourier transform the of the molecular lifetime fit residuals for the $t_{\text{dwell}} =$ (a) 0.15 t_n data from figure 9.1, (b) 0.2 t_n data from figure 9.5, (c) 0.3 t_n data from figure 9.6, and (d) 0.5 t_n data from figure 9.7. We expected 7 kHz oscillations in the residuals if the atoms were in a superposition of both the dimer and trimer molecule states, we do not see any clear 7 kHz peaks in the Fourier transforms. See the text for why this result does not negate our superposition theory.

9.4 Suggested analysis technique: fix dimer lifetime

We have not shown that our superposition theory is correct, however we speculate that due to residual many-body effects there is a density-induced hybridized state with characteristics of both dimers and trimers, whose decay would then be a combination of the two:

$$\tau_{\mathrm{H}} = \frac{\tau_{\mathrm{D}} + \tau_{\mathrm{D}}}{2\,\tau_{\mathrm{D}}\,\tau_{\mathrm{T}}} \tag{9.5}$$

Because the trimer lifetime is significantly smaller than the dimer lifetime, we can approximate $\tau_{\mathrm{H}} \to 2\,\tau_{\mathrm{T}}$. It is worth noting that there is no immediately intuitive picture of what this hybridized state physically is. Because there are a greater number of dimers than trimers, not all of the dimers can be hybridized, whereas all of the trimers could. For analysis purposes, we will assume that there are no **pure** trimers in the system, only dimers and our strange hybridized state. Therefore we will assume that the lifetime of **most** dimers is the predicted value, which we will fix. We then evaluate our t_{dwell} data (in Appendix C) for t_1, see figure 9.9. We see that the trimer lifetime fits near the expected value of 100 μs when $t_{\mathrm{dwell}} \geq 1\,t_n$, and fits near 200 μs from all shorter values of t_{dwell}. It is particularly interesting that this lifetime halves abruptly, rather than slowly. In our current paradigm, this suggests that all the trimers in the system take a characteristic time of 1 t_n to be established. The fact that the trimer lifetime for $t_{\mathrm{dwell}} < 1\,t_n$ is always near 200 μs and does not vary with t_{dwell} agrees with our theory this odd behavior is due to (all) trimers being a hybridized molecule.

From these fits we can extract A_1, A_2 and A_3 as a function of t_{dwell}, see figure 9.10. A_2 is the number of pure (i.e. non-hybridized) dimers, A_1 (for $t_{\mathrm{dwell}} < 1\,t_n$) the number of hybridized molecules, and A_3 (for $t_{\mathrm{dwell}} \geq 1\,t_n$) the number of pure trimers. The number of dimers peaks near $t_{\mathrm{dwell}} = 1.5\,t_n$. For shorter dwell times we see that the number of hybridized molecules is greater than the number of full dimers. This is surprising because the bound value of the trimer state on resonance suggests that a finite time is needed to form these states, and therefore the number of dimers would should at first be larger than A_1. However, if we surmise that the mechanism to create dimers and trimers is not the same, and that perhaps one molecule has greater production value during the evolution on resonance and the other during the ramp away, then these results are less intimidating.

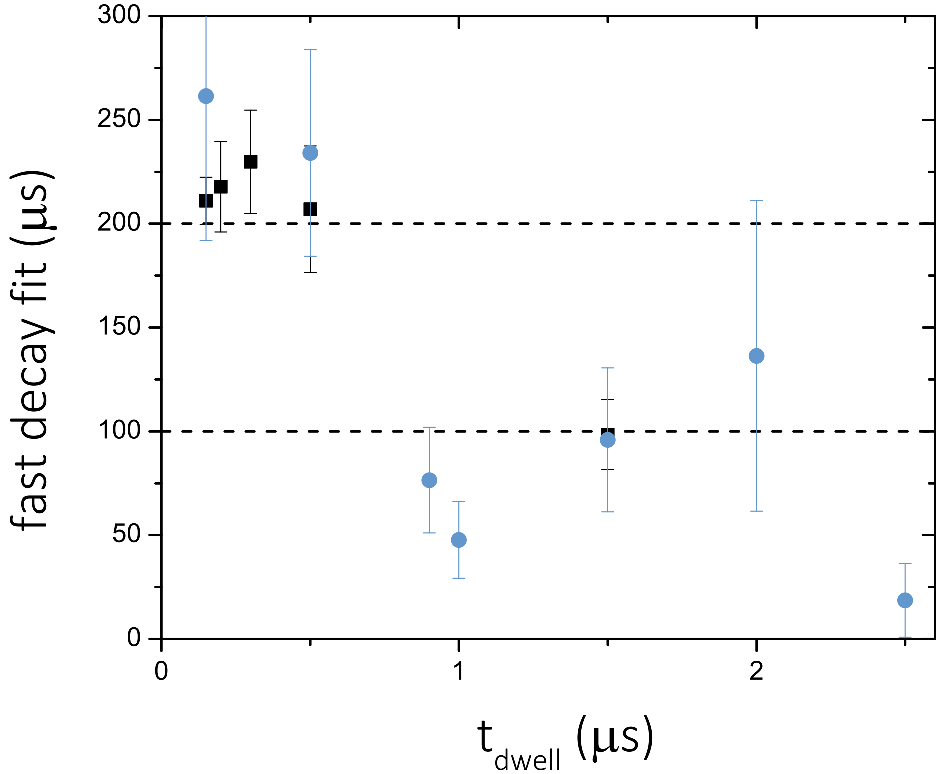

Figure 9.9: The fitted trimer lifetime measured in $n = 1.32$ E12/cc ($t_n = 146\,\mu$s) clouds at $a_f = 700\,a_0$ for various resonance dwell times. For these fits, we fixed t_2 to 1250 μs. The black squares are fits from the high-density-of points data, like those from figure 9.5; the blue circles are the fits from less full datasets from Appendix C and therefore have larger error bars. We see that the trimer lifetime fits near the expected value of 100 μs when $t_{\rm dwell} \geq 1\,t_n$, and fits near 200 μs from all shorter $t_{\rm dwell}$'s. It is particularly interesting that this lifetime doubles as quick as a step function, rather than slowly changing.

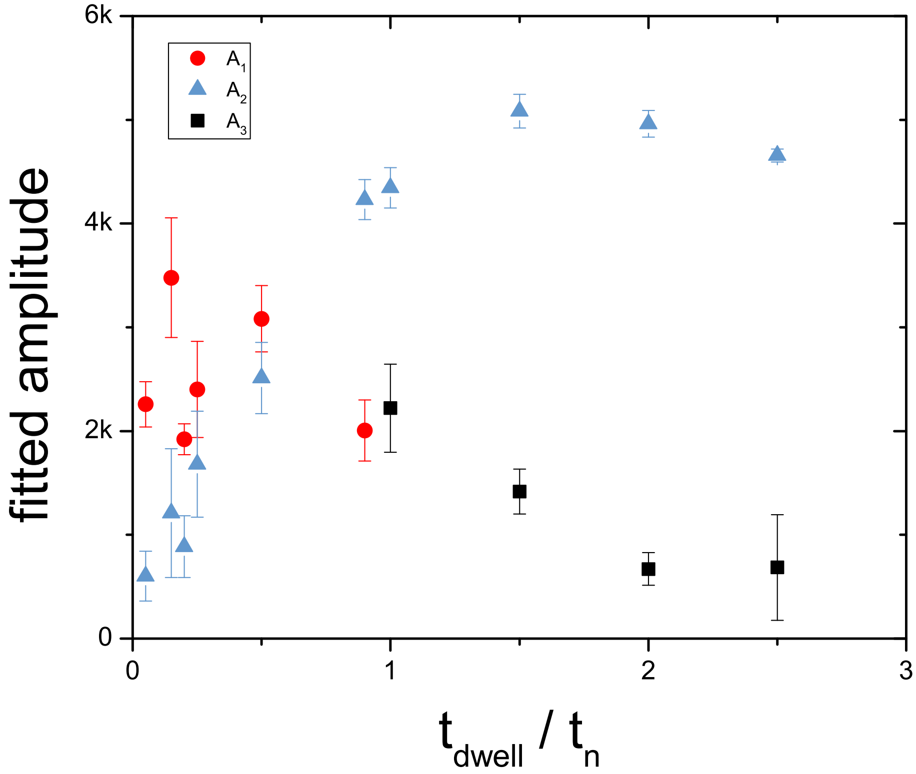

Figure 9.10: The fitted molecule amplitudes, A_1, A_2, and A_3, as a function of t_{dwell}, after analyzing the lifetime data from Appendix C with t_1 free and t_2 fitted to 1241 μs. The initial condensate had density $n = 1.36$ E12/cc and was ramped to $a_f = 700\,a_0$ in ramp time = 100 μs. A_1 (red points) is the number of hybridized molecules identified by their 200 μs lifetime, and is greater than the number of full dimers (A_2, blue triangles) at short dwell times. A_3 (black squares) is the number of full trimers, identified by their 100 μs lifetime.

9.5 Re-examining the molecule size predictions

In Chapter 7 we examined the large role the ramp away from resonance plays in forming the Feshbach molecules, now we wonder: does it play an equal role in producing trimers? And hybridized molecules?

To answer these questions (or maybe develop more), we must change our interpretive perspective. Instead of thinking as the molecules being “created” during the dwell time on resonance or during the ramp away, we will instead only consider the probability to form molecules, and how this relates to the distance between individual atoms at resonance.

Recall from Chapter 7 the model for production of Feshbach molecules assumes that at resonance there are molecule-like correlations with characteristic size a'. The number of atoms swept into Feshbach molecules was then proportional to

$$N = 4A\frac{a_* \cdot a'}{\left(a_* + a'\right)^2}, \tag{9.6}$$

where A is an undetermined amplitude and a_* is a critical value of scattering length where the ramp appears to go from diabatic to adiabatic, defined in our earlier model to be $\left(\frac{\alpha\hbar}{4m\dot{B}}\right)$. With our universal perspective, we assumed that a' was proportional to $1/\kappa_n$, where κ_n is the density momentum defined in Chapter 2. This model fit very well to our ramp out data (evolved on resonance for $t_{\mathrm{dwell}} = 1.5\, t_n$), plotted again as the dashed lines in figure 9.11(a).

Turning our attention now to 9.11(b), we see that the density dependence of the ramp out rate becomes less defined when we evolve our system on density for a shorter amount of time. This suggests that the effect that the ramp out rate has on forming molecules depends on how much the system evolves on resonance. We define a new molecule size of adjusted size, s/κ_f, to account for this change in density dependence. A smaller s increases the molecule number at longer ramp times for lower density datasets and also make the initial growth in molecule number steeper for the medium density data - see dashed lines in figure 9.11. We find that we have to include a density dependence s for the short t_{dwell} dataset that removes the universal scaling. We are not fully convinced of the validity of this approach.

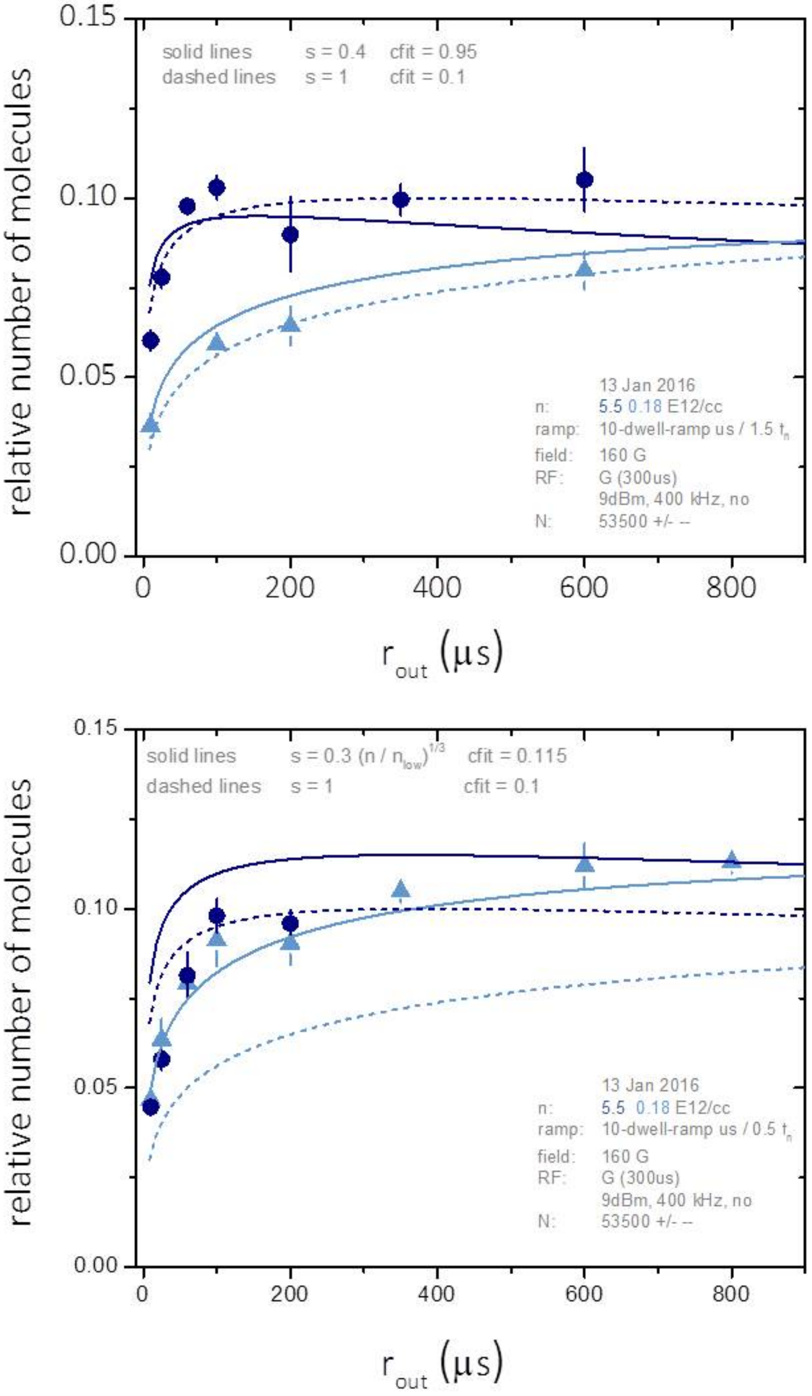

Figure 9.11: (a) The number of molecules imaged with a 300 μs Gaussian pulse as a function of ramp out rate after $t_{\text{dwell}} = 1.5\,t_n$ for clouds of initial densities of $n = 5.5$ (blue points, $t_n = 57\,\mu$s) and 0.18 (cyan triangles, $t_n = 553\,\mu$s) E12/cc. The dashed lines are the predicted number of molecules to be produced assuming the molecule size is defined by $1/\kappa_n$, we see good agreement with data. The solid line is the same model except the molecule size is assumed to be s/κ_f where $s = 0.4$. (b) The number of molecules imaged with a 300 μs Gaussian pulse as a function of ramp out rate after $t_{\text{dwell}} = 0.5\,t_n$. The dashed lines are the predicted number of molecules to be produced assuming the molecule size is defined by $1/\kappa_n$, we see very poor agreement with the data. The solid line is the same model except the molecule size is assumed to be s/κ_n where s has a density dependence of $s = 0.3(n/n_{\text{low}})^{1/3}$, this changes the density dependence of a', and therefore the expected density dependence of the ramp out data.

9.5.1 Changing molecule size

The difference in the ramp out data as we change dwell time on resonance suggests that the molecule size may be changing as the cloud evolves. To study this we consider now data of the molecular number measured as a function dwell time on resonance. The data in figure 9.12 were taken using a 300 μs Gaussian pulse, a long pulse in which we expect the fast-decaying timers to not be transferred to the imaging state; we see good agreement between this data and the molecule number determined by fitting the decay for A_2 (figure 9.10) and therefore conclude this number represents only dimers.

The solid lines in figure 9.12 are the number of molecules predicted to be produced using equation 9.6 and assuming that a' grows linearly in time:

$$a' = \frac{t_{\text{dwell}} / \left(C_{\text{grow}} \cdot t_n \right)}{\left(6\pi n \right)^{1/3}}. \tag{9.7}$$

We see that this linear growth of a' predicts the increase and later decrease in molecular production very well. However, the characteristic growth rate (C_{grow}) of these two datasets are in slight disagreement, the larger density has a faster growth of 4.20(22) while the lower density dataset grows slower, at 3.61(47). These values are **barely** in agreement with each other.

The value and agreement of fitted growth rates has a very large dependency on the value a_*. For this analysis we used equation (7.5); for ramp time = 50 μs then, a_* becomes 502 a0. However, as we discussed at the end of chapter 7, this definition of a_* is not without problems. This experiment would be better then if we could remove the uncertainty of a_* by instead controlling it.

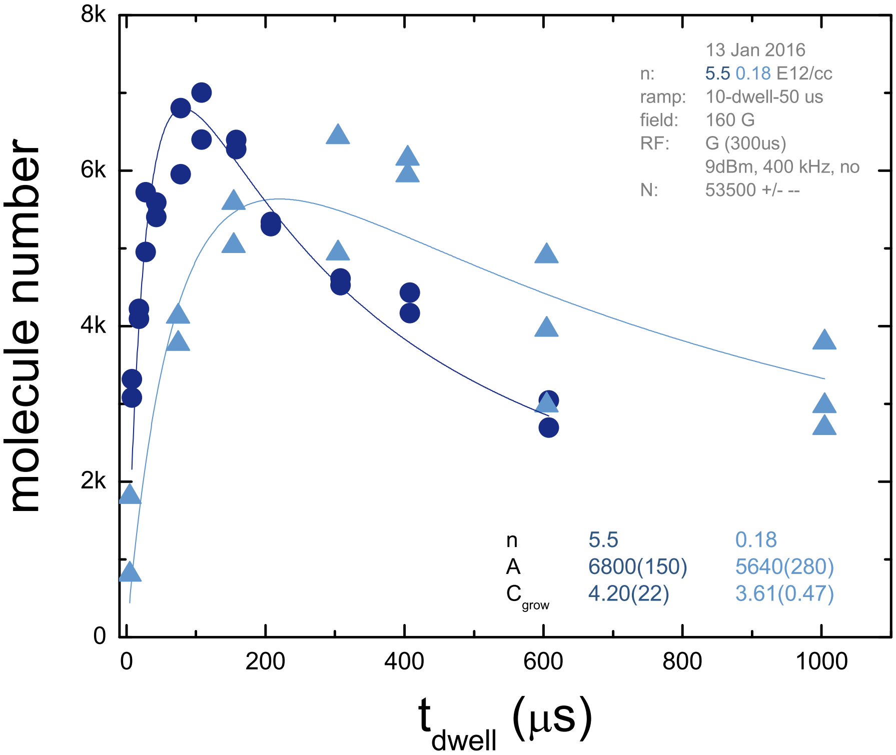

Figure 9.12: The number of molecules transferred to the imaging state by a 300 μs Gaussian pulse following a ramp time = 50 μs away from resonance to $a_f = 500\,a_0$ for condensates of initial densities of $n = 5.5$ (blue points, $t_n = 57\,\mu$s) and 0.18 (cyan triangles $t_n = 553\,\mu$s) E12/cc. The solid lines are fits to the molecular number using equations 9.6 and 9.7.

9.5.2 Experiment Suggestion

We present now a suggested experiment to remove the uncertainty of a_*. By fixing a_* we can determine a' (and its dependence on dwell time) through the change in produced molecule number. The timeline is shown in figure 9.13. The experiment involves evolving the system on resonance for various dwell times, then ramping away with a two-component ramp that is at first very fast, then very slow. The scattering length at which the ramp rate changes is called a_c, for critical value of a. In effect, this creates a ramp where the value of a_* is known experimentally, and is equal to a_c.

The two-component ramp that is at first fast, then later slow, is essentially forcing a_*. We

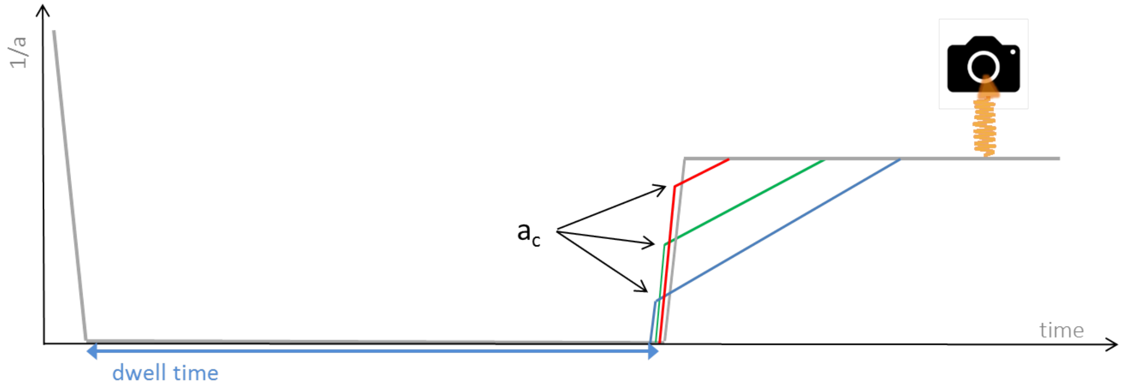

Figure 9.13: A suggested experimental timeline for determining how a' varies with t_{dwell}. After evolving on resonance for various t_{dwell}, ramp away at first very fast, then very slow. The critical time that the ramp rate switches is called a_c.

can then rewrite the expected number from equation (9.6) replacing a_* with a_c. The measured number will be a maximum when $a' = a_c$, and we call the dwell time that this maximum occurs t_c. Qualitative predictions for the number as a function of t_{dwell} are shown for three different ramp out a_c values in figure 9.14(a). By plotting t_c as a function of a_c, we can fit the data with an as-yet undetermined function. The inverse of the fitted function is $a'(t_{\text{dwell}})$, we could know how the molecular size changes as the cloud evolves on resonance.

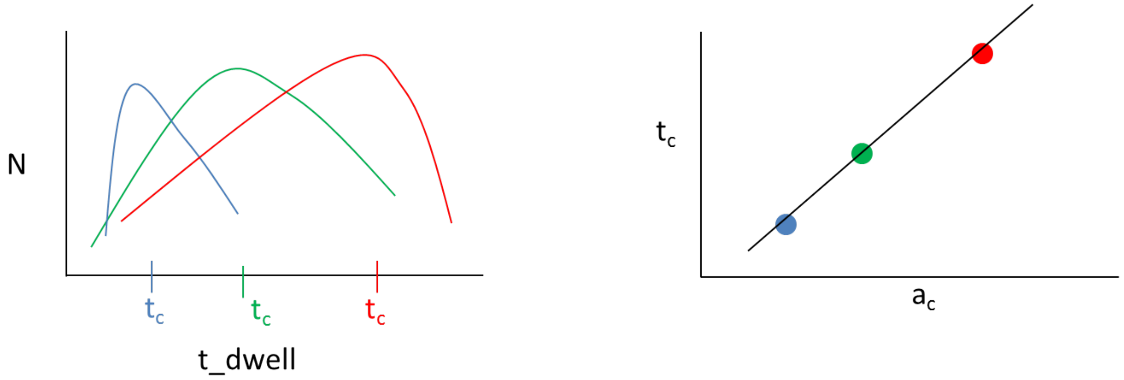

Figure 9.14: (a) Qualitative prediction of the number of molecules produced as a function of t_{dwell} for ramp outs with various values of a_c (corresponding the a_c lines drawn in figure 9.13). The number will be maximum when $a' = a_c$. We define the dwell time that yields maximum number as t_c. (b) Now plotting t_c as a function of a_c should yield a linear line if the growth rate on resonance is linear. The inverse of this function yeilds a' as a function of t_{dwell}. We could know how the molecular size changes as the cloud evolves at unitarity.

9.5.3 Future goals

The apparatus, or machine, that produced all of the data presented in this thesis has been dismantled. A new apparatus is currently being built in the basement of JILA. This new apparatus will have the capability to probe the molecule clouds within the matrix of various controllable parameters (dwell time, ramp out rate, hold time, and density) much faster, to eventually determine how the ramp out rate and dwell time on resonance combine to sweep atoms into shallow molecules of both dimers and trimers. This experiment will be able to create condensates of both ^{85}Rb (like all experiments in this thesis) and ^{39}K, and therefore have a knob to vary the characteristic width of the Efimov resonance, η_*.

The oddities explored in this final chapter will therefore be explored and demystified in the near future. Much like how our scientific perspective drastically changed when we switched from atom-loss-rate probes to molecule-production probes, I have no doubt that understanding the evolution of a degenerate Bose gas on resonance, and how this evolution translates into propensity to be swept into shallow molecules, will again require fresh perspectives.

Bibliography

[1] TD Lee and CN Yang. Many-body problem in quantum mechanics and quantum statistical mechanics. Physical Review, 105(3):1119, 1957.

[2] V Efimov. Yad. fiz 12, 1080 (1970). Sov. J. Nucl. Phys, 12:589, 1971.

[3] V Efimov. Energy levels of three resonantly interacting particles. Nuclear Physics A, 210(1):157–188, 1973.

[4] Eric Braaten and H-W Hammer. Universality in few-body systems with large scattering length. Physics Reports, 428(5):259–390, 2006.

[5] Javier von Stecher, Jose P DIncao, and Chris H Greene. Signatures of universal four-body phenomena and their relation to the efimov effect. Nature Physics, 5(6):417–421, 2009.

[6] JP DIncao, J Von Stecher, and Chris H Greene. Universal four-boson states in ultracold molecular gases: Resonant effects in dimer-dimer collisions. Physical review letters, 103(3):033004, 2009.

[7] Scott E Pollack, Daniel Dries, and Randall G Hulet. Universality in three-and four-body bound states of ultracold atoms. Science, 326(5960):1683–1685, 2009.

[8] Jia Wang, JP DIncao, BD Esry, and Chris H Greene. Origin of the three-body parameter universality in efimov physics. Physical review letters, 108(26):263001, 2012.

[9] Yujun Wang, Jose P DIncao, Brett D Esry, and CC Lin. Ultracold few-body systems. Advances in Atomic, Molecular, and Optical Physics, 62:1–115, 2013.

[10] Swann Piatecki and Werner Krauth. Efimov-driven phase transitions of the unitary bose gas. Nature communications, 5, 2014.

[11] D Hudson Smith, Eric Braaten, Daekyoung Kang, and Lucas Platter. Two-body and three-body contacts for identical bosons near unitarity. Physical review letters, 112(11):110402, 2014.

[12] M Kira. Coherent quantum depletion of an interacting atom condensate. Nature communications, 6, 2015.

[13] Mike H Anderson, Jason R Ensher, Michael R Matthews, Carl E Wieman, and Eric A Cornell. Observation of bose-einstein condensation in a dilute atomic vapor. science, 269(5221):198, 1995.

[14] Kendall B Davis, M-O Mewes, Michael R Andrews, NJ Van Druten, DS Durfee, DM Kurn, and Wolfgang Ketterle. Bose-einstein condensation in a gas of sodium atoms. Physical review letters, 75(22):3969, 1995.

[15] Cl C Bradley, CA Sackett, JJ Tollett, and Randall G Hulet. Evidence of bose-einstein condensation in an atomic gas with attractive interactions. Physical Review Letters, 75(9):1687, 1995.

[16] Brian DeMarco and Deborah S Jin. Onset of fermi degeneracy in a trapped atomic gas. Science, 285(5434):1703–1706, 1999.

[17] Christopher J Pethick and Henrik Smith. Bose-Einstein condensation in dilute gases. Cambridge university press, 2002.

[18] Franco Dalfovo, Stefano Giorgini, Lev P Pitaevskii, and Sandro Stringari. Theory of bose-einstein condensation in trapped gases. Reviews of Modern Physics, 71(3):463, 1999.

[19] N Bogoliubov. On the theory of superfluidity. J. Phys, 11(1):23, 1947.

[20] R. K. Pathria and Paul D. Beale. Statistical Mechanics. Academic Press, 3rd edition, 2011.

[21] Cheng Chin, Rudolf Grimm, Paul Julienne, and Eite Tiesinga. Feshbach resonances in ultracold gases. Reviews of Modern Physics, 82(2):1225, 2010.

[22] Christopher J Foot. Atomic physics, volume 7. Oxford University Press, 2005.

[23] AJ Moerdijk, BJ Verhaar, and A Axelsson. Resonances in ultracold collisions of li 6, li 7, and na 23. Physical Review A, 51(6):4852, 1995.

[24] Neil R Claussen, SJJMF Kokkelmans, Sarah T Thompson, Elizabeth A Donley, E Hodby, and CE Wieman. Very-high-precision bound-state spectroscopy near a 85 rb feshbach resonance. Physical Review A, 67(6):060701, 2003.

[25] Tsin D Lee, Kerson Huang, and Chen N Yang. Eigenvalues and eigenfunctions of a bose system of hard spheres and its low-temperature properties. Physical Review, 106(6):1135, 1957.

[26] PO Fedichev, MW Reynolds, and GV Shlyapnikov. Three-body recombination of ultracold atoms to a weakly bound s level. Physical review letters, 77(14):2921, 1996.

[27] BD Esry, Chris H Greene, and James P Burke Jr. Recombination of three atoms in the ultracold limit. Physical review letters, 83(9):1751, 1999.

[28] Paulo F Bedaque, Eric Braaten, and H-W Hammer. Three-body recombination in bose gases with large scattering length. Physical Review Letters, 85(5):908, 2000.

[29] Eric Braaten and H-W Hammer. Three-body recombination into deep bound states in a bose gas with large scattering length. Physical review letters, 87(16):160407, 2001.

[30] Tino Weber, Jens Herbig, Michael Mark, Hanns-Christoph Nägerl, and Rudolf Grimm. Three-body recombination at large scattering lengths in an ultracold atomic gas. Physical review letters, 91(12):123201, 2003.

[31] SB Papp, JM Pino, RJ Wild, S Ronen, Carl E Wieman, Deborah S Jin, and Eric A Cornell. Bragg spectroscopy of a strongly interacting rb 85 bose-einstein condensate. Physical review letters, 101(13):135301, 2008.

[32] Robert P Smith, Robert LD Campbell, Naaman Tammuz, and Zoran Hadzibabic. Effects of interactions on the critical temperature of a trapped bose gas. Physical review letters, 106(25):250403, 2011.

[33] Nir Navon, Swann Piatecki, Kenneth Günter, Benno Rem, Trong Canh Nguyen, Frédéric Chevy, Werner Krauth, and Christophe Salomon. Dynamics and thermodynamics of the low-temperature strongly interacting bose gas. Physical review letters, 107(13):135301, 2011.

[34] RJ Wild, P Makotyn, JM Pino, EA Cornell, and DS Jin. Measurements of tan's contact in an atomic bose-einstein condensate. Physical review letters, 108(14):145305, 2012.

[35] Philip Makotyn, Catherine E Klauss, David L Goldberger, EA Cornell, and Deborah S Jin. Universal dynamics of a degenerate unitary bose gas. Nature Physics, 10(2):116–119, 2014.

[36] Philip Makotyn. Experimental studies of a degenerate unitary Bose gas. PhD thesis, University of Colorado at Boulder, 2014.

[37] BS Rem, AT Grier, I Ferrier-Barbut, U Eismann, T Langen, N Navon, L Khaykovich, F Werner, DS Petrov, F Chevy, et al. Lifetime of the bose gas with resonant interactions. Physical review letters, 110(16):163202, 2013.

[38] Richard J Fletcher, Alexander L Gaunt, Nir Navon, Robert P Smith, and Zoran Hadzibabic. Stability of a unitary bose gas. Physical review letters, 111(12):125303, 2013.

[39] Ulrich Eismann, Lev Khaykovich, Sébastien Laurent, Igor Ferrier-Barbut, Benno S Rem, Andrew T Grier, Marion Delehaye, Frédéric Chevy, Christophe Salomon, Li-Chung Ha, et al. Universal loss dynamics in a unitary bose gas. Physical Review X, 6(2):021025, 2016.

[40] Richard J. Fletcher, Raphael Lopes, Jay Man, Nir Navon, Robert P. Smith, Martin W. Zwierlein, and Zoran Hadzibabic. Two- and three-body contacts in the unitary bose gas. Science, 355(6323):377–380, 2017.

[41] JM Diederix, TCF Van Heijst, and HTC Stoof. Ground state of a resonantly interacting bose gas. Physical Review A, 84(3):033618, 2011.

[42] Xiao Yin and Leo Radzihovsky. Quench dynamics of a strongly interacting resonant bose gas. Phys. Rev. A, 88:063611, Dec 2013.

[43] AG Sykes, JP Corson, JP D'Incao, AP Koller, CH Greene, AM Rey, KRA Hazzard, and JL Bohn. Quenching to unitarity: Quantum dynamics in a three-dimensional bose gas. Physical Review A, 89(2):021601, 2014.

[44] A. Rançon and K. Levin. Equilibrating dynamics in quenched bose gases: Characterizing multiple time regimes. Phys. Rev. A, 90:021602, Aug 2014.

[45] Sébastien Laurent, Xavier Leyronas, and Frédéric Chevy. Momentum distribution of a dilute unitary bose gas with three-body losses. Physical review letters, 113(22):220601, 2014.

[46] Maurizio Rossi, Luca Salasnich, Francesco Ancilotto, and Flavio Toigo. Monte carlo simulations of the unitary bose gas. Physical Review A, 89(4):041602, 2014.

[47] John P Corson and John L Bohn. Bound-state signatures in quenched bose-einstein condensates. Physical Review A, 91(1):013616, 2015.

[48] Shao-Jian Jiang, Jeff Maki, and Fei Zhou. Long-lived universal resonant bose gases. Physical Review A, 93(4):043605, 2016.

[49] Pascal Naidon and Shimpei Endo. Efimov physics: a review. Reports on Progress in Physics, 80(5):056001, 2017.

[50] Eric Braaten and H-W Hammer. Efimov physics in cold atoms. Annals of Physics, 322(1):120–163, 2007.

[51] T Kraemer, M Mark, P Waldburger, JG Danzl, C Chin, B Engeser, AD Lange, K Pilch, A Jaakkola, H-C Nägerl, et al. Evidence for efimov quantum states in an ultracold gas of caesium atoms. Nature, 440(7082):315–318, 2006.

[52] Matteo Zaccanti, Benjamin Deissler, Chiara D'Errico, Marco Fattori, Mattia Jona-Lasinio, Stefan Müller, Giacomo Roati, Massimo Inguscio, and Giovanni Modugno. Observation of an efimov spectrum in an atomic system. Nature Physics, 5(8):586–591, 2009.

[53] M Berninger, A Zenesini, B Huang, W Harm, H-C Nägerl, F Ferlaino, R Grimm, PS Julienne, and JM Hutson. Universality of the three-body parameter for efimov states in ultracold cesium. Physical review letters, 107(12):120401, 2011.

[54] Noam Gross, Zav Shotan, Servaas Kokkelmans, and Lev Khaykovich. Nuclear-spin-independent short-range three-body physics in ultracold atoms. Physical review letters, 105(10):103203, 2010.

[55] JH Huckans, JR Williams, EL Hazlett, RW Stites, and KM O'Hara. Three-body recombination in a three-state fermi gas with widely tunable interactions. Physical review letters, 102(16):165302, 2009.

[56] G Barontini, C Weber, F Rabatti, J Catani, G Thalhammer, M Inguscio, and F Minardi. Observation of heteronuclear atomic efimov resonances. Physical review letters, 103(4):043201, 2009.

[57] S Knoop, F Ferlaino, M Mark, M Berninger, H Schöbel, H-C Nägerl, and R Grimm. Observation of an efimov-like trimer resonance in ultracold atom–dimer scattering. Nature Physics, 5(3):227–230, 2009.

[58] Shuta Nakajima, Munekazu Horikoshi, Takashi Mukaiyama, Pascal Naidon, and Masahito Ueda. Nonuniversal efimov atom-dimer resonances in a three-component mixture of li 6. Physical review letters, 105(2):023201, 2010.

[59] Alessandro Zenesini, Bo Huang, Martin Berninger, H-C Nägerl, Francesca Ferlaino, and Rudolf Grimm. Resonant atom-dimer collisions in cesium: Testing universality at positive scattering lengths. Physical Review A, 90(2):022704, 2014.

[60] Ruth S Bloom, Ming-Guang Hu, Tyler D Cumby, and Deborah S Jin. Tests of universal three-body physics in an ultracold bose-fermi mixture. Physical review letters, 111(10):105301, 2013.

[61] T Lompe, TB Ottenstein, F Serwane, K Viering, AN Wenz, G Zürn, and S Jochim. Atom-dimer scattering in a three-component fermi gas. Physical review letters, 105(10):103201, 2010.

[62] Thomas Lompe, Timo B Ottenstein, Friedhelm Serwane, Andre N Wenz, Gerhard Zürn, and Selim Jochim. Radio-frequency association of efimov trimers. Science, 330(6006):940–944, 2010.

[63] Olga Machtey, Zav Shotan, Noam Gross, and Lev Khaykovich. Association of efimov trimers from a three-atom continuum. Physical review letters, 108(21):210406, 2012.

[64] Shuta Nakajima, Munekazu Horikoshi, Takashi Mukaiyama, Pascal Naidon, and Masahito Ueda. Measurement of an efimov trimer binding energy in a three-component mixture of li 6. Physical review letters, 106(14):143201, 2011.

[65] Maksim Kunitski, Stefan Zeller, Jörg Voigtsberger, Anton Kalinin, Lothar Ph H Schmidt, Markus Schöffler, Achim Czasch, Wieland Schöllkopf, Robert E Grisenti, Till Jahnke, et al. Observation of the efimov state of the helium trimer. Science, 348(6234):551–555, 2015.

[66] Paul Mestrom, Jia Wang, Chris H Greene, and Jose P D'Incao. Efimov universality for ultracold atoms with positive scattering lengths. arXiv preprint arXiv:1609.02857, 2016.

[67] Tino Weber, Jens Herbig, Michael Mark, Hanns-Christoph Nägerl, and Rudolf Grimm. Bose-einstein condensation of cesium. Science, 299(5604):232–235, 2003.

[68] Esben Nielsen and JH Macek. Low-energy recombination of identical bosons by three-body collisions. Physical review letters, 83(8):1566, 1999.

[69] José P DIncao, Hiroya Suno, and Brett D Esry. Limits on universality in ultracold three-boson recombination. Physical review letters, 93(12):123201, 2004.

[70] Frederic Chevy and Christophe Salomon. Strongly correlated bose gases. Journal of Physics B: Atomic, Molecular and Optical Physics, 49(19):192001, 2016.

[71] Noam Gross, Zav Shotan, Servaas Kokkelmans, and Lev Khaykovich. Observation of universality in ultracold li 7 three-body recombination. Physical review letters, 103(16):163202, 2009.

[72] F Ferlaino, A Zenesini, M Berninger, B Huang, H-C Nägerl, and R Grimm. Efimov resonances in ultracold quantum gases. Few-Body Systems, 51(2-4):113–133, 2011.

[73] Scott B Papp. Experiments with a two-species Bose-Einstein condensate utilizing widely tunable interparticle interactions. PhD thesis, University of Colorado at Boulder, 2007.

[74] Juan Manuel Pino II. Strongly interacting Bose-Einstein condensates: probes and techniques. PhD thesis, University of Colorado at Boulder, 2010.

[75] Robert Johannes Wild. Contact measurements on a strongly interacting Bose gas. PhD thesis, University of Colorado at Boulder, 2012.

[76] Jacob Lyman Roberts. Bose-Einstein condensates with tunable atom-atom interactions: The first experiments with rubidium-85 BECs. PhD thesis, 2001.

[77] David Goldberger. Improving Imaging Resolution For In-Situ Measurements of Bose-Einstein Condensates. B.S. Thesis, University of Colorado at Boulder, 2015.

[78] G Reinaudi, T Lahaye, Z Wang, and D Guéry-Odelin. Strong saturation absorption imaging of dense clouds of ultracold atoms. Optics letters, 32(21):3143–3145, 2007.

[79] Daniel A Steck. Alkali d line data. URL http://steck. us/alkalidata, 2012.

[80] Alexander L Gaunt, Tobias F Schmidutz, Igor Gotlibovych, Robert P Smith, and Zoran Hadzibabic. Bose-einstein condensation of atoms in a uniform potential. Physical review letters, 110(20):200406, 2013.

[81] Tara E Drake. Measuring local properties of a Fermi gas in the BCS-BEC crossover. PhD thesis, University of Colorado, 2015.

[82] Victor M Perez-Garcia, Humberto Michinel, JI Cirac, M Lewenstein, and P Zoller. Dynamics of bose-einstein condensates: Variational solutions of the gross-pitaevskii equations. Physical Review A, 56(2):1424, 1997.

[83] Benno S Rem. The Road to the Unitary Bose Gas. PhD thesis, Ecole Normale Supérieure de Paris-ENS Paris, 2013.

[84] private communication with J. P. D'Incao.

[85] Elizabeth A Donley, Neil R Claussen, Sarah T Thompson, and Carl E Wieman. Atom–molecule coherence in a bose–einstein condensate. Nature, 417(6888):529–533, 2002.

[86] Cheng Chin and Paul S. Julienne. Radio-frequency transitions on weakly bound ultracold molecules. Phys. Rev. A, 71:012713, Jan 2005.

[87] Eric W. Weisstein. Blackman function, 1999.

[88] Ehud Altman and Ashvin Vishwanath. Dynamic projection on feshbach molecules: A probe of pairing and phase fluctuations. Physical review letters, 95(11):110404, 2005.

[89] P Dyke, SE Pollack, and RG Hulet. Finite-range corrections near a feshbach resonance and their role in the efimov effect. Physical Review A, 88(2):023625, 2013.

[90] Thorsten Koehler, Eite Tiesinga, and Paul S Julienne. Spontaneous dissociation of long-range feshbach molecules. Physical review letters, 94(2):020402, 2005.

[91] Eric Braaten and H-W Hammer. Enhanced dimer relaxation in an atomic and molecular bose-einstein condensate. Physical Review A, 70(4):042706, 2004.

[92] Eric Braaten and H-W Hammer. Resonant dimer relaxation in cold atoms with a large scattering length. Physical Review A, 75(5):052710, 2007.

[93] S. T. Thompson, E. Hodby, and C. E. Wieman. Spontaneous dissociation of ^{85}Rb feshbach molecules. Phys. Rev. Lett., 94:020401, Jan 2005.

Appendix A

Plot Legend

Because there are many knobs in our experiment, we have created a legend to record each variable. the legend is printed in gray on most plots, an example is shown in figure A.1; if more than one dataset is plotted, the legend may vary in color. The legend (in order) includes: the date the data was taken \\ the magnetic ramp to resonance as r_{in} - dwell time - r_{out} / the calculated t_{dwell} in units of t_n \\ the final B-field (in Gauss) for imaging \ a_f in a_0 (only if the field was measured precisely) \\ the shape of the RF pulse (sq = square, G = Gaussian, c = curved, ARP = adiabatic rapid passage) with the duration in μs or ms \\ The set RF power in dBm, the detuning of the RF from the atomic line shape in kHz, and whether the RF was adjusted with dwell time to track the falling cloud (represented by binary 1 or 0) \\ the average BEC number, before resonance.

If this data has variation of any of these parameters, the name will appear in place of an actual value. For some plots, this information may be omitted altogether.

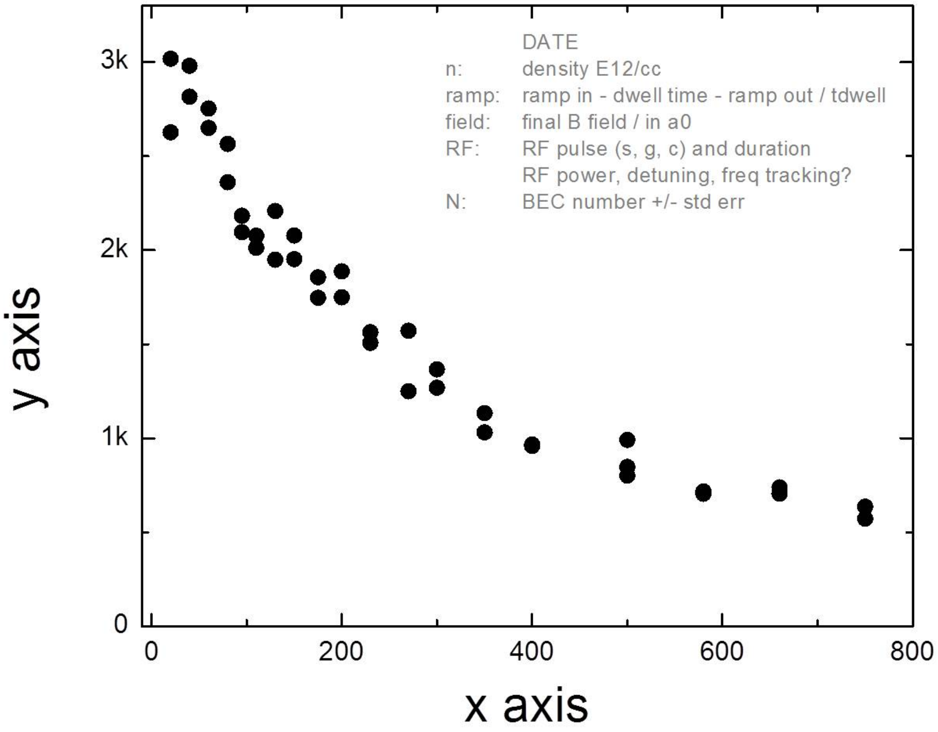

Figure A.1: An example data set with a plot legend in the upper right corner.

Appendix B

Dimer lifetime fits

Here are nine datasets measuring molecular number as a function of hold time at $a_f = 500$, 700, or 1000 a_0. The initial densities of the condensate before the resonance jump are about $n =$ 0.2, 1.3, and 5 E12/cc. The molecules were created by spending $t_{\mathrm{dwell}} = 1.5\, t_n$ on resonance before ramping away to a_f at a rate of ramp time = 100 μs. We fit these times beyond 500 μs to extract the dimer lifetime.

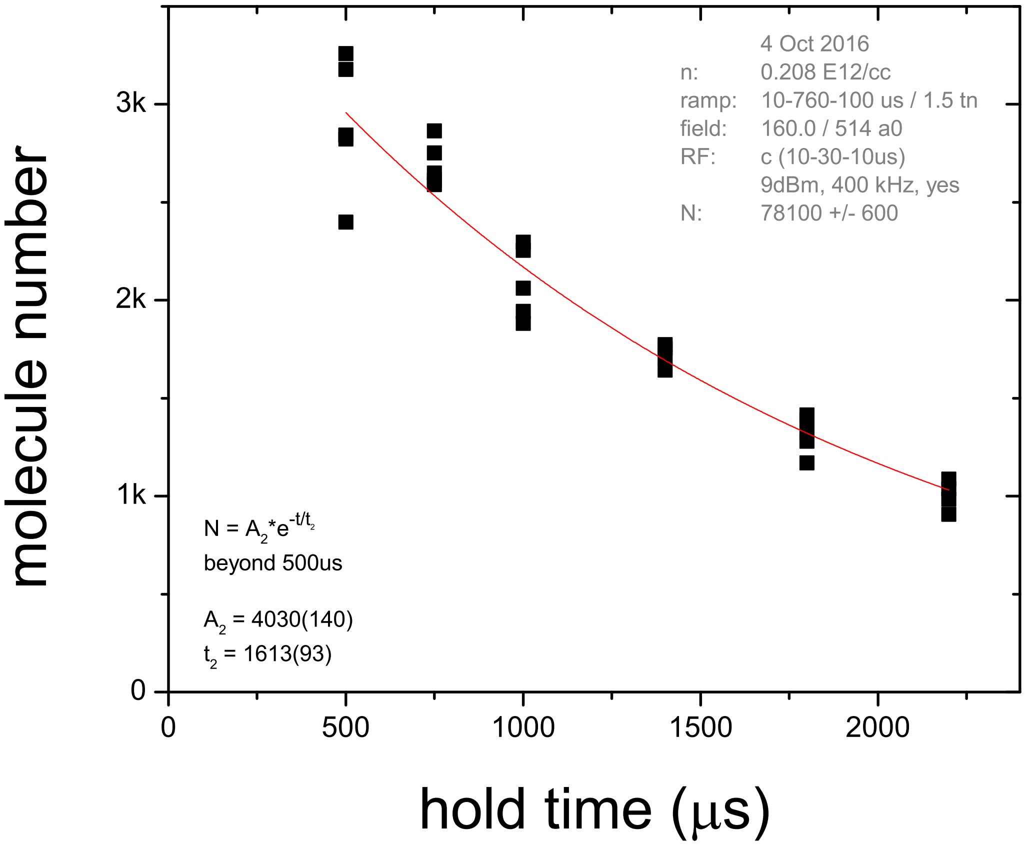
4 Oct 2016
n: 0.208 E12/cc
ramp: 10-760-100 us / 1.5 tn
field: 160.0 / 514 a0
RF: c (10-30-10us)
9dBm, 400 kHz, yes
N: 78100 +/- 600
N = A2*e^-t/t2
beyond 500us
A2 = 4030(140)
t2 = 1613(93)
molecule number
0
1k
2k
3k
0
500
1000
1500
2000
hold time (μs)

Figure B.1

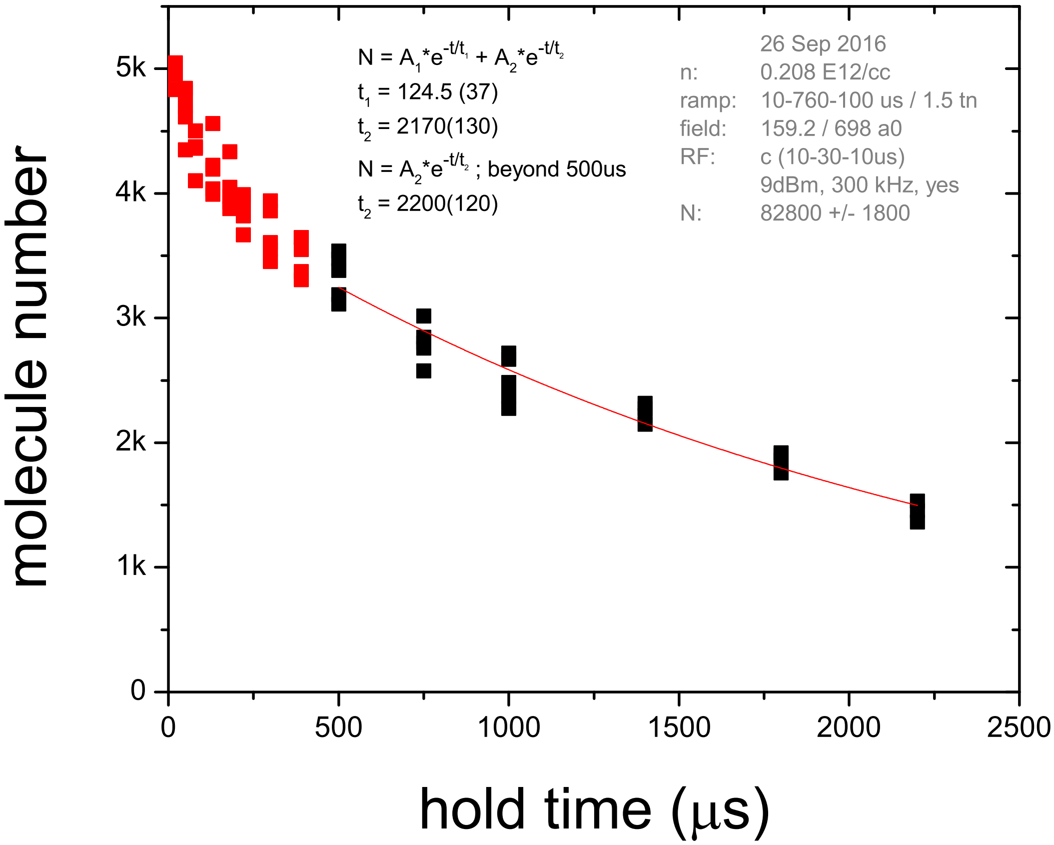

N = A$_1$*e$^{-t/t_1}$ + A$_2$*e$^{-t/t_2}$
t$_1$ = 124.5 (37)
t$_2$ = 2170(130)
N = A$_2$*e$^{-t/t_2}$; beyond 500us
t$_2$ = 2200(120)
26 Sep 2016
n: 0.208 E12/cc
ramp: 10-760-100 us / 1.5 tn
field: 159.2 / 698 a0
RF: c (10-30-10us)
9dBm, 300 kHz, yes
N: 82800 +/- 1800
molecule number
0
1k
2k
3k
4k
5k
0
500
1000
1500
2000
2500
hold time (μs)

Figure B.2

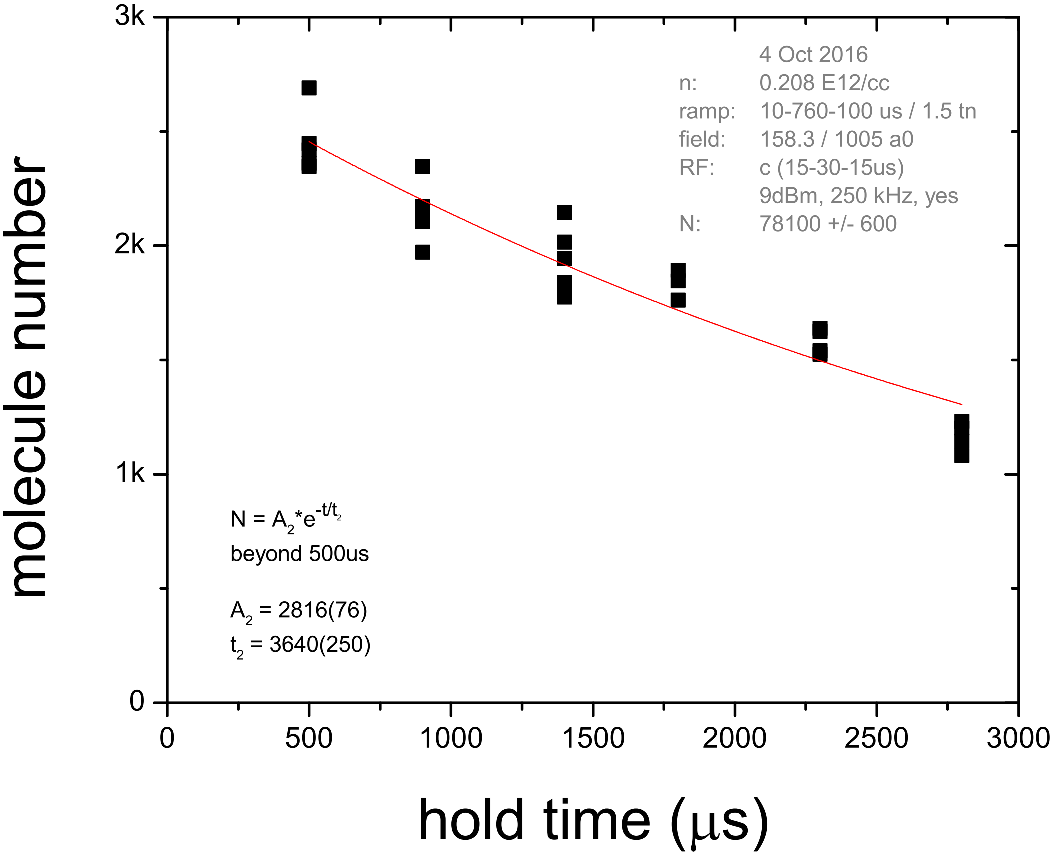
3k
2k
1k
0
0
500
1000
1500
2000
2500
3000
molecule number
hold time (μs)
4 Oct 2016
n: 0.208 E12/cc
ramp: 10-760-100 us / 1.5 tn
field: 158.3 / 1005 a0
RF: c (15-30-15us)
9dBm, 250 kHz, yes
N: 78100 +/- 600
N = A2*e-t/t2
beyond 500us
A2 = 2816(76)
t2 = 3640(250)

Figure B.3

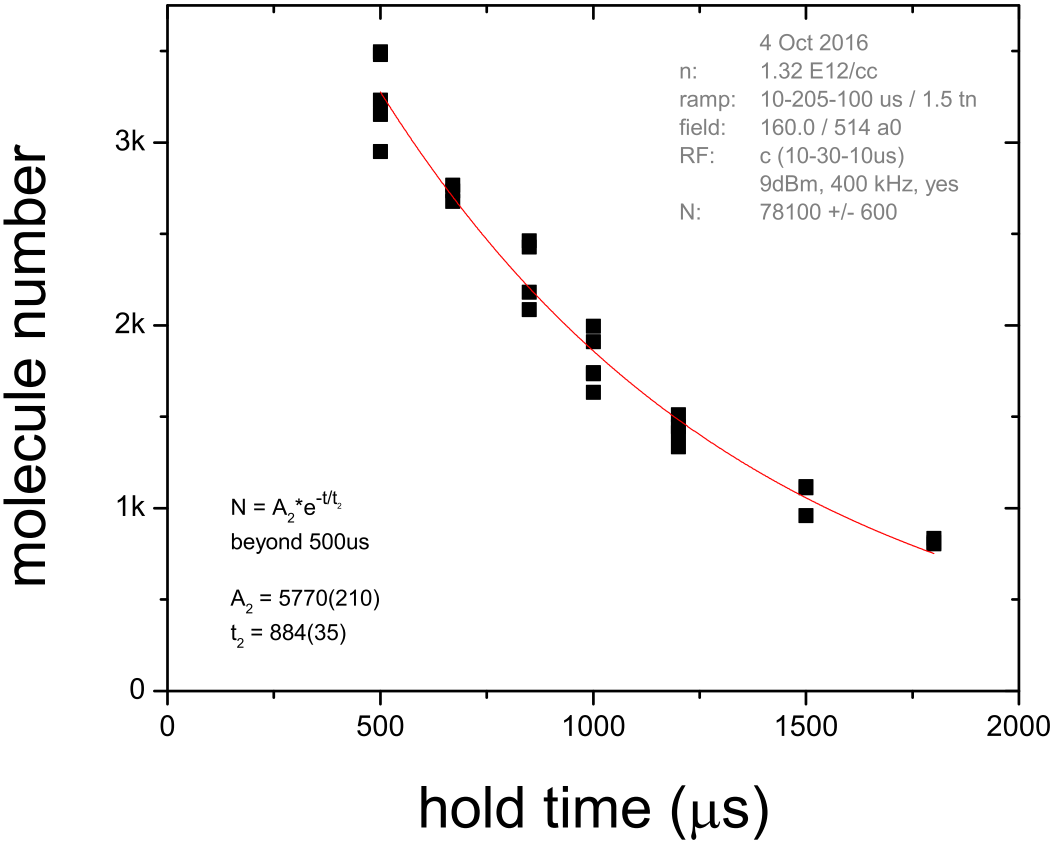

4 Oct 2016
n: 1.32 E12/cc
ramp: 10-205-100 us / 1.5 tn
field: 160.0 / 514 a0
RF: c (10-30-10us)
9dBm, 400 kHz, yes
N: 78100 +/- 600
$N = A_2 * e^{-t/t_2}$
beyond 500us
A_2 = 5770(210)
t_2 = 884(35)
molecule number
0
1k
2k
3k
0
500
1000
1500
2000
hold time (μs)

Figure B.4

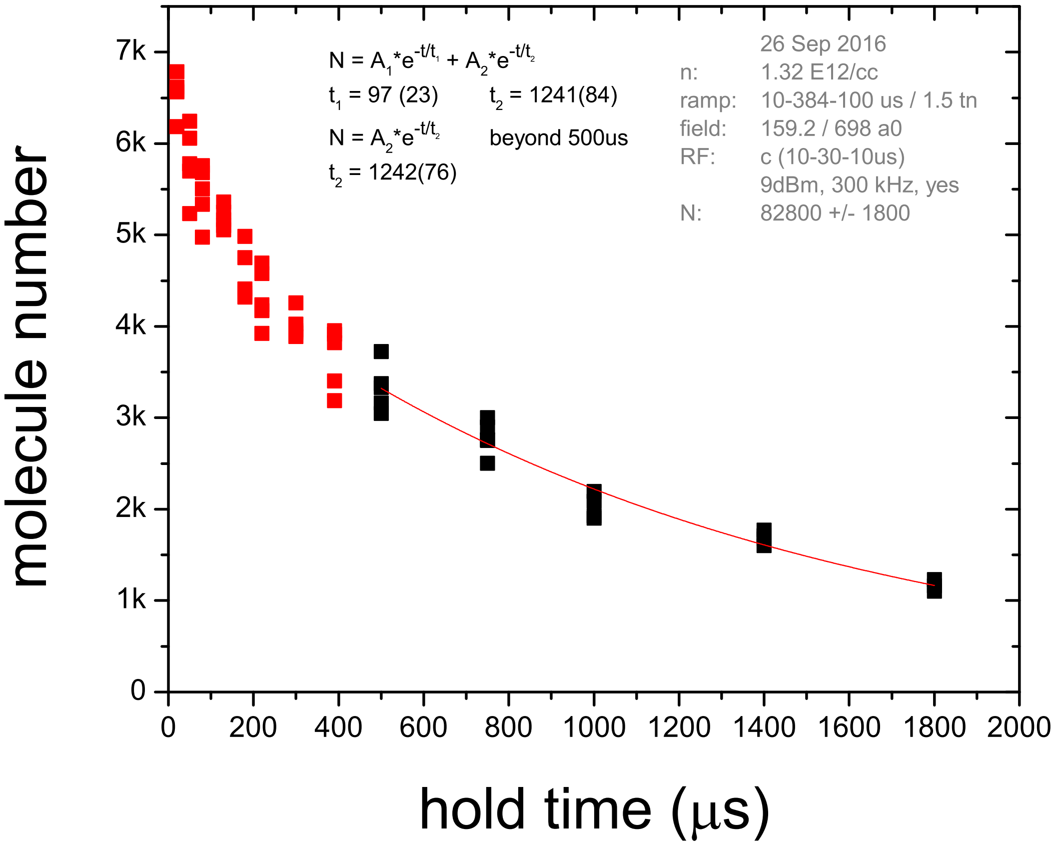

molecule number
7k
6k
5k
4k
3k
2k
1k
0
0
200
400
600
800
1000
1200
1400
1600
1800
2000
hold time (μs)
N = A$_1$*e$^{-t/t_1}$ + A$_2$*e$^{-t/t_2}$
t$_1$ = 97 (23)
t$_2$ = 1241(84)
N = A$_2$*e$^{-t/t_2}$
beyond 500us
t$_2$ = 1242(76)
26 Sep 2016
n: 1.32 E12/cc
ramp: 10-384-100 us / 1.5 tn
field: 159.2 / 698 a0
RF: c (10-30-10us)
9dBm, 300 kHz, yes
N: 82800 +/- 1800

Figure B.5

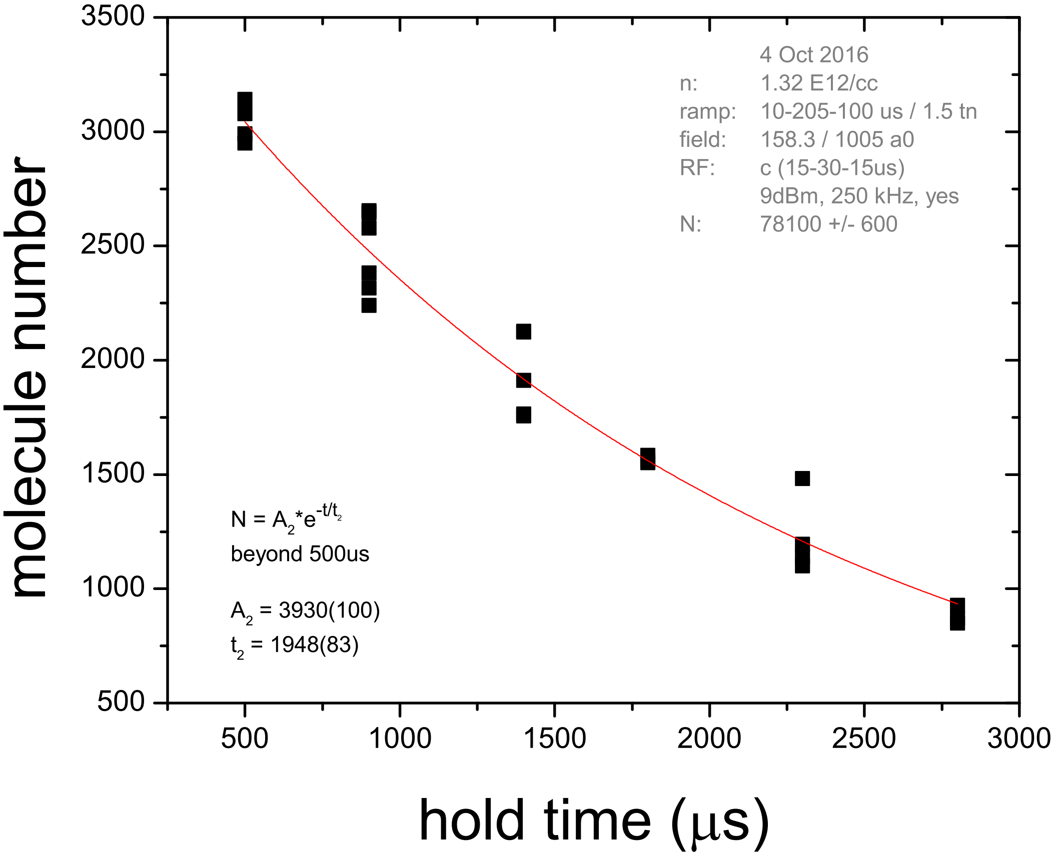

3500
3000
2500
2000
1500
1000
500
molecule number
500
1000
1500
2000
2500
3000
hold time (μs)
4 Oct 2016
n: 1.32 E12/cc
ramp: 10-205-100 us / 1.5 tn
field: 158.3 / 1005 a0
RF: c (15-30-15us)
9dBm, 250 kHz, yes
N: 78100 +/- 600
$N = A_2 * e^{-t/t_2}$
beyond 500us
A_2 = 3930(100)
t_2 = 1948(83)

Figure B.6

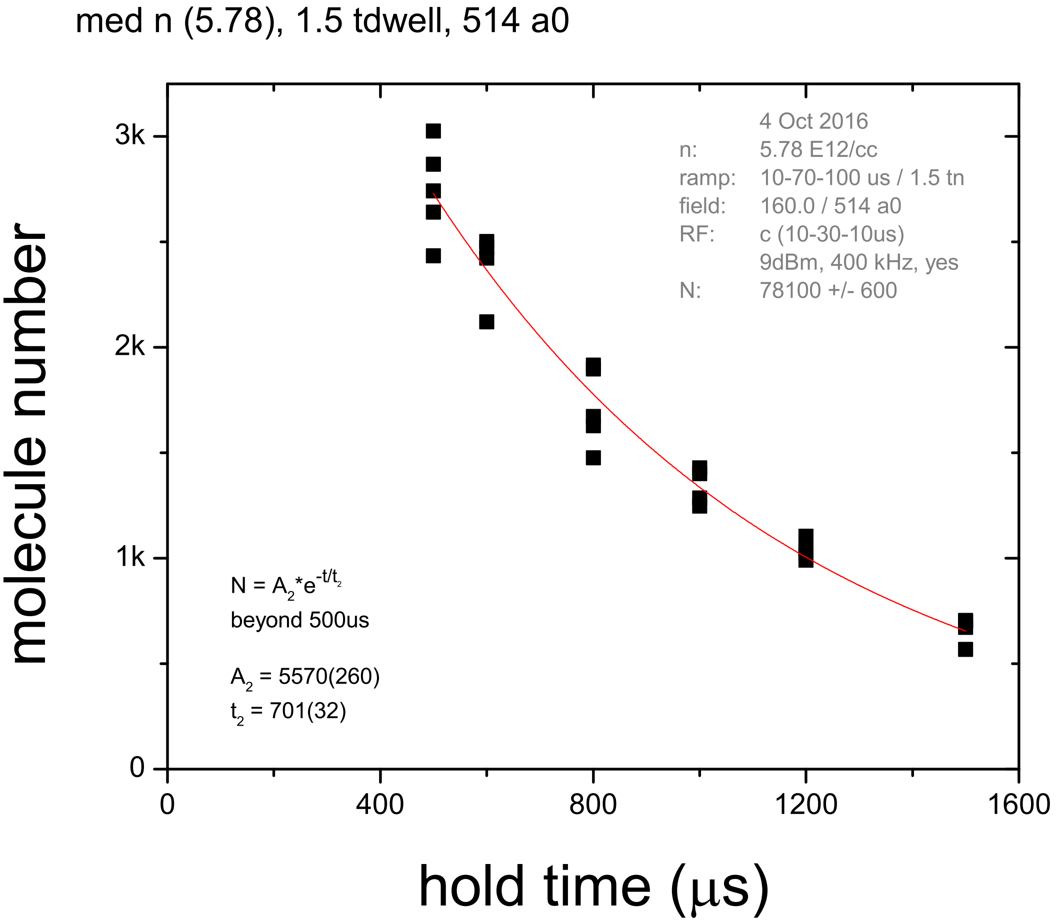
med n (5.78), 1.5 tdwell, 514 a0
4 Oct 2016
n: 5.78 E12/cc
ramp: 10-70-100 us / 1.5 tn
field: 160.0 / 514 a0
RF: c (10-30-10us)
9dBm, 400 kHz, yes
N: 78100 +/- 600
N = A$_2$*e$^{-t/t_2}$
beyond 500us
A$_2$ = 5570(260)
t$_2$ = 701(32)
molecule number
3k
2k
1k
0
0
400
800
1200
1600
hold time (μs)

Figure B.7

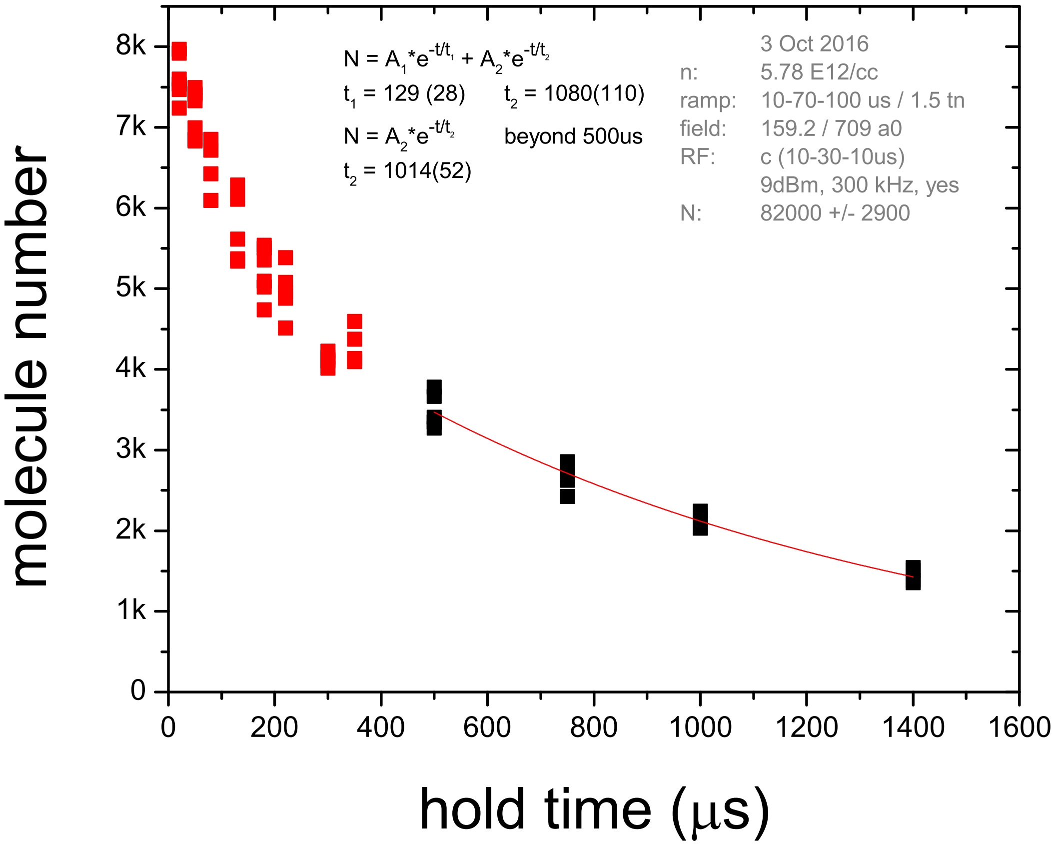
N = A1*e-t/t1 + A2*e-t/t2
t1 = 129 (28)
t2 = 1080(110)
N = A2*e-t/t2
beyond 500us
t2 = 1014(52)
3 Oct 2016
n: 5.78 E12/cc
ramp: 10-70-100 us / 1.5 tn
field: 159.2 / 709 a0
RF: c (10-30-10us)
9dBm, 300 kHz, yes
N: 82000 +/- 2900
molecule number
0
1k
2k
3k
4k
5k
6k
7k
8k
hold time (μs)
0
200
400
600
800
1000
1200
1400
1600

Figure B.8

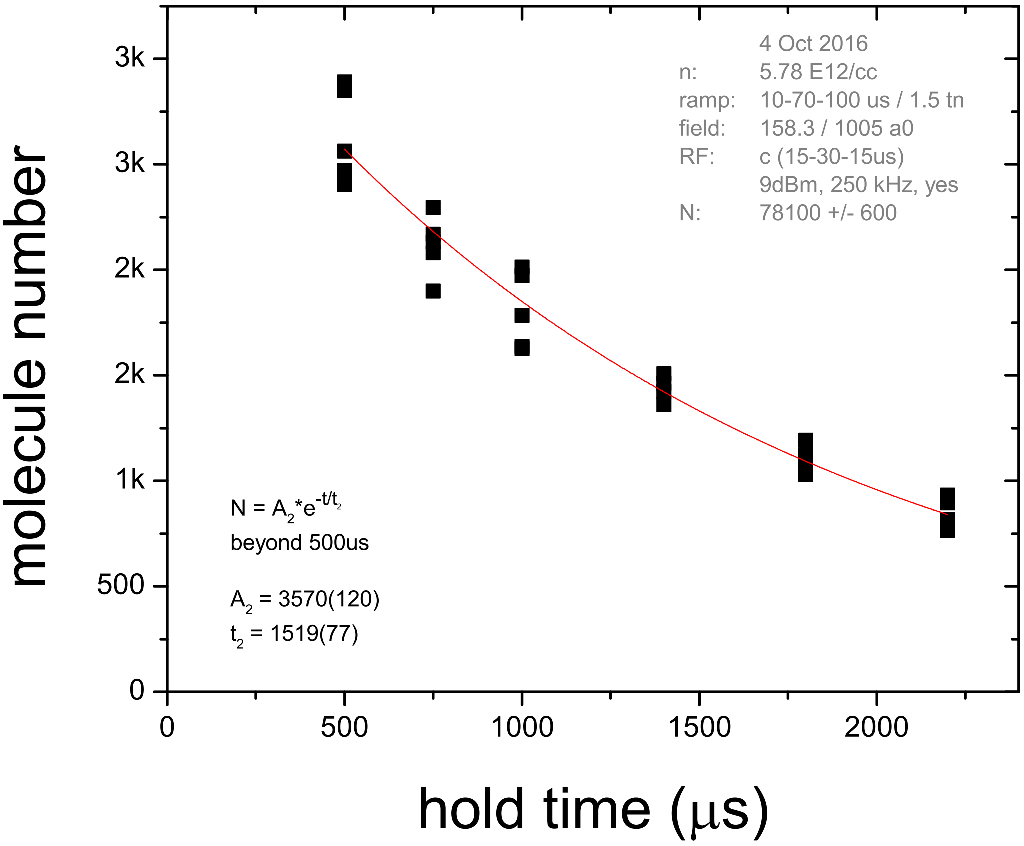
4 Oct 2016
n: 5.78 E12/cc
ramp: 10-70-100 us / 1.5 tn
field: 158.3 / 1005 a0
RF: c (15-30-15us)
9dBm, 250 kHz, yes
N: 78100 +/- 600
N = A$_2$*e$^{-t/t_2}$
beyond 500us
A$_2$ = 3570(120)
t$_2$ = 1519(77)
molecule number
3k
3k
2k
2k
1k
500
0
0
500
1000
1500
2000
hold time (μs)

Figure B.9

Appendix C

Trimer and Dimer lifetime measurements vs dwell time

Here are ten datasets measuring molecular number as a function of hold time at $a_f = 700$ a_0. The initial density of the condensate before the resonance jump was either $n = 1.36$ E12/cc or $n = 1.32$ E12/cc. The molecules were created by spending a variable amount of time on resonance, t_{dwell} before ramping away to a_f at a rate of ramp time = 100 μs (for the first eight datasets - the last two datasets vary the ramp out rate). They were all imaged using a 50 μs curved microwave pulse detuned 300 kHz from the atomic resonance. We attempted to fit these times with a sum of two exponentials to extract both the dimer and trimer amplitudes. Due to the strange behavior, we at times had to fit while fixing either t_1 (green) or t_2 (blue) to their expected values.

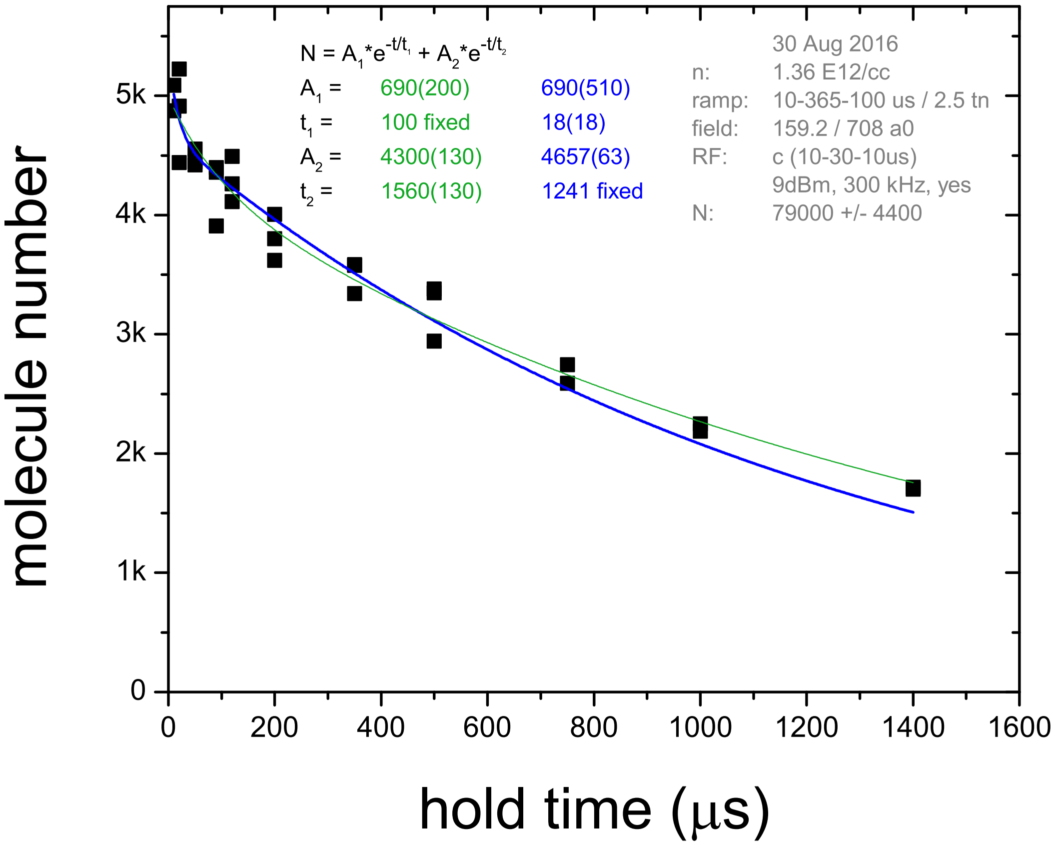
N = A1*e^-t/t1 + A2*e^-t/t2
A1 = 690(200) 690(510)
t1 = 100 fixed 18(18)
A2 = 4300(130) 4657(63)
t2 = 1560(130) 1241 fixed
30 Aug 2016
n: 1.36 E12/cc
ramp: 10-365-100 us / 2.5 tn
field: 159.2 / 708 a0
RF: c (10-30-10us)
9dBm, 300 kHz, yes
N: 79000 +/- 4400
molecule number
0
1k
2k
3k
4k
5k
0
200
400
600
800
1000
1200
1400
1600
hold time (μs)

Figure C.1

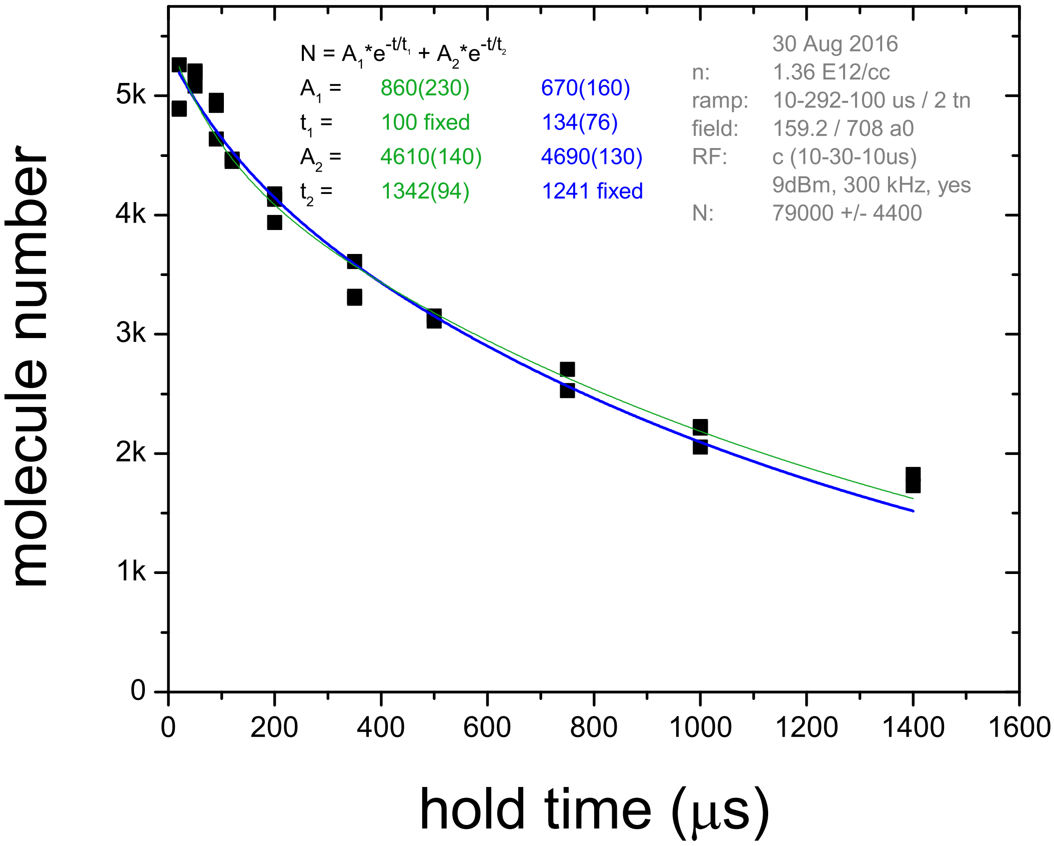
N = A₁*e^-t/t₁ + A₂*e^-t/t₂
A₁ = 860(230) 670(160)
t₁ = 100 fixed 134(76)
A₂ = 4610(140) 4690(130)
t₂ = 1342(94) 1241 fixed
30 Aug 2016
n: 1.36 E12/cc
ramp: 10-292-100 us / 2 tn
field: 159.2 / 708 a0
RF: c (10-30-10us)
9dBm, 300 kHz, yes
N: 79000 +/- 4400
molecule number
0
1k
2k
3k
4k
5k
0
200
400
600
800
1000
1200
1400
1600
hold time (μs)

Figure C.2

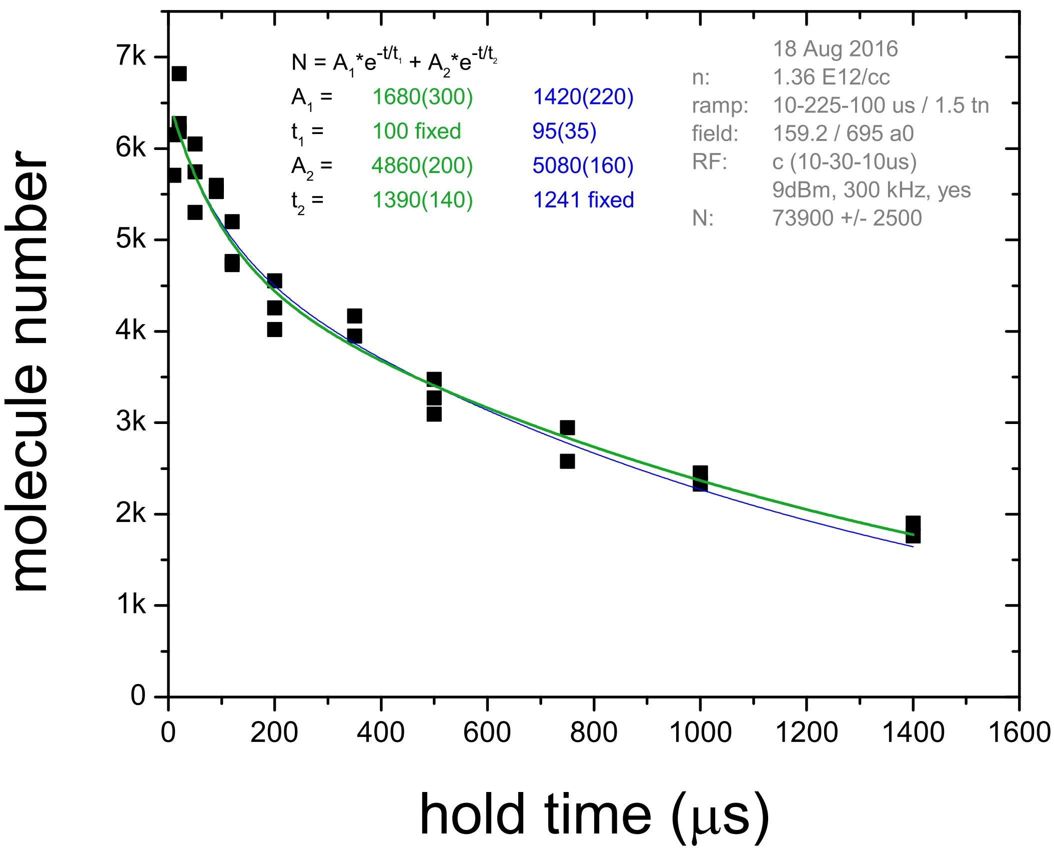

N = A1*e^-t/t1 + A2*e^-t/t2
A1 = 1680(300) 1420(220)
t1 = 100 fixed 95(35)
A2 = 4860(200) 5080(160)
t2 = 1390(140) 1241 fixed
18 Aug 2016
n: 1.36 E12/cc
ramp: 10-225-100 us / 1.5 tn
field: 159.2 / 695 a0
RF: c (10-30-10us)
9dBm, 300 kHz, yes
N: 73900 +/- 2500
molecule number
7k
6k
5k
4k
3k
2k
1k
0
0
200
400
600
800
1000
1200
1400
1600
hold time (μs)

Figure C.3

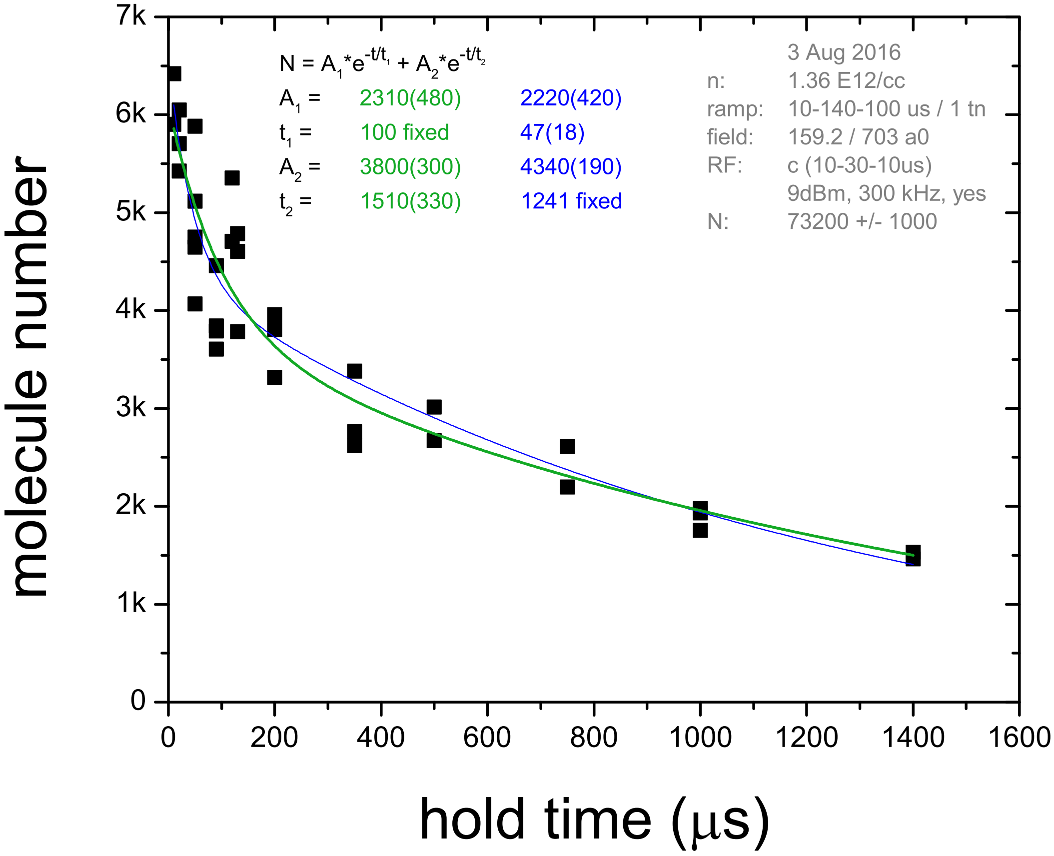
N = A$_1$*e$^{-t/t_1}$ + A$_2$*e$^{-t/t_2}$
A$_1$ = 2310(480) 2220(420)
t$_1$ = 100 fixed 47(18)
A$_2$ = 3800(300) 4340(190)
t$_2$ = 1510(330) 1241 fixed
3 Aug 2016
n: 1.36 E12/cc
ramp: 10-140-100 us / 1 tn
field: 159.2 / 703 a0
RF: c (10-30-10us)
9dBm, 300 kHz, yes
N: 73200 +/- 1000
molecule number
hold time (μs)
0
1k
2k
3k
4k
5k
6k
7k
0
200
400
600
800
1000
1200
1400
1600

Figure C.4

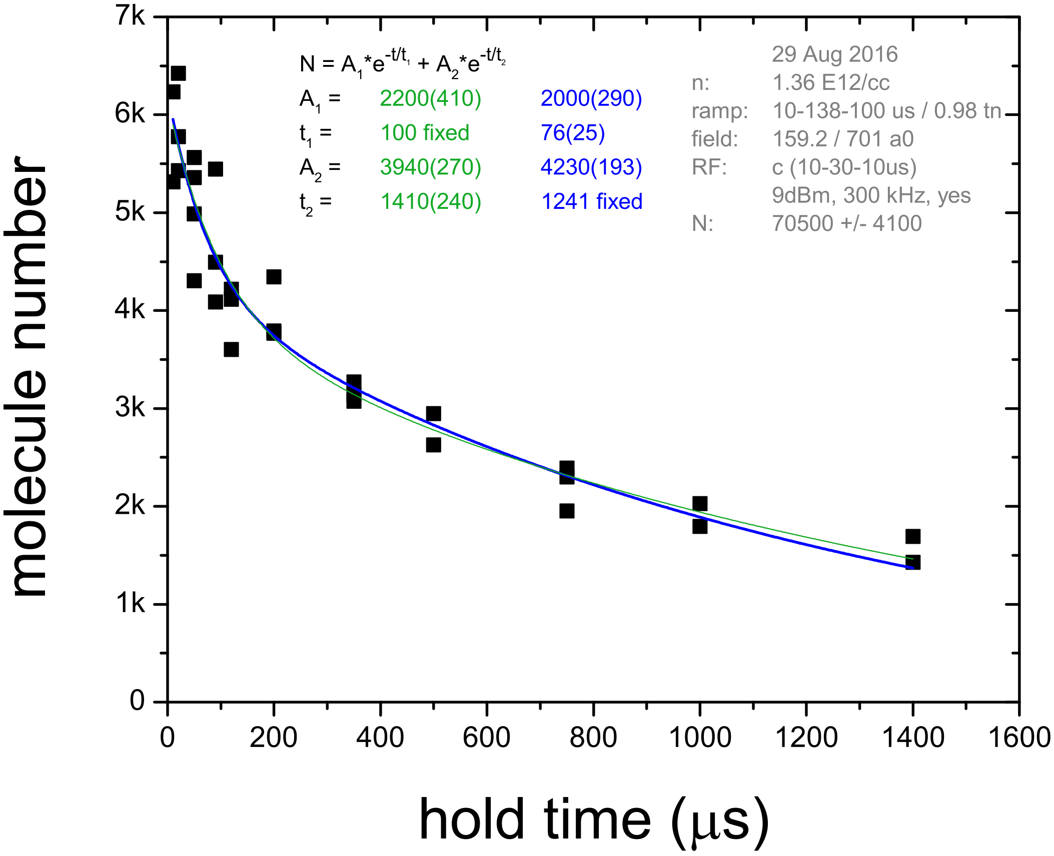

7k
6k
5k
4k
3k
2k
1k
0
0
200
400
600
800
1000
1200
1400
1600
molecule number
hold time (μs)
$N = A_1 * e^{-t/t_1} + A_2 * e^{-t/t_2}$
A_1 = 2200(410) 2000(290)
t_1 = 100 fixed 76(25)
A_2 = 3940(270) 4230(193)
t_2 = 1410(240) 1241 fixed
29 Aug 2016
n: 1.36 E12/cc
ramp: 10-138-100 us / 0.98 tn
field: 159.2 / 701 a0
RF: c (10-30-10us)
9dBm, 300 kHz, yes
N: 70500 +/- 4100

Figure C.5

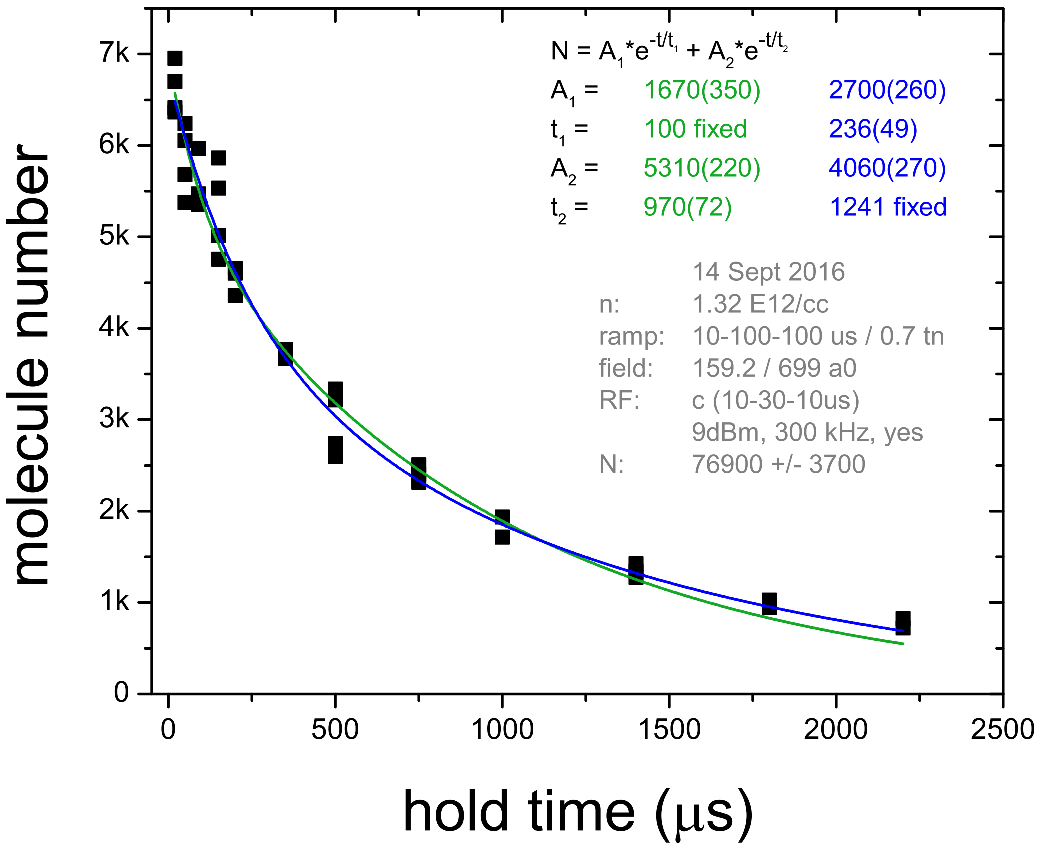
$N = A_1 * e^{-t/t_1} + A_2 * e^{-t/t_2}$
A_1 = 1670(350) 2700(260)
t_1 = 100 fixed 236(49)
A_2 = 5310(220) 4060(270)
t_2 = 970(72) 1241 fixed
14 Sept 2016
n: 1.32 E12/cc
ramp: 10-100-100 us / 0.7 tn
field: 159.2 / 699 a0
RF: c (10-30-10us)
9dBm, 300 kHz, yes
N: 76900 +/- 3700
7k
6k
5k
4k
3k
2k
1k
0
0
500
1000
1500
2000
2500
molecule number
hold time (μs)

Figure C.6

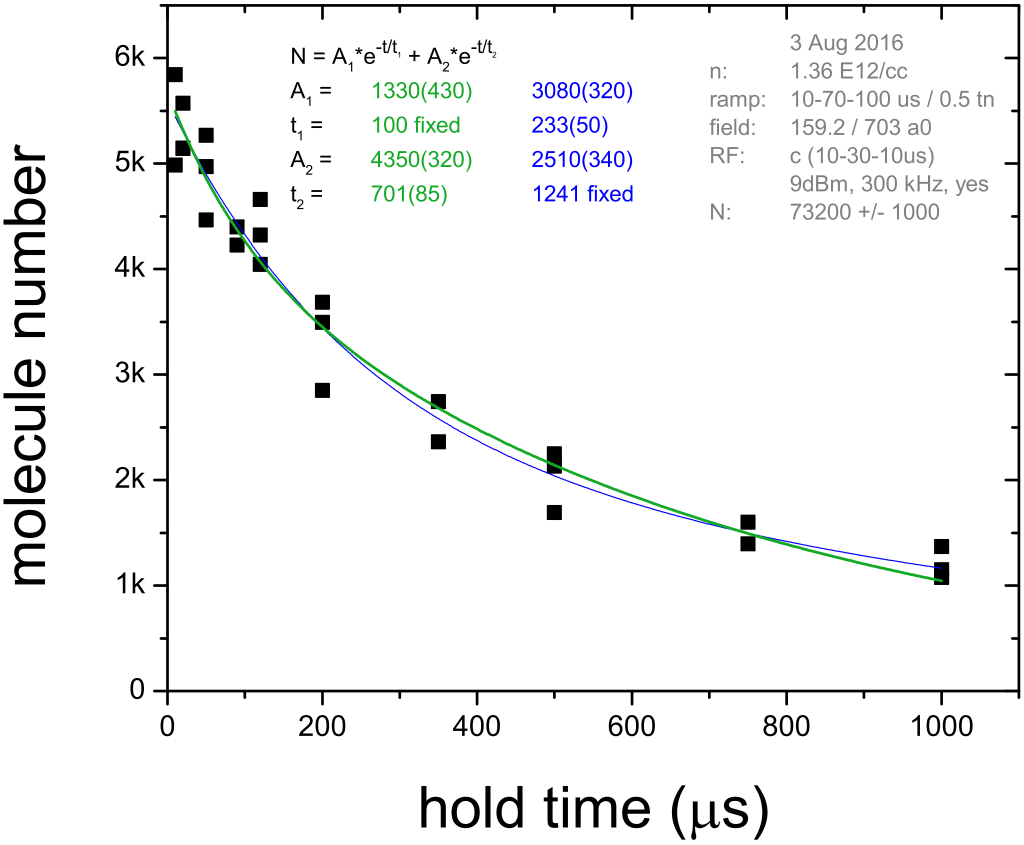
N = A_1*e^{-t/t_1} + A_2*e^{-t/t_2}
A_1 = 1330(430) 3080(320)
t_1 = 100 fixed 233(50)
A_2 = 4350(320) 2510(340)
t_2 = 701(85) 1241 fixed
3 Aug 2016
n: 1.36 E12/cc
ramp: 10-70-100 us / 0.5 tn
field: 159.2 / 703 a0
RF: c (10-30-10us)
9dBm, 300 kHz, yes
N: 73200 +/- 1000
molecule number
6k
5k
4k
3k
2k
1k
0
0
200
400
600
800
1000
hold time (μs)

Figure C.7

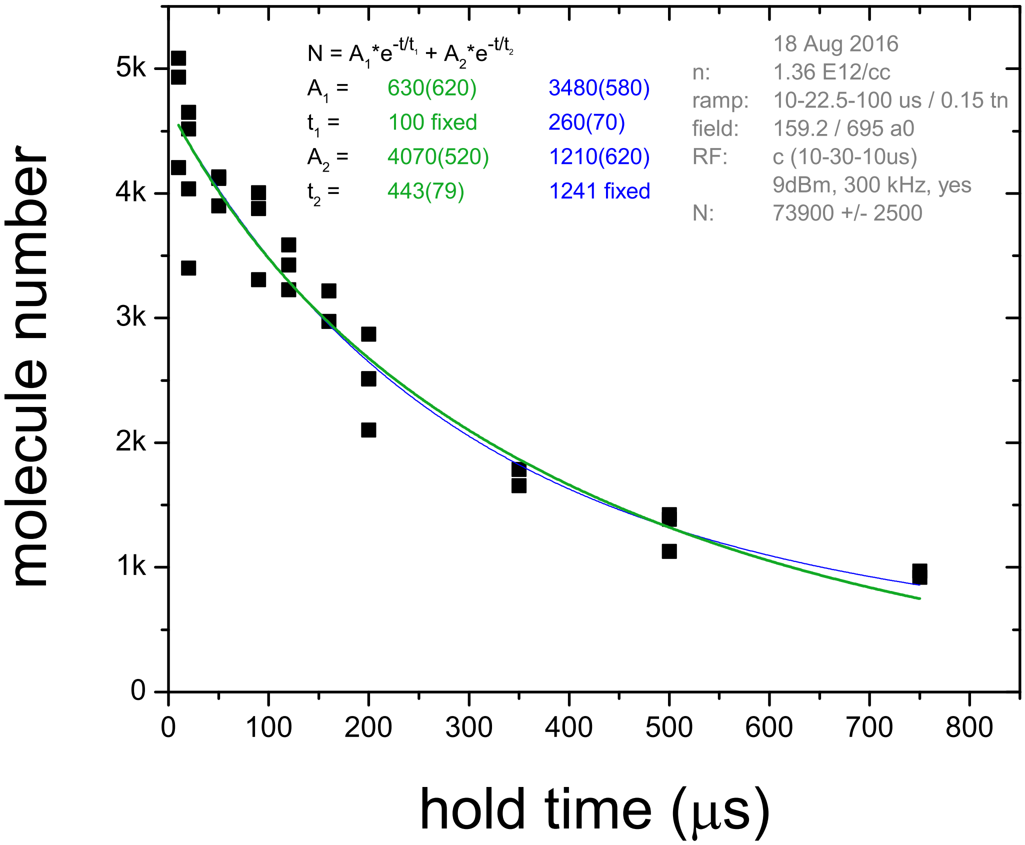
N = A1*e^-t/t1 + A2*e^-t/t2
A1 = 630(620) 3480(580)
t1 = 100 fixed 260(70)
A2 = 4070(520) 1210(620)
t2 = 443(79) 1241 fixed
18 Aug 2016
n: 1.36 E12/cc
ramp: 10-22.5-100 us / 0.15 tn
field: 159.2 / 695 a0
RF: c (10-30-10us)
9dBm, 300 kHz, yes
N: 73900 +/- 2500
molecule number
0
1k
2k
3k
4k
5k
hold time (μs)
0
100
200
300
400
500
600
700
800

Figure C.8

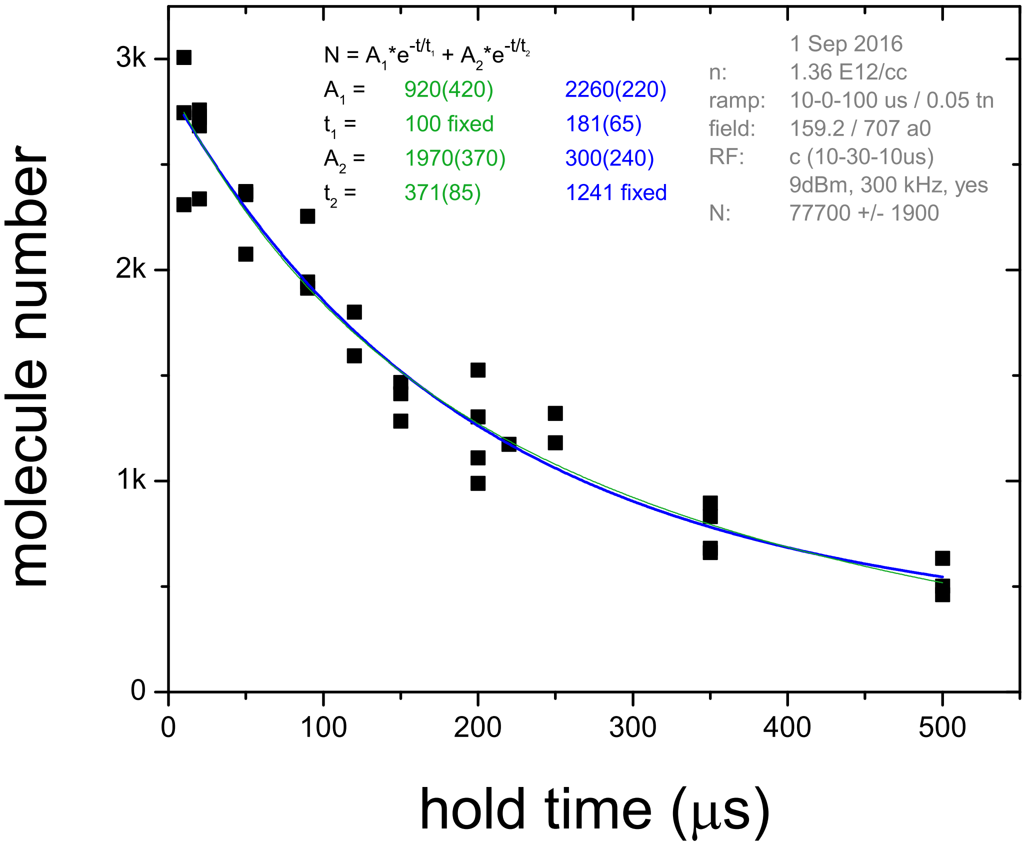
N = A_1*e^-t/t_1 + A_2*e^-t/t_2
A_1 = 920(420) 2260(220)
t_1 = 100 fixed 181(65)
A_2 = 1970(370) 300(240)
t_2 = 371(85) 1241 fixed
1 Sep 2016
n: 1.36 E12/cc
ramp: 10-0-100 us / 0.05 tn
field: 159.2 / 707 a0
RF: c (10-30-10us)
9dBm, 300 kHz, yes
N: 77700 +/- 1900
molecule number
0
1k
2k
3k
0
100
200
300
400
500
hold time (μs)

Figure C.9

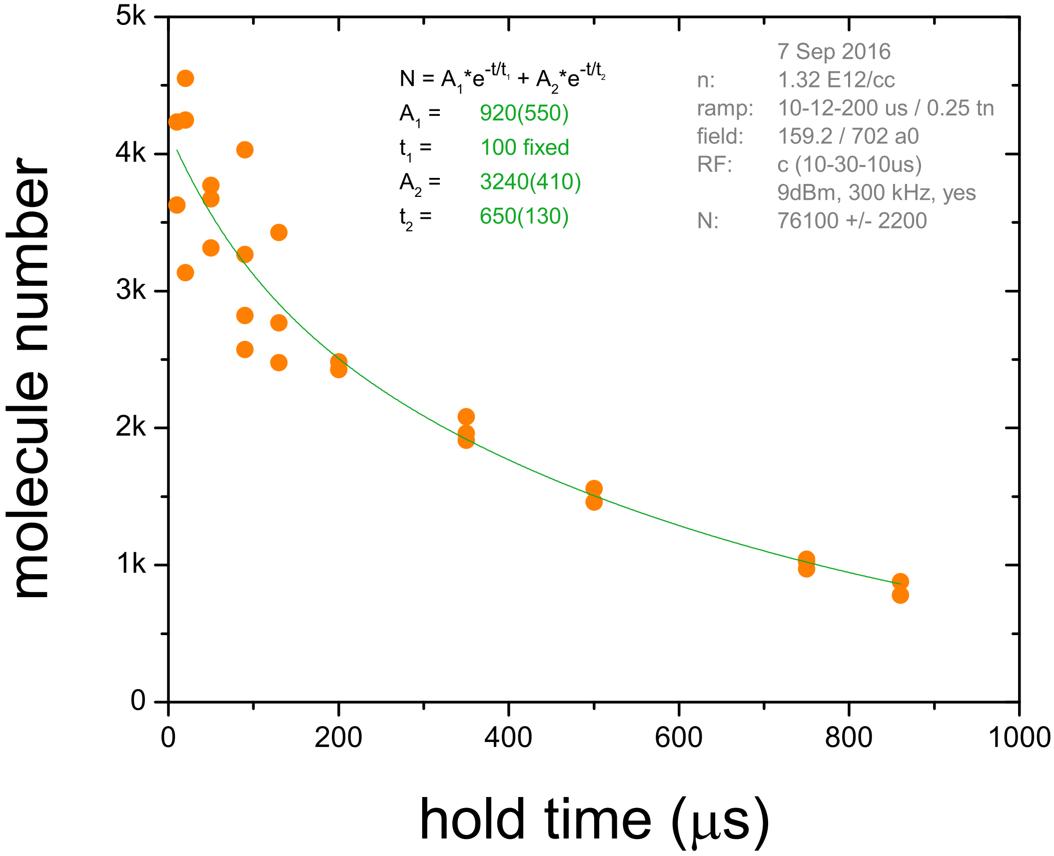

Figure C.10: $r_{\text{out}} = 200\ \mu\text{s}$

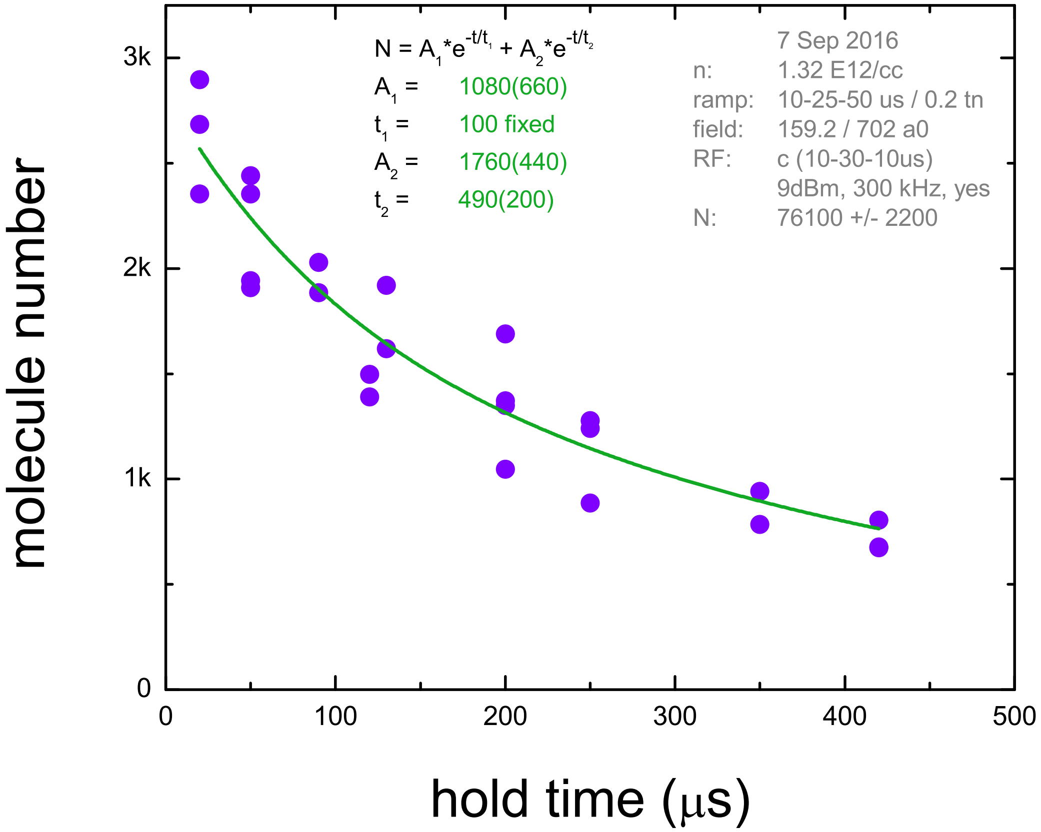

Figure C.11: $r_{\text{out}} = 50\ \mu\text{s}$

Appendix D

More molecule lifetime measurements

In this appendix we present more molecule lifetime measurements. All of these measurements were imaged using a 50 μs curved microwave pulse detuned 300 kHz from the atomic resonance. We attempted to fit these times with a sum of two exponentials to extract both the dimer and trimer amplitudes.

The first six plots have an initial density of $n = 0.167$ E12/cc. Five datasets measure the molecular number as a function of hold time at $a_f = 700\, a_0$, for the sixth dataset $a_f = 1000\, a_0$. The molecules were created by spending a variable amount of time on resonance, t_{dwell} before ramping away to a_f at a rate of ramp time $= 100$ μs. See figure 6.21 (green triangles) for an additional lifetime measurement with similar conditions, $t_{\mathrm{dwell}} = 0.5\, t_n$.

The next 6 plots are molecule lifetimes of various density, a_f, and t_{dwell} values.

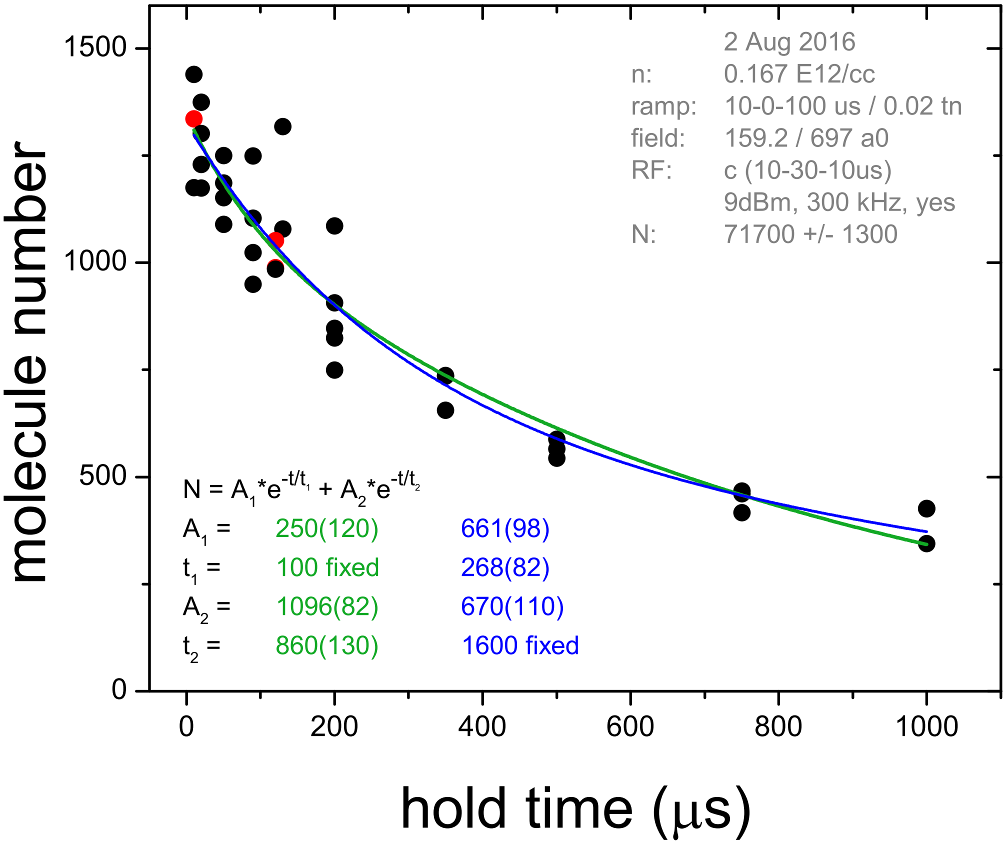
2 Aug 2016
n: 0.167 E12/cc
ramp: 10-0-100 us / 0.02 tn
field: 159.2 / 697 a0
RF: c (10-30-10us)
9dBm, 300 kHz, yes
N: 71700 +/- 1300
N = A_1*e^{-t/t_1} + A_2*e^{-t/t_2}
A_1 = 250(120) 661(98)
t_1 = 100 fixed 268(82)
A_2 = 1096(82) 670(110)
t_2 = 860(130) 1600 fixed
molecule number
0
500
1000
1500
0
200
400
600
800
1000
hold time (μs)

Figure D.1

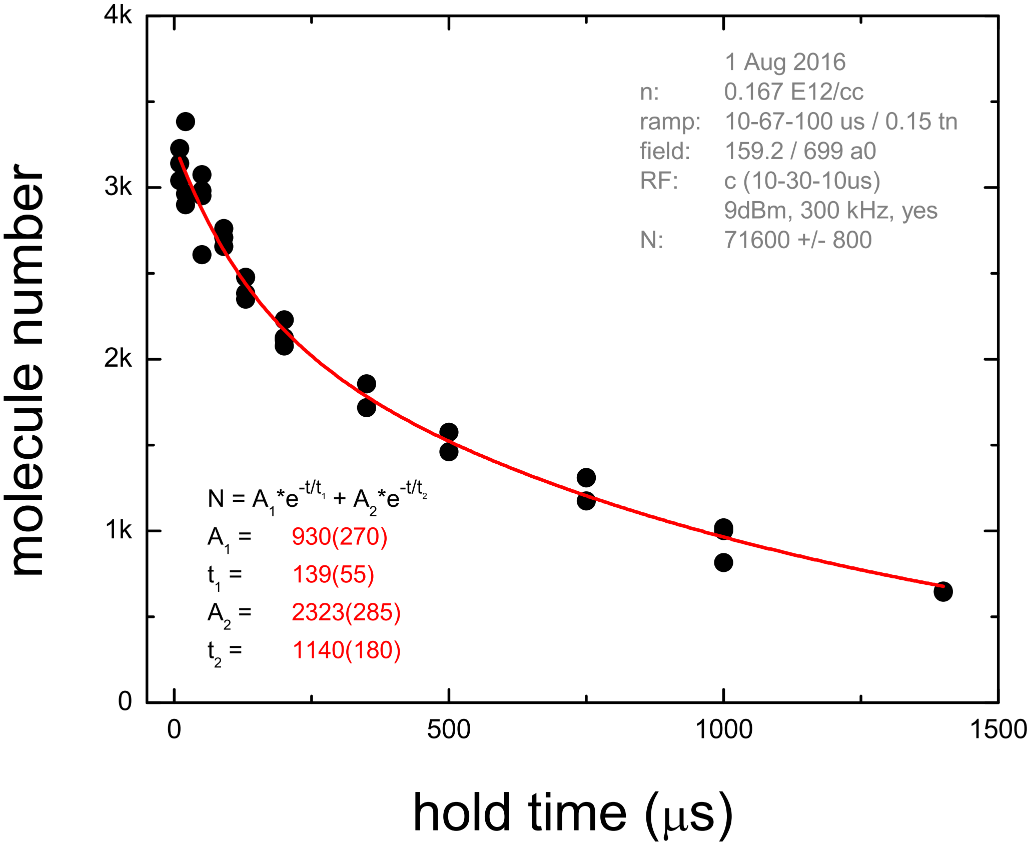
4k
3k
2k
1k
0
molecule number
0
500
1000
1500
hold time (μs)
1 Aug 2016
n: 0.167 E12/cc
ramp: 10-67-100 us / 0.15 tn
field: 159.2 / 699 a0
RF: c (10-30-10us)
9dBm, 300 kHz, yes
N: 71600 +/- 800
N = A$_1$*e$^{-t/t_1}$ + A$_2$*e$^{-t/t_2}$
A$_1$ = 930(270)
t$_1$ = 139(55)
A$_2$ = 2323(285)
t$_2$ = 1140(180)

Figure D.2

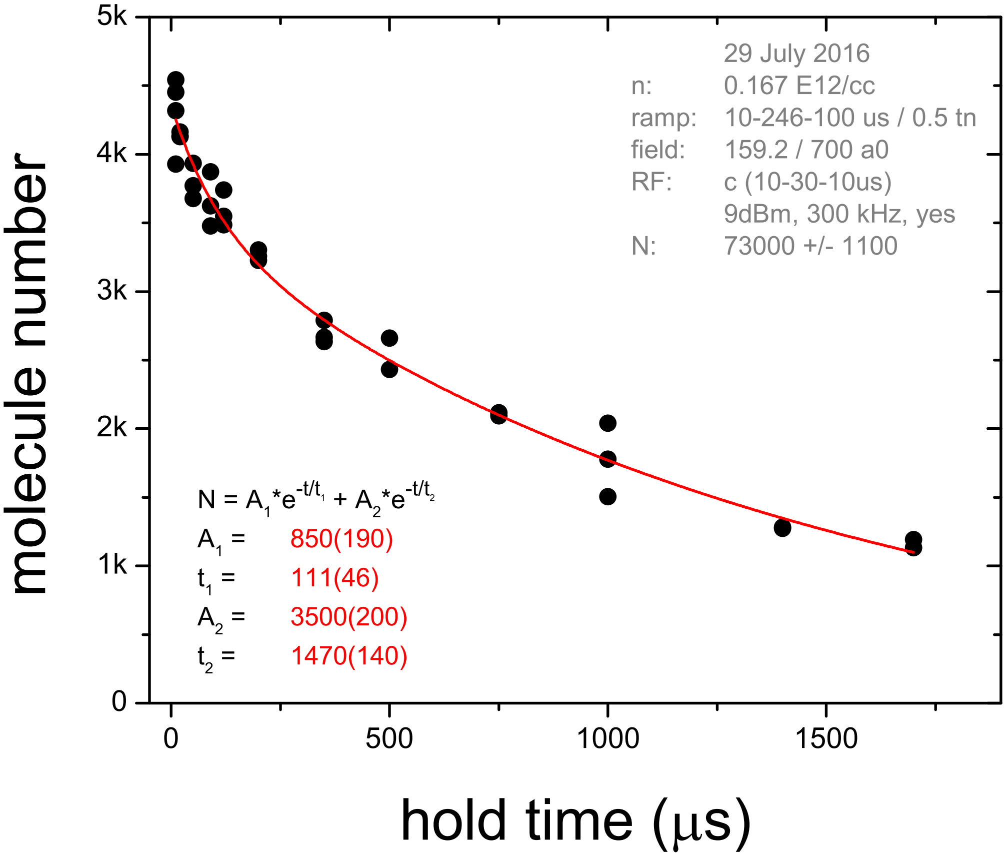
5k
4k
3k
2k
1k
0
0
500
1000
1500
molecule number
hold time (μs)
29 July 2016
n: 0.167 E12/cc
ramp: 10-246-100 us / 0.5 tn
field: 159.2 / 700 a0
RF: c (10-30-10us)
9dBm, 300 kHz, yes
N: 73000 +/- 1100
N = A1*e^-t/t1 + A2*e^-t/t2
A1 = 850(190)
t1 = 111(46)
A2 = 3500(200)
t2 = 1470(140)

Figure D.3

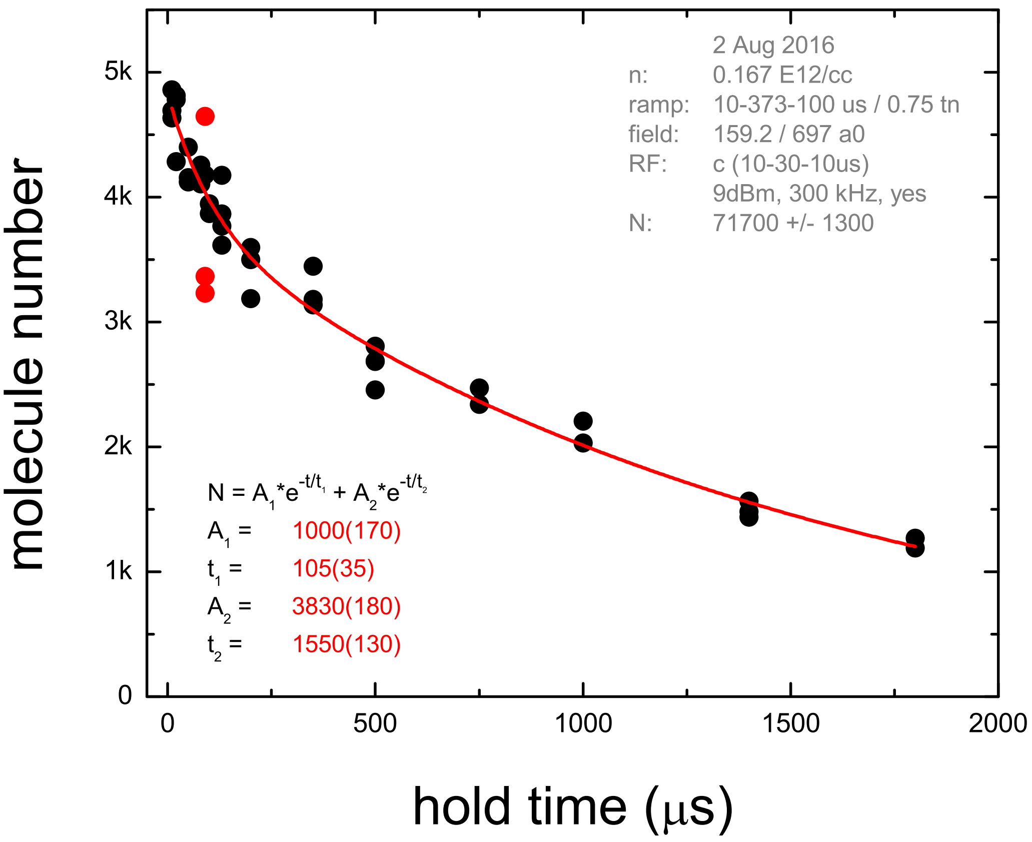

2 Aug 2016
n: 0.167 E12/cc
ramp: 10-373-100 us / 0.75 tn
field: 159.2 / 697 a0
RF: c (10-30-10us)
9dBm, 300 kHz, yes
N: 71700 +/- 1300
$N = A_1 * e^{-t/t_1} + A_2 * e^{-t/t_2}$
A_1 = 1000(170)
t_1 = 105(35)
A_2 = 3830(180)
t_2 = 1550(130)
molecule number
0
1k
2k
3k
4k
5k
0
500
1000
1500
2000
hold time (μs)

Figure D.4

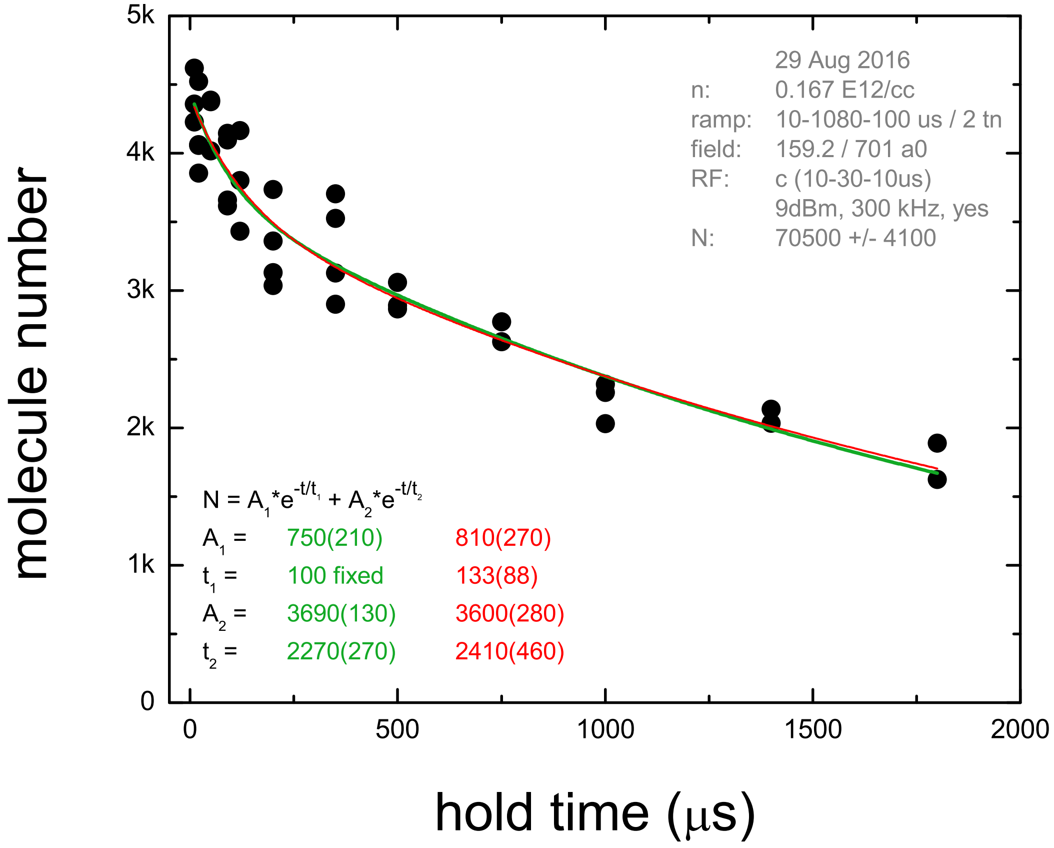
molecule number
hold time (μs)
0
1k
2k
3k
4k
5k
0
500
1000
1500
2000
29 Aug 2016
n: 0.167 E12/cc
ramp: 10-1080-100 us / 2 tn
field: 159.2 / 701 a0
RF: c (10-30-10us)
9dBm, 300 kHz, yes
N: 70500 +/- 4100
N = A1*e-t/t1 + A2*e-t/t2
A1 = 750(210) 810(270)
t1 = 100 fixed 133(88)
A2 = 3690(130) 3600(280)
t2 = 2270(270) 2410(460)

Figure D.5

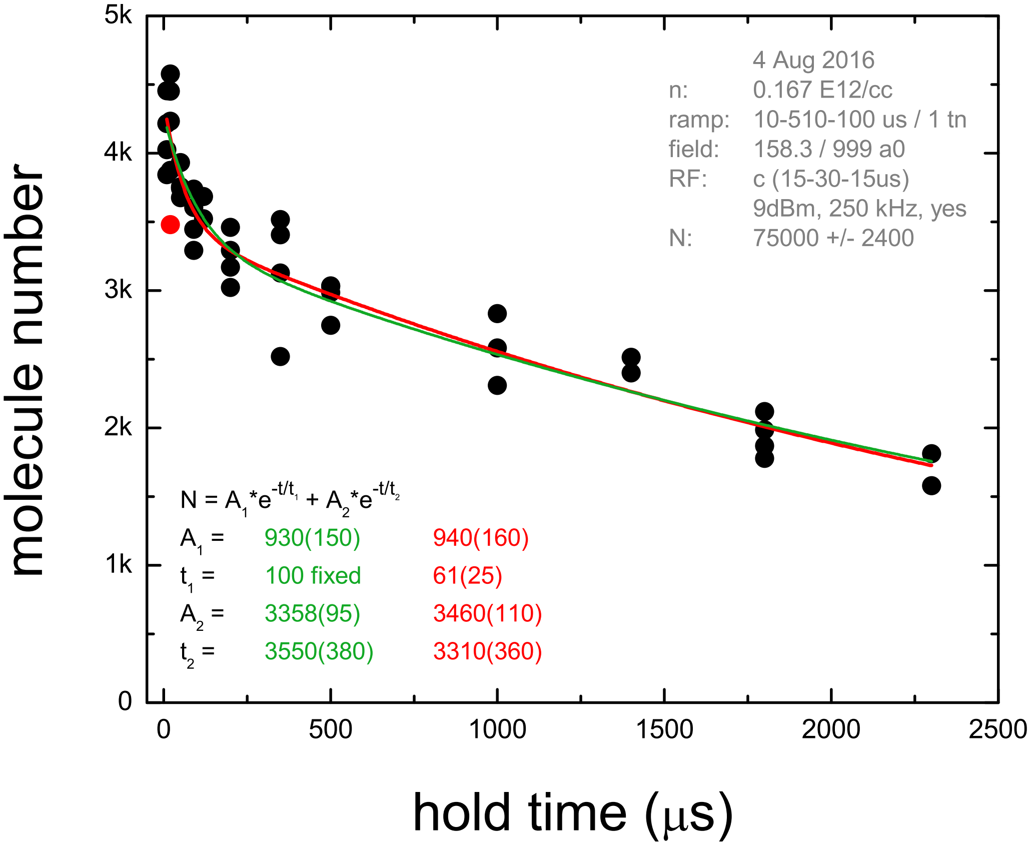

Figure D.6: $a_f = 1000\ a_0$

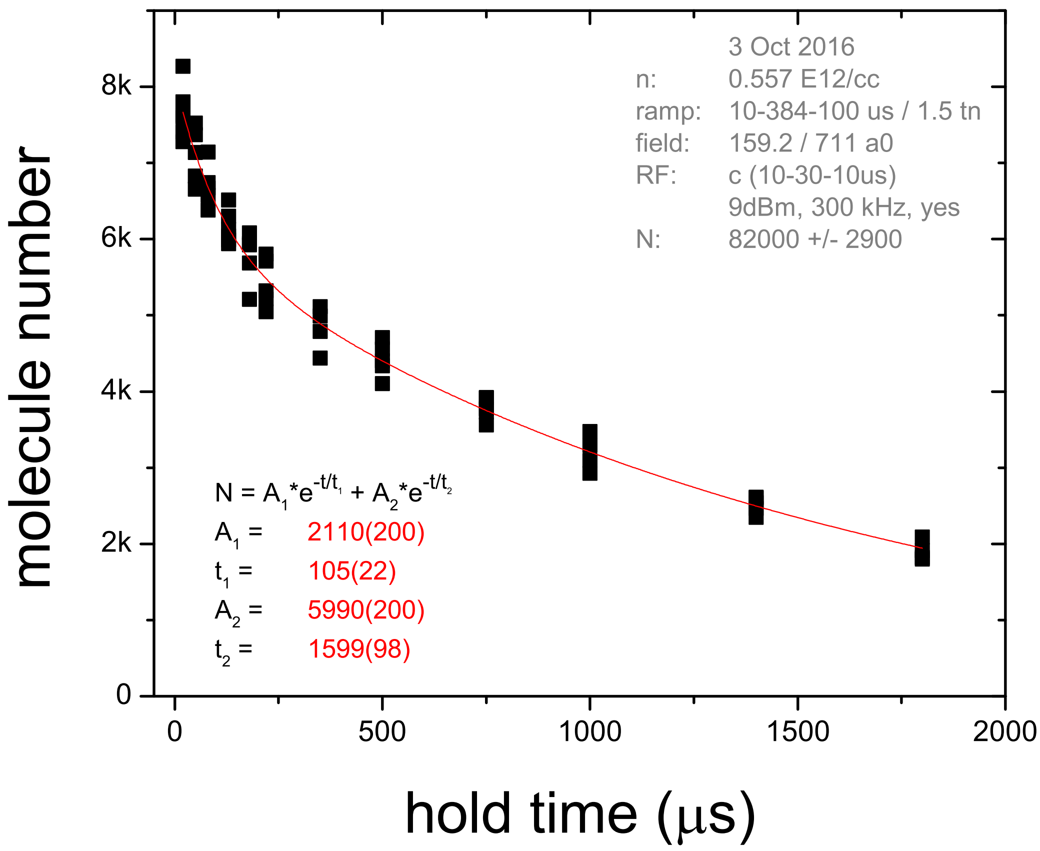
molecule number
8k
6k
4k
2k
0
0
500
1000
1500
2000
hold time (μs)
3 Oct 2016
n: 0.557 E12/cc
ramp: 10-384-100 us / 1.5 tn
field: 159.2 / 711 a0
RF: c (10-30-10us)
9dBm, 300 kHz, yes
N: 82000 +/- 2900
N = A1*e^-t/t1 + A2*e^-t/t2
A1 = 2110(200)
t1 = 105(22)
A2 = 5990(200)
t2 = 1599(98)

Figure D.7

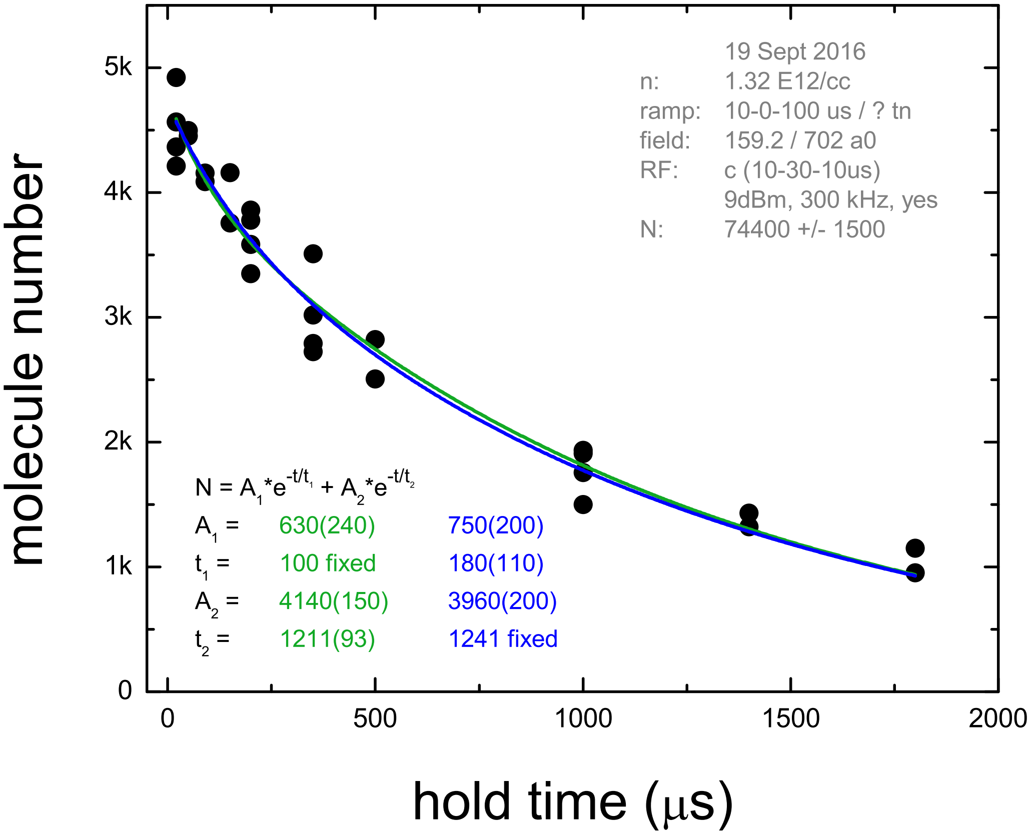
19 Sept 2016
n: 1.32 E12/cc
ramp: 10-0-100 us / ? tn
field: 159.2 / 702 a0
RF: c (10-30-10us)
9dBm, 300 kHz, yes
N: 74400 +/- 1500
N = A$_1$*e$^{-t/t_1}$ + A$_2$*e$^{-t/t_2}$
A$_1$ = 630(240) 750(200)
t$_1$ = 100 fixed 180(110)
A$_2$ = 4140(150) 3960(200)
t$_2$ = 1211(93) 1241 fixed
molecule number
0
1k
2k
3k
4k
5k
hold time (μs)
0
500
1000
1500
2000

Figure D.8

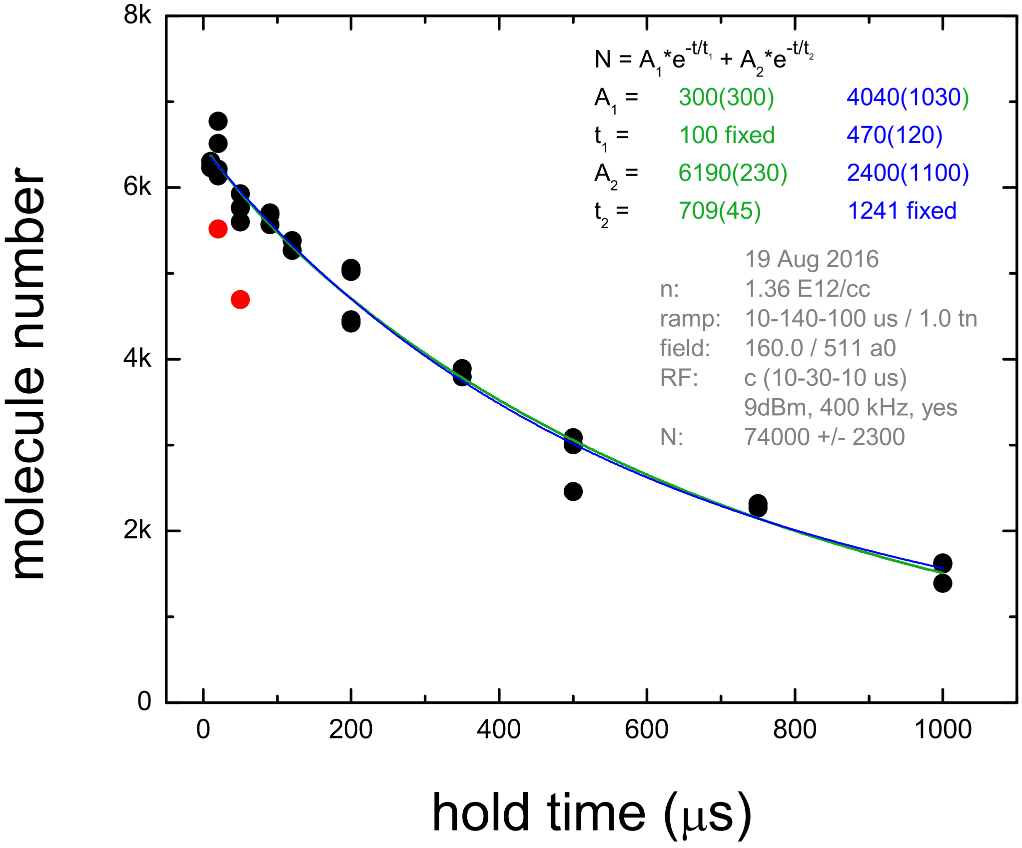

8k
6k
4k
2k
0
0
200
400
600
800
1000
molecule number
hold time (μs)
N = A1*e^-t/t1 + A2*e^-t/t2
A1 = 300(300) 4040(1030)
t1 = 100 fixed 470(120)
A2 = 6190(230) 2400(1100)
t2 = 709(45) 1241 fixed
19 Aug 2016
n: 1.36 E12/cc
ramp: 10-140-100 us / 1.0 tn
field: 160.0 / 511 a0
RF: c (10-30-10 us)
9dBm, 400 kHz, yes
N: 74000 +/- 2300

Figure D.9

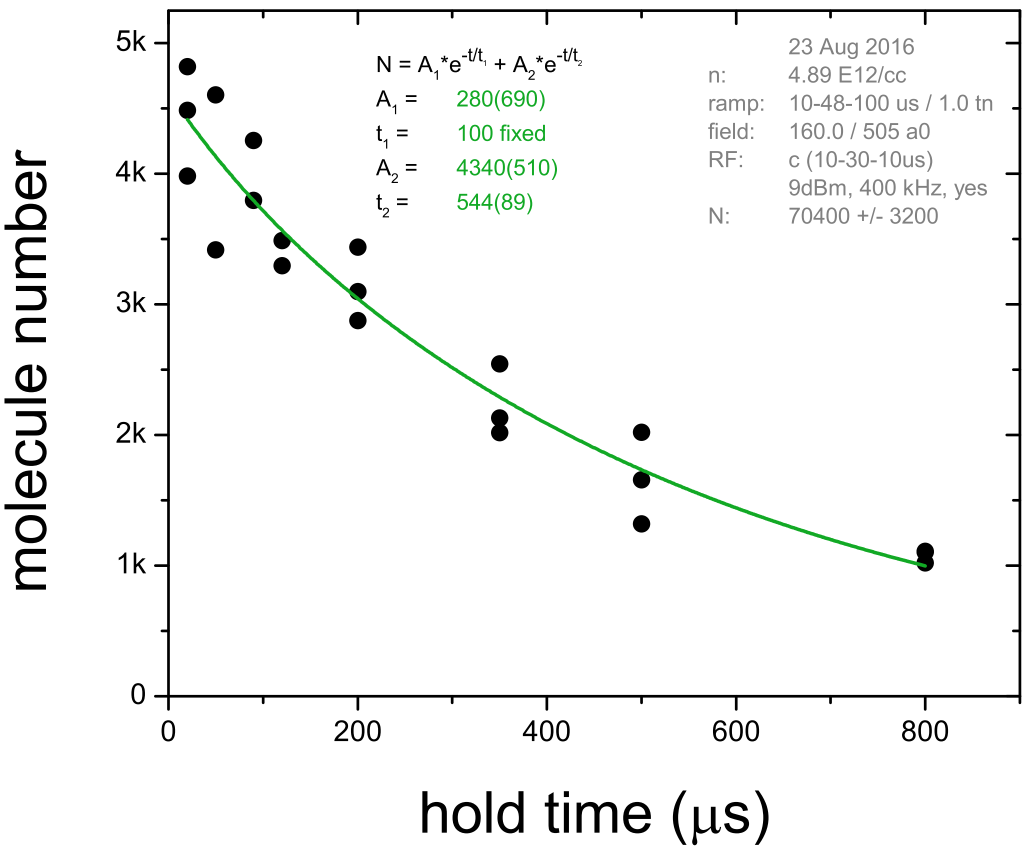
N = A₁*e^-t/t₁ + A₂*e^-t/t₂
A₁ = 280(690)
t₁ = 100 fixed
A₂ = 4340(510)
t₂ = 544(89)
23 Aug 2016
n: 4.89 E12/cc
ramp: 10-48-100 us / 1.0 tn
field: 160.0 / 505 a0
RF: c (10-30-10us)
9dBm, 400 kHz, yes
N: 70400 +/- 3200
molecule number
0
1k
2k
3k
4k
5k
hold time (μs)
0
200
400
600
800

Figure D.10

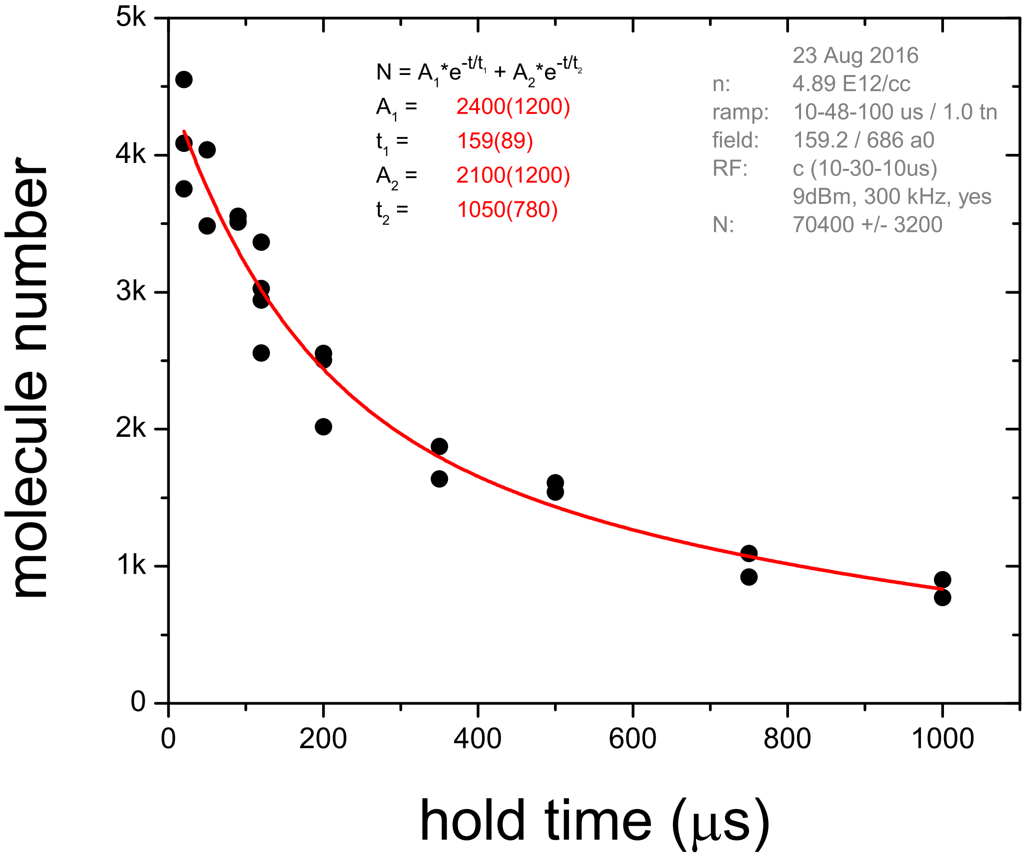

$N = A_1{*}e^{-t/t_1} + A_2{*}e^{-t/t_2}$
A_1 = 2400(1200)
t_1 = 159(89)
A_2 = 2100(1200)
t_2 = 1050(780)
23 Aug 2016
n: 4.89 E12/cc
ramp: 10-48-100 us / 1.0 tn
field: 159.2 / 686 a0
RF: c (10-30-10us)
9dBm, 300 kHz, yes
N: 70400 +/- 3200
molecule number
0
1k
2k
3k
4k
5k
hold time (μs)
0
200
400
600
800
1000

Figure D.11

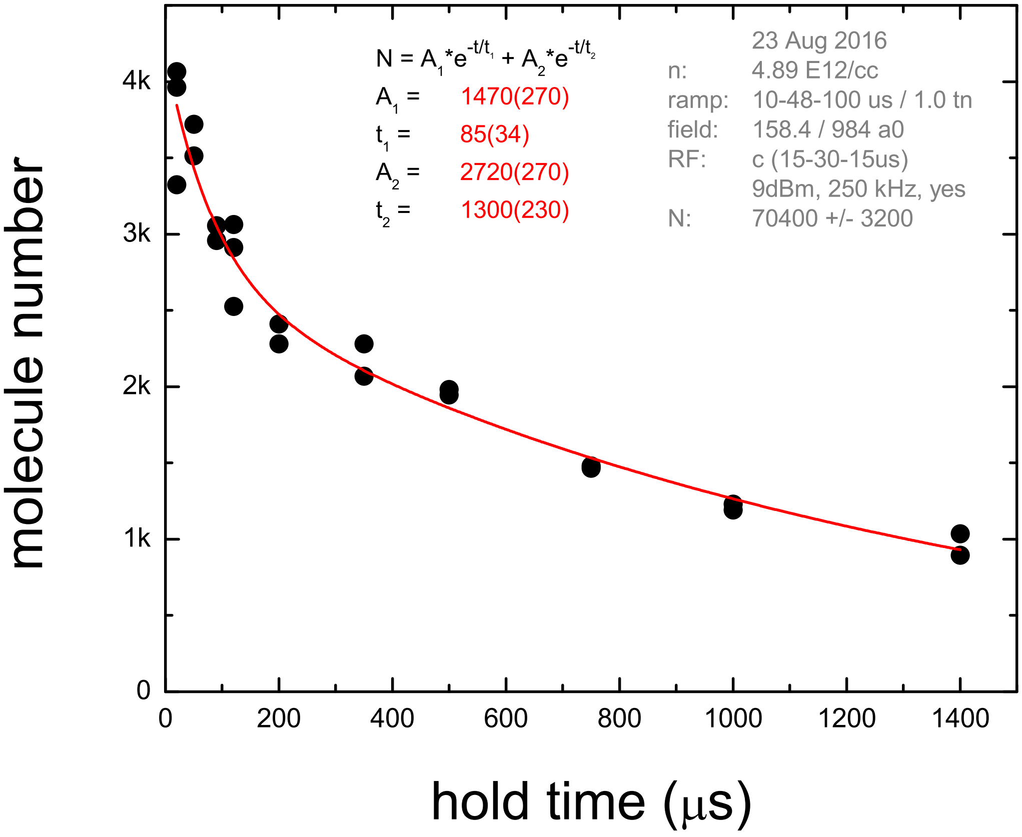
N = A_1*e^-t/t_1 + A_2*e^-t/t_2
A_1 = 1470(270)
t_1 = 85(34)
A_2 = 2720(270)
t_2 = 1300(230)
23 Aug 2016
n: 4.89 E12/cc
ramp: 10-48-100 us / 1.0 tn
field: 158.4 / 984 a0
RF: c (15-30-15us)
9dBm, 250 kHz, yes
N: 70400 +/- 3200
molecule number
0
1k
2k
3k
4k
0
200
400
600
800
1000
1200
1400
hold time (μs)

Figure D.12

Appendix E

Molecule lifetime measurements with square microwave pulses

Here are the remaining molecule lifetime measurements obtained using a square microwave pulse. As the original data were contaminated by background atoms, these data were analyzed using either the atom stripes (“stripe fit”) or atom subtraction with frequency tracking methods (“sub constant”), see chapter 6 for more details. Additional data that fit this category can be find in figures 6.12, 6.14, and 6.21

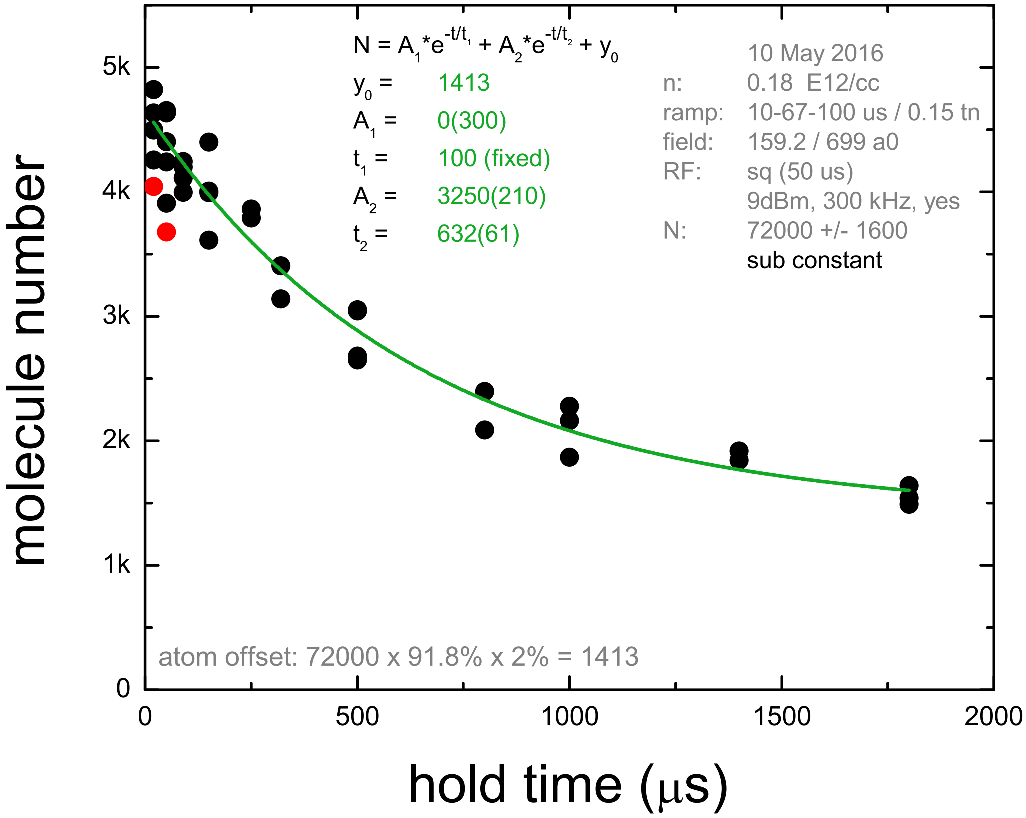
N = A_1*e^-t/t_1 + A_2*e^-t/t_2 + y_0
y_0 = 1413
A_1 = 0(300)
t_1 = 100 (fixed)
A_2 = 3250(210)
t_2 = 632(61)
10 May 2016
n: 0.18 E12/cc
ramp: 10-67-100 us / 0.15 tn
field: 159.2 / 699 a0
RF: sq (50 us)
9dBm, 300 kHz, yes
N: 72000 +/- 1600
sub constant
atom offset: 72000 x 91.8% x 2% = 1413
molecule number
hold time (μs)
0
1k
2k
3k
4k
5k
0
500
1000
1500
2000

Figure E.1

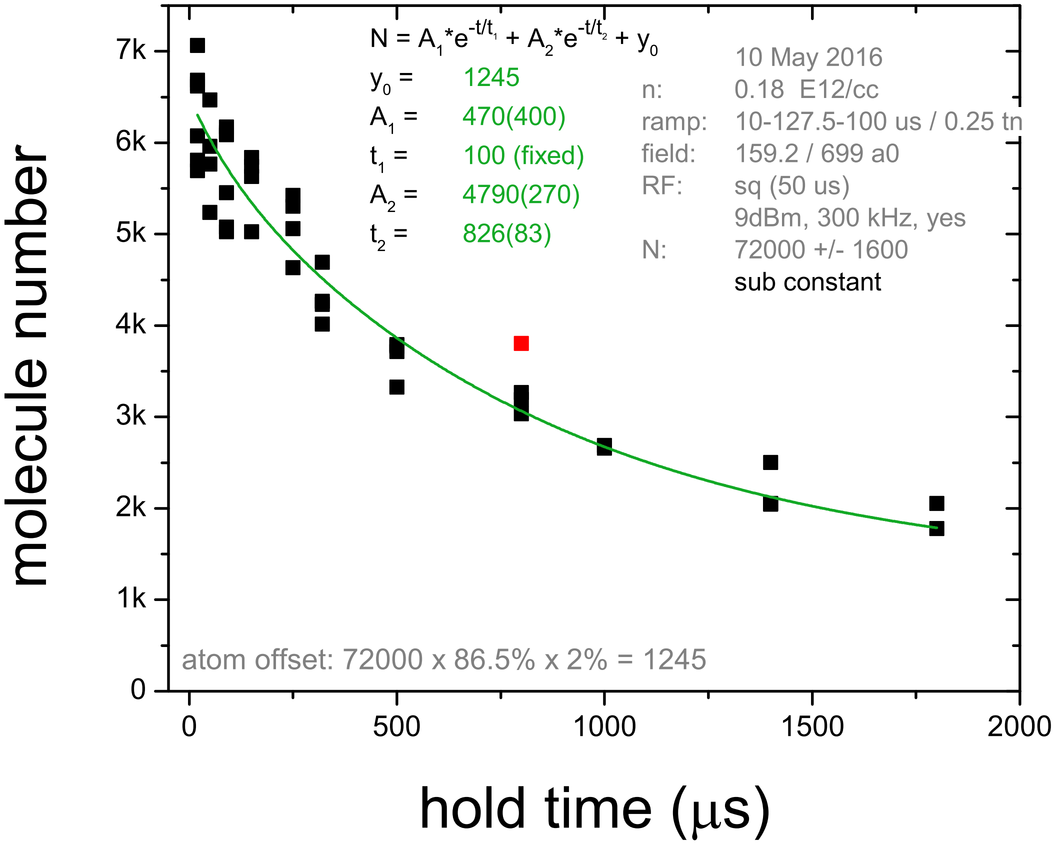
$N = A_1{*}e^{-t/t_1} + A_2{*}e^{-t/t_2} + y_0$
y_0 = 1245
A_1 = 470(400)
t_1 = 100 (fixed)
A_2 = 4790(270)
t_2 = 826(83)
10 May 2016
n: 0.18 E12/cc
ramp: 10-127.5-100 us / 0.25 tn
field: 159.2 / 699 a0
RF: sq (50 us)
9dBm, 300 kHz, yes
N: 72000 +/- 1600
sub constant
atom offset: 72000 x 86.5% x 2% = 1245
molecule number
0
1k
2k
3k
4k
5k
6k
7k
0
500
1000
1500
2000
hold time (μs)

Figure E.2

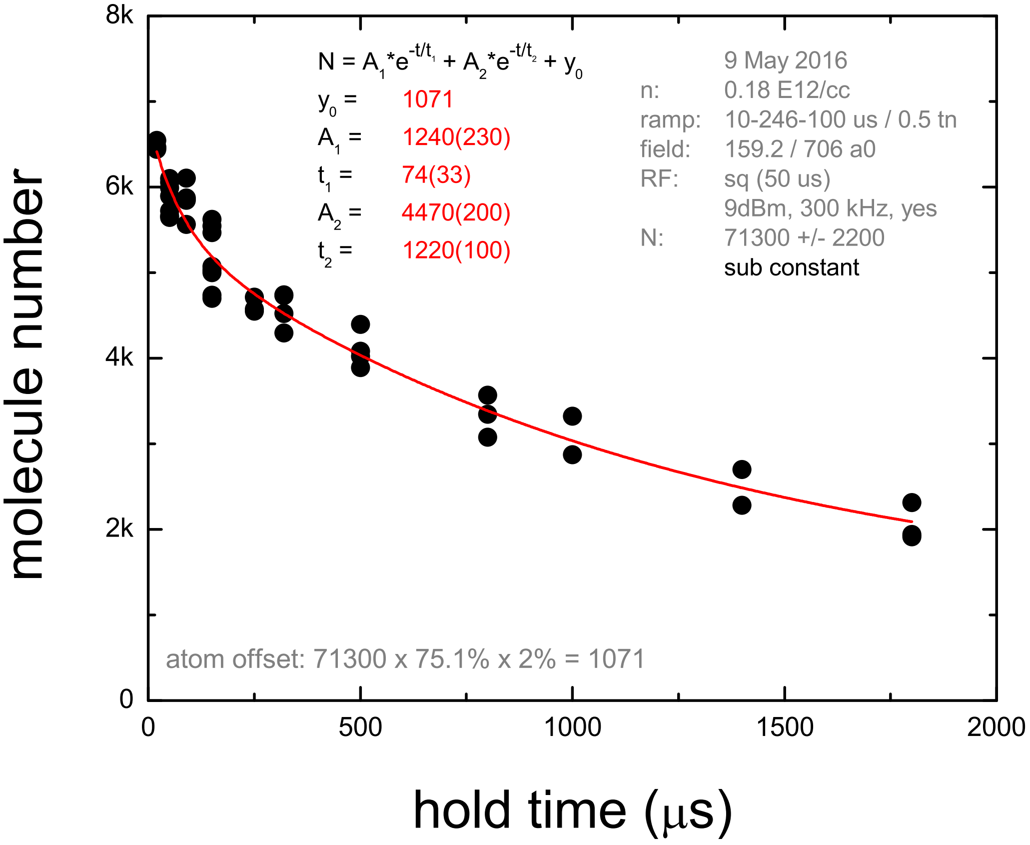
N = A1*e^-t/t1 + A2*e^-t/t2 + y0
y0 = 1071
A1 = 1240(230)
t1 = 74(33)
A2 = 4470(200)
t2 = 1220(100)
9 May 2016
n: 0.18 E12/cc
ramp: 10-246-100 us / 0.5 tn
field: 159.2 / 706 a0
RF: sq (50 us)
9dBm, 300 kHz, yes
N: 71300 +/- 2200
sub constant
atom offset: 71300 x 75.1% x 2% = 1071
8k
6k
4k
2k
0
0
500
1000
1500
2000
molecule number
hold time (μs)

Figure E.3

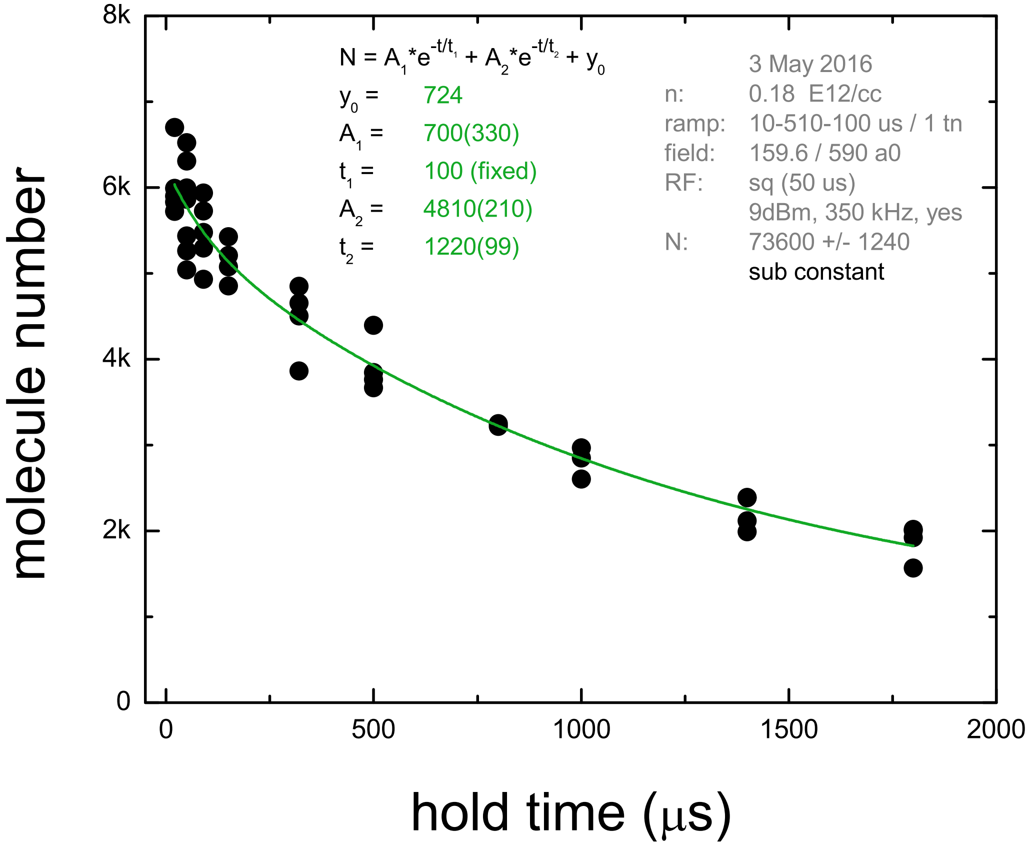

Figure E.4: $a_f = 590\ a_0$.

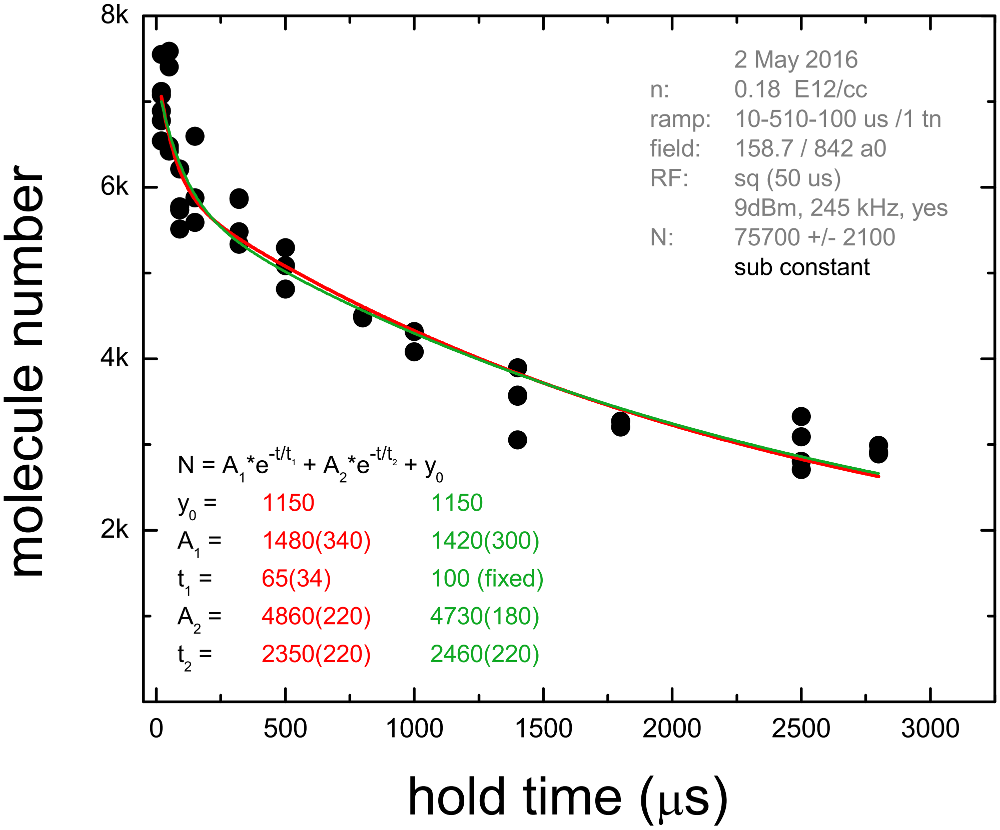

Figure E.5: $a_f = 840\ a_0$.

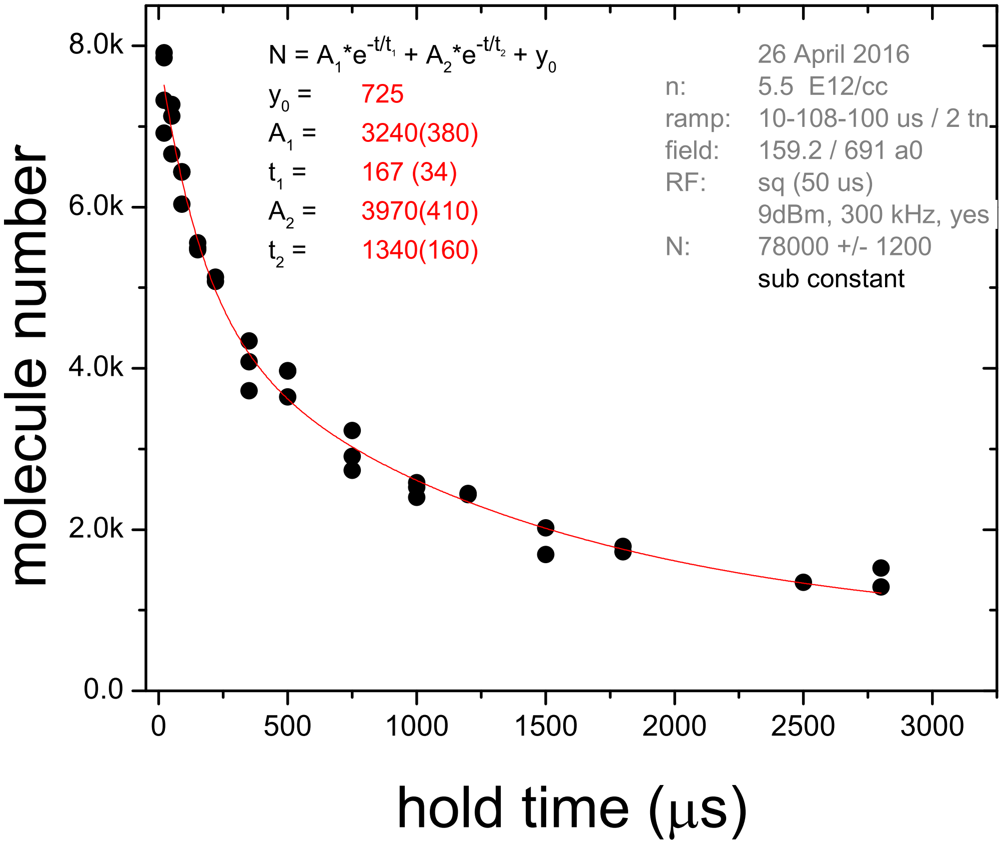
molecule number
hold time (μs)
0.0
2.0k
4.0k
6.0k
8.0k
0
500
1000
1500
2000
2500
3000
N = A_1*e^-t/t_1 + A_2*e^-t/t_2 + y_0
y_0 = 725
A_1 = 3240(380)
t_1 = 167 (34)
A_2 = 3970(410)
t_2 = 1340(160)
26 April 2016
n: 5.5 E12/cc
ramp: 10-108-100 us / 2 tn
field: 159.2 / 691 a0
RF: sq (50 us)
9dBm, 300 kHz, yes
N: 78000 +/- 1200
sub constant

Figure E.6

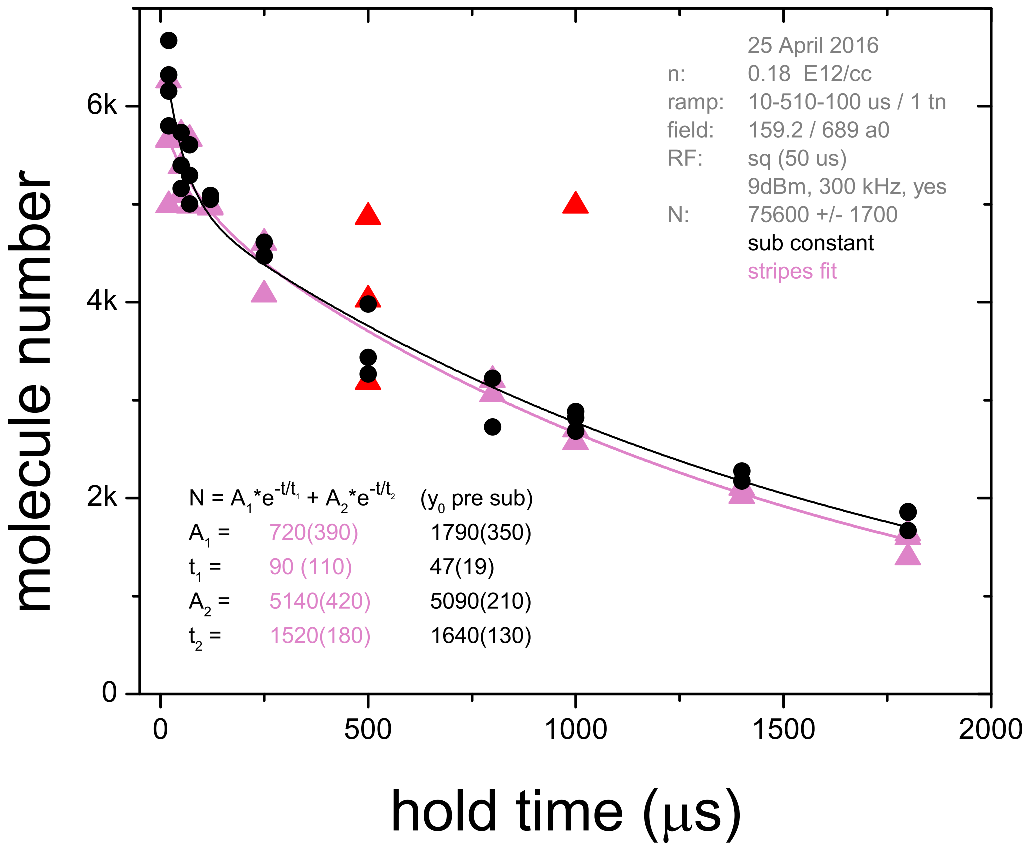
molecule number
hold time (μs)
0
2k
4k
6k
0
500
1000
1500
2000
25 April 2016
n: 0.18 E12/cc
ramp: 10-510-100 us / 1 tn
field: 159.2 / 689 a0
RF: sq (50 us)
9dBm, 300 kHz, yes
N: 75600 +/- 1700
sub constant
stripes fit
N = A1*e-t/t1 + A2*e-t/t2
(y0 pre sub)
A1 = 720(390) 1790(350)
t1 = 90 (110) 47(19)
A2 = 5140(420) 5090(210)
t2 = 1520(180) 1640(130)

Figure E.7

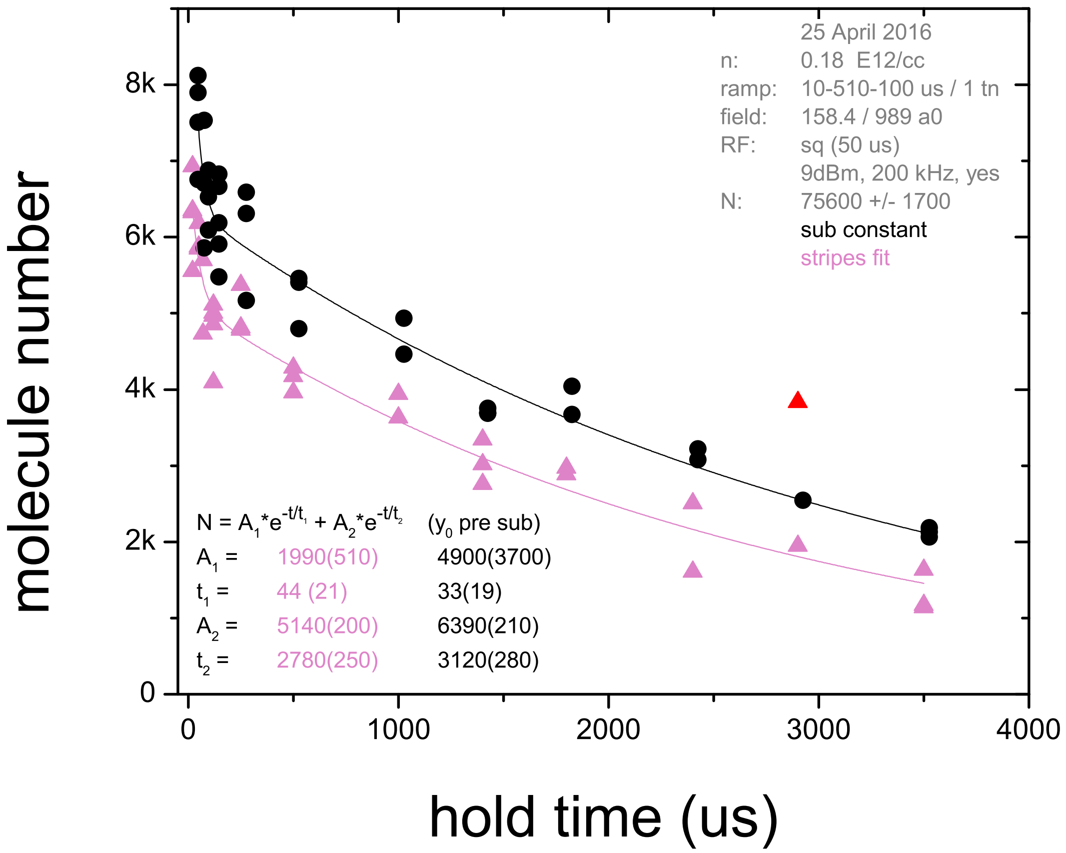

Figure E.8: $a_f = 990\ a_0$.

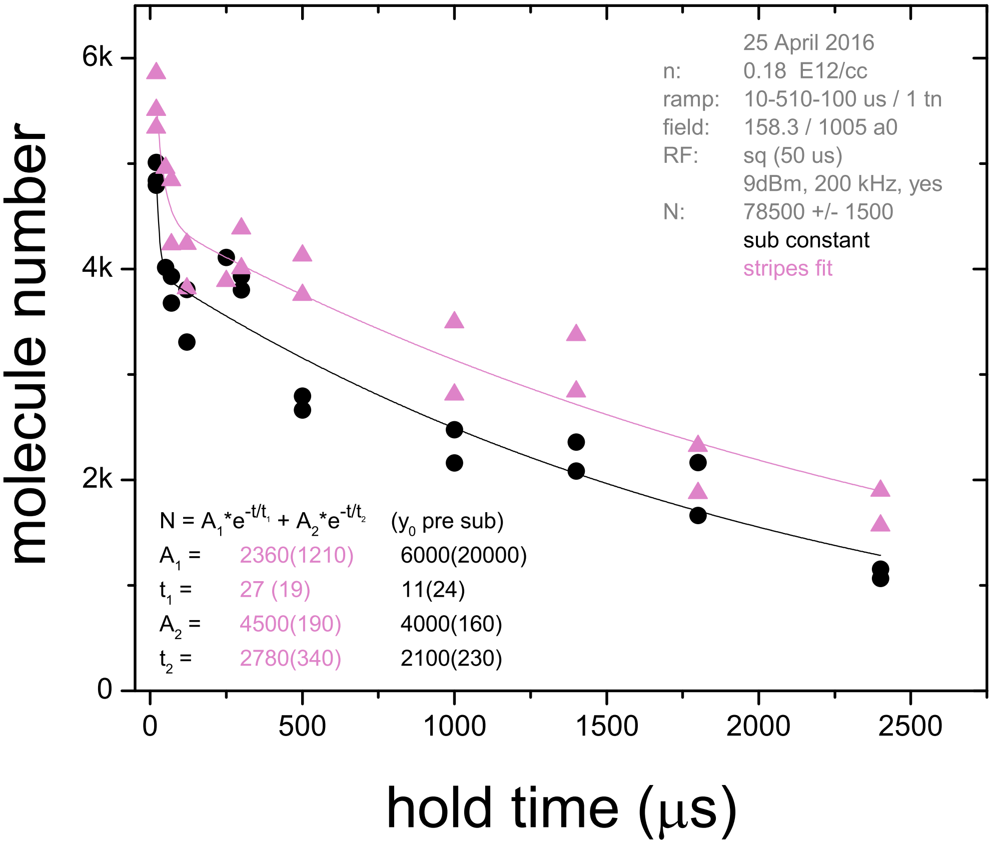

Figure E.9: $a_f = 1005\ a_0$.

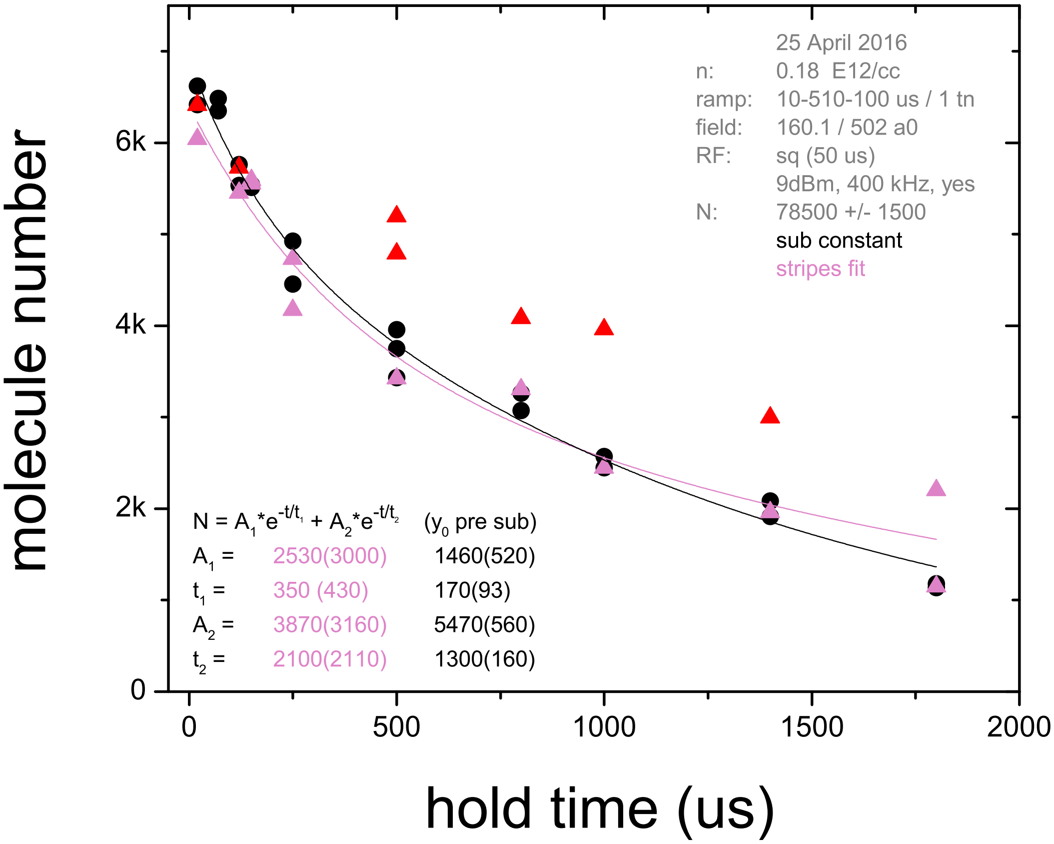

Figure E.10: $a_f = 1005\ a_0$.

Appendix F

Dwell data

More data, of both atom and molecule number, as a function of dwell time on resonance.

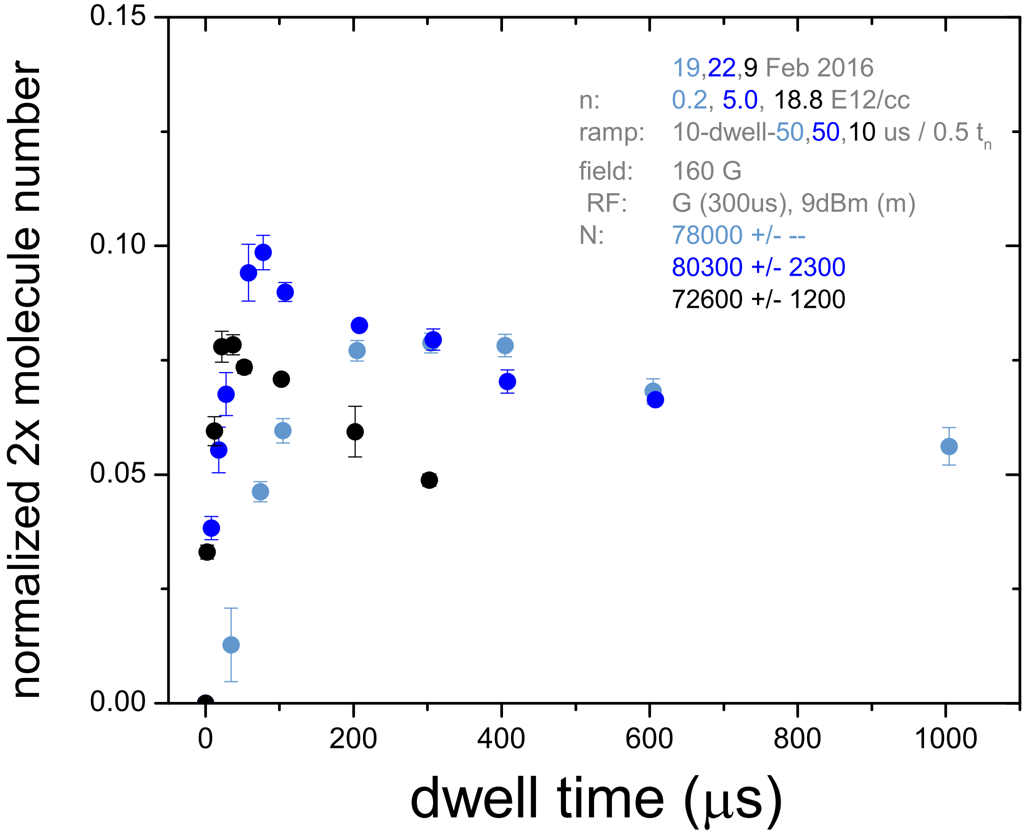

Figure F.1

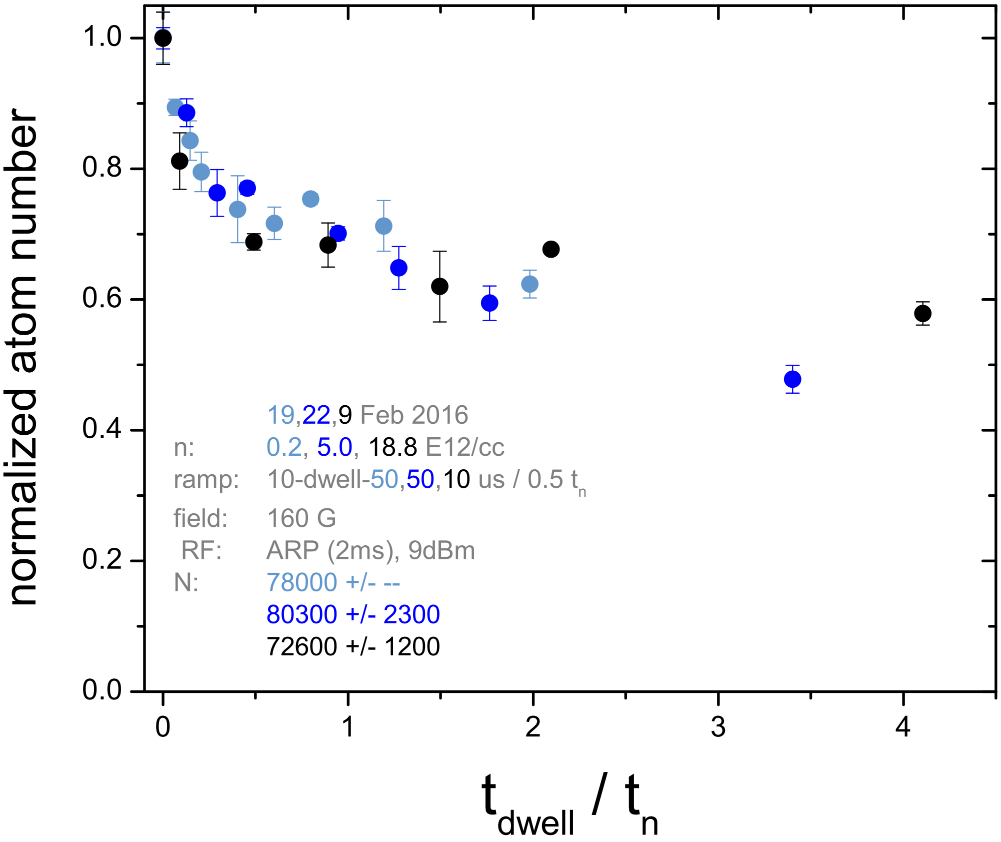

normalized atom number
1.0
0.8
0.6
0.4
0.2
0.0
0
1
2
3
4
t_{dwell} / t_n
19,22,9 Feb 2016
n: 0.2, 5.0, 18.8 E12/cc
ramp: 10-dwell-50,50,10 us / 0.5 t_n
field: 160 G
RF: ARP (2ms), 9dBm
N: 78000 +/- --
80300 +/- 2300
72600 +/- 1200

Figure F.2

Appendix G

Rampout data

More molecule ramp out data.

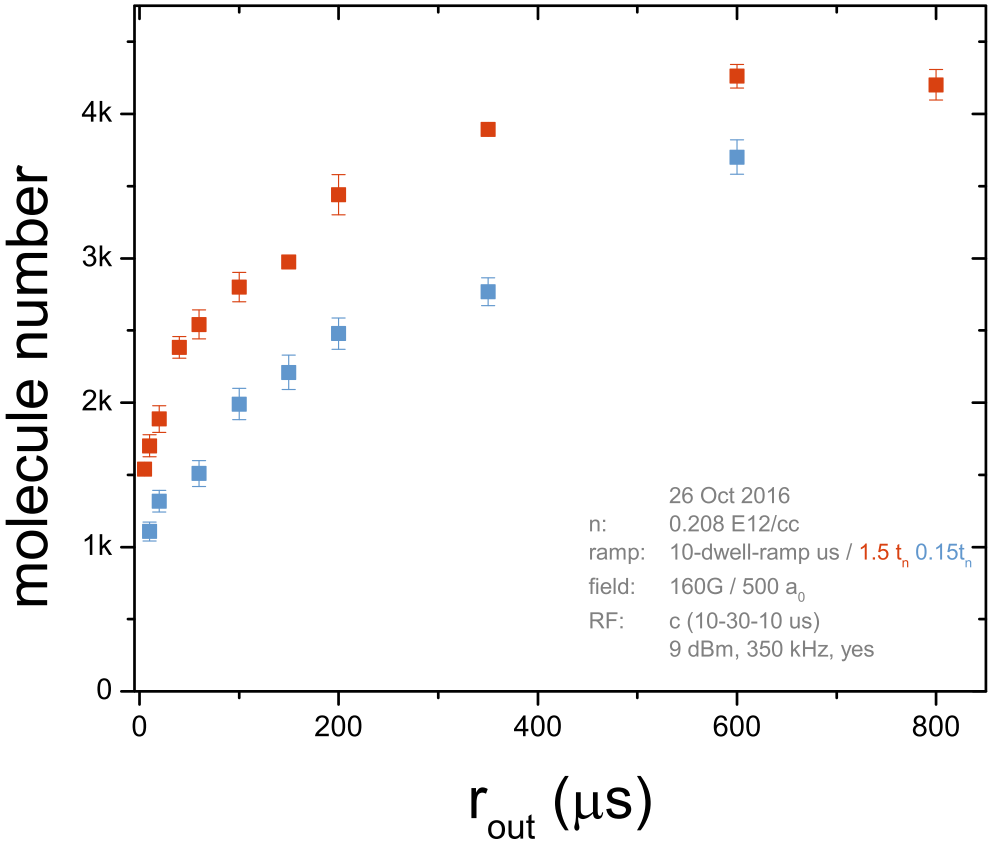

Figure G.1: curved RF envelope, waited hold time = 500 μs at a_f before beginning RF pulse.

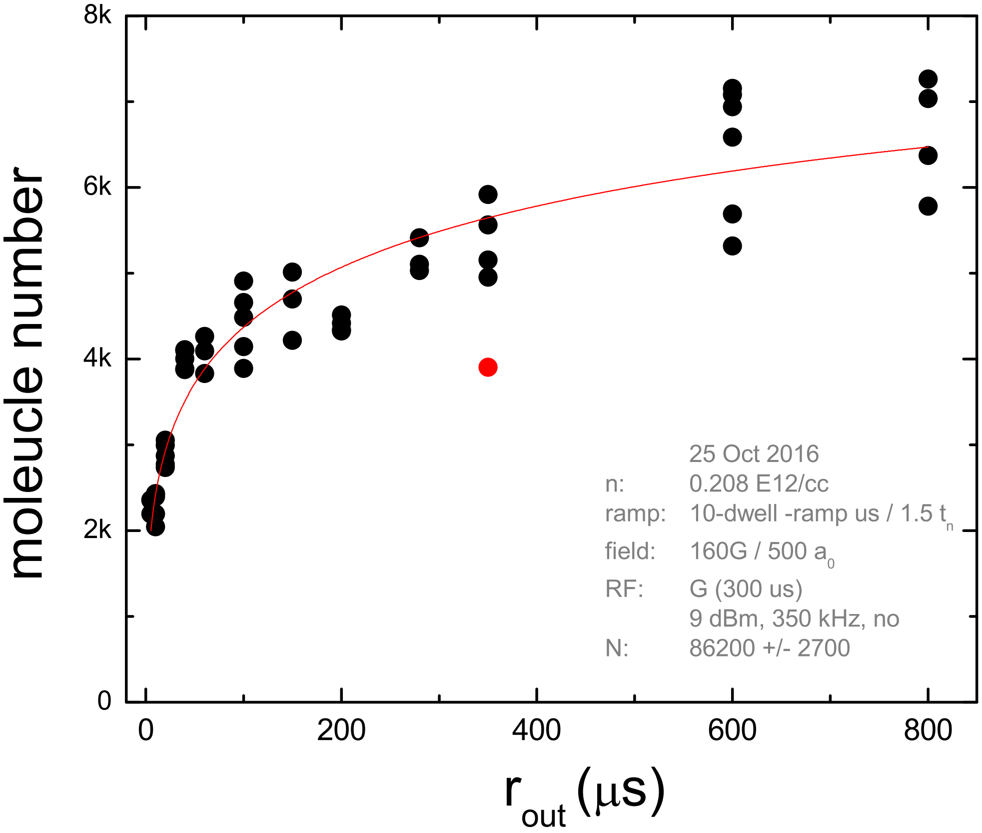
8k
6k
4k
2k
0
moleucle number
0
200
400
600
800
r_{out} (μs)
25 Oct 2016
n: 0.208 E12/cc
ramp: 10-dwell -ramp us / 1.5 t_n
field: 160G / 500 a_0
RF: G (300 us)
9 dBm, 350 kHz, no
N: 86200 +/- 2700

Figure G.2

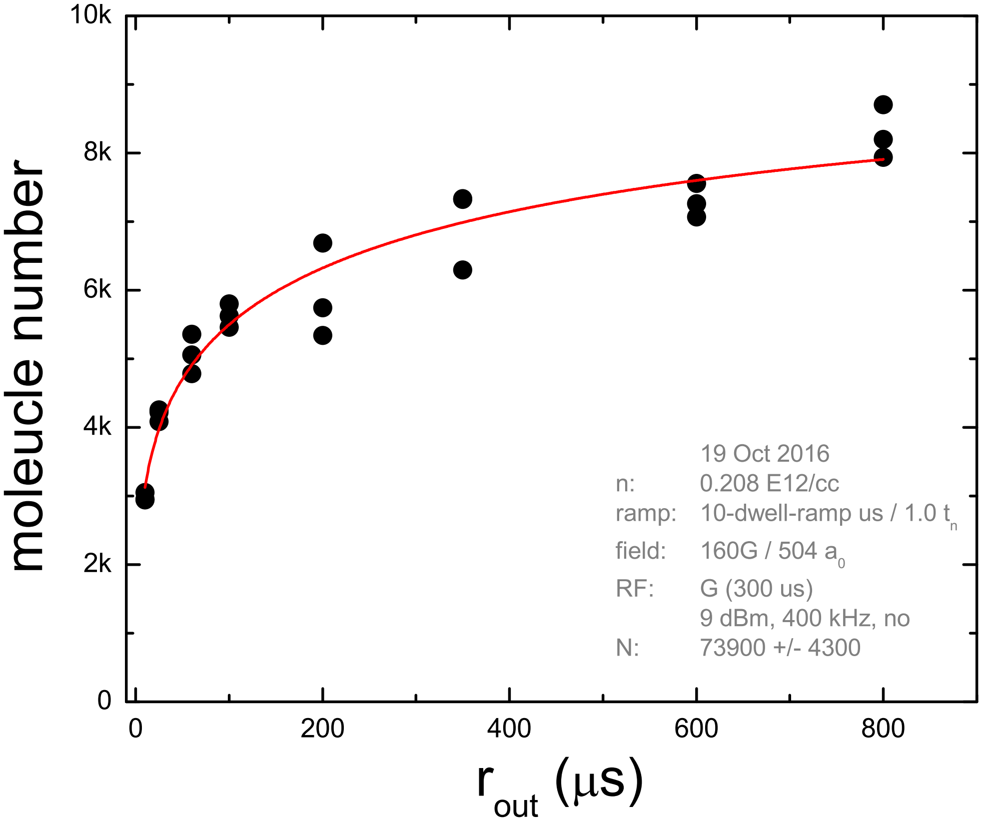
10k
8k
6k
4k
2k
0
moleucle number
0
200
400
600
800
r_{out} (μs)
19 Oct 2016
n: 0.208 E12/cc
ramp: 10-dwell-ramp us / 1.0 t_n
field: 160G / 504 a_0
RF: G (300 us)
9 dBm, 400 kHz, no
N: 73900 +/- 4300

Figure G.3

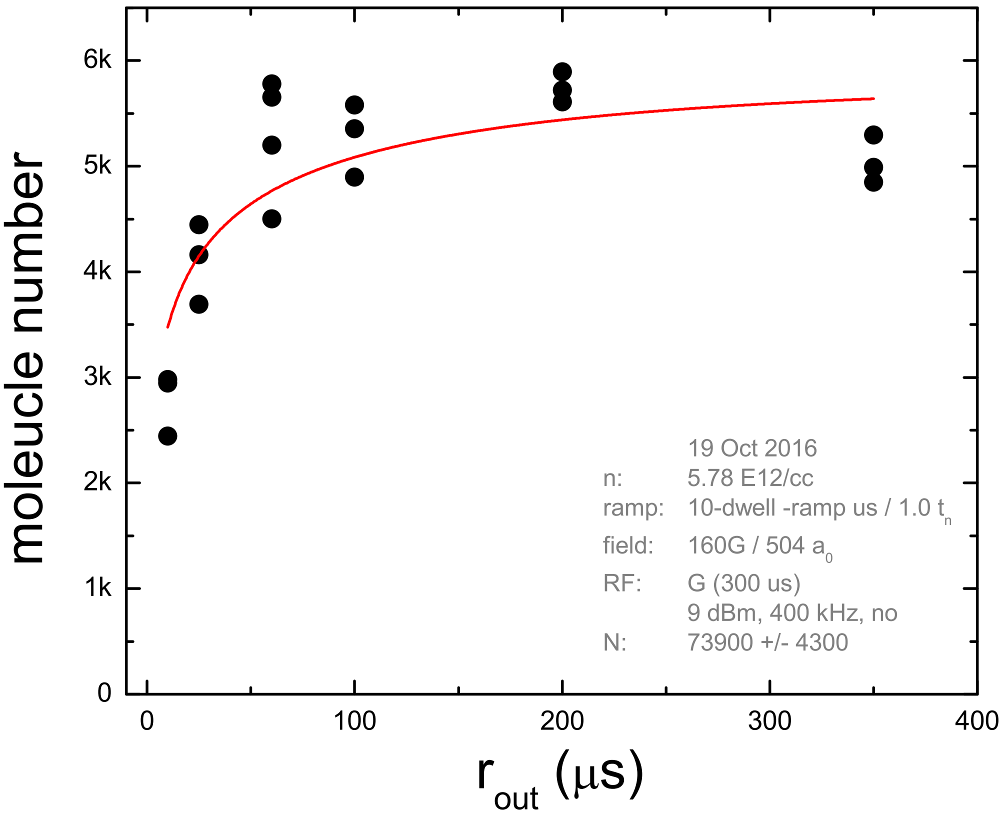

moleucle number
6k
5k
4k
3k
2k
1k
0
0
100
200
300
400
r_{out} (μs)
19 Oct 2016
n: 5.78 E12/cc
ramp: 10-dwell -ramp us / 1.0 t_n
field: 160G / 504 a_0
RF: G (300 us)
9 dBm, 400 kHz, no
N: 73900 +/- 4300

Figure G.4

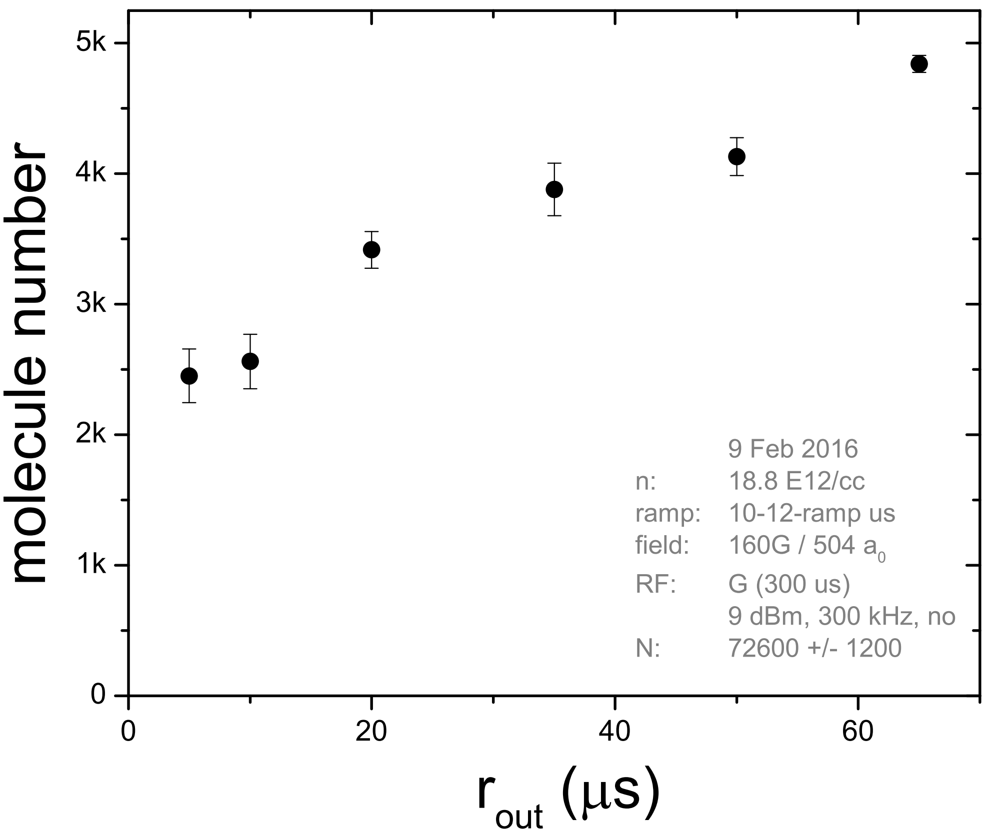

molecule number
0
1k
2k
3k
4k
5k
0
20
40
60
r_{out} (μs)
9 Feb 2016
n: 18.8 E12/cc
ramp: 10-12-ramp us
field: 160G / 504 a_0
RF: G (300 us)
9 dBm, 300 kHz, no
N: 72600 +/- 1200

Figure G.5

Appendix H

Data reference tables

FT* = frequency tracking?

Table H.1: Molecule Rampout Data

Figure	**Date**	**Density**	t_{dwell}	a_f	**RF envelope**	**RF duration**	δ	**FT***	**BEC** N	σ_N
G.1	26 Oct	0.208	0.15	500	curved	50	350	1	77600	2000
G.1	26 Oct	0.208	1.5	500	curved	50	350	1	77600	2000
G.2	25 Oct	0.208	1.5	500	Gaussian	300	350	0	86200	2700
G.3	19 Oct	0.208	1	504	Gaussian	300	400	0	73900	4300
G.4	19 Oct	5.78	1	504	Gaussian	300	400	0	73900	4300
6.19	8 Jun	5.5	0.5	498	square	50	400	0	70000	–
6.19	7 Jun	5.5	0.5	496	Gaussian	300	400	0	78000	–
G.5	9 Feb	18.8	0.5	504	Gaussian	300	300	0	72600	1200
7.6	13 Jan	0.18	0.5	500	Gaussian	300	400	0	53500	–
7.6	13 Jan	5.5	0.5	500	Gaussian	300	400	0	53500	–

Table H.2: Molecule Lifetime Data

Figure	**Date**	**Density**	t_{dwell}	**dwell time**	r_{out}	r_{in}	a_f	**RF envelope**	**RF duration**	δ	**BEC** N	σ_N
–	2016	E12/cc	t_n	μs	μs	μs	a_0	–	μs	kHz	–	–
9.5	16 Nov	1.3	0.2	30	100	10	683.5	curved	50 (10-30-10)	300	83900	3600
9.6	16 Nov	1.3	0.5	75	100	10	683.5	curved	50 (10-30-10)	300	83900	3600
9.7	16 Nov	1.3	0.3	45	100	10	683.5	curved	50 (10-30-10)	300	83900	3600
B.1	4 Oct	0.208	1.5	760	100	10	514	curved	50 (10-30-10)	400	78100	600
B.3	4 Oct	0.208	1.5	760	100	10	1005	curved	60 (15-30-15)	250	78100	600
B.4	4 Oct	1.32	1.5	205	100	10	514	curved	50 (10-30-10)	400	78100	600
B.6	4 Oct	1.32	1.5	205	100	10	1005	curved	60 (15-30-15)	250	78100	600
B.7	4 Oct	5.78	1.5	70	100	10	514	curved	50 (10-30-10)	400	78100	600
B.9	4 Oct	5.78	1.5	70	100	10	1005	curved	60 (15-30-15)	250	78100	600
B.8	3 Oct	5.78	1.5	70	100	10	709	curved	50 (10-30-10)	300	82000	2900
D.7	3 Oct	0.557	1.5	384	100	10	711	curved	50 (10-30-10)	300	82000	2900
B.2	26 Sep	0.208	1.5	760	100	10	698	curved	50 (10-30-10)	300	82800	1800
B.5	26 Sep	1.32	1.5	205	100	10	698	curved	50 (10-30-10)	300	82800	1800
D.8	19 Sep	1.32	0.02	0	100	550	702	curved	50 (10-30-10)	300	74400	1500
9.1	14 Sep	1.32	0.15	22.5	100	10	699	curved	50 (10-30-10)	300	76900	3700
C.6	14 Sep	1.32	0.7	100	100	10	699	curved	50 (10-30-10)	300	76900	3700
9.3	12 Sep	1.36	1	121	200	10	705	curved	50 (10-30-10)	300	73700	2100
9.3	12 Sep	1.36	1	143.6	50	10	705	curved	50 (10-30-10)	300	73700	2100
9.4	8 Sep	1.36	0.15	22.5	100	10	694	curved	50 (10-30-10)	300(250)	75900	2700
C.11	7 Sep	1.36	0.2	30	50	10	702	curved	50 (10-30-10)	300	76100	2200
C.10	7 Sep	1.36	0.25	12	200	10	702	curved	50 (10-30-10)	300	76100	2200
C.9	1 Sep	1.36	0.05	0	100	10	707	curved	50 (10-30-10)	300	77700	1900
C.2	30 Aug	1.36	2	292	100	10	708	curved	50 (10-30-10)	300	79000	4400
C.1	30 Aug	1.36	2.5	365	100	10	708	curved	50 (10-30-10)	300	79000	4400
D.5	29 Aug	0.167	2	1080	100	10	701	curved	50 (10-30-10)	300	70500	4100
C.5	29 Aug	1.36	0.98	138	100	10	701	curved	50 (10-30-10)	300	70500	4100
D.12	23 Aug	4.89	1	48	100	10	984	curved	60 (15-30-15)	250	70400	3200
D.11	23 Aug	4.89	1	48	100	10	686	curved	50 (10-30-10)	300	70400	3200
D.10	23 Aug	4.89	1	48	100	10	505	curved	50 (10-30-10)	400	70400	3200
D.9	19 Aug	1.36	1	140	100	10	511	curved	50 (10-30-10)	400	74900	2300
8.2	19 Aug	1.36	1	140	100	10	1006	curved	60 (15-30-15)	250	74900	2300
C.3	18 Aug	1.36	1.5	225	100	10	695	curved	50 (10-30-10)	300	73900	2500
C.8	18 Aug	1.36	0.15	22.5	100	10	695	curved	50 (10-30-10)	300	73900	2500
D.6	4 Aug	0.167	1	510	100	10	999	curved	60 (15-3-15)	250	75000	2400
C.4	3 Aug	1.36	1	140	100	10	703	curved	50 (10-30-10)	300	73200	1000
C.7	3 Aug	1.36	0.5	70	100	10	703	curved	50 (10-30-10)	300	73200	1000
D.4	2 Aug	0.167	0.75	373	100	10	697	curved	50 (10-30-10)	300	71700	1300
D.1	2 Aug	0.167	0.02	0	100	10	697	curved	50 (10-30-10)	300	71700	1300
D.2	1 Aug	0.167	0.15	67	100	10	699	curved	50 (10-30-10)	300	71600	800
D.3	29 July	0.167	0.5	246	100	10	700	curved	50 (10-30-10)	300	73000	1100
6.21	29 July	0.167	1.5	760	100	10	700	curved	50 (10-30-10)	300	73000	1100
E.3	9 May	0.18	0.5	246	100	10	706	square	50	300	71300	2200
6.21	9 May	0.18	1.5	756	100	10	706	square	50	300	71300	2200
E.1	10 May	0.18	0.15	67	100	10	699	square	50	300	72000	1600
E.2	10 May	0.18	0.25	127.5	100	10	699	square	50	300	72000	1600
E.4	3 May	0.18	1	510	100	10	590	square	50	350	73600	1240
E.5	2 May	0.18	1	510	100	10	842	square	50	245	75700	2060
E.6	26 April	5.5	2	108	100	10	691	square	50	300	78000	1200
E.7	25 April	0.18	1	510	100	10	689	square	50	300	75600	1700
E.8	25 April	0.18	1	510	100	10	989	square	50	200	75600	1700
E.9	20 April	0.18	1	510	100	10	1005	square	50	200	78500	1500
E.10	20 April	0.18	1	510	100	10	502	square	50	400	78500	1500
6.14	12 April	0.18	1	510	100	10	710	square	50	300	75000	1600
6.12	5 April	0.18	1	510	100	10	690	square	50	300	72300	1200